Title
Cosmic Microwave Background Polarization Science and Optical Design of the POLARBEAR and Simons Array Experiments

Author
Matsuda, Frederick Takayuki

Publication Date
2017

Peer reviewed|Thesis/dissertation

UNIVERSITY OF CALIFORNIA, SAN DIEGO

Cosmic Microwave Background Polarization Science and Optical Design of the POLARBEAR and Simons Array Experiments

A dissertation submitted in partial satisfaction of the
requirements for the degree
Doctor of Philosophy

in

Physics

by

Frederick Takayuki Matsuda

Committee in charge:

Professor Brian Keating, Co-Chair
Professor Hans Paar, Co-Chair
Professor Craig Callender
Professor Gabriel Rebeiz
Professor Shelley Wright

2017

The dissertation of Frederick Takayuki Matsuda is approved, and it is acceptable in quality and form for publication on microfilm and electronically:

Co-Chair

Co-Chair

University of California, San Diego

2017

TABLE OF CONTENTS

LIST OF FIGURES

LIST OF TABLES

ACKNOWLEDGEMENTS

First I would like to thank my co-advisor Brian Keating for providing me with many research opportunities in the project, for all the advice throughout my graduate school career, and various funding and award opportunities. I would also like to thank my co-advisor Hans Paar for all the valuable guidance he has given me over the years especially in the FTS project.

I would like to thank Adrian Lee for all of the opportunities and guidance he has given me from Berkeley in the POLARBEAR collaboration. I would like to give special thanks to Paul Richards who taught me a great amount of scientific and instrumentation knowledge tied closely to optics. I thank Kam Arnold and Akito Kusaka for all the advice and management of project tasks that both have done for the collaboration as well as for me. I thank Yuji Chinone and Haruki Nishino who have been very friendly to me throughout the years and have taught me great amounts of analysis work right when I joined the project.

I would like to thank all my co-workers in the POLARBEAR collaboration. The POLARBEAR and Simons Array experiments cannot be achieved without the hard work from all the members. I really appreciated everyone's help and advice pertaining to not only my area of expertise but also in areas that I needed help and detailed input in.

I feel very fortunate to have been able to work in such a great laboratory with wonderful people at UCSD. I thank all my lab-mates: Nathan Miller, Nate Stebor, Dave Boettger, Chang Feng, Darcy Barron, Praween Siritanasak, Marty Navaroli, David Leon, Tucker Elleflot, Logan Howe, Lindsay Lowry, Alex Zahn, Grant Teply, Nick Galitzki, and Max Silva-Feaver. The experience would definitely not have been as great as it has been without these people.

I would also like to thank all my family and friends who have supported me in my private life throughout the 7 years I was in San Diego. I would of definitely not have been successful without the warm support from the people around me.

OFFICIAL ACKNOWLEDGEMENTS

Figures 3.1, 3.13. 3.14, and 3.15 are reprints of materials as appears in:

The POLARBEAR Collaboration: P. A. R. Ade, Y. Akiba, A. E. Anthony, K. Arnold, M. Atlas, D. Barron, D. Boettger, J. Borrill, S. Chapman, Y. Chinone, M. Dobbs, T. Elleflot, J. Errard, G. Fabbian, C. Feng, D. Flanigan, A. Gilbert, W. Grainger, N. W. Halverson, M. Hasegawa, K. Hattori, M. Hazumi, W. L. Holzapfel, Y. Hori, J. Howard, P. Hyland, Y. Inoue, G. C. Jaehnig, A. H. Jaffe, B. Keating, Z. Kermish, R. Keskitalo, T. Kisner, M. Le Jeune, A. T. Lee, E. M. Leitch, E. Linder, M. Lungu, F. Matsuda, T. Matsumura, X. Meng, N. J. Miller, H. Morii, S. Moyerman, M. J. Myers, M. Navaroli, H. Nishino, A. Orlando, H. Paar, J. Peloton, D. Poletti, E. Quealy, G. Rebeiz, C. L. Reichardt, P. L. Richards, C. Ross, I. Schanning, D. E. Schenck, B. D. Sherwin, A. Shimizu, C. Shimmin, M. Shimon, P. Siritanasak, G. Smecher, H. Spieler, N. Stebor, B. Steinbach, R. Stompor, A. Suzuki, S. Takakura, T. Tomaru, B. Wilson, A. Yadav, O. Zahn. A Measurement of the Cosmic Microwave Background B-mode Polarization Power Spectrum at Sub-degree Scales with POLARBEAR. The Astrophysical Journal, Vol. 794, No 2, pp. 171-192 , October 2014, doi:10.1088/0004-637X/794/2/171. The dissertation author made essential contributions to many aspects of this work especially in the data analysis.

Figures 3.2 (left), 3.3, and 3.5 (right) are reprints of materials as appears in: D. Barron, P. Ade, A. Anthony, K. Arnold, D. Boettger, J. Borrill, S. Chapman, Y. Chinone, M. Dobbs, J. Edwards, J. Errard, G. Fabbian, D. Flanigan, G. Fuller, A. Ghribi, W. Grainger, N. Halverson, M. Hasegawa, K. Hattori, M. Hazumi, W. Holzapfel, J. Howard, P. Hyland, G. Jaehnig, A. Jaffe, B. Keating, Z. Kermish, R. Keskitalo, T. Kisner, A. T. Lee, M. Le Jeune, E. Linder, M. Lungu, F. Matsuda, T. Matsumura, X. Meng, N. J. Miller, H. Morii, S. Moyerman, M. Meyers, H. Nishino, H. Paar, J. Peloton, E. Quealy, G. Rebeiz, C. L. Reichart, P. L. Richards, C. Ross, A. Shimizu, C. Shimmin, M. Shimon, M. Sholl, P. Siritanasak, H. Spieler, N. Stebor, B. Steinbach, R. Stompor, A. Suzuki, T. Tomaru, C. Tucker, A. Yadav, O. Zahn. The POLARBEAR Cosmic Microwave Background Polarization Experiment. Journal of Low Temperature Physics, Vol. 176, No 5-6, pp. 726-732, September 2014, doi:10.1007/s10909-013-1065-5. The dissertation author made essential contributions to many aspects of this work especially in instrument optical design and deployment.

Figures 3.5 (left) and 3.6 are reprints of materials as appears in: K. Arnold, P. A. R. Ade, A. E. Anthony, D. Barron, D. Boettger, J. Borrill, S. Chapman, Y. Chinone, M. A. Dobbs, J. Errard, G. Fabbian, D. Flanigan, G. Fuller, A. Ghribi, W. Grainger, N. Halverson, M. Hasegawa, K. Hattori, M. Hazumi, W. L. Holzapfel, J. Howard, P. Hyland, A. Jaffe, B. Keating, Z. Kermish, T. Kisner, M. Le Jeune, A. T. Lee, E. Linder, M. Lungu, F. Matsuda, T. Matsumura, N. J. Miller, X. Meng, H. Morii, S. Moyerman, M. J. Myers, H. Nishino, H. Paar, E. Quealy, C. Reichardt, P. L. Richards, C. Ross, A. Shimizu, C. Shimmin, M. Shimon, M. Sholl, P. Siritanasak, H. Speiler, N. Stebor, B. Steinbach, R. Stompor, A. Suzuki, T. Tomaru, C. Tucker, O. Zahn. The bolometric focal plane array of the POLARBEAR CMB experiment. Millimeter, Submillimeter, and Far-Infrared Detectors and Instrumentation for Astronomy VI, Proc SPIE 8452, 84521D, September 24, 2012, doi:10.1117/12.927057. The dissertation author made essential contributions to many aspects of this work especially in instrument optical design and deployment.

Chapter 4 includes material in preparation for publication for: F. Matsuda and The POLARBEAR Collaboration. Spectroscopic Characterization of the POLARBEAR Instrument. In preparation. The dissertation author is the first author of this material in preparation and lead this project.

Figures 5.1, 5.3 (left), 5.4, 5.5, and 5.6 are reprints of materials as appears in: N. Stebor, P. Ade, Y. Akiba, C. Aleman, K. Arnold, C. Baccigalupi, B. Barch, D. Barron, S. Beckman, A. Bender, D. Boettger, J. Borrill, S. Chapman, Y. Chinone, A. Cukierman, T. de Haan, M. Dobbs, A. Ducout, R. Dunner, T. Elleflot, J. Errard, G. Fabbian, S. Feeney, C. Feng, T. Fujino, G. Fuller, A. J. Gilbert, N. Goeckner-Wald, J. Groh, G. Hall, N. Halverson, T. Hamada, M. Hasegawa, K. Hattori. M. Hazumi, C. Hill, W. L. Holzapfel, Y. Hori, L. Howe, Y. Inoue, F. Irie, G. Jaehnig, A. Jaffe, O. Jeong, N. Katayama, J. P. Kaufman, K. Kazemzadeh, B. G. Keating, Z. Kermish, R. Keskitalo, T. Kisner, A. Kusaka, M. Le Jeune, A. T. Lee, D. Leon, E. V. Linder, L. Lowry, F. Matsuda, T. Matsumura, N. Miller, J. Montgomery, M. Navaroli, H. Nishino, H. Paar, J. Peloton, D. Poletti, G. Puglisi, C. R.

Raum, G. M. Rebeiz, C. L. Reichardt, P. L. Richards, C. Ross, K. M. Rotermund, Y. Segawa, B. D. Sherwin, I. Shirley, P. Siritanasak, L. Steinmetz, R. Stompor, A. Suzuki, O. Tajima, S. Takada, S. Takatori, G. P. Teply, A. Tikhomirov, T. Tomaru, B. Westbrook, N. Whitehorn, A. Zahn, O. Zahn. The Simons Array CMB polarization experiment. Millimeter, Submillimeter, and Far-Infrared Detectors and Instrumentation for Astronomy VIII, Proc SPIE 9914, 99141H, July 20, 2016, doi:10.1117/12.2233103. The dissertation author made essential contributions to many aspects of this work especially in instrument optical design and development.

Figure 7.1 was provided by Yuji Chinone. The dissertation author made essential contributions to many aspects of this work.

VITA

2010	B. A. in Physics, University of California, Berkeley
2010	B. A. in Astrophysics, University of California, Berkeley
2011-2017	Graduate Student Researcher, University of California, San Diego
2017	Ph. D. in Physics, University of California, San Diego

PUBLICATIONS

The POLARBEAR Collaboration: P. A. R. Ade, M. Aguilar, Y. Akiba, K. Arnold, C. Baccigalupi, D. Barron, D. Beck, F. Bianchini, D. Boettger, J. Borrill, S. Chapman, Y. Chinone, K. Crowley, A. Cukierman, M. Dobbs, A. Ducout, R. Dunner, T. Elleflot, J. Errard, G. Fabbian, S. M. Feeney, C. Feng, T. Fujino, N. Galitzki, A. Gilbert, N. Goeckner-Wald, J. Groh, T. Hamada, G. Hall, N. W. Halverson, M. Hasegawa, M. Hazumi, C. Hill, L. Howe, Y. Inoue, G. C. Jaehnig, A. H. Jaffe, O. Jeong, D. Kaneko, N. Katayama, B. Keating, R. Keskitalo, T. Kisner, N. Krachmalnicoff, A. Kusaka, M. Le Jeune, A. T. Lee, E. M. Leitch, D. Leon, E. Linder, L. Lowry, F. Matsuda, T. Matsumura, Y. Minami, J. Montgomery, M. Navaroli, H. Nishino, H. Paar, J. Peloton, A. T.. P. Pham, D. Poletti, G. Puglisi, C. L. Reichardt, P. L. Richards, C. Ross, Y. Segawa, B. D. Sherwin, M. Silva, P. Siritanasak, N. Stebor, R. Stompor, A. Suzuki, O. Tajima, S. Takakura, S. Takatori, D. Tanabe, G. P. Teply, T. Tomaru, C. Tucker, N. Whitehorn, A. Zahn. A Measurement of the Cosmic Microwave Background *B*-Mode Polarization Power Spectrum at Sub-Degree Scales from 2 years of POLARBEAR Data. Astro-ph.IM, eprint 1705.02907, May, 2017.

S. Takakura, M. Aguilar, Y. Akiba, K. Arnold, C. Baccigalupi, D. Barron, S. Beckman, D. Boettger, J. Borrill, S. Chapman, Y. Chinone, A. Cukierman, A. Ducout, T. Elleflot, J. Errard, G. Fabbian, T. Fujino, N. Galitzki, N. Goeckner-Wald, N. W. Halverson, M. Hasegawa, K. Hattori, M. Hazumi, C. Hill, L. Howe, Y. Inoue, A. H. Jaffe, O. Jeong, D. Kaneko, N. Katayama, B. Keating, R. Keskitalo, T. Kisner, N. Krachmalnicoff, A. Kusaka, A. T. Lee, D. Leon, L. Lowry, F. Matsuda, T. Matsumura, M. Navaroli, H. Nishino, H. Paar, J. Peloton, D. Poletti, G. Puglisi, C. L. Reichardt, C. Ross, P. Siritanasak, A. Suzuki, O. Tajima, S. Takatori, G. Teply. Performance of a continuously rotating half-wave plate on the POLARBEAR telescope. Journal of Cosmology and Astroparticle Physics, Vol. 2017, No 5, pp. 8, May 2017. doi:10.1088/1475-7516/2017/05/008.

Y. Inoue, P. Ade, Y. Akiba, C. Aleman, K. Arnold, C. Baccigalupi, B. Barch, D. Barron, A. Bender, D. Boettger, J. Borrill, S. Chapman, Y. Chinone, A. Cukierman, T. de Haan, M. A. Dobbs, A. Ducout, R. Dünner, T. Elleflot, J. Errard, G. Fabbian, S. Feeney, C. Feng, G. Fuller, A. J. Gilbert, N. Goeckner-Wald, J. Groh, G. Hall, N. Halverson, T. Hamada, M. Hasegawa, K. Hattori, M. Hazumi, C. Hill, W. L. Holzapfel, Y. Hori, L. Howe, F. Irie, G. Jaehnig, A. Jaffe, O. Jeong, N. Katayama, J. P. Kaufman, K. Kazemzadeh, B. G. Keating, Z. Kermish, R. Keskitalo, T. S. Kisner, A. Kusaka, M. Le Jeune, A. T. Lee, D. Leon, E. V. Linder, L. Lowry, F. Matsuda, T. Matsumura, N. Miller, K. Mizukami, J. Montgomery, M. Navaroli, H. Nishino, H. Paar, J. Peloton, D. Poletti, G. Puglisi, C. R. Raum, G. M. Rebeiz, C. L. Reichardt, P. L. Richards, C. Ross, K. M. Rotermund, Y. Segawa, B. D. Sherwin, I. Shirley, P. Siritanasak, N. Stebor, R. Stompor, J. Suzuki, A. Suzuki, O. Tajima, S. Takada, S. Takatori, G. P. Teply, A. Tikhomirov, T. Tomaru, N. Whitehorn, A. Zahn, O. Zahn. POLARBEAR-2: an instrument for CMB polarization measurements. Millimeter, Submillimeter, and Far-Infrared Detectors and Instrumentation for Astronomy VIII, Proc SPIE 9914, 99141I, August 8, 2016. doi:10.1117/12.2231961

D. Poletti, G. Fabbian, M. Le Jeune, J. Peloton, K. Arnold, C. Baccigalupi, D. Barron, S. Beckman, J. Borrill, S. Chapman, Y. Chinone, A. Cukierman, A. Ducout, T. Elleflot, J. Errard, S. Feeney, N. Goeckner-Wald, J. Groh, G. Hall, M. Hasegawa, M. Hazumi, C. Hill, L. Howe, Y. Inoue, A. H. Jaffe, O. Jeong, N. Katayama, B. Keating, R. Keskitalo, T. Kisner, A. Kusaka, A. T. Lee, D. Leon, E. Linder, L. Lowry, F. Matsuda, M. Navaroli, H. Paar, G. Puglisi, C. L. Reichardt, C. Ross, P. Siritanasak, N. Stebor, B. Steinbach, R. Stompor, A. Suzuki, O. Tajima, G. Teply, N. Whitehorn. Making maps of Cosmic Microwave Background polarization for B-mode studies: the POLARBEAR example. astro-ph.IM, eprint 1608.01624, August 5, 2016.

N. Stebor, P. Ade, Y. Akiba, C. Aleman, K. Arnold, C. Baccigalupi, B. Barch, D. Barron, S. Beckman, A. Bender, D. Boettger, J. Borrill, S. Chapman, Y. Chinone, A. Cukierman, T. de Haan, M. Dobbs, A. Ducout, R. Dunner, T. Elleflot, J. Errard, G. Fabbian, S. Feeney, C. Feng, T. Fujino, G. Fuller, A. J. Gilbert, N. Goeckner-Wald, J. Groh, G. Hall, N. Halverson, T. Hamada, M. Hasegawa, K. Hattori. M. Hazumi, C. Hill, W. L. Holzapfel, Y. Hori, L. Howe, Y. Inoue, F. Irie, G. Jaehnig, A. Jaffe, O. Jeong, N. Katayama, J. P. Kaufman, K. Kazemzadeh, B. G. Keating, Z. Kermish, R. Keskitalo, T. Kisner, A. Kusaka, M. Le Jeune, A. T. Lee, D. Leon, E. V. Linder, L. Lowry, F. Matsuda, T. Matsumura, N. Miller, J. Montgomery, M. Navaroli, H. Nishino, H. Paar, J. Peloton, D. Poletti, G. Puglisi, C. R. Raum, G. M. Rebeiz, C. L. Reichardt, P. L. Richards, C. Ross, K. M. Rotermund, Y. Segawa, B. D. Sherwin, I. Shirley, P. Siritanasak, L. Steinmetz, R. Stompor, A. Suzuki, O. Tajima, S. Takada, S. Takatori, G. P. Teply, A. Tikhomirov, T. Tomaru, B. Westbrook, N. Whitehorn, A. Zahn, O. Zahn. The Simons Array CMB polarization experiment. Millimeter, Submillimeter, and Far-Infrared De-

tectors and Instrumentation for Astronomy VIII, Proc SPIE 9914, 99141H, July 20, 2016. doi:10.1117/12.2233103

C. A. Hill, S. Beckman, Y. Chinone, N. Goeckner-Wald, M. Hazumi, B. Keating, A. Kusaka, A. T. Lee, F. Matsuda, R. Plambeck, A. Suzuki, S. Takakura. Design and development of an ambient-temperature continuously-rotating achromatic half-wave plate for CMB polarization modulation on the POLARBEAR-2 experiment. Millimeter, Submillimeter, and Far-Infrared Detectors and Instrumentation for Astronomy VIII, Proc SPIE 9914 , 99142U, July 19, 2016. doi:10.1117/12.2232280

A. Suzuki, P. A. R. Ade, Y. Akiba, C. Aleman, K. Arnold, C. Baccigalupi, B. Barch, D. Barron, A. Bender, D. Boettger, J. Borrill, S. Chapman, Y. Chinone, A. Cukierman, M. Dobbs, A. Ducout, R. Dunner, T. Elleflot, J. Errard, G. Fabbian, S. Feeney, C. Feng, T. Fujino, G. Fuller, A. Gilbert, N. Goeckner-Wald, J. Groh, T. De Haan, G. Hall, N. W. Halverson, T. Hamada, M. Hasegawa, K. Hattori, M. Hazumi, C. Hill, W. L. Holzapfel, Y. Hori, L. Howe, Y. Inoue, F. Irie, G. C. Jaehnig, A. H. Jaffe, O. Jeong, N. Katayama, J. Kaufman, K. Kazemzadeh, B. Keating, Z. Kermish, R. Keskitalo, T. Kisner, A. Kusaka, M. Le Jeune, A. T. Lee, D. Leon, E. Linder, L. Lowry, F. Matsuda, T. Matsumura, N. J. Miller, K. Mizukami, J. Montgomery, M. Navaroli, H. Nishino, J. Peloton, D. Poletti, G. Puglisi, G. Rebeiz, C. Raum, C. L. Reichardt, P. L. Richards, C. Ross, K. Rotermund, Y. Segawa, B. D. Sherwin, I. Shirley, P. Siritanasak, N. Stebor, R. Stompor, J. Suzuki, O. Tajima, S. Takada, S. Takakura, S. Takatori, A. Tikhomirov, T. Tomaru, B. Westbrook, N. Whitehorn, T. Yamashita, A. Zahn, O. Zahn. The POLARBEAR-2 and the Simons Array Experiments. Journal of Low Temperature Physics, Vol. 184, No 3, pp. 805-810, January 2016. doi:10.1007/s10909-015-1425-4

The POLARBEAR Collaboration: P. A. R. Ade, Y. Akiba, A. E. Anthony, K. Arnold, M. Atlas, D. Barron, D. Boettger, J. Borrill, S. Chapman, Y. Chinone, M. Dobbs, T. Elleflot, J. Errard, G. Fabbian, C. Feng, D. Flanigan, A. Gilbert, W. Grainger, N. W. Halverson, M. Hasegawa, K. Hattori, M. Hazumi, W. L. Holzapfel, Y. Hori, J. Howard, P. Hyland, Y. Inoue, G. C. Jaehnig, A. H. Jaffe, B. Keating, Z. Kermish, R. Keskitalo, T. Kisner, M. Le Jeune, A. T. Lee, E. M. Leitch, E. Linder, M. Lungu, F. Matsuda, T. Matsumura, X. Meng, N. J. Miller, H. Morii, S. Moyerman, M. J. Myers, M. Navaroli, H. Nishino, A. Orlando, H. Paar, J. Peloton, D. Poletti, E. Quealy, G. Rebeiz, C. L. Reichardt, P. L. Richards, C. Ross, I. Schanning, D. E. Schenck, B. D. Sherwin, A. Shimizu, C. Shimmin, M. Shimon, P. Siritanasak, G. Smecher, H. Spieler, N. Stebor, B. Steinbach, R. Stompor, A. Suzuki, S. Takakura, T. Tomaru, B. Wilson, A. Yadav, O. Zahn. A Measurement of the Cosmic Microwave Background B-mode Polarization Power Spectrum at Sub-degree Scales with POLARBEAR. The Astrophysical Journal, Vol. 794, No 2, pp. 171-192 , October 2014. doi:10.1088/0004-637X/794/2/171

D. Barron, P. Ade, A. Anthony, K. Arnold, D. Boettger, J. Borrill, S. Chapman, Y. Chinone, M. Dobbs, J. Edwards, J. Errard, G. Fabbian, D. Flanigan, G. Fuller,

A. Ghribi, W. Grainger, N. Halverson, M. Hasegawa, K. Hattori, M. Hazumi, W. Holzapfel, J. Howard, P. Hyland, G. Jaehnig, A. Jaffe, B. Keating, Z. Kermish, R. Keskitalo, T. Kisner, A. T. Lee, M. Le Jeune, E. Linder, M. Lungu, F. Matsuda, T. Matsumura, X. Meng, N. J. Miller, H. Morii, S. Moyerman, M. Meyers, H. Nishino, H. Paar, J. Peloton, E. Quealy, G. Rebeiz, C. L. Reichart, P. L. Richards, C. Ross, A. Shimizu, C. Shimmin, M. Shimon, M. Sholl, P. Siritanasak, H. Spieler, N. Stebor, B. Steinbach, R. Stompor, A. Suzuki, T. Tomaru, C. Tucker, A. Yadav, O. Zahn. The POLARBEAR Cosmic Microwave Background Polarization Experiment. Journal of Low Temperature Physics, Vol. 176, No 5-6, pp. 726-732, September 2014. doi:10.1007/s10909-013-1065-5

K. Arnold, N. Stebor, P. A. R. Ade, Y. Akiba, A. E. Anthony, M. Atlas, D. Barron, A. Bender, D. Boettger, J. Borrill, S. Chapman, Y. Chinone, A. Cukierman, M. Dobbs, T. Elleflot, J. Errard, G. Fabbian, C. Feng, A. Gilbert, N. Goeckner-Wald, N. W. Halverson, M. Hasegawa, K. Hattori, M. Hazumi, W. L. Holzapfel, Y. Hori, Y. Inoue, G. C. Jaehnig, A. H. Jaffe, ăN. Katayama, B. Keating, Z. Kermish, R. Keskitalo, T. Kisner, M. Le Jeune, A. T. Lee, E. M. Leitch, E. Linder, F. Matsuda, T. Matsumura, X. Meng, N. J. Miller, H. Morii, M. J. Myers, M. Navaroli, H. Nishino, T. Okamura, H. Paar, J. Peloton, D. Poletti, C. Raum, G. Rebeiz, C. L. Reichardt, P. L. Richards, C. Ross, K. Rotermund, D. E. Schenck, B. D. Sherwin, I. Shirley, M. Sholl, P. Siritanasak, G. Smecher, B.Steinbach, R. Stompor, A. Suzuki, J. Suzuki, S. Takada, S. Takakura, T. Tomaru, B. Wilson, A. Yadav, O. Zahn. The Simons Array: expanding POLARBEAR to three multi-chroic telescopes. Millmeter, Submillmeter, and Far-Infrared Detectors and Instrumentation for Astronomy VII, Proc SPIE 9153, 91531F, August 2014. doi:10.1117/12.2057332

Y. Inoue, N. Stebor, P. A. R. Ade, Y. Akiba, K. Arnold, A. E. Anthony, M. Atlas, D. Barron, A. Bender, D. Boettger, J. Borrill, S. Chapman, Y. Chinone, A. Cukierman, M. Dobbs, T. Elleflot, J. Errard, G. Fabbian, C. Feng, A. Gilbert, N. W. Halverson, M. Hasegawa, K. Hattori, M. Hazumi, W. L. Holzapfel, Y. Hori, G. C. Jaehnig, A. H. Jaffe, ăN. Katayama, B. Keating, Z. Kermish, R. Keskitalo, T. Kisner, M. Le Jeune, A. T. Lee, E. M. Leitch, E. Linder, F. Matsuda, T. Matsumura, X. Meng, H. Morii, M. J. Myers, M. Navaroli, H. Nishino, T. Okamura, H. Paar, J. Peloton, D. Poletti, G. Rebeiz, C. L. Reichardt, P. L. Richards, C. Ross, D. E. Schenck, B. D. Sherwin, P. Siritanasak, G. Smecher, M. Sholl, B.Steinbach, R. Stompor, A. Suzuki, J. Suzuki, S. Takada, S. Takakura, T. Tomaru, B. Wilson, A. Yadav, H. Yamaguchi, O. Zahn. Thermal and optical characterization for POLARBEAR-2 optical system. Millmeter, Submillmeter, and Far-Infrared Detectors and Instrumentation for Astronomy VII, Proc SPIE 9153, 91533A, August 2014. doi:10.1117/12.2055572

The POLARBEAR Collaboration: P. A. R. Ade, Y. Akiba, A. E. Anthony, K. Arnold, M. Atlas, D. Barron, D. Boettger, J. Borrill, S. Chapman, Y. Chinone, M. Dobbs, T. Elleflot, J. Errard, G. Fabbian, C. Feng, D. Flanigan, A. Gilbert,

W. Grainger, N. W. Halverson, M. Hasegawa, K. Hattori, M. Hazumi, W. L. Holzapfel, Y. Hori, J. Howard, P. Hyland, Y. Inoue, G. C. Jaehnig, A. H. Jaffe, B. Keating, Z. Kermish, R. Keskitalo, T. Kisner, M. Le Jeune, A. T. Lee, E. M. Leitch, E. Linder, M. Lungu, F. Matsuda, T. Matsumura, X. Meng, N. J. Miller, H. Morii, S. Moyerman, M. J. Myers, M. Navaroli, H. Nishino, H. Paar, J. Peloton, E. Quealy, G. Rebeiz, C. L. Reichardt, P. L. Richards, C. Ross, I. Schanning, D. E. Schenck, B. D. Sherwin, A. Shimizu, C. Shimmin, M. Shimon, P. Siritanasak, G. Smecher, H. Spieler, N. Stebor, B. Steinbach, R. Stompor, A. Suzuki, S. Takakura, T. Tomaru, B. Wilson, A. Yadav, O. Zahn. Measurement of the Cosmic Microwave Background Polarization Lensing Power Spectrum with the POLARBEAR Experiment. Physical Review Letters, Vol. 113, No 2, pp. 021301, July 2014. doi:10.1103/PhysRevLett.113.021301

The POLARBEAR Collaboration: P. A. R. Ade, Y. Akiba, A. E. Anthony, K. Arnold, M. Atlas, D. Barron, D. Boettger, J. Borrill, C. Borys, S. Chapman, Y. Chinone, M. Dobbs, T. Elleflot, J. Errard, G. Fabbian, C. Feng, D. Flanigan, A. Gilbert, W. Grainger, N. W. Halverson, M. Hasegawa, K. Hattori, M. Hazumi, W. L. Holzapfel, Y. Hori, J. Howard, P. Hyland, Y. Inoue, G. C. Jaehnig, A. H. Jaffe, B. Keating, Z. Kermish, R. Keskitalo, T. Kisner, M. Le Jeune, A. T. Lee, E. M. Leitch, E. Linder, M. Lungu, F. Matsuda, T. Matsumura, X. Meng, N. J. Miller, H. Morii, S. Moyerman, M. J. Myers, M. Navaroli, H. Nishino, H. Paar, J. Peloton, D. Poletti, E. Quealy, G. Rebeiz, C. L. Reichardt, P. L. Richards, C. Ross, K. Rotermund, I. Schanning, D. E. Schenck, B. D. Sherwin, A. Shimizu, C. Shimmin, M. Shimon, P. Siritanasak, G. Smecher, H. Spieler, N. Stebor, B. Steinbach, R. Stompor, A. Suzuki, S. Takakura, A. Tikhomirov, T. Tomaru, B. Wilson, A. Yadav, O. Zahn. Evidence for Gravitational Lensing of the Cosmic Microwave Background Polarization from Cross-Correlation with the Cosmic Infrared Background. Physical Review Letters, Vol. 112, No 13, pp. 131302, April 2014. doi:10.1103/PhysRevLett.112.131302

T. Matsumura, P. Ade, K. Arnold, D. Barron, J. Borrill, S. Chapman, Y. Chinone, M. Dobbs, J. Errard, G. Fabbian, A. Ghribi, W. Grainger, N. Halverson, M. Hasegawa, K. Hattori, M. Hazumi, W. L. Holzapfel, Y. Inoue, S. Ishii, Y. Kaneko, B. Keating, Z. Kermish, N. Kimura, T. Kisner, W. Kranz, A. T. Lee, F. Matsuda, H. Morii, M. J. Myers, H. Nishino, T. Okamura, E. Quealy, C. Reichardt, P. L. Richards, D. Rosen, C. Ross, A. Shimizu, M. Sholl, P. Siritanasak, P. Smith, N. Stebor, R. Stompor, A. Suzuki, J. Suzuki, S. Takada, K. Tanaka, T. Tomaru, O. Zahn. POLARBEAR-2 optical and polarimeter designs. Millimeter, Submillimeter, and Far-Infrared Detectors and Instrumentation for Astronomy VI, Proc SPIE 8452, 84523E, October 5, 2012. doi:10.1117/12.926770

T. Tomaru, M. Hazumi, A. T. Lee, P. Ade, K. Arnold, D. Barron, J. Borrill, S. Chapman, Y. Chinone, M. Dobbs, J. Errard, G. Fabbian, A. Ghribi, W. Grainger, N. Halverson, M. Hasegawa, K. Hattori, W. L. Holzapfel, Y. Inoue, S. Ishii, Y.

Kaneko, B. Keating, Z. Kermish, N. Kimura, T. Kisner, W. Kranz, F. Matsuda, T. Matsumura, H. Morii, M. J. Myers, H. Nishino, T. Okamura, E. Quealy, C. L. Reichardt, P. L. Richards, D. Rosen, C. Ross, A. Shimizu, M. Sholl, P. Siritanasak, P. Smith, N. Stebor, R. Stompor, A. Suzuki, J. Suzuki, S. Takada, K. Tanaka, O. Zahn. The POLARBEAR-2 experiment. Millimeter, Submillimeter, and Far-Infrared Detectors and Instrumentation for Astronomy VI, Proc SPIE 8452, 84521H, September 24, 2012. doi:10.1117/12.926158

Z. D. Kermish, P. Ade, A. Anthony, K. Arnold, D. Barron, D. Boettger, J. Borrill, S. Chapman, Y. Chinone, M. A. Dobbs, J. Errard, G. Fabbian, D. Flanigan, G. Fuller, A. Ghribi, W. Grainger, N. Halverson, M. Hasegawa, K. Hattori, M. Hazumi, W. L. Holzapfel, J. Howard, P. Hyland, A. Jaffe, B. Keating, T. Kisner, A. T. Lee, M. Le Jeune, E. Linder, M. Lungu, F. Matsuda, T. Matsumura, X. Meng, N. J. Miller, H. Morii, S. Moyerman, M. J. Myers, H. Nishino, H. Paar, E. Quealy, C. L. Reichardt, P. L. Richards, C. Ross, A. Shimizu, M. Shimon, C. Shimmin, M. Sholl, P. Siritanasak, H. Spieler, N. Stebor, B. Steinbach, R. Stompor, A. Suzuki, T. Tomaru, C. Tucker, O. Zahn. The POLARBEAR experiment. Millimeter, Submillimeter, and Far-Infrared Detectors and Instrumentation for Astronomy VI, Proc SPIE 8452, 84521C, September 24, 2012. doi:10.1117/12.926354

K. Arnold, P. A. R. Ade, A. E. Anthony, D. Barron, D. Boettger, J. Borrill, S. Chapman, Y. Chinone, M. A. Dobbs, J. Errard, G. Fabbian, D. Flanigan, G. Fuller, A. Ghribi, W. Grainger, N. Halverson, M. Hasegawa, K. Hattori, M. Hazumi, W. L. Holzapfel, J. Howard, P. Hyland, A. Jaffe, B. Keating, Z. Kermish, T. Kisner, M. Le Jeune, A. T. Lee, E. Linder, M. Lungu, F. Matsuda, T. Matsumura, N. J. Miller, X. Meng, H. Morii, S. Moyerman, M. J. Myers, H. Nishino, H. Paar, E. Quealy, C. Reichardt, P. L. Richards, C. Ross, A. Shimizu, C. Shimmin, M. Shimon, M. Sholl, P. Siritanasak, H. Speiler, N. Stebor, B. Steinbach, R. Stompor, A. Suzuki, T. Tomaru, C. Tucker, O. Zahn. The bolometric focal plane array of the POLARBEAR CMB experiment. Millimeter, Submillimeter, and Far-Infrared Detectors and Instrumentation for Astronomy VI, Proc SPIE 8452, 84521D, September 24, 2012. doi:10.1117/12.927057

ABSTRACT OF THE DISSERTATION

Cosmic Microwave Background Polarization Science and Optical Design of the POLARBEAR and Simons Array Experiments

by

Frederick Takayuki Matsuda

Doctor of Philosophy in Physics

University of California, San Diego, 2017

Professor Brian Keating, Co-Chair
Professor Hans Paar, Co-Chair

The cosmic microwave background (CMB) radiation contains great amounts of information that allow for studying the physics of the early universe through constraining cosmological parameters in the standard ΛCDM model. The CMB temperature signal has been measured to high precision, but measuring the CMB polarization signal is still in its early stages.

The theoretically small primordial CMB polarization B-mode signal has not yet been measured, but has principle importance in that its existence would be strong evidence of inflation. This measurement allows one to probe the earliest state of the universe at energy scales of 10^{16} GeV thought to be near the Grand

Unified Theory scale. The B-mode signal arising from weak gravitational lensing by large scale structures provides information about the matter composition of the universe and puts strong constraints on the sum of the neutrino masses.

This dissertation discusses the optical design, instrumentation, data analysis, and first season science results of the POLARBEAR experiment, a CMB polarization telescope aimed to measure the B-mode signal. The results show the first evidence of non-zero lensing B-modes at sub-degree angular scales on the sky. The development and measurement results of the Fourier transform spectrometer calibration instrument used to characterize the spectral response of the POLARBEAR detectors are also described. The optical design development and systematic studies for the Simons Array, the next generation installment of the experiment, are described as well. The cross polarization effect of Mizuguchi-Dragone breaking due to a prime focus half-wave plate, and the optical redesign of the Simons Array re-imaging optics for increased optical performance at higher frequencies were studied in detail. The Simons Array is planned to fully deploy in 2018 to further study the CMB with enhanced sensitivity.

Chapter 1

Introduction

1.1 Standard Model of Cosmology

The theory that the universe started off with the Big Bang has become widely accepted. The Big Bang cosmological model is parameterized by the ΛCDM model where the Λ represents the cosmological constant and CDM is short for cold dark matter. The ΛCDM model is built upon the conceptual framework of Einstein's general relativity and the cosmological principle stating that the distribution of energy in the universe is uniform everywhere (homogenous) and has no preferred direction (isotropic). This ΛCDM model is known as the standard model of cosmology that explains the astronomical observations of the current universe made in the last few decades.

In general relativity the 4-dimensional metric tensor $g_{\mu\nu}$ is a fundamental mathematical object that defines any spacetime coordinate system. It is in general defined as

$$ds^2 = g_{\mu\nu} dx^\mu dx^\nu \tag{1.1}$$

where the indices ranges from 0 to 3 and a summation over common indices is understood. The metric defines how time and space relate in any particular coordinate system. In general relativity gravity can be fully described by the metric through the Einstein equations that describe how the metric interacts with matter and energy. The Einstein equations are [1]

$$G_{\mu\nu} \equiv R_{\mu\nu} - \frac{1}{2} g_{\mu\nu} R = 8\pi G T_{\mu\nu} \tag{1.2}$$

where $G_{\mu\nu}$ is the Einstein tensor, $R_{\mu\nu}$ and R are the Ricci tensor and scalar, G is Newton's constant, and $T_{\mu\nu}$ is the energy-momentum tensor. Hence the metric is intricately correlated with the energy of the universe as given by this equation.

In this framework of general relativity, the Friedmann-Lemaître-Robertson-Walker (FLRW) metric describes a universe based off the cosmological principle that can spatially expand and contract. The FLRW metric is given by

$$ds^2 = -c^2 dt^2 + a(t)^2 \left[\frac{dr^2}{1 - kr^2} + r^2 \left(d\theta^2 + \sin^2\theta d\phi^2 \right) \right] \tag{1.3}$$

where c is the speed of light, and the spatial coordinates are represented in spherical coordinates. k represents the curvature of space and can only have the values of $\{-1, 0, +1\}$. The parameter $a(t)$ is the called the scale factor that depends on time. The scale factor governs the expansion and contraction of space and relates coordinate distances to physical distances in the universe. Through understanding the evolution of the scale factor, one can use it as a proxy for the time of the universe. One useful quantity defined is the redshift z given by

$$1 + z \equiv \frac{1}{a(t)}. \tag{1.4}$$

z is commonly used to describe the chronological order of eras in the universe as well as the age of galaxies and stars.

The FLRW metric is an exact solution to the Einstein equations and through mathematically plugging in the FLRW metric into the Einstein equations one can derive the Friedmann equations. The first Friedmann equation is

$$\left[\frac{\dot{a}(t)}{a(t)} \right]^2 = \frac{8\pi G}{3} \frac{\epsilon(t)}{c^2} - \frac{kc^2}{a^2(t)}. \tag{1.5}$$

Related to the left hand side of this equation, it is typically defined such that

$$H(t) \equiv \frac{\dot{a}(t)}{a(t)} \tag{1.6}$$

which is known as the Hubble parameter. $\epsilon(t)$ is the energy density of the universe as a function of time. The second Friedmann equation, typically called the Friedmann acceleration equation, is

$$\frac{\ddot{a}(t)}{a(t)} = \frac{4\pi G}{3c^2}\left[\epsilon(t) + 3P\right] \tag{1.7}$$

where P is the pressure.

As can be seen in equation 1.5, the value of k represents the geometry of spatial curvature in the universe and will influence how the universe can evolve. For $k = 0$ the universe is flat with no curvature. For $k < 0$ the universe will have negative curvature and will be an open hyperbolic geometry. For $k > 0$ the universe will have positive curvature and will be a closed spherical geometry. For example if $k < 0$ the universe is infinite in extent. If the universe is already expanding and $k < 0$ the universe will continue to have accelerated expansion forever. But if $k > 0$ the universe is finite in extent and cannot evolve in a similar manner. For $k = 0$ the universe can also be infinite in extent under certain conditions [2].

Solving equation 1.5 for a flat universe one obtains ϵ_{cr}, the critical energy density, given by

$$\frac{\epsilon_{cr}}{c^2} = \frac{3H^2(t)}{8\pi G}. \tag{1.8}$$

ϵ_{cr} is the critical energy density at which the the sign of the curvature of the universe changes. Therefore the following relations hold

$$\epsilon = \epsilon_{cr} \Rightarrow k = 0 \tag{1.9}$$

$$\epsilon < \epsilon_{cr} \Rightarrow k < 0 \tag{1.10}$$

$$\epsilon > \epsilon_{cr} \Rightarrow k > 0. \tag{1.11}$$

Hence according to the energy density of the universe at any point in time, the evolution of space and time can differ due to a different spatial geometry. Typically the density is represented as a dimensionless parameter $\Omega \equiv \epsilon/\epsilon_{cr}$. The physical content of the energy density also makes significant difference in how the universe evolves. Radiation, matter, and Λ dominated universes will have differently evolving $a(t)$ and therefore the speed of expansion will change respectively. It is theorized that the current universe has gone through multiple eras and changes in its expansion history. H_0 represents the Hubble parameter value today which is commonly defined as the Hubble constant H_0. In this way the Friedmann equations describe the evolution of the scale factor and are the bases of the ΛCDM model that is commonly used today. The cosmological constant Λ is now conceptualized as dark energy that has constant energy density throughout all of space.

The ΛCDM model can be constrained using only 6 parameters: the baryon density $\Omega_b h^2$, the dark matter density $\Omega_m h^2$, the age of the universe t_0, the scalar spectral index n_s, the curvature fluctuation amplitude Δ_R^2, and the reionization optical depth τ. The greatest successes of the ΛCDM model are its agreements with various observational evidences up until the present day. Out of the many, three main observational findings that support the Big Bang theory are: the accelerated expansion of the universe observed by Hubble and type Ia Supernovae [3], light element abundance measurements [4], and the cosmic microwave background (CMB) radiation observations [5].

1.2 The Cosmic Microwave Background

13.8 billion years ago [6] the universe started with the Big Bang. Initially the universe can be approximated as a hot ionized plasma where photons, quarks, and matter are all in equilibrium as a "baryon-photon" fluid. The plasma is very homogenous and isotropic. This era of the universe is considered to be radiation dominated due to the high temperature plasma with very high energy photons. From the Friedmann equations it can be shown that $a \propto t^{1/2}$ and hence the universe will expand as time proceeds.

As the universe expands the temperature of the plasma will gradually decrease according to the laws of thermal dynamics. As the temperature of the plasma decreases, the reaction rates between photons and particles in equilibrium will decrease respectively. As the reaction rates of various particles fall below the expansion rate of the universe, each respective particle will decouple from the plasma. An example of this is the relativistic neutrinos. Approximately when the temperature of the universe decreases below 1 MeV the neutrino-electron coupling rate will drop below the expansion rate, and the neutrinos will decouple from the plasma. Theoretically this background of neutrinos should be observable today as the cosmic neutrino background.

As the temperature of the plasma further decreases to less than ~ 1 eV, the rate of hydrogen ionization starts to fall below the expansion rate. Neutral hydrogen begins to form and the matter decouples from the photons. This occurs at $z \sim 1100$ or 380,000 years after the Big Bang, and is known as recombination. Once recombination occurs, the photons that were coupled to the matter through Compton scattering off electrons can now "free-stream" through space. Characteristically this point in time is called the "surface of last scattering" and these photons that free-stream toward the observer now are known as the cosmic microwave background (CMB). The CMB radiation is the earliest observable light in the current universe and thus contains valuable information about the beginning of the universe.

1.2.1 CMB Observations

The very first observations of the CMB were measured by Penzias and Wilson in 1964 using Bell Laboratory's Holmdel horn antenna in New Jersey [7]. Although the existence of the CMB was predicted as early as in the 1950s by Gamow [8], the discovery of the CMB was made accidentally. Penzias and Wilson described that the measured temperature of the CMB at a wavelength of 7.35 cm was $3.5 \pm 0.1\ K$. Due to this great discovery that was supported by multiple theorist, the CMB observational field was started and continues today with far superior precision measurements.

In 1992 the CMB was measured by the COsmic Background Explorer (COBE) satellite [9, 10]. Three different instruments were mounted on the COBE satellite: the Differential Microwave Radiometer (DMR), the Far Infrared Absolute Spectrophotometer (FIRAS), and the Diffuse Infrared Background Experiment (DIRBE). FIRAS measured that the CMB was nearly a perfect blackbody spectrum, as expected from theory, with an absolute temperature of $2.725 \pm 0.001\ K$ [11]. DMR measured full sky maps of the intrinsic anisotropies of the CMB. These small fluctuations on the orders of tens to hundreds of μK are related to the initial density fluctuations of the universe and allow for probing the earliest physics of the universe.

In 2003 further precision full sky CMB anisotropy measurements were made by the Wilkinson Microwave Anisotropy Probe (WMAP) satellite [12]. WMAP played a key role in further establishing the current ΛCDM model. In 2013 the current most precise full sky CMB anisotropy measurements were made by the Planck satellite mounted with two instruments: the Low Frequency Instrument (LFI) and the High Frequency Instrument (HFI) [13]. Planck put further tight constraints on the cosmological parameters in the ΛCDM model as well as provided measurements of potential foreground contamination through measurements across a wide range of frequencies between 30-857 GHz.

Various ground-based experiments have also measured the CMB temperature anisotropies to very high precision especially at small angular scales. Due to size and weight limitations of satellite missions it is very difficult to launch large aperture telescopes into space. While ground-based experiments have geological limitations on observing the full CMB sky, they typically can be made to have much larger optical apertures to measure the CMB with high resolutions that are not currently feasible by satellite missions. For example the CMB temperature anisotropies have been measured to extremely high precision at small angular scales by experiments such as the South Pole Telescope (SPT) [14] and the Atacama Cosmology Telescope (ACT) [15].

1.2.2 CMB Anisotropies

The CMB has been theorized and measured to be nearly a perfect blackbody spectrum as described by the standard Planck's law:

$$I(\nu, T) = \frac{2h\nu^3}{c^2}\frac{1}{e^{\frac{h\nu}{k_B T}} - 1} \tag{1.12}$$

where h is the Planck constant, k_B is the Boltzmann constant, ν is the frequency of light, and T is the temperature. Currently the best measurement of the CMB blackbody temperature is 2.72548 ± 0.00057 K obtained from an analysis using

FIRAS and WMAP data [16]. The current CMB temperature can be calculated through understanding the physics at recombination as well as the history of the expansion of the universe until today.

As briefly mention earlier, recombination is the time in which neutral hydrogen starts to form within the plasma and causes the photons and matter to decouple. As the temperature of the universe drops below ~ 1 eV the free electron fraction X_e also gradually decreases as the rate of ionization starts to become dominated by the rate of neutral Hydrogen formation. These physics can be described by the Boltzmann and Saha equations to model the evolution of X_e throughout this time of recombination. As X_e drops below $\sim 10^{-2}$ the photons decouple.

The temperature of the photons when they decouple is theorized to be ~ 3000 K. Wien's displacement law is given by

$$\lambda_{max} = \frac{b}{T} \tag{1.13}$$

where b is Wien's displacement constant. Wien's law describes that any blackbody spectrum peaks at a wavelength inversely proportional to the temperature of the photons. Hence the change in any blackbody spectrum can be determined from the change in temperature or the peak wavelength. Because the universe continues to expand even after the photons start to free-stream, as the universe evolves the wavelength of light will be redshifted accordingly which corresponds to a decrease in the blackbody temperature as described by the above equation. Therefore the CMB light observed today must theoretically be at a much lower temperature around ~ 3 K peaking at the millimeter wavelengths. This CMB temperature is observed to be very uniform to one part in 10^4.

Even though the CMB is known to be very uniform, CMB anisotropies of less than 100s of μK have also been measured to great precision. These CMB anisotropies originate from the initial inhomogeneities of the universe and contain vast amounts of information that allow us to probe the state of the very early universe. These initial inhomogeneities are theorized to arise from the mechanism of inflation as will be described in section 1.3. The inhomogeneities give rise to perturbations in both the radiation and matter of the initial plasma as well as the dark matter which evolve with different physics as the universe evolves.

In order to parametrize the inhomogeneities in the framework of general relativity, the perturbations must be introduced into the metric. In this particular case the perturbations are scalar metric perturbations given by

$$g_{00}(\vec{x},t) = -1 - 2\Psi(\vec{x},t) \tag{1.14}$$

$$g_{0i}(\vec{x},t) = 0 \tag{1.15}$$

$$g_{ii}(\vec{x},t) = a^2\delta_{ij}(1 + 2\Phi(\vec{x},t)) \tag{1.16}$$

where Ψ is a perturbation of the form of the Newtonian potential and Φ is the perturbation of spatial curvature. These perturbations can be plugged into the Einstein equations to show how they affect the photon and matter distributions of the universe. Because the perturbations are assumed to be small in the initial plasma, the equations stay linear. Hence when working with the differential linear equations that arise from the Einstein equations, it is convenient to take the Fourier transform and work in the Fourier space. With this assumption all Fourier modes $\vec{k}$ evolve independently which simplifies the interpretation because each k mode can be understood independently. It must be noted that for the matter perturbations this technique does not work for matter evolution today at small scales due to arising nonlinearities but is still applicable for early matter evolution.

Applying the scalar perturbations and taking the Fourier transform, the Einstein equations for the plasma of the early universe can be written as

$$k^2\Phi + 3\frac{\dot{a}}{a}\left(\dot{\Phi} - \Psi\frac{\dot{a}}{a}\right) = 4\pi G a^2\left(\rho_m\delta_m + 4\rho_r\Theta_{r,0}\right) \tag{1.17}$$

$$k^2\left(\Phi + \Psi\right) = -32\pi G a^2\rho_r\Theta_{r,2} \tag{1.18}$$

where the subscript m and r represents matter and radiation components. Θ is the perturbation to the radiation distribution and the subscript represents the multipole moment. These equations apply to the early universe and show that the higher order moments of Θ are negligibly small. The evolution of the scalar perturbations in the plasma are primarily determined by the lower order moments. These equations describe how the perturbations evolve within the plasma up to the time of decoupling to determine the CMB anisotropies seen today.

The evolution of the Fourier modes can be interpreted as acoustic oscillations of the plasma. The scalar perturbations create initial over and under dense regions within the plasma and dark matter distributions. As time goes on the matter will tend to fall into the over dense regions due to gravity and gradually accumulate. Because the photons and matter are in equilibrium within the plasma, the photon pressure will oppose the gravitational infall. The opposing forces will create oscillating modes that will propagate at the speed of sound within the plasma. The evolution of these acoustic modes will continue until decoupling, but "freeze-in" after the photons start to free-stream because there are no more strong interactions between the photons and matter. Different size modes evolve differently in the plasma and this determines the final anisotropies in the observed CMB.

The comoving horizon is the maximum distance a photon could have traveled since the beginning of the universe. Because information cannot travel faster than the speed of light, this comoving horizon is the largest distance in which two locations in space can be causally connected in the universe. The comoving horizon grows as a function of conformal time η

$$\eta = \int_0^t \frac{dt'}{a(t')} \tag{1.19}$$

but the universe is also expanding. Hence there are modes that enter the horizon before decoupling (sub-horizon) and modes that never enter the horizon before decoupling (super-horizon).

Sub-horizon perturbation modes start to evolve and oscillate as these modes enter the comoving horizon. According to the time that the modes entered the horizon, the amplitude of the modes at the time of decoupling will differ. There will be modes that have grown to their maximum at the time of decoupling as well as modes that entered the horizon slightly earlier which will have already started to diminish in amplitude to show a minimum. Even smaller modes may have gone through multiple oscillations by decoupling. Perturbation modes on super-horizon scales do not evolve much and approximately maintain their primordial amplitude because they never oscillated. The accumulation of the amplitudes of these modes on various angular scales at the time of decoupling determine the final CMB anisotropy signal.

1.2.3 Power Spectra

Because the CMB is Gaussian field, the statistical properties of the CMB fluctuations can be fully characterized by calculating the power spectrum. From Earth one observes the CMB sky in polar coordinates, and hence it is natural to decompose the sky signal into spherical harmonics. The temperature anisotropies Θ can be written as

$$\Theta(\theta,\phi) = \sum_{\ell=1}^{\infty}\sum_{m=-\ell}^{\ell} a_{\ell m}^{T} Y_{\ell m}(\theta,\phi) \tag{1.20}$$

where (θ,ϕ) are the polar coordinates, $Y_{\ell m}$ are the spherical harmonic eigenfunctions, $a_{\ell m}^{T}$ are the magnitudes of the temperature modes, and the subscripts ℓ and m represent the multipole moment of the mode. The multipole moment is a representation of the angular scale on the sky and hence approximately has the relation

$$\theta_{scale} \propto \frac{180^\circ}{\ell}. \tag{1.21}$$

The spherical harmonics are normalized according to

$$\int d\Omega Y_{\ell m}(\theta,\phi) Y_{\ell' m'}^{*}(\theta,\phi) = \delta_{\ell\ell'}\delta_{mm'}. \tag{1.22}$$

According to the properties of the Gaussian field, each $a_{\ell m}$ is drawn from a Gaussian distribution with a mean value of zero and finite variance. Hence the CMB anisotropies are described by the value of the variance and this variance should have the same value for a given angular scale ℓ. The power spectrum is a mathematical representation of the variance in $a_{\ell m}$ and is given by

$$C_{\ell}^{TT} = \frac{1}{2\ell+1}\sum_{m=-\ell}^{\ell} a_{\ell m}^{T} a_{\ell m}^{T*} = \langle a_{\ell m}^{T} a_{\ell m}^{T*}\rangle \tag{1.23}$$

where C_{ℓ}^{TT} is the temperature power spectrum. Because the power spectrum C_ℓ is a measure of the variance, there is a fundamental uncertainty in the measurement due to the limited number of samples of these modes that can be measured even from the full sky. This is the most prominent at large angular scales or low ℓ modes that span large fractions of the sky. This limit is called cosmic variance given by

$$\frac{\Delta C_\ell}{C_\ell} = \sqrt{\frac{2}{2\ell+1}}. \tag{1.24}$$

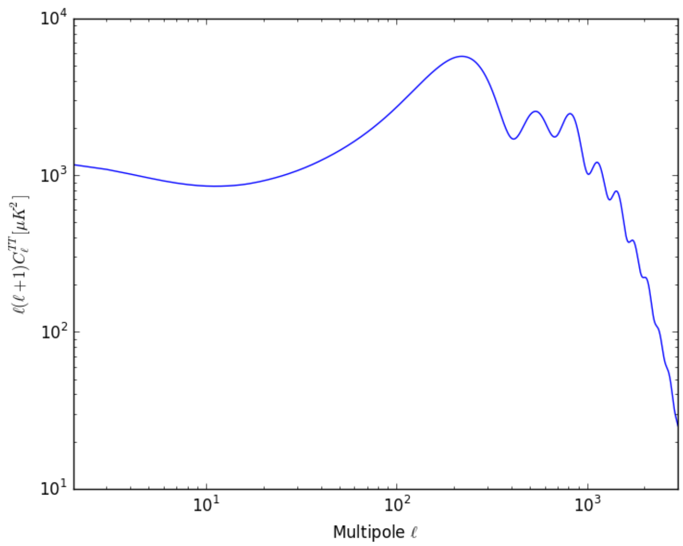

Figure 1.1: **Theoretical CMB temperature power spectrum** — The theoretical CMB power spectrum of the temperature anisotropies due to scalar perturbations based off the current ΛCDM cosmological model is shown. The power spectrum was calculated using the CAMB package [17].

A theoretical temperature power spectrum that agrees with current observations is shown in Figure 1.1. At small ℓ or the largest angular scales no oscillatory behavior is seen because these are super-horizon modes that do not evolve much within the initial plasma. One predominant source of the large scale anisotropies is called the Sachs-Wolfe effect [18]. For smaller scales the acoustic oscillations can be readily observed with the $\ell \sim 200$ mode at a maximum at the time of decoupling. Because decoupling is not instantaneous but occurs over finite time, modes that are smaller than the photon random walk distance during recombination are damped. Hence the higher ℓ modes show a damping tail.

1.3 Inflation

The CMB anisotropy measurements are strong evidences that support the basic Big Bang model, but at the same time raise various theoretical issues that must be solved. A now widely accepted solution to these issues is the mechanism of inflation.

1.3.1 Cosmological Issues

There are three issues that arose from the cosmological observations out of which two are directly observable from the CMB measurements. The most easily observable being the Horizon problem. The CMB today is very isotropic or uniform across the sky with only very small anisotropies smaller than one part in 10^4. But based off current observations, the universe is theorized to have started out with initial inhomogeneities across all scales, and hence different locations on the sky would have started out with slightly different temperatures. At the time of decoupling, approximately when the age of the universe was 380,000 years, the comoving horizon only spans a finite angular scale on the sky of less than $\sim 2^{\circ}$. It is theoretically difficult for different parts of the sky that are separated by distances much larger than the horizon to become so uniform today. Without causal contact this homogeneity today is difficult to achieve.

The second issue that can be observed from the CMB as well as other astronomical observations is the Flatness problem. The angular scales of the CMB fluctuations depend greatly on the curvature of the universe. The position of the acoustic peaks provide a precise probe in measuring the energy density of the universe correlated with the curvature. The CMB measurements closely agree with a very flat universe today. This implies that the energy density of the universe today is essential equal to the critical energy density of the universe as explained by equation 1.8. It is difficult to theorize that the universe is so "finely tuned" such that the universe is exactly flat. Even very small deviations away from flatness at early times in the universe would evolve the universe away from the current flat state and hence the current evolution of the universe is once again difficult to statistically achieve.

The third issue is not observable from the CMB but is known as the Relic problem. Magnetic monopoles have not yet been observed in the universe while in the Big Bang model stable magnetic monopoles should have been created in the high energy plasma and persisted to today. This lack of magnetic monopoles today is unexplained by the Big Bang models.

1.3.2 Inflationary Model

Cosmic inflation is an extension of the Big Bang model that solves the issues mentioned in the previous section. Inflation is a short period of superluminal expansion in the beginning moments of the universe, 10^{-36} seconds after the Big Bang. During inflation the space in the universe expands exponentially by greater than 64 e-folds or the scale factor increases by a factor of 10^{28}.

Inflation is able to solve the Horizon problem because super-horizon modes that never entered the comoving horizon before decoupling are now thought to have been in causal contact before inflation occurred. Before inflation essentially all modes are contained within the comoving horizon and in causal contact. Inflation then stretches space and the modes to much larger scales greater than the comoving horizon. Hence a very homogenous CMB temperature becomes possible.

The Flatness problem is also solved by inflation. By space rapidly expanding, any curvature that may have existed is also stretched to very long radii. Therefore the current universe may just look very flat to the extent that can be observed from Earth but actually may have some curvature. The Relic problem is very similarly solved in that even though magnetic monopoles may exist, their distribution is diluted by the rapid expansion of space such that the statistical probability of observing magnetic monopoles from Earth is miniscule and improbable in the human lifetime. Inflation solves these latter two problems by arguing the current universe is not "fine-tuned" or statistically special but rather apparently looks that way from the observers' perspective.

Inflation also explains the origins of the initial inhomogeneities of the universe. Quantum mechanical fluctuations that are initially very small are stretched to large scales by inflation which provide the initial inhomogeneities of the universe. These stretched quantum fluctuations are also called the "seeds of struture" and provide the basis for further evolution of the universe. Without the initial inhomogeneities, gravitational instability cannot accumulate matter into over-dense regions or create the acoustic oscillations observed in the CMB signal.

The mechanism that inflation occurs is purely theoretical, and one of the most commonly known theories is slow-roll inflation. In slow-roll inflation, inflation occurs by a scalar field slowly rolling down a potential energy well. This scalar field is typically called the inflaton field [1].

One product of inflation is the primordial gravitational waves created by the tensor perturbations to the metric. The tensor perturbation evolve separately from the scalar perturbations. Similar to equation 1.14 the tensor perturbations can be represented mathematically by

$$g_{00} = -1 \tag{1.25}$$

$$g_{0i} = 0 \tag{1.26}$$

$$g_{ij} = a^2 \begin{bmatrix} 1+h_+ & h_\times & 0 \\ h_\times & 1-h_+ & 0 \\ 0 & 0 & 1 \end{bmatrix} \tag{1.27}$$

where h_+ and $h_\times$ are the perturbations to the metric. Unlike the scalar perturbations, tensor perturbations do not affect the evolution of large scale structure but do affect the fluctuations in the CMB signal. Hence the CMB contains a signal correlated with the primordial gravitational waves from inflation that is theorized to be observable in the CMB polarization signal.

1.4 CMB Polarization

The CMB contains a polarized signal that is more than an order of magnitude smaller than the unpolarized or temperature CMB signal power. The CMB becomes polarized due to Compton scattering or scattering of photons off electrons during the time of decoupling. Compton scattering can only create linear polarization if the incident radiation has a nonzero quadrupole moment. Before decoupling the photons and electrons are in equilibrium and hence the quadrupole moment of the CMB temperature is small. Therefore this small quadrupole leads to a much smaller CMB polarization signal compared to the CMB temperature. But similar to the temperature signal, the CMB polarization will also have a distinct acoustic signature.

When measuring the polarized signal from the CMB, the Stokes parameters are typically used to characterize the magnitude and angle of the sky polarization.

The Stokes parameters are defined as

$$I = |E_x|^2 + |E_y|^2 \tag{1.28}$$

$$Q = |E_x|^2 - |E_y|^2 \tag{1.29}$$

$$U = 2Re(E_x E_y^*) \tag{1.30}$$

$$V = -2Im(E_x E_y^*) \tag{1.31}$$

where x and y represent orthogonal components of the electric field defined on the sky coordinate system. I represents the total intensity or power, Q and U represent linear polarization, and V represents circular polarization. In the CMB it is theorized that there is no V or circularly polarized component. A V signal currently has not been measured in the CMB and only upper limits have been placed [19]. An example of the pattern of the orthogonal Stokes Q and U parameters is shown in Figure 1.2. At any location on the sky, the linear polarization signal can

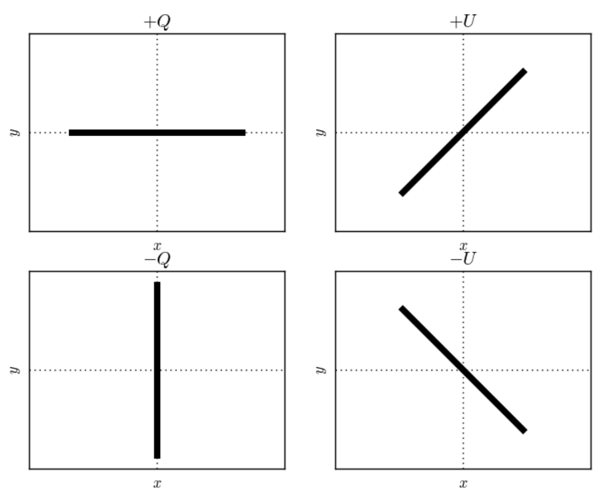

Figure 1.2: **Stokes Q and U polarization components** — Graphical illustrations of the Stokes Q (left) and U (right) parameters is shown. Q is defined along the coordinate axes and U is defined 45° relative to the axes.

be fully represented as linear combinations of the measured Q and U components at that location. Typical useful quantities that can be measured are given by

$$I_p = \sqrt{Q^2 + U^2} \tag{1.32}$$

$$\theta = \frac{1}{2}\tan^{-1}(U/Q) \tag{1.33}$$

where I_p is the linearly polarized intensity and θ is the polarization angle. Many sources on the sky are not fully polarized and hence the linear polarization fraction is given by I_p/I.

The Stokes parameters are by definition coordinate dependent. This arises from the fact that polarization is not a scalar quantity and cannot be characterized by a single quantity at every location. Therefore according to one's choice of coordinates that may be suitable for geographical or celestial reasons, the amplitudes of Q and U will differ even for a measurement at the same location on the sky. The Stokes parameters are useful because they are easy to measure experimentally, but typically need to be re-parameterized in terms of coordinate (rotationally) invariant quantities which are the E and B-modes.

E-modes are even parity curl free modes and B-modes are odd parity divergence free modes. Hence the E and B-mode decomposition is analogous to decomposing a vector into curl free and divergence free components. With this definition E and B-modes are non-local quantities and, unlike Stokes Q and U components, cannot be measured at a single location on the sky. E and B-modes represent the global properties of the polarization field which is simplistically illustrated in Figure 1.3.

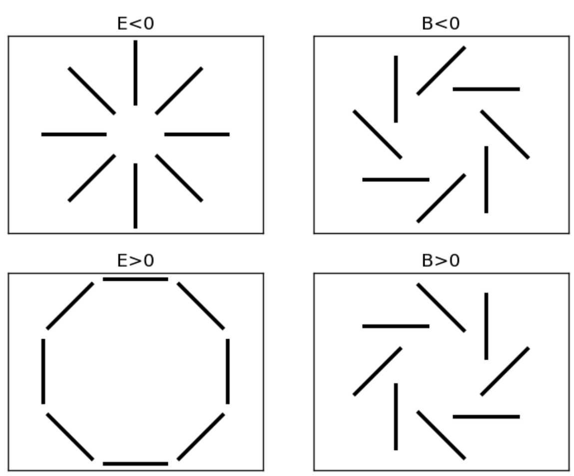

Figure 1.3: **E and B-mode polarization components** — A graphical illustration of E (left) and B-mode (right) polarization patterns is shown.

Similar to the temperature signal, the polarization signal can be decomposed into the spherical harmonics representing the E and B-mode components. Because polarization is not a scalar quantity, the spin-2 spherical harmonics are required in the expansion. Mathematically the decomposition is given by

$$Q \pm iU = \sum_{\ell=0}^{\infty} \sum_{m=-\ell}^{\ell} \left(a_{\ell m}^{E} \mp i a_{\ell m}^{B}\right)_{\mp 2} Y_{\ell m} \tag{1.34}$$

where the $a_{\ell m}$ are analogous to those in equation 1.21. Similar to equation 1.23 the power spectra for the E and B-modes as well as cross-correlations can be calculated as

$$C_\ell^{TT} = \langle a_{\ell m}^{T} a_{\ell m}^{T*} \rangle \tag{1.35}$$

$$C_\ell^{EE} = \langle a_{\ell m}^{E} a_{\ell m}^{E*} \rangle \tag{1.36}$$

$$C_\ell^{BB} = \langle a_{\ell m}^{B} a_{\ell m}^{B*} \rangle \tag{1.37}$$

$$C_\ell^{TE} = \langle a_{\ell m}^{T} a_{\ell m}^{E*} \rangle \tag{1.38}$$

$$C_\ell^{TB} = \langle a_{\ell m}^{T} a_{\ell m}^{B*} \rangle \tag{1.39}$$

$$C_\ell^{EB} = \langle a_{\ell m}^{E} a_{\ell m}^{B*} \rangle. \tag{1.40}$$

Because B-modes have opposite parity to T and E-modes, by definition C_ℓ^{TE} and C_ℓ^{TB} should be zero for parity conservation. Mathematically analogous to the temperature signal, the power spectra for the CMB polarization signal can be calculated through the E and B-mode decomposition.

The theoretical CMB polarization power spectra are shown in Figure 1.4 for the current ΛCDM cosmology. The C_ℓ^{BB} spectrum is more than an order of magnitude smaller than the C_ℓ^{EE} spectrum across all multipoles. Currently studying the CMB polarization signal has become the main interest in the CMB field with a large focus on measuring the CMB B-mode signal. The B-modes are theorized to be composed mainly of two components: the primordial signal from inflation and the lensing signal from weak gravitational lensing.

1.4.1 Primordial CMB

As previously stated, the CMB is polarized due to Compton scattering at the time of decoupling and can only create linear polarization if there is a nonzero

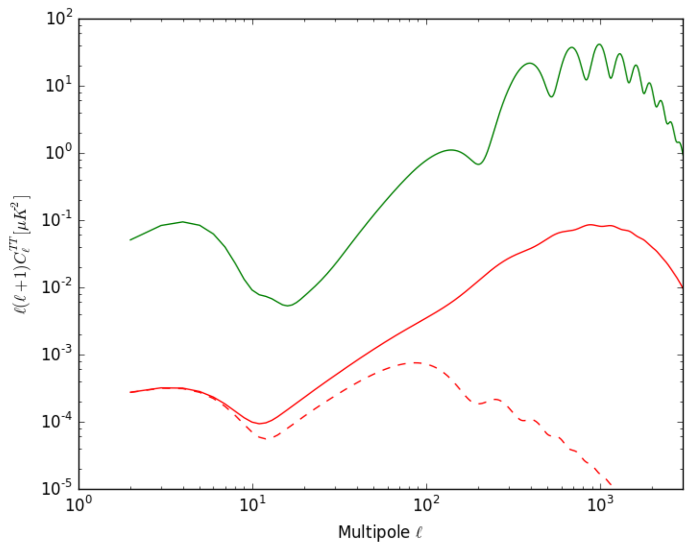

Figure 1.4: **Theoretical CMB polarization power spectra** — The theoretical CMB power spectra for the polarization signal due to scalar and tensor perturbations are shown. The C_ℓ^{EE} spectrum is in green and C_ℓ^{BB} spectrum is shown in red. The dotted C_ℓ^{BB} spectrum represents the primordial $r = 0.01$ component while the solid line includes the lensing component as well.

quadrupole temperature anisotropy. These quadrupole anisotropies are created from the acoustic oscillations of the plasma that originate from the initial quantum fluctuations and perturbations. Therefore it is natural that the polarization signal also contains characteristic acoustic features that has a shape that depends on evolution of this plasma.

The scalar perturbations, explained in section 1.2.2, create the temperature anisotropies and hence the E-modes also originate from the same physical phenomena. There is a distinct correlation between the temperature and E-modes which is apparent from the nonzero C_ℓ^{TE} power spectrum. Scalar perturbations create a symmetric $m = 0$ quadrupole, and this quadrupole field around an electron in Compton scattering can only generate linear polarization that is parallel or perpendicular to the direction of the density perturbation. Therefore scalar perturbations can only create E-modes in the CMB.

The tensor perturbations, discussed in section 1.3.2, create differing pattern $m = 2$ quadrupoles. The gravitational waves that are created by the tensor perturbations will stretch spacetime parallel and perpendicular to the perturbation direction as described by the h_+ term as well as ± 45 degrees relative to the perturbation direction as described by the $h_\times$ term. The quadrupole moment generated by these gravitational waves do not have the symmetry as in the $m = 0$ quadrupole case. Therefore the linear polarization generated by Compton scatter from the $m = 2$ quadrupole is not confined to be only parallel or perpendicular to the perturbation direction. This results in the tensor perturbation creating both E and B-modes in the CMB polarization.

Because B-modes can only be created by the tensor perturbations that are distinct products of the mechanism of inflation, the B-mode power spectrum is theorized to be the strongest evidence that inflation may have occurred in the early universe. This component of the B-mode signal arising from inflation is called the primordial B-mode signal, and its amplitude is proportional to the energy scale of inflation parameterized by the tensor-to-scalar ratio r. The parameter r is given by

$$r \equiv \frac{P_t}{P_s} \tag{1.41}$$

where P_t and P_s are the amplitudes of the tensor and scalar perturbations respectively. Typically the r value is quoted at a pivot scale of 0.05 Mpc^{-1}. An approximate relation between r and the energy scale of inflation is given by

$$V^{1/4} = 1.06 \times 10^{16} \times \left(\frac{r}{0.01}\right)^{1/4} GeV \tag{1.42}$$

where V is the inflaton potential. As can be seen in Figure 1.4, the primordial signal peaks at $\ell \sim 100$ and its amplitude is proportional to r.

The exact value of r has not yet been measured and only upper limits have been placed [20]. The primordial B-mode signal has not yet been measured and is one of the main goals of current generation CMB experiments in order to potentially further strengthen support for the inflationary Big Bang models. Based off current B-mode measurements it is hypothesized that the primordial signal is sub-dominant to the lensing B-mode signal even at low ℓ, and will require further higher sensitivity instruments to measure in the future.

1.4.2 Gravitational Lensing

Another astronomical phenomenon that can create B-modes is weak gravitational lensing by large scale structure. As the CMB photons free-stream toward the observer, the evolving matter distribution between the last scattering surface and the observer will gravitationally influence the photon trajectories. The CMB photons will be deflected by the intervening high matter density large scale structure through weak gravitational lensing. This will not only smear out sharp features in the power spectra, but also convert E-modes into B-modes as the photons reach the observer. These effects that occur after decoupling are typically called secondary anisotropies.

The CMB B-mode signal will contain a component known as the lensing B-modes that peaks at smaller angular scales at $\ell \sim 1000$ as shown in Figure 1.4 because the lensing effect dominantly occurs over small angular scales. This lensing signal has a theoretical shape that distinguishes it from the primordial signal. Because the lensing signal contaminates the primordial signal at low ℓ, typically the lensing signal must be measured accurately in order to "de-lens" and recover the primordial signal.

Even though the lensing signal potentially contaminates the primordial signal, the lensing signal itself has interesting cosmology within it as well. The lensing signal is correlated with the matter distribution of the universe from decoupling until now. Structural formation is suppressed by massive neutrinos due to the pressure from massive neutrinos competing with the gravitational forces clustering dark matter. The scales at which this suppression occurs will depend on the mass of the neutrinos, and hence measurements of the lensing B and E-modes allow us to calculate the lensing potential and put constraints on the sum of the neutrino masses.

1.4.3 CMB Polarization Observations

Due to the much smaller amplitude of the CMB polarization signal, polarization measurements are much more difficult to make and have become a focus of the CMB field in the last decade. The E-mode signals have been measured to high precision by the Planck satellite [13] as well as the BICEP and Keck Array [21], SPTpol [22] and ACTpol [23] ground-based experiments.

The B-mode signals are further smaller in amplitude than the E-mode signals. The lensing B-mode signal has recently been measured by various ground-based CMB polarization experiments such as the polarization specific POLARBEAR experiment that will be described further in chapter 3 as well as BICEP and the Keck Array [21], SPTpol [24], and ACTpol [23]. The primordial B-modes have not yet been measured but currently upper limits on r have been placed [20].

Future generation ground based CMB experiments such as the Simons Array that will be described in chapter 5 are currently in development and are aimed to achieve superior sensitivities to measure the primordial signal and place better constraints on r.

1.5 Foreground Contamination

The photons from the CMB originate from the initial plasma of the earliest state of the universe. Due to the finite speed of light, these initial photons are equivalent to the farthest light that can be observed from the Earth today. Due to this fact there are various sources of excess light that are introduced into the observations that must be carefully distinguished from the CMB signal. These extra sources of light are typically called foreground contamination.

1.5.1 Atmosphere

For ground-based experiments, the largest foreground signal is the atmosphere itself. In the microwave frequencies the atmosphere is opaque as can be seen in Figure 1.5. Due to the hydrogen and oxygen molecular composition of the atmosphere, these strong emission features or "lines" make observations at certain frequencies virtually impossible. The oxygen emission line is located $\sim$ 120 GHz and the hydrogen emission line is located $\sim$ 190 GHz. Near the spectral peak of the CMB, there are several atmospheric windows between the atmospheric emission lines where the transmission is comparatively higher. Hence ground-based CMB

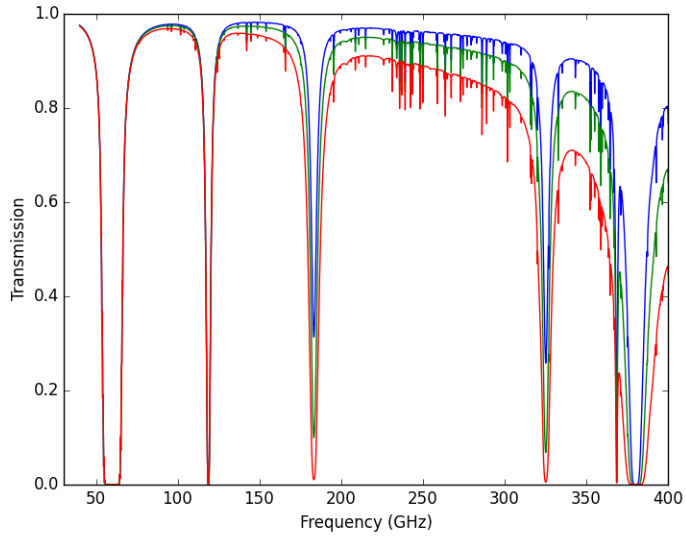

Figure 1.5: **Atmospheric transmission in Chile** — The theoretical atmospheric transmission in the Atacama Desert is shown. The plot shows the transmission observed at elevation 60° with PWV = 0.5 mm (blue), 1.0 mm (green), and 2.0 mm (red). The atmospheric model is calculated using AM [25].

experiments design their instruments to be sensitive within these atmospheric windows in order to reduce the atmospheric contamination as much as possible. But the atmosphere is not expected to be polarized unlike other sources of contamination.

Especially at microwave frequencies the precipitable water vapor (PWV) is an important figure of merit used to describe dry weather atmospheric conditions needed for CMB observations. Thermal emission from the atmosphere provides extra loading on the instrument detectors and reduce their sensitivities due to higher photon noise. Thus high atmospheric transmission is essential. As can be seen in Figure 1.5, atmospheric transmission decreases with higher PWV, and typically CMB observations require PWV < 4 mm. Currently the Atacama desert in Chile and the South Pole are considered to be the driest places on Earth and optimal locations for CMB observations due to the low PWV.

Other than the atmospheric emission, the stability of the atmosphere is also crucial. Wind, clouds, and associated water vapor dynamically move across the sky and vary quickly with time in a mere seconds. This changing atmosphere creates variable loading on the detectors and increases the low temporal frequency noise in the measurement. The excess low temporal frequency noise as well as high loading make CMB observations at higher than ~ 300 GHz light difficult from the ground. The low temporal frequency noise can be mitigated by fast scanning of the telescope. Fast scanning of the telescope at several degrees per second allows for effectively modulating the CMB signal and reducing the varying atmospheric noise.

One of the largest advantages of satellite and balloon-based experiments is that they observe above the atmosphere and do not suffer from atmospheric contamination. But mechanical challenges in weight of these experiments typically limit the size and number of detectors. Even though the instantaneous sensitivity per detector is much higher than that for ground-based experiments, the limit on the instrument size and the shear number of detectors provide observational challenges and limit sensitivity in many cases as well.

1.5.2 Dust

There are two major sources of polarized contamination in the universe. One source being polarized emission from interstellar dust that is apparent at high frequencies above ~ 70 GHz. The exact mechanism and physics of polarized dust emission is still unknown. It is hypothesized that dust grains in the interstellar medium are thermally emitting, and can produce polarized light due to vibrational, rotational, and magnetic excitation [26, 27]. If dust grains can become spatially aligned across various angular sizes on the sky due to physical mechanisms such as galactic magnetic fields, then a net linear polarization will be emitted and become a large source of contamination in the CMB signal.

If polarized emission from dust is highly correlated with its thermal emission, then temperature foreground maps from WMAP can be used to estimate the polarized dust contamination across various regions of the sky assuming a possibly varying polarization fraction. But this may not always be the case, and hence polarized foreground maps from Planck at 353 GHz [13] are typically used to estimate the foreground dust contamination. A naive power law scaling such as $T \propto \nu^{\alpha_{dust}}$

is used to estimate the dust contamination at other frequencies. In order to provide much more accurate dust contamination estimates, direct measurements of the foregrounds at many frequencies are necessary in order to correctly model the foreground. Currently in the CMB field dust foreground contamination has become a large issue because the polarized foreground power is thought to be on similar scales or potentially larger than the primordial B-mode signal and can overwhelm the CMB signal [28].

1.5.3 Synchrotron Radiation

A second source of polarized contamination comes from synchrotron radiation and dominates at low frequencies. Synchrotron radiation is emission due to the acceleration of cosmic ray relativistic electrons through interaction with galactic magnetic fields. Synchrotron radiation has a power law frequency dependence as $T \propto \nu^{-\alpha_{synch}}$ where the spectral index α_{synch} is hypothesize to have a value $2.7 \sim 3.0$ [29]. The polarization fraction depends on the magnetic field shape and with this value of α_{synch} the polarization fraction is theorized to be high. Hence Synchrotron radiation will be a dominant foreground for low frequency observations, and will spatially vary according to the galactic magnetic fields. Currently measurements of the synchrotron radiation are limited, but have not yet been measured to be a dominant contaminant in the CMB windows.

For polarization CMB measurements, the spectral index dependencies of foreground contamination from dust and synchrotron radiation are still unknown in many cases, and not well constrained across different regions of sky. Hence much more full and partial sky measurements of foregrounds across frequencies are needed in order to accurately determine the foreground contribution within the measured signal. Foreground contamination especially in the B-mode spectra are known to be problematic in measuring the primordial signal and needs far greater care than ever before with the increasing sensitivity of CMB experiments.

Chapter 2

Telescope Optics

When designing a telescope and instrument for astronomical observations the initial optical design is very important because this will determine the ultimate optical capabilities and sensitivity of an instrument in terms of its sky resolution, field of view (FOV), optical loading, and polarization systematics. This chapter will briefly explain the terminology and general considerations in optical designing of a telescope and instrument. The concepts in this chapter will be used to describe the designs of the POLARBEAR experiment in chapter 3 and the Simons Array experiment in chapters 5 and 6.

2.1 Optical Design

In general telescope and instrument designs consist of reflective and refractive optical elements that have the role of focusing the light from the sky onto detectors that physically measure the incoming signal. Both particle and wave effects of light must be carefully considered in a realistic optical design. Considering computational costs, typically it is convenient to start designs using particle or geometric ray optics and then gradually incorporate wave effects. Certain optical characteristics are easier to estimate in geometric ray optics while other effects can only be fully explained by wave optics.

Starting with geometric ray optics, an ideal telescope optical design is made such that plane waves or collimated rays from astronomical sources on the sky enter the telescope optics and end up at a perfect focus on the detectors within the instrument. The degree to which the rays are not at a perfect focus at the detectors can be called aberrations within the optical system. Aberrations exist to varying degrees within a design and will degrade the optical performance.

Telescopes with arrays of detectors are designed such that collimated rays from the sky coming into the optical system at different angles focus on different spatial locations on the detector arrays. The plane or surface at which all the foci exist and the detector arrays are placed is called the focal plane. Therefore each detector in the array is effectively looking at a different angular location on the sky in polar coordinates. The angular size and range that a telescope can instantaneously observe with all its detectors is called the FOV of the telescope. An example of such a system is shown in Figure 2.1.

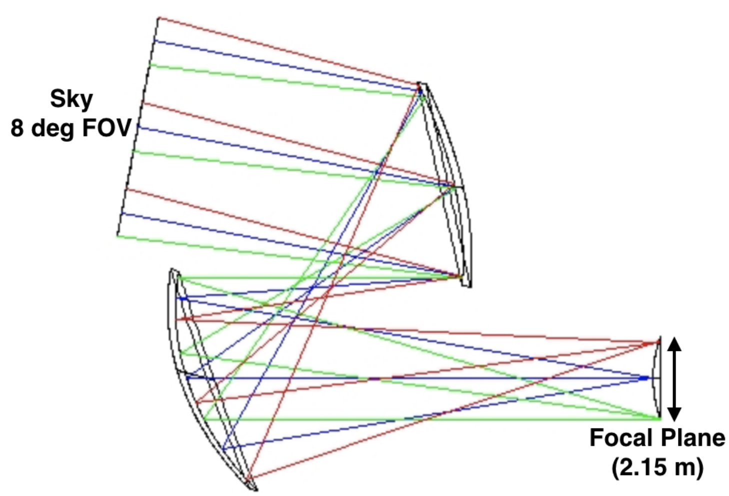

Figure 2.1: **Example of telescope optics** — This is an example of a Gregorian-Dragone dual reflector optical design with a $\pm 4^\circ$ FOV focusing on a 2.15 m curved focal plane. The $+4^\circ$ (red) and -4° (green) fields focus at opposite edges of the focal plane. In this design the focal plane is at the Gregorian focus.

In optical designing it is common to use two different frames: the forward time frame and the reverse time frame. The forward time frame is the real photon propagation frame where light is emitted from a source and enters the detector as explained above. The reverse time frame is a frame in which one assumes that the detector is emitting light and photons propagate out toward the source.

For the case of a telescope in the reverse time frame the light will propagate out toward the sky. Both frames are of great use because the forward time frame allows for designing based on real light propagation direction, and the reverse time frame allows for designing based on what the detector will actually observe as light propagates through an optical system.

Returning to the geometric ray optics example of a telescope, in the reverse time frame rays are emitted from a perfect focus from a detector, are propagated through the telescope, and end up as collimated rays pointing at an angular location on the sky. In the reverse time frame aberrations can be interpreted as any deviation away from perfect collimation at the sky. With aberrations this means that the geometric rays from a detector will no longer be pointing at one exact angular location on the sky but a non-uniform finite angular region on the sky. The effects of diffraction are not included in this illustration and will be discussed in terms of wave optics in section 2.1.1.

The f-number f or the focal ratio is a parameter commonly used to describe an optical system. It is defined as

$$f = \frac{F}{D} \tag{2.1}$$

where F is the focal length and D is the diameter of the aperture. The f-number can be also defined in terms of the opening half angle of the rays θ_r as

$$f = \frac{1}{2\tan\theta_r}. \tag{2.2}$$

The f-number represents how fast or slow geometric rays within the system are converging or diverging. Hence an f-number can be defined at any point in the optical design. In common practice "fast" optics are low f-number systems because the rays focus within a smaller distance and converge quickly. Similarly "slow" optics are high f-number systems that focus rays across a longer distance. Typically low f-number optics tend to have more aberrations compared to higher f-number optics. This is because in order to converge or diverge rays quickly more curved reflectors and refractors are needed. More curved surfaces will introduce higher levels of aberration due to increased large incident angle reflection and refraction at each surface.

There are currently many geometric ray-based optical design software used within the field. One of the most commonly used is the software ZEMAX [30]. ZEMAX allows for fast analysis and optimization of reflective and refractive optical designs as well as physical optics propagation analyses in the paraxial approximation. The ZEMAX software will be referenced and utilized in various parts of this dissertation.

2.1.1 Diffraction Limited System

Because photons have both particle (or ray) and wave characteristics, the geometric ray optics interpretation does not fully encapsulate the physics. Even if one were able to design a telescope that had no aberrations, realistically this would still not mean that each detector would be observing exactly one polar coordinate location on the sky. Due to the limitations by the effects of diffraction, each detector will physically be observing a finite angular region. This finite angular region in the absence of aberrations is called an Airy pattern and its smallest possible angular size is approximately given by

$$\theta \sim 1.22\frac{\lambda}{D} \tag{2.3}$$

where D is the aperture diameter. For a telescope D is the size of the main or primary reflector. At a given observation frequency, the size of the primary reflector determines the smallest possible angular resolution on the sky that the telescope is able to observe at. The sky resolution is typically referred to as the beam of the telescope. The Airy pattern contains a central peak and diffraction rings. In generic terms the central peak that can be approximated by a Gaussian shape is called the main beam and any characteristic outside of the main beam such as the diffraction rings are considered the side-lobes.

The above equation is only true for the case that the aperture is fully illuminated across its full diameter with uniform power. For realistic detectors the illumination of any aperture will have a non-uniform shape such as a Gaussian profile. In this case the far-field or Fraunhofer diffraction calculation must be made with this illumination profile. In general the Fraunhofer diffraction is given by [31]

$$E\left(\frac{\ell}{\lambda},\frac{m}{\lambda}\right) \propto \int\int_A A\left(x,y\right) e^{-i\frac{2\pi}{\lambda}\left(\ell x+my\right)} dxdy \tag{2.4}$$

where $A(x,y)$ is the aperture function representing the spatial illumination profile of the aperture and ℓ and m are the direction cosines of x and y. In this case the direction cosines translate to the polar coordinates on the sky.

In general the angular size will increase with any non-uniform illumination pattern. For example if one assumes a Gaussian illumination profile that is truncated at the aperture edges, the beam size will increase but the diffraction ring power in the Airy pattern will decrease. A Gaussian illumination profile is effectively using a smaller portion of the aperture and makes the angular size larger. But because the power in the diffraction rings depends on the amplitude of the beam power at the aperture edges, if the truncation occurs at the Gaussian tails the diffraction ring power will diminish accordingly. Therefore a truncated Gaussian profile will potentially have a larger main beam but smaller side-lobes. This is illustrated in Figure 2.2 for a POLARBEAR like design with a 2.5 m diameter aperture using the analytical calculation in equation 2.4.

For the wave interpretation in the reverse time frame, one can imagine that a Gaussian beam of finite size determined by the characteristics of the detector propagates through the optical system and eventually toward the sky. This interpretation of a propagating Gaussian beam emitted from the detectors helps conceptualize how each aperture in the system will be illuminated and how diffraction will also propagate throughout the the system with each consecutive optical aperture.

This optics interpretation is called Gaussian beam optics (propagation). The Gaussian beam is assumed to be a transverse electromagnetic TEM mode. This method is a paraxial approximation and assumes that the electric field amplitude is a solution to the paraxial Helmholtz equation in order to calculate the beam's propagation through the optics system. The electric and magnetic fields are characterized by a Gaussian beam with the beam waist as its sole determining parameter. The beam waist w_0 is the beam size at the focus of the optics system, in this case it would be at the detector. The beam size propagates according to

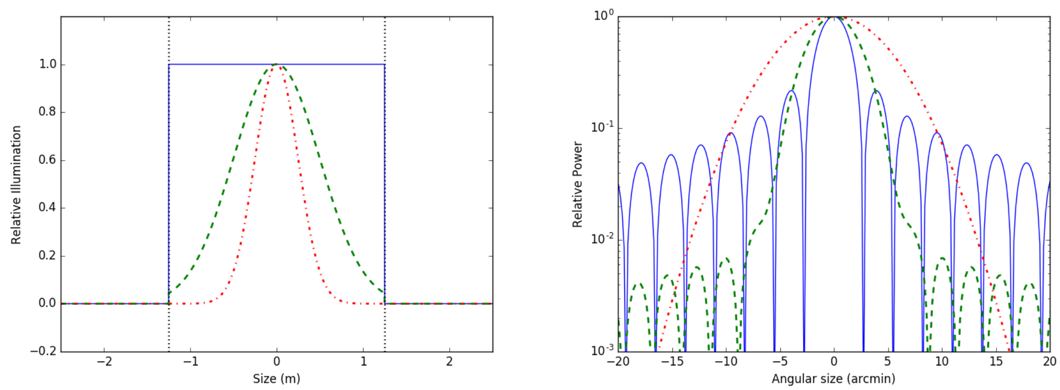

Figure 2.2: **Fraunhofer diffraction with varying illumination profile** — The left plot is the illumination profile at the 2.5 m aperture, and the right is the beam at the sky according to the Fraunhofer diffraction equation. The calculated cases are for uniform illumination (blue), Gaussian illumination with $\sigma = 0.5$ m (green dash), and Gaussian illumination with $\sigma = 0.25$ m (red dash-dot). The uniform illumination has the smallest beam but largest diffraction ringing power while the Gaussian illuminations have larger beams but much smaller diffraction ringing.

the equations

$$w(z) = w_0\sqrt{1 + \left(\frac{z}{z_R}\right)} \tag{2.5}$$

$$z_R = \frac{\pi w_0^2}{\lambda} \tag{2.6}$$

where the beam propagates in the z direction and z_R is the Rayleigh range. Relating this to geometric optics, the divergence half angle of the beam θ_d is given approximately by

$$\theta_d \simeq \frac{\lambda}{\pi w_0} \tag{2.7}$$

which is analogous to the opening half angle of the rays θ_r but not identical in definition. Therefore in the Gaussian beam optics approximation, knowledge of the beam waist allows one to determine the propagation of a beam from a focus toward an optics chain. Then the Gaussian beam is propagated through each optical element using various physical optics calculations in combination.

Any beam power that is not contained within any optical aperture of the system is called spillover power. Spillover power typically ends up on non-optical surfaces such as the telescope structure, baffling surfaces, and the inner walls of the receiver. Spillover power must be calculated for every aperture in the system such as at each lens and reflector in order to assess how much loading contribution there is from spillover at each surface. This is important because a design should reduce spillover at any surface in order to decrease the overall detector loading. With larger amplitudes of total spillover, there will be fractionally less sky power going into the detectors.

Realistically spillover cannot be eliminated completely in any design. Hence the total amount of detector loading due to spillover power can be reduced by controlling the temperature of the non-optical surface at which the spillover goes. The detector loading will be lower if the spillover ends up on a cold surface rather than a warm surface. Therefore in CMB experiments some or all optical components are contained in receivers that are cryogenically cooled to low temperatures. A successful optical design thus needs to reduce as much as possible spillover at surfaces that are at ambient temperatures compared to cryogenic temperatures in order to decrease the overall detector loading.

Realistically any optical design and system will contain aberrations. An optical system is considered to be diffraction limited if the effects of aberrations in the system are sub-dominant to the effects of diffraction for all detectors in the instrument. It is preferential that any telescope or instrument is diffraction limited because the effects of diffraction are typically much easier to model compared to the effects of aberrations. The Airy pattern can be approximated well as a 2D Gaussian-like profile and typically contains symmetry. On the other hand, the effects of aberrations will completely depend on the specific optical system and can vary the beam shape widely and asymmetrically across the focal plane with no particularly standard model.

A common figure of merit used to define if a design is diffraction limited is the Strehl ratio. The Strehl ratio is a measure of the quality of an optical image that an optical design produces. The Strehl ratio only has values between 0 and 1 with 1 equating to an system with no aberrations. Typically it is defined such that if an optical system has a Strehl ratio > 0.8 then it is diffraction limited and the aberrations are sub-dominant to the effects of diffraction.

Historically the Strehl ratio has many different analytical definitions and according to the definition what is considered diffraction limited will change. One of the first definitions was presented by Rayleigh [32] and stated that a system is diffraction limited if the wavefront errors are $< \frac{\lambda}{4}$. But it has been argued that according to the shape of the wavefront error, such as a very asymmetric error, this criterion does not meet a diffraction limited system [33]. Hence even today there is no one exact definition of the Strehl ratio. One common definition used based off the RMS wavefront error δ across the aperture is given by

$$S = \left| \int_A e^{i\frac{2\pi}{\lambda}\delta(x,y)} dA \right|^2 = \left| \int_A e^{i2\pi\sigma(x,y)} dA \right|^2 \tag{2.8}$$

where S is the Strehl ratio, σ is the RMS phase deviation, and the integral is taken over the aperture of interest. The software ZEMAX uses an approximation to this equation of the following

$$S = e^{-(2\pi\sigma)^2} \tag{2.9}$$

and this is claimed to be accurate for Strehl ratio values above 0.1 [30]. In this definition a diffraction limited system continues to be defined with a Strehl ratio > 0.8 but it must be noted that this is only a benchmark value, and typically higher values are preferred. Aberrations will be significantly different for every type of optical design and emerge in the optical image in complex ways. Even small aberration effects are far more difficult to model than diffraction effects.

Typically optical systems will have varying levels of aberrations dependent on the focal plane or FOV position. The FOV on the sky, and corresponding area of the focal plane, in which the aberrations are sub-dominant to diffraction is called the diffraction limited field of view (DLFOV). Most telescope systems will only place detectors within this DLFOV to sustain diffraction limited performance. As a trend many optical systems in astronomy that only use conical surface shapes are designed such that there is a central optical axis that the design is based off and has the lowest aberrations. Deviating in any direction away from the central optical axis on the focal plane increases aberrations for these designs.

2.2 Optical Systems

In order achieve high sensitivity measurements of the CMB, high throughput and high resolution optical designs are absolutely essential for observations at any frequency. Optical designs can be described by multiple categories: refractive, reflective, and hybrids.

2.2.1 Refractive Based Systems

Refractive based optical systems are designs that only have refractive components or basically lenses. Refractive based systems are relatively straight forward in design and can achieve high throughput. They are typically more compact compared to reflective optics and usually axially symmetric. BICEP and Keck Array [34] are CMB telescopes that have purely refractive optics. Compared to reflective based optics, refractive based optical designs can more readily be enhanced to have higher throughput, but have more difficulties in terms of material properties and sizes. Realistically usable high index and low loss dielectric materials are difficult to obtain and harder to machine into large aperture elements. Hence the optical design is more constrained by materials. The limitation on lens size makes high resolution difficult as well. Also multi-chroic detectors using the same optics necessitate multi-layer anti-reflection (AR) coatings that are not trivial to develop.

2.2.2 Reflective Based Systems

Reflective based optical systems are designs that only have reflective components or mirrors. Many large dish ground-based telescopes as well as satellites like WMAP [35] are reflective based optical systems. Recent telescopes typically contain 2 to 3 reflectors used in combination to obtain higher throughput and a larger DLFOV. Theoretically larger numbers of reflectors can be used to further increase performance, but quickly become physically difficult to implement. Reflectors are typically easier to machine to large sizes than refractors and hence high resolution telescopes all use reflectors as their limiting aperture or as their primary reflector. Also reflectors do not need AR coatings applied to them. Off-axis reflective systems are typically more prone to certain types of aberrations such as astigmatism and coma.

On-axis reflective systems are designs that utilize on-axis parabolic primary reflectors. Due to its symmetric nature, on-axis systems typically are more ideal in terms of optical properties such as aberrations and systematics. At the same time the throughput is decreased due to the necessity of blocking off the central portion of the FOV where the focus is to place other reflectors or detectors. These systems can obtain low levels of aberrations even with just one reflector.

Off-axis reflective systems utilize off-axis parabolic mirrors instead and do not have the disadvantage of blocking the center of the FOV. Two historical configurations of off-axis dual reflector systems are Cassegrain and Gregorian designs. Cassegrain designs have a parabolic primary and a convex hyperbolic secondary, and Gregorian designs have a parabolic primary and elliptical secondary. Due to its off-axis nature the aberrations are typically worse than on-axis designs and a secondary reflector is necessary to get to larger DLFOV. Dragone introduced specific off-axis designs that have more ideal optical properties and are now the most commonly used designs as described later in chapter 6.

2.2.3 Hybrid Systems

Hybrid optical systems are designs that have both refractive and reflective optics. Typically the sky-side optics are reflective followed by refractive optics toward the detector focal plane. The main optics are the reflective optics to ensure a large primary aperture. The refractive optics are used to reduce aberrations, adjust the f-number at the focal plane, make the focal plane flat and telecentric, and create a Lyot stop that can be cryogenically cooled. Due to higher performance many current ground-based telescopes are hybrid designs. POLARBEAR is an example of a hybrid design and will be explain in detail in chapter 3.

The size of the reflective optics becomes large for high resolution telescopes and very expensive. Hence size and cost commonly limit the parameter space of reflective designs that can be chosen from. The reflective optics will define the size of the DLFOV of a telescope, but currently with a greater need for large numbers of detectors in one instrument, further enhancement of the DLFOV using refractive re-imaging optics has become common. With the added degrees of freedom of the refractive optics typically the aberrations for FOV regions with Strehl ratios approximately $0.6 \sim 0.7$ can be corrected to be above the diffraction limit of 0.8 and increase the DLFOV. Theoretically adding more reflectors and refractors allow for correcting larger aberrations but at the cost of more complexity in the optical design.

A large advantage of hybrid systems is the greater adjustability of the f-number of the optics. For current CMB detector technologies it is common to couple the detectors to the telescope and instrument using feed horns or lenslets. According to the spacing, shape, and size of these feed horns and lenslets, the gain and directivity of the detector antennas will greatly vary in shape and angular sensitivity. Hence the f-number of the optical design at the focal plane must be adjusted using the refractive optics in order to ensure efficient coupling to the chosen detector technology. If the f-number at the focal plane is too low then each optical aperture in the system will be under-illuminated by the detector and not fully utilizing the throughput of the designed system. If the f-number at the focal plane is too high then the detector will be accepting more light from the surrounding surfaces compared to the light from the sky. In this case there will be increased detector loading due to increased spillover.

The f-number also correlates with the size of the focal plane. The focal plane and Gregorian focus are both an optical field stop that will approximately scale with the f-number for a constant FOV. As the f-number of an optical system increases the size of the field stop will also increase and vice versa. This is simply a result of the magnification power of the optical design changing as a function of f-number. Thus the f-number at the focal plane must also be optimized according to any technological limits placed on the total size of the focal plane along with the optical coupling explained above.

Telecentricity is defined as the optical characteristic that the chief geometric rays across the FOV enter (exit) perpendicular to the image (object) plane [31]. In the forward time frame, the focal plane is telecentric when all the chief rays are incident perpendicular to the focal plane itself for all detectors. When implementing detector arrays into an instrument it is usually more convenient to make arrays planar or piecewise flat. Hence in the optical design the focal plane must be optically flat and telecentric across for planar detector arrays to couple correctly to the instrument optical design. If the detector technology permits fabrication of highly controllable curved detector arrays, the focal plane does not necessarily need to be flat, but telecentricity is usually needed for both cases. A flat and telecentric focal plane can usually be managed with the reflective optics combined with one refractive lens.

A Lyot stop is an optical aperture stop that specifically reduces spillover and flare caused by the effects of diffraction of other apertures in the system. An aperture stop is an optical location in the design where the rays from or going to each detector overlap exactly to form a common image. Reducing the physical size of an aperture stop reduces the power from the sky going to each detector across the focal plane equivalently. The Lyot stop is typically cryogenically cooled and an exact image of the primary reflector. Therefore truncating the detector beams at the Lyot stop is equivalent to truncating the illumination profile on the primary. This allows for minimizing the spillover at the primary reflector which is usually at ambient temperature and rather creating spillover at the Lyot stop which is at a much lower temperature such as < 5 K. This significantly decreases the detector loading.

Most dual reflector systems either do not have an ideal aperture stop or have an aperture stop that is similar in size to the reflector sizes. These aperture stops are usually difficult to utilize as a Lyot stop in many cases due to various limitations such as size. Therefore multiple (typically two or more) refractive lens are used to create a Lyot stop that is relatively compact in size and can be cryogenically cooled within the instrument.

2.3 Polarization Contamination

The need for higher sensitivity in polarized CMB measurements of the gravitational wave B-mode signal has driven the field to develop optical designs that are able to reduce instrumental systematics and provide a large DLFOV. Mitigating and understanding instrumental sources of contamination allow for differentiating the systematics not only from the CMB signal but also foreground contamination such as dust and synchrotron radiation.

There are two broad categories of optics-induced instrumental systematic effects that create spurious polarization signals: instrumental polarization and cross polarization. Analytical calculations to differentiate between the two categories using the Jones formalism can be found in Tran 2003 [36] and using the Stokes formalism can be found in Garcia 2012 [37]. A qualitative explanation will be made below.

2.3.1 Instrumental Polarization

Instrumental polarization is the systematic contamination of the signal from spurious polarized light caused by unpolarized photons. Typically terms such as $T \rightarrow P$ or $I \rightarrow Q, U$ leakage are used to describe this category of contamination. This systematic arises due to the finite conductivity of reflective and refractive optical elements in the system and differential reflection through refractive interfaces. This leakage also depends on the oblique angle of reflection and transmission through the optics which typically makes off-axis designs more affected than on-axis designs.

One source is the thermal emission of the material surfaces that typically depend on the temperatures of the elements. This leakage can be subtracted out to a degree through utilizing physical temperature information of the optical elements. In a system like POLARBEAR, where all the refractive optical elements are cryogenically cooled and only the reflective components exposed to the ambient environment, the dominant contamination due to emission will come from the reflectors. In an ideal thermally quasi-stable environment this term would simplify into an offset contamination that slowly varies with temperature.

The second source is due differential reflection of reflected and transmitted polarization components that can leak the unpolarized signal to the polarized signal. According to the Fresnel equations, the transmission and reflection of orthogonal polarization states differ and depend on the incident angle and the index difference at the refractive interface. If the transmission and reflection coefficients along one polarization direction are different from the orthogonal polarization direction, then an unpolarized photon will be converted into a polarized signal. For CMB experiments this means that the atmospheric signal and temperature CMB signal can leak into the much smaller polarized CMB signal. Theoretically this can be subtracted by comparison of the unpolarized signal to the polarized signal and by correctly modeling atmosphere and temperature CMB signals.

2.3.2 Cross Polarization

Cross polarization is the contamination due to the rotation of linear polarization through an optics system. Typically terms such as "Q, U mixing" or $Q \leftrightarrow U$ leakage are used. This systematic arises even in ideal reflectors that have perfect conductivity.

For refractors, differences between the reflection of s and p polarizations at non-normal angles described by the Fresnel equations give rise to a rotation of the polarized signal at each optical element. For reflectors, pure 3D oblique angle reflections give rise to polarization rotation dependent on the relation between the reflector rotation and incidence plane. This mixes the measured Q and U signals which in turn mixes the E and B-mode signals. This leakage also depends on the oblique angle of reflection and transmission and hence any surface with high curvature will typically have larger cross polarization unless correctly accounted for. Hence low f-number optical systems are more prone to this systematic in general.

Because cross polarization is a direct consequence of the optical design such as surface shapes rather than material properties, limiting the cross polarization systematic must be considered very carefully when designing the optics. Theoretically with better material properties and AR coatings the instrumental polarization can be reduced but the cross polarization cannot. Hence the lower limit on the cross polarization is determined by the optical design. Minimization of the cross polarization in an optical design has historically been studied in detail and will be further discussed in chapter 6.

Chapter 3

The POLARBEAR Experiment

3.1 Introduction

The POLARBEAR experiment is a polarization sensitive CMB experiment located at the James Ax Observatory on Cerro Toco mountain at 5200 m altitude in the Atacama desert in Chile. The POLARBEAR receiver is installed on the 2.5 m mirror Huan Tran Telescope (HTT). POLARBEAR observes 150 GHz light and has been observing for multiple seasons since early 2012. POLARBEAR is observing the CMB polarization anisotropies in order to put constraints on r and the sum of the neutrino masses as discussed in section 1.4.

3.2 POLARBEAR Science

More than 50 years have passed since the discovery of the CMB, and many generations of experiments have continued to produce further refined CMB measurements and cosmological science. Accurate measurements of the temperature and E-mode spectra have put stringent constraints on cosmological parameters of the ΛCDM model and deepened the understanding of the early universe. Current generation experiments such as POLARBEAR are mainly aimed to measure the CMB B-modes that allow for uniquely probing the inflationary paradigm of the standard model.

3.2.1 B-Mode Science

POLARBEAR is a dedicated CMB polarization experiment with its primary focus on measuring the CMB B-mode signal from inflation and gravitational lensing. POLARBEAR is designed to be able to characterize the CMB B-mode for both large and small angular scales on the sky.

As discussed in section 1.4.1, the primordial B-mode signal is the strongest evidence of inflation, and allows one to probe the energy scale of inflation, thought to be near Grand Unified Theory (GUT) scales, through constraining the value of the tensor-to-scalar ratio r. Even though the exact value of r and hence the amplitude of the primordial signal is unknown, the primordial signal is expected to peak at angular scales of ~ 2 degrees on the sky. This corresponds to $\ell \sim 100$ which the POLARBEAR experiment is designed to measure through an accessible large fraction of the sky in the Atacama as well as the fast scanning capabilities of the telescope.

At small angular scales the gravitational lensing B mode signal is dominant, as explained in section 1.4.2, and is theorized to peak at $\ell \sim 1000$ or arcminute scales which is expected from the weak gravitational lensing due to large scale structures in the universe. POLARBEAR has a 3.5 arcmin sky resolution and allows the instrument to be sufficiently sensitive up to $\ell \sim 2500$ which is well above the lensing peak. This small angular scale measurement helps constrain the sum of neutrino masses. The overlap of the POLARBEAR observation patches on the sky with infrared and optical galactic survey data allows for cross-correlation analyses to further study the CMB lensing in detail.

3.2.2 Observation Strategy

The POLARBEAR experiment is located on the Cerro Toco mountain in the Atacama desert in Chile at a latitude of $-22.958°$, longitude of $292.214°$, and an altitude of 5200 m. As discussed in section 1.5.1, the atmosphere is one of the largest sources of contamination in the CMB observations. The historically dry climate of the Atacama desert with frequently low PWV of < 1 mm as well as the high altitude allow for stable and minimal atmospheric loading compared to other locations on Earth.

For astronomical telescopes where low atmospheric loading is crucial for observations, the elevation or how many degrees from the horizon a telescope observes at is important. Atmospheric loading is minimal at the zenith (90° elevation) and increases with lower elevation due to the geometric effect of looking through more atmosphere closer to the horizon. Also at lower elevation loading due to ground pick-up tends to become more significant and makes observations harder. Ground pick-up is any signal introduced into the data due to thermal emission and light reflections off the ground or terrain. Hence it is typical that CMB telescopes conservatively observe above 30° elevation in order to minimize both effects.

In order to measure large angular scale CMB anisotropies larger surveys of the sky are needed. Typically the observed sky fraction is parameterized as f_{sky}. One large advantage of the POLARBEAR site is that theoretically 80% of the CMB sky or $f_{sky} \sim 0.8$ is observable from this Southern hemisphere Chilean location throughout the year. The South Pole, which typically has a more stable atmosphere, can only observe $f_{sky} \sim 0.2$ in comparison. This allows for a much more flexible scan strategy and wider choice of CMB patches to observe. CMB patches are chosen based on factors such as previous knowledge of low foregrounds in certain regions of the sky and overlap with other surveys.

The first two seasons of POLARBEAR observations were primarily aimed to detect the lensing B-mode peak at small angular scales. The observation strategy was designed to observe a total of ~ 25 square degrees on the sky across three different patches each $\sim 3^\circ \times 3^\circ$ in size. These particular patches were chosen based off previous studies showing expected low galactic foregrounds. The three patches are called RA4.5, RA12, and RA23 based off the right ascension coordinate value approximately at the center of each patch. The three patches and their respective locations are shown in Figure 3.1.

POLARBEAR observes using constant elevation scans (CESs) which are scans across in azimuth at constant elevation. For small patch observations the telescope will scan in azimuth enough to cover the patch size with a few degrees extra for turning around to rescan the same range in the other direction. This

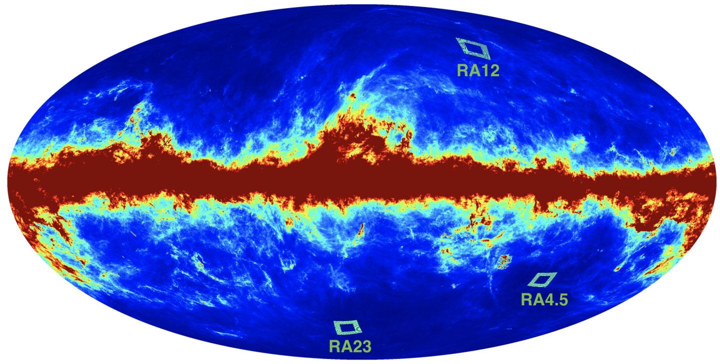

Figure 3.1: **Polarbear first and second season CMB patches** — The Polarbear first and second season CMB observation patches are shown overplotted on a full sky WMAP 857 GHz map [13]. This figure is taken from [38].

scanned observation data arranged sequentially in time is called time ordered data (TOD). The CESs are designed such that each respective patch will drift through the CES's center azimuth and elevation coordinate with time as the patches move across the sky with the Earth's rotation. Because the Chilean site is much more of a mid-latitude location than the South Pole, each patch of sky rotates in orientation with respect to the telescope much more.

Scanning across the CMB patches at different angles allows for better sky rotation or repeated data sampling of the same patch under different orientations and conditions. This helps mitigate systematics that may correlate with the instrument and telescope orientation as well as environmental conditions such as the ground pick-up that will also depend on the relative position of the telescope with respect to the site terrain.

3.3 The Huan Tran Telescope

The Polarbear instrument is installed on the Huan Tran Telescope (HTT). The HTT consists of a parabolic primary reflector and an elliptical secondary reflector. The two reflectors are an off-axis Gregorian-Dragone design that satisfies the Mizuguchi-Dragone condition. The theoretical details will be discussed in section 6.1.1. The Mizuguchi-Dragone condition is a relation between the shapes and the tilt between the axes of rotation of the two conical reflectors such that when satisfied the two reflectors together effectively act as an equivalent on-axis parabolic reflector system. This characteristic allows for low aberrations and low cross polarization systematics [39, 40]. This design allows for a maximal DLFOV for an off-axis telescope system which in turn provides the capability of installing many detectors to maximize the instrument sensitivity. An image of the HTT and a geometric ray trace design drawing are shown in Figure 3.2.

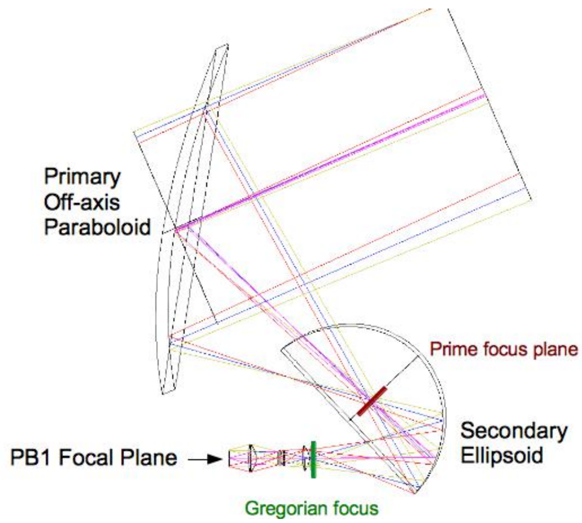

Figure 3.2: **HTT and Polarbear design** — The left is an image of the HTT currently in Chile. This image is taken from [41]. The right is an geometric ray trace image of the HTT reflectors and Polarbear instrument consisting of three refractive lenses.

The primary reflector is a 2.5 m projected diameter monolithic aluminum alloy mirror machined to a surface RMS accuracy of 53 microns. The high surface accuracies of the reflectors are necessary in order to reduce the amount of scattered power due to the roughness of the reflectors. In the reverse time frame, any instrument beam power lost due to this effect will scatter to the side-lobes or far side-lobes. This power can potentially scatter to the surroundings such as the telescope structure or ground which emit at temperatures orders of magnitude larger than the CMB anisotropies. This scattered power will introduce extra loading on the detectors and reduce sensitivity. This effect is known as Ruze scattering [42] and is given by

$$G = G_0 e^{-(4\pi\epsilon/\lambda)^2} \tag{3.1}$$

where G is the gain or beam power, G_0 is the gain without surface roughness, and ϵ is the surface RMS error. With worse surface RMS accuracy more of the main beam power will be lost from scattering. The scattering pattern (Ruze envelope) is dependent on the correlation length and can be distributed across a wide range of angles. For POLARBEAR observing at 150 GHz the gain is only reduced by $< 10\%$.

Around the primary are lower precision guard ring panels that extend the diameter to 3.5 m. The HTT and POLARBEAR receiver are optically designed such that the illumination of the primary reflector is approximately a truncated Gaussian-like profile. The majority of the beam from the instrument illuminates the monolithic primary and the guard rings only catch the beam edge power at approximately ≤ -10 dB relative to the peak power of the beam. This guard ring allows for effectively utilizing the monolithic 2.5 m diameter to minimize the angular size of the beam on the sky while also decreasing the diffraction side-lobe power. In the POLARBEAR experiment with this optical system the sky resolution is 3.5 arcmin full width at half maximum (FWHM) on the sky.

Any spillover power that is not directed to the sky ends up adding loading power to the detector and decreases its sensitivity. The guard rings on the primary also have an advantage of redirecting this potential spillover at the monolithic primary toward the sky to reduce loading. But it also potentially creates side-lobes of non-ideal shape in the telescope beam.

The HTT also contains a co-moving ground shield, prime focus baffle, and secondary reflector enclosure. The co-moving ground shield prevents stray light from the surroundings from entering the telescope optics and contaminating the signal. The prime focus baffle and secondary enclosure contain the spillover from the POLARBEAR receiver and secondary from propagating to the surrounding environment. The insides are blackened with a blackbody absorber in order to control the excess loading introduced. The reflectors, shield, baffles, and enclosures are supported by an upper and lower boom structure that provide the basic structural framework of the telescope. This boom structure also supports the POLARBEAR receiver.

3.4 Polarbear Receiver

Because the CMB photons are much lower in power compared to the surroundings and other astronomical sources, the CMB field has evolved toward utilizing large detector arrays with detector technology that must be cryogenically cooled to increase sensitivity. The Polarbear receiver is a cryostat that contains a 637 pixel lenslet coupled focal plane and cold re-imaging (refractive) optics in order to achieve this. The Polarbear receiver was designed to be coupled near the Gregorian focus of the off-axis Gregorian-Dragone reflectors for optimal optical performance. The Polarbear receiver is shown in Figure 3.3.

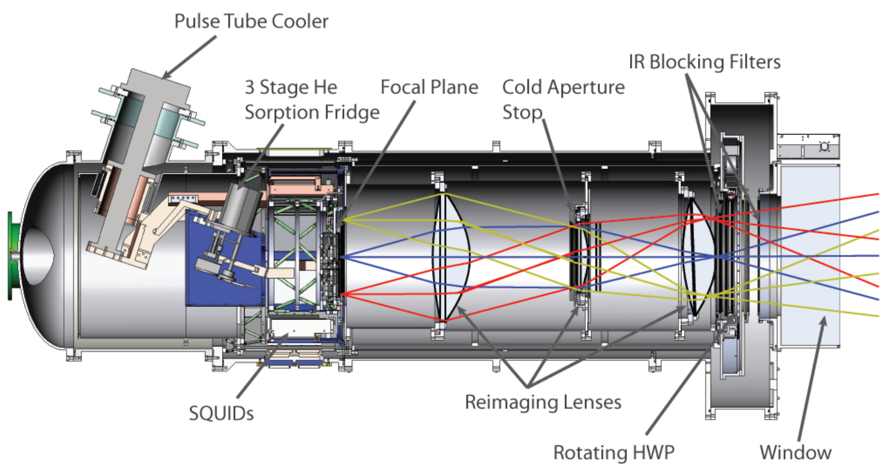

Figure 3.3: **Polarbear receiver optical and mechanical design** — The optical and mechanical design of the Polarbear receiver instrument is shown. The geometric ray traces are over-layed to illustrate the optical path from the focal plane and through the three re-imaging lenses. This figure is taken from [41].

3.4.1 Optics Design

In order to ensure high optical performance, the Polarbear receiver contains three conically shaped ultra-high-molecular-weight polyethylene (UHMWPE) refractive lenses as re-imaging optics. All three lenses are double convex in shape with spherical or hyperbolic surface shapes, and the index of refraction is 1.548. The lenses range from the smallest being 18 cm in diameter to the largest being 33 cm in diameter. The lenses are called the Collimator, Aperture, and Field lenses in order starting from the focal plane, and named according to their optical capabilities and stop type. For current generation telescopes, typically reflectors alone are optically not enough to couple with a focal plane of many detectors in an efficient manner. Hence refractive optics are designed along with reflective optics in order to accomplish this. As explained in section 2.2.3, POLARBEAR is a hybrid design and uses re-imaging lenses primarily to create a flat and telecentric focal plane, and create a compact and cryogenic Lyot stop that can fit within the receiver.

As stated before, the Mizuguchi-Dragone condition for an off-axis dual reflector design is used to ensure a large DLFOV, and for the case of the POLARBEAR instrument the DLFOV provided by the dual reflector design alone is sufficient in FOV size. Therefore the re-imaging optics design is not aimed to increase the possible DLFOV. This provides the advantage that large and high focusing power re-imaging optics are not needed, and potentially reduces the overall size of the receiver.

Figure 3.4 illustrates the DLFOV for the HTT reflective optical design which is approximately elliptical with 3.0 degrees (major axis) by 2.7 degrees (minor axis) at 150 GHz. The full FOV of POLARBEAR is designed to be circular with 2.4 degrees diameter at 150 GHz which is contained within the telescope DLFOV. The re-imaging optics are used to couple this FOV with a 19 cm diameter focal plane. The f-number at the Gregorian focus and focal plane are $f \sim 1.8$. In this particular POLARBEAR system the DLFOV can be further enhanced with high focusing power lenses as will be shown in section 5.1.1 for the Simons Array.

As can be seen from Figures 2.1 and 3.4, it is characteristic of an off-axis Gregorian-Dragone dual reflector design that the Gregorian focus is curved and highly non-telecentric. Therefore any sort of detector technology is difficult to couple at the Gregorian focus. Another characteristic of this dual reflector design is the existence of an aperture stop between the secondary reflector and the Gregorian focus. This is more easily seen in Figure 2.1. This particular location

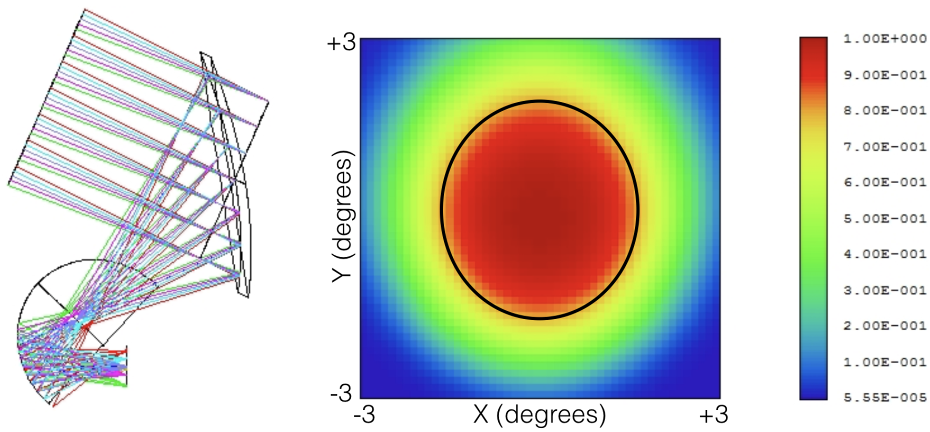

Figure 3.4: **HTT dual reflector design DLFOV** — On the left is a geometric ray trace of the HTT Gregorian-Dragone dual reflector design. The right is a 2D Strehl ratio plot illustrating the DLFOV of the reflector system. The black ellipse represents the size DLFOV area.

is difficult to utilize as a Lyot stop due to the large size and proximity to other rays. This aperture stop in the POLARBEAR dual reflector design is > 1 m in size, and impossible to cryogenically cool due to the difficulty in creating a large cryogenic enclosure around it without vignetting the prime focus rays. Therefore the re-imaging optics are needed to create both a flat and telecentric focal plane as well as a compact Lyot stop within a cryogenic receiver that is modest in size. The POLARBEAR receiver contains a ~ 15.7 cm diameter Lyot stop near the aperture lens.

3.4.2 Instrument

As briefly mentioned earlier, highly sensitive detector technology is needed to be able to measure the small CMB signal. For astronomical CMB observations the fundamental noise limit is given by the photon shot noise. Therefore it is ideal to reduce the thermal carrier noise of the detectors themselves such that the dominant noise is in fact the photon noise. The POLARBEAR receiver accomplishes this by using transition edge sensor (TES) detectors on a focal plane that is cryogenically cooled to 250 mK.

All optical components including the reflectors, lenses, and filters are by nature emissive, and hence all elements will add to the detector loading. In order to reduce this loading contribution as much as possible, any optical component that can be cryogenically cooled is contained within the receiver and sustained to ≤ 4 K. The re-imaging optics and filters are cooled for this reason as well as to reduce detector loading from spillover at these elements as previously described.

Other than the three UHMWPE lenses, the receiver includes filters and a rotating half-wave plate (HWP). The HWP is made of birefringent crystal sapphire with a thickness of 3.1 mm. The HWP can be rotated in steps in increments of 11.25 degrees. By rotating the HWP between observation days, various systematics can be averaged over similar to sky rotation mitigation. All the lenses, filters, and HWP are AR coated in order to reduce the reflections when light propagates through any refractive interface.

The POLARBEAR receiver is cooled down to 4 K using a two-stage pulse tube refrigerator (PTC). Sub-Kelvin temperature cooling is achieved using a closed cycle three-stage Helium sorption refrigerator. This refrigerator is able to cool the focal plane and detectors down to 250 mK, but must be recycled every $1 \sim 2$ days in order to sustain these sub-Kelvin temperatures.

The focal plane consists of 7 hexagonal wafer detector arrays each with 96 spatial pixels. Each pixel contains two orthogonally oriented slotted dipole antennas that are each connected to a TES detector. In each spatial pixel the two TES detectors measure orthogonal linear polarization signals. Taking the sum and difference of the orthogonal detector TOD signals in one pixel allow for measuring the temperature (I) and polarization (Q, U) signals respectively. In a simplified model the TOD signal is given by

$$s_{\parallel/\perp}(t) = I_{sky}(t) + Q_{sky}(t)\cos\Theta_{\parallel/\perp}(t) + U_{sky}(t)\sin\Theta_{\parallel/\perp}(t) \tag{3.2}$$

where $\parallel$ and $\perp$ subscripts represent the two orthogonal polarization signals and t is time. s is the TOD detector signal and Θ is the detector polarization-sensitive angle projected on the sky in equatorial coordinates. Θ is given by

$$\Theta_{\parallel/\perp}(t) = \left(\frac{\pi}{2} - \theta_{d,\parallel/\perp}\right) + \theta_{PA}(t) \tag{3.3}$$

where θ_d is the detector polarization-sensitive angle projected on the sky in horizontal coordinates and θ_{PA} is the parallactic angle used to convert between the horizontal and equatorial coordinate systems. Thus by definition $\Theta_\parallel = \frac{\pi}{2} + \Theta_\perp$ because the two detectors are orthogonally oriented. In an ideal instrument the temperature d_I and polarization d_P TOD signals are given by

$$d_I(t) = \frac{1}{2}\left(s_\parallel(t) + s_\perp(t)\right) \tag{3.4}$$

$$d_P(t) = \frac{1}{2}\left(s_\parallel(t) - s_\perp(t)\right). \tag{3.5}$$

Polarization analysis using the difference of two orthogonally sensitive detectors in one pixel is called pair differencing. Pair differencing is a useful technique in measuring a linear polarization signal.

In total there are 1274 detectors in the POLARBEAR focal plane. An image of the focal plane tower and the detectors are shown in Figure 3.5. Each pixel on the

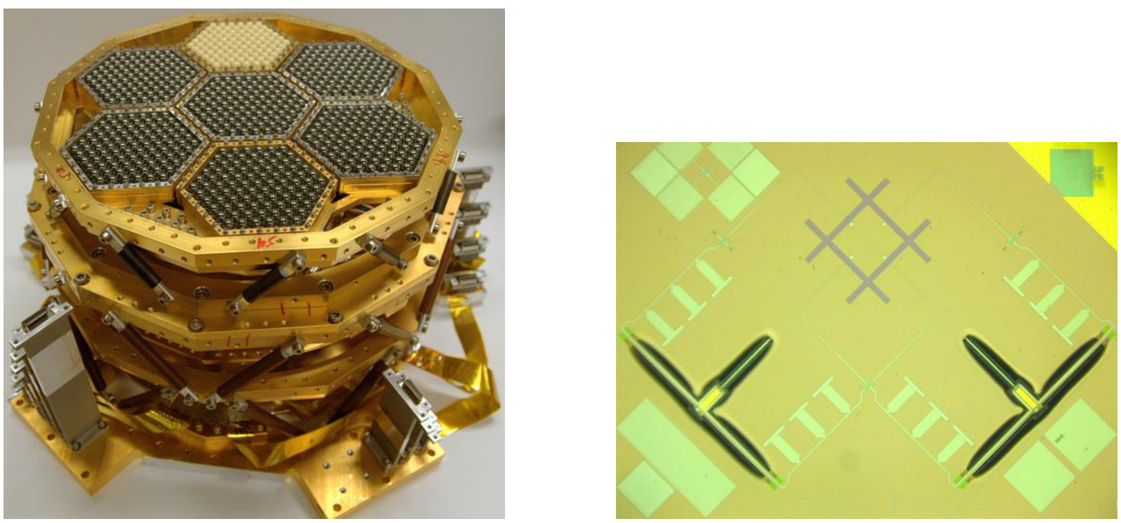

Figure 3.5: **POLARBEAR focal plane tower and detector** — The left is an image of the POLARBEAR focal plane tower with the 7 detector wafer focal plane mounted. The AR coated lenslets are installed on top of the detectors. This image is taken from [43]. The right is an image of the slotted dipole antenna coupled TES detectors. This image is taken from [41].

focal plane is coupled to the instrument optics using AR coated lenslets. Lenslets are small hemispherical dielectric lenses that amplify the gain and directivity of the detector antennas. Lenslets have a similar role to feed horns and determine the angular response of the detectors in order to couple efficiently with the instrument optics. Further details of the instrument can be found in [44].

3.4.3 Spectral Response

As discussed in section 1.5.1, atmospheric contamination within the measured signal is an important systematic that must be dealt with carefully. This systematic can be greatly minimize by designing the spectral response of the detectors to fit within the atmospheric windows where the transmission is much higher. For the Polarbear instrument, microstrip filters fabricated directly on the detector wafers determine the band width and central frequency of the spectral response of each detector. The detectors were designed to observe within the atmospheric window centered at 150 GHz which includes the peak emission of the CMB blackbody spectrum. The detector passbands must be designed wide enough to collect as much CMB photon power to increase sensitivity, but at the same time must be correctly centered and narrow enough to avoid the atmospheric emission lines that can potentially introduce large amounts of atmospheric contamination into the measurement.

The designed detector spectral response is centered at 148 GHz with a band width of 38 GHz [43]. The pre-deployment detector spectral response as measured for a subset of pixels in a laboratory set-up is shown in Figure 3.6. It is usually difficult to measure the spectral response of the detectors in the receiver in a laboratory setting due to difficulties in coupling the interferometer to the receiver efficiently. The receiver and re-imaging optics within it are designed specifically to couple to the HTT reflectors directly. The HTT reflectors are too large for use in a typical laboratory setting. Therefore for this laboratory measurement a spare warm UHMWPE lens was used instead to couple the receiver to the interferometer. This set-up is not optically ideal and hence creates procedural difficulties and systematics that will also depend on the focal plane position due to the sub-optimal coupling. Systematics can also be introduced due to optical effects from the extra coupling lens that will differ from when the actual Polarbear instrument is installed on the HTT.

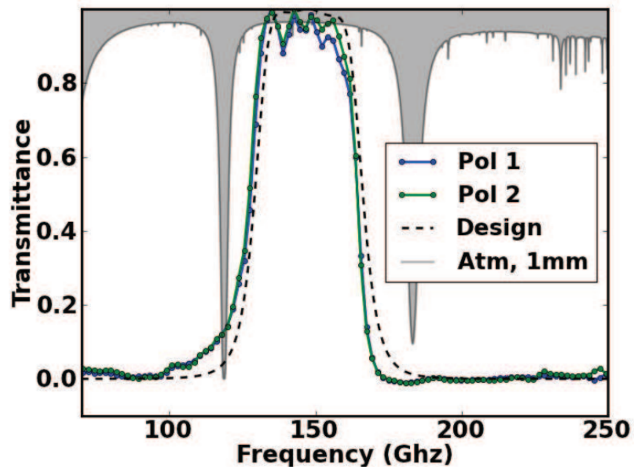

Figure 3.6: **POLARBEAR pre-deployment detector spectral response** — This is a plot of the spectral response of the POLARBEAR detectors measured before deployment. The two orthogonal polarization detectors in one pixel are compared to the theoretical design. The atmospheric transmission is over-plotted for the case with PWV = 1 mm. This figure is taken from [43].

Typically obtaining quality spectra for a large fraction of the detectors in a laboratory set-up is time consuming and in practice not done for many CMB experiments. This was the case for POLARBEAR as well and only a small subset of the detector spectra were measured in the laboratory. Therefore it was necessary to measure the detector spectral responses across the focal plane in the field once the POLARBEAR receiver had been fully deployed and installed on the HTT. The installed instrument in the field is the exact set-up that will be used to observe the CMB, and hence spectral measurements in this situation are the most accurate measurements that fully characterize the response of the instrument. This field measurement is explained later in chapter 4.

3.5 Pointing Data Analysis

As outlined in section 3.2.2, CMB observations are done using CESs with fast scanning of the telescope with scan speeds between $0.5 - 4$ degrees per second according to the type of observation scan. This scanned data is the recorded TOD. The TOD eventually gets mapped into a two dimensional (2D) CMB map through knowing the exact telescope pointing. Pointing is the position on the sky where the telescope is looking at at any particular time. In order to accurately map the CMB sky this pointing must be known to high accuracy, but the telescope's mechanical encoder read out pointing coordinate can differ from the telescope's true pointing coordinate on the sky. Therefore the pointing must be calibrated and reconstructed in order to account for structural imperfections and environmental effects that can introduce pointing error. Incorrect pointing can create systematic errors in analyzed CMB maps and spectra, and typically the pointing needs to be accurate to tens of arcseconds (1 arcsec = 1/3600 degrees) on the sky. I was in charge of the pointing reconstruction data analysis for the first two seasons of POLARBEAR data.

3.5.1 Pointing Reconstruction

The telescope observes in the horizontal coordinate system which is a celestial coordinate system using the observer's horizon as the fundamental plane. In this case the observer is the telescope. The coordinate system is parameterized by the azimuth (AZ) and elevation (EL) angular coordinates. Azimuth is the angular distance parallel to the horizon that goes from North eastward. Elevation is angular distance perpendicular to the horizon and increases in value "upward". Azimuth ranges from $0-360$ degrees and elevation ranges from $0-90$ degrees with $EL = 90°$ pointing toward the zenith. This horizontal coordinate system is fixed to the Earth and the observer's position. Hence celestial objects that have a constant position in the equatorial coordinate system (RA, DEC) will move through the horizontal coordinate system (AZ, EL) along with the rotation of the Earth.

The telescope's mechanical encoders read out horizontal pointing coordinates in (AZ, EL) through recording the physical rotation position of the azimuth and elevation bearings of the telescope as it is moved. But this can differ from the true pointing of the telescope on the sky due to physical structural imperfections and environmental effects deforming the telescope in complex ways. Figure 3.7 illustrates an exaggerated example of the entire telescope tilted relative to the ground.

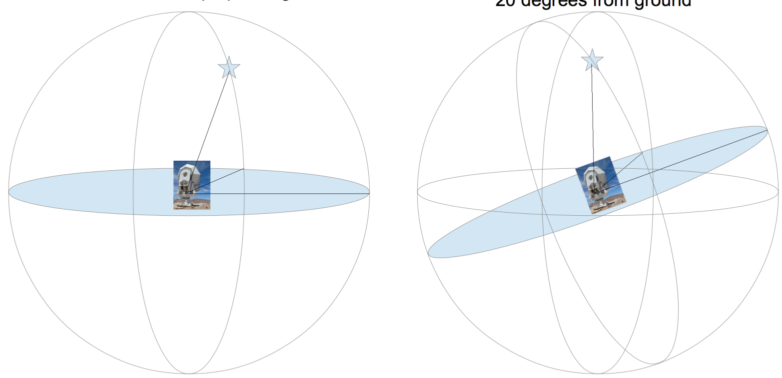

Figure 3.7: **Pointing error due to telescope tilt** — This is an exaggerated illustration comparing the error introduced into the recorded pointing due to the entire telescope being tilted relative to the ground. The left is the ideal case with no structural tilt, and the right is the case with a 20 degree structural tilt.

In this example the mechanical orientations of the telescope will be the same for the ideal and tilted telescope cases so the encoder read out pointing will be identical for both cases. But the location that the telescope is observing at on the sky is different due to the tilt. Hence without correcting for these pointing imperfections the TOD cannot be accurately transformed into a 2D CMB map. Even small pointing errors on the orders of arcminutes will introduce large errors in the high ℓ regions of the CMB power spectra. The pointing imperfections arise from physical deformations in the telescope structure and will vary as a function of the azimuth and elevation as well as a function of environmental conditions such as ambient temperature, solar radiation, and wind.

The analysis for correcting these pointing imperfections in the data is called pointing reconstruction. Physically trying to make a telescope not deform under gravity, mechanical stress, and environmental effects is very difficult and expensive to build. Therefore pointing reconstruction calibration is done to correct the encoder recorded (AZ_{enc}, EL_{enc}) pointing data to an accurate sky (AZ, EL) through modeling these imperfections based off specific radio pointing observations. This model is called the pointing model and is applied to all CMB data as a calibration. The pointing reconstruction error is calculated by taking the RMS error between the pointing model fit and the data points.

3.5.2 Radio Pointing Observations

Observations specifically taken for the pointing analysis in order to calculate the pointing model are called radio pointing observations. Radio pointing observations are observations of bright extended and point-like millimeter wave sources selected from known source catalogs [45, 13] with accurately known fixed (RA, DEC) coordinate locations on the sky. Radio pointing observations are taken at least once per day and observe $6-9$ sources within 1.5 hours. The sources are chosen such that their sky locations span a wide range in azimuth and elevation at the time the observations are done. In addition observations from planets, that have very accurately known equatorial sky positions as a function of time, were also used for the pointing analysis.

The theoretical (AZ_{th}, EL_{th}) locations of these sources can be determined with sub-arsecond accuracies from the known (RA, DEC) coordinates and the exact time of observation from a GPS clock. Comparing the theoretical location to the encoder derived location from the telescope recorded pointing gives the necessary pointing correction at that specific (AZ_{enc}, EL_{enc}). Figure 3.8 is an example of a pointing offset that must be corrected. Fitting these pointing corrections measured across the (AZ, EL) space to a pointing model allow for reconstructing the true telescope pointing across the sky.

Typically one season of Polarbear radio pointing observations accumulate $200-400$ data points from these catalog sources, and all are used to fit one pointing model per observation season. Quality pointing data are difficult to obtain due to the limited number of bright known sources, weather conditions, and sky location.

Because many sources at many sky locations must be observed, the amount of time spent observing each source is limited to $10-15$ minutes. Long observations of a source are not preferential for analysis because the sources will drift in (AZ, EL) with time. Therefore the sources must be bright enough at 150 GHz to obtain enough signal-to-noise within the observation time. Due to limited availability of source catalogs measured at 150 GHz, the target sources are chosen from catalogs measured at different frequencies based off the source brightness at that

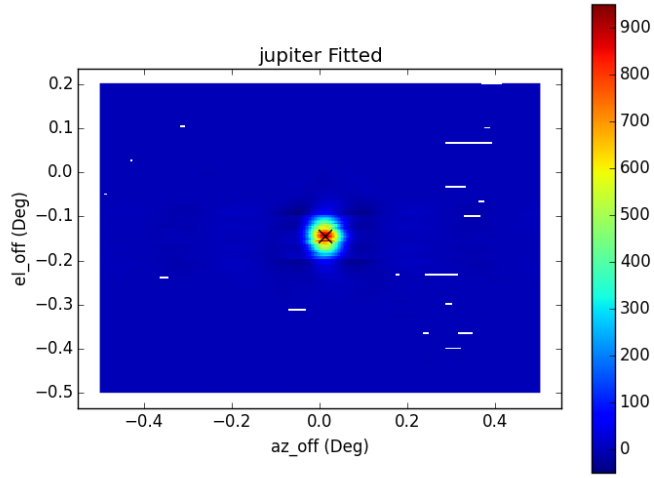

Figure 3.8: **Radio pointing observation** — This is a radio pointing observation for Jupiter. The map is calculated in the source centered coordinates based off the encoder pointing. It can be seen that the source is not located at $(0, 0)$ in the map and represents that the encoder pointing is off by $\sim 0.15°$ for this observation location on the sky.

catalog's frequency. It is found that only a small fraction of the target sources are sufficiently bright (approximately ≥ 1000 mJy) and observable by POLARBEAR.

The weather at the time of observation is also a large factor that further limits the number of quality data points. Furthermore measuring quality data points uniformly across (AZ, EL) is also limited by the number of sufficiently bright sources and source locations in (RA, DEC). Certain regions of the sky do not have readily available bright sources to observe in many cases. Thus the radio pointing observations are focused to observe sources that move within the CMB patch trajectories to be able to better constrain the pointing model within the CMB patches.

3.5.3 Pointing Model

The POLARBEAR pointing model comprises of 10 parameters out of which 5 correct for structural imperfections, 1 corrects for a timing error, and 4 correct for environmental effects. The environmental correction parameters are unique to the

Table 3.1:: Pointing model parameters — This is a description of all the pointing model parameters used in POLARBEAR. This list includes the pointing parameters adopted from other experiments as well as pointing parameters specific to POLARBEAR.

Parameter	Description
ia	AZ_{enc} offset
ie	EL_{enc} offset and collimation error in elevation
ca	Collimation error in azimuth
an	Tilt of AZ axis from vertical in north direction
aw	Tilt of AZ axis from vertical in west direction
dt	Timing error in hour angle direction
te1	Linear order in temperature flexure in elevation
ta1	Linear order in temperature flexure in azimuth
se	Differential solar heating flexure in elevation
sa	Differential solar heating flexure in azimuth

POLARBEAR analysis while the rest are adopted from other experiments [46, 47]. A description of the 10 parameters is given in Table 3.1. The 5 structural imperfection parameters are consider to be the standard pointing model that had been historically used in POLARBEAR, and the timing correction and environmental corrections are improvements to the standard pointing model.

The pointing model for the structural imperfections are given by

$$\Delta AZ = ia\cos AZ_{enc} - ca - an\sin AZ_{enc}\sin EL_{enc} - aw\cos AZ_{enc}\sin EL_{enc} \tag{3.6}$$

$$\Delta EL = -ie + an\cos AZ_{enc} - aw\sin AZ_{enc} \tag{3.7}$$

where ΔAZ and ΔEL are the pointing corrections. These terms only depend on (AZ_{enc}, EL_{enc}) and hence they are assumed to be structural imperfections that are quasi-stable with time. The timing error correction is given by

$$\Delta AZ = dt\,(-\sin LAT + \cos AZ_{enc}\cos LAT\tan EL_{enc}) \tag{3.8}$$

$$\Delta EL = -dt\cos LAT\sin AZ_{enc} \tag{3.9}$$

where LAT is the latitude of the POLARBEAR site location. This term is also considered quasi-stable with time and is a timing correction in the hour angle direction potentially caused by small synchronization errors between clocks and ephemerides.

In the radio pointing data of the first two POLARBEAR seasons, large correlations of the pointing RMS error with solar radiation and ambient temperature were observed. Therefore 4 new pointing parameters that depend on environmental effects were introduced into the pointing model. The thermal parameters are linear order in temperature corrections in both azimuth and elevation that account for pointing corrections due to thermal contraction and expansion of the telescope structure as a whole. They are given simply by

$$\Delta AZ = ta1T \tag{3.10}$$

$$\Delta EL = te1T \tag{3.11}$$

where T is the ambient temperature which is known to fluctuate between $-10°$C to $+20°$C from night to day at the POLARBEAR site on a daily basis.

The solar parameters model structural flexure due to differential solar heating. As the sun transits across the sky, different parts of the telescope structure will be heated depending on the orientation of the telescope. This can create thermal gradients across the telescope structure that cause differential thermal contraction and make the pointing drift. Using thermometers mounted on the HTT, temperature gradients of 5°C were measured across the telescope structure. The parameters are given by

$$\Delta AZ = sa \sin\theta_s \sin\phi_s \tag{3.12}$$

$$\Delta EL = se \sin\theta_s \cos\phi_s \tag{3.13}$$

where (θ_s, ϕ_s) represents sun-center coordinates. Sun-centered coordinates are a polar coordinate system that represents where the sun is relative to the boresight of the telescope. θ_s is the angular distance between the boresight and Sun, and ϕ_s is the direction of the Sun. The coordinate system is defined such that $\phi_s = 0°$ represents that the sun is located on the structurally "top" side of the telescope and $\phi_s = 180°$ represents that the sun is located on the side of the telescope structure where the receiver is located. Thus the sun-centered coordinates represent the relative orientation of the telescope with respect to the sun at all times.

In order to accommodate daily differences in solar radiation due to weather such as clouds covering the sun, a dependence on the solar irradiance can be introduced into the solar parameters. The solar irradiance is constantly monitored at the POLARBEAR site using a weather station monitoring system. Therefore the solar parameters can also be modeled as

$$\Delta AZ = sai \left(\frac{I_S}{I_{S,0}}\right)^{1/4} \sin\theta_s \sin\phi_s \tag{3.14}$$

$$\Delta EL = sei \left(\frac{I_S}{I_{S,0}}\right)^{1/4} \sin\theta_s \cos\phi_s \tag{3.15}$$

where sai and sei are the new solar parameters, I_S is the solar irradiance which varies with time, and $I_{S,0}$ is a normalization constant. This model also naturally accommodates when the sun is below the horizon.

3.5.4 Pointing Results

A pointing model is calculated separately for each individual season. Even though it is expected that the dominant portion of the pointing model should be quasi-stable over time, small structural changes of the telescope such as installation of new equipment and baffling can potentially change the pointing of the telescope. Therefore a log of all physical changes to the telescope are kept and checked for any pointing variations. Also gradual changes of the telescope structure over year timespans due to degradation and weather can similarly cause pointing changes. For example observation seasons are usually separated by the Bolivian winter season when snow accumulates on the telescope. Therefore as a conservative approach each observation season is treated individually for the pointing reconstruction.

For the first two POLARBEAR observation seasons, 484 and 240 quality data points were used in the pointing model fit respectively for the first and second seasons. The difference in the number of data points between the seasons was simply due to larger availability of time for radio pointing observations in the first season compared to the second. These datasets included radio pointing sources as well as planet sources such as Jupiter, Saturn, and Venus that were observed daily for other calibration purposes as well. The coverage map of data points used in the pointing analysis for the two seasons is shown in Figure 3.9.

Correlations between the pointing error and ambient temperature as well

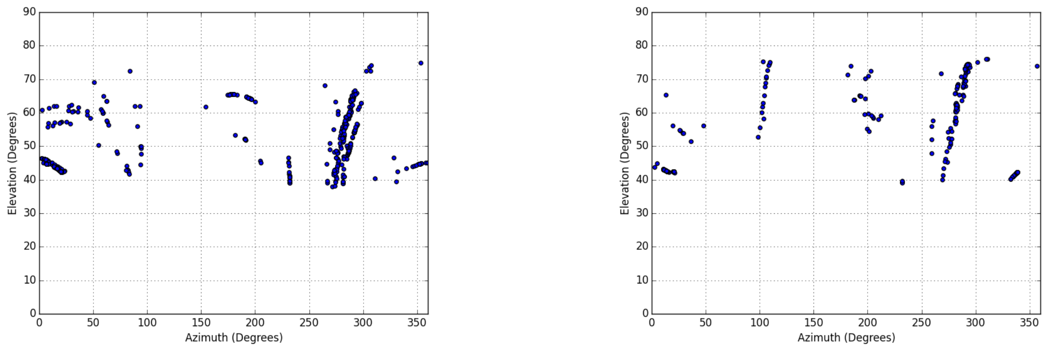

Figure 3.9: **Pointing observation sky coverage** — The left plot is the coverage of the 484 pointing data points across the (AZ, EL) sky for the first season. The right is for the 240 pointing data points for second season.

as the solar angular distance were observed. An approximate linear trend with ambient temperature was observed in the pointing error as shown in Figure 3.10. A much more complex correlation with relation to (θ_s, ϕ_s) in both azimuth and elevation error was observed as shown in Figure 3.11. It was found that pointing errors from daily Saturn observations seemed to have the strongest correlation with angular distance θ_s which was understood by the fact that Saturn covered the longest range in θ_s up to $\theta_s \sim 150°$ and was the only source in the dataset that transited to within $\theta_s < 20°$ of the Sun.

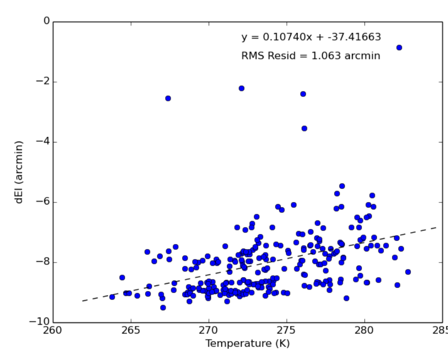

Figure 3.10: **Temperature correlation of pointing error** — This is a plot of the elevation pointing error as a function of the ambient temperature. A linear trend can be observed showing increased pointing error with higher temperatures.

A table comparing the RMS pointing reconstruction errors for second season

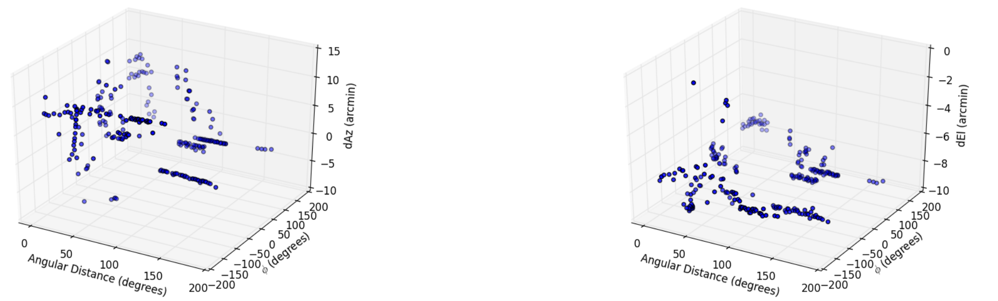

Figure 3.11: **Solar position correlation of pointing error** — These are three dimensional plots of the azimuth (left) and elevation (right) pointing error as a function of the sun's angular distance and sun's location relative to the telescope boresight. Large increase in pointing errors can be observed for small angular separation from the sun. All data points with angular distances $< 20°$ is Saturn.

Table 3.2:: **Pointing reconstruction RMS error for pointing models** — This is the pointing RMS error for various pointing models using second season data. The RMS errors of the standard model and the addition of various pointing parameters are listed. All models in the table use the standard 5 parameters.

	Standard	+dt	+ta1 te1	+sa se	+dt ta1 te1 sa se	+dt sai sei
RMS AZ	29.279"	17.282"	27.359"	27.054"	16.097"	16.248"
RMS EL	37.165"	33.841"	33.477"	31.596"	25.815"	24.927"
RMS Total	47.313"	37.998"	43.234"	41.596"	30.422"	29.754"

using various combinations of the pointing parameters is shown in Table 3.2. The 10 parameter model used as a baseline in POLARBEAR is the pointing model with the standard 5 parameters, timing correction (dt), thermal corrections ($ta1, te1$), and the solar corrections (sa, se). It can be seen that without the inclusion of the timing, thermal, and solar parameters the RMS error increases by $\sim$ 17" of which the timing correction contributes $\sim$ 9" and the thermal and solar corrections contribute $\sim$ 8". Therefore in CMB experiments where accuracies of tens of arcseconds are needed, thermal and solar effects are large and need to be modeled for sufficient pointing reconstruction.

Comparing day and night datasets, where one would expect the largest differences in the thermal and solar effects, using the 10 parameter model it was found that the RMS error was $\sim$ 27" and $\sim$ 14" respectively. These values are in approximate agreement with the quoted mechanical pointing accuracy tolerances supplied by the GDMS company that manufactured the HTT. The mechanical pointing accuracy tolerances were analyzed to be ~ 24" and ~ 9" for the cases of 5°C thermal gradients and no thermal gradients across the HTT structure respectively. Therefore the 10 parameter pointing reconstruction seems to be accurate to potentially the level of mechanical HTT tolerances. These results also show that the pointing reconstruction can be further improved by preventing thermal gradients across the HTT structure using better insulation.

Using the pointing model with 10 parameters, the final RMS pointing error was found to be 27.184" and 30.422" respectively for the first and second seasons. Figure 3.12 shows the pointing model fit compared to the data points for each season. These pointing models are valid to reconstruct the pointing at ~ 30" accuracies across the full range in AZ and between $30° < EL < 80°$ on the sky which covers the entire scan range used for CMB observations. Both seasons even

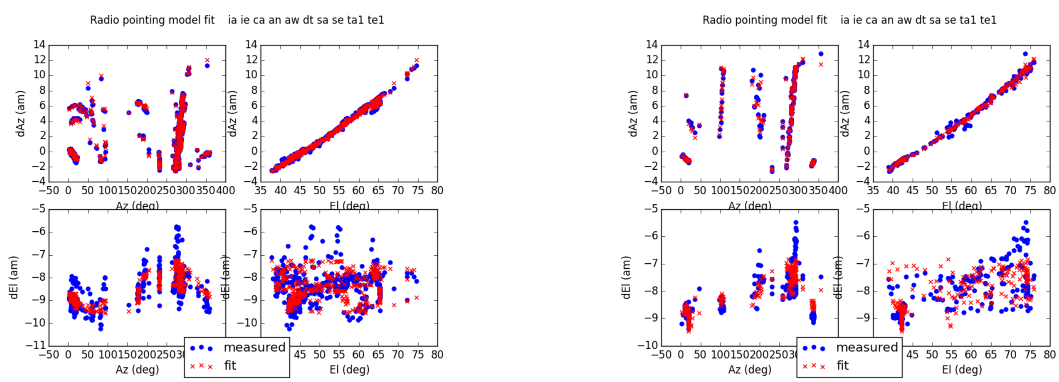

Figure 3.12: **Pointing model fit** — These plots show the pointing model fit compared to the pointing data for the first (left) and second (right) seasons. The blue dots are the measured data and the red x's are the pointing model fits. The pointing model agrees well with the data, but it can also be seen there is some residual structure in the data.

with very different data points agree well in terms of the parameter values and RMS errors. These pointing models are used for the pointing reconstruction calibration for the POLARBEAR science results for the first two seasons. The addition of further structural flexure correction parameters was found to only improve the RMS errors by sub-arcsecond levels. Due to the degeneracy between parameters and the lack of observational evidence, further structural flexure parameters were not included.

Table 3.2 also shows the RMS error with the improved solar parameters (sai, sei). With the inclusion of the dependency on measured solar irradiance, it was found that a similar RMS pointing reconstruction error of 29.754" could be obtained with with only 8 parameters: standard 5 parameter, timing correction (dt), and improved solar parameters (sai, sei). Therefore the improved solar parameters potentially seem to accommodate both the thermal and solar effects. The improved parameters show great promise but further study is still needed before implementation.

3.6 First Season Results

The POLARBEAR collaboration published three results from the first season observations in 2014 [38, 48, 49]. As explained in section 3.2.2, the first season of observations was primarily aimed to measure the small angular scale peaking lensing B-mode signal. Very deep observations on small sky fraction patches allowed the instrument to achieve high map depth and strong sensitivities to the lensing signal. The measured first season CMB polarization maps for the RA23 patch can be seen in Figure 3.13. This lensing signal was measured using three different analysis techniques.

The first was a direct measurement of the C_ℓ^{BB} power spectrum across angular scales of $500 < \ell < 2100$ [38]. The data was binned into four multipole bins with bin centers and widths carefully chosen to have negligible bin-to-bin correlations. The spectrum is shown in Figure 3.14. Within this multipole range the dominant source of sky polarization signal is from the lensing signal and thus no primordial component is detected. This result rejected the null hypothesis of no gravitational lensing B modes at the 97.2% confidence level. This result also was the first C_ℓ^{BB} measurement with $> 2\sigma$ significance.

The POLARBEAR result was compared with the standard ΛCDM model based off the WMAP-9 cosmological parameters. Fitting the POLARBEAR band

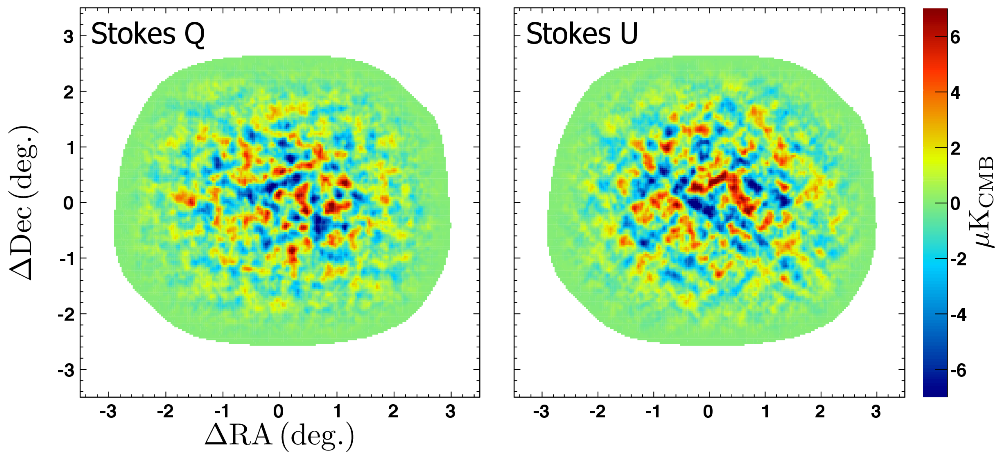

Figure 3.13: **Measured RA23 CMB polarization maps** — These are the first season CMB polarization maps for Q (left) and U (right) for the RA23 patch. This figure is taken from [38].

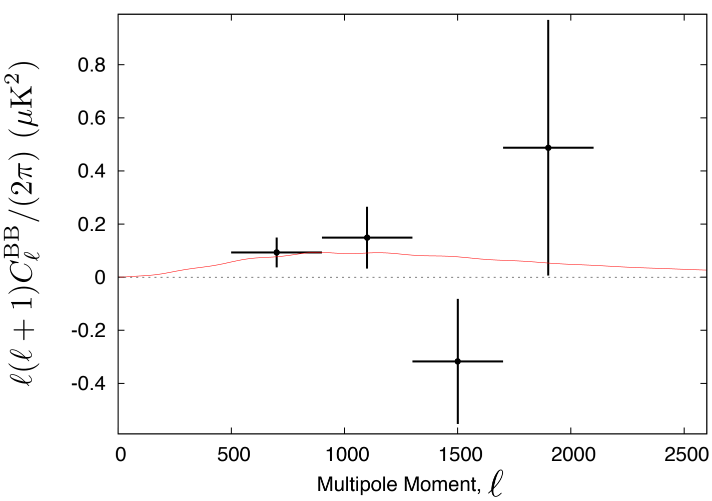

Figure 3.14: C_ℓ^{BB} **power spectrum measurement** — This is the measured C_ℓ^{BB} power spectrum for the first season of data. The theoretical lensing signal is plotted in red. This figure is taken from [38].

powers to this ΛCDM C_ℓ^{BB} model with the amplitude of lensing A_{BB} as its free parameter, it was found that $A_{BB} = 1.12 \pm 0.61(\text{stat})^{+0.04}_{-0.12}(\text{sys}) \pm 0.07(\text{multi})$, where $A_{BB} = 1$ is defined as the WMAP-9 derived theory. Here "stat" represents the statistical error, "sys" represents the additive component of the systematic error, and "multi" represents the multiplicative component of the systematic error. The additive systematic errors are a linear addition of the instrumental systematics, and the multiplicative systematic errors are a quadrature sum of systematics such as the calibration errors that affect the spectrum multiplicatively.

Systematic errors can easily create spurious B-mode signals if not correctly estimated or modeled. Hence a detailed study and estimation of all known instrumental systematic errors were done as well in order to assure that the measured B-mode signal is not dominated by systematics. Full TOD simulations were calculated incorporating known instrumental systematic errors based off calibration measurements taken from the observations. Simulated systematic errors and the accumulated additive error are shown in Figure 3.15. This shows that the cumulative systematic error is more than an order of magnitude below the theoretical B-mode signal and the statistical error. The systematic error due to the standard 5 parameter pointing model is also included within this simulation. It was found that the high accuracy pointing calibration minimized the pointing error to less than 1% of the measured lensing B-mode signal.

Two more complimentary analyses were used to probe the lensing B-mode signal. The deflection power spectrum C_ℓ^{dd} was calculated from the first season results [48]. C_ℓ^{dd} is a 4 point correlation function and is the power spectrum of the lensing quadratic estimators for EE and EB. Because gravitational lensing converts E-modes into B-modes through deflecting the CMB photon trajectories, the lensing deflection field can be calculated from the E and B-mode information by distinguishing the non-Gaussian lensing anisotropies. C_ℓ^{dd} was estimated using two four point estimators $<$EEEB$>$ and $<$EBEB$>$ as well as the combination of the two estimators. The result was similarly fit to a C_ℓ^{dd} model based off the WMAP-9 cosmological parameters, and the amplitude of observed lensing in the deflection power spectrum was found to be $A_{dd} = 1.06 \pm 0.47^{+0.32}_{-0.27}$, where $A_{dd} = 1$

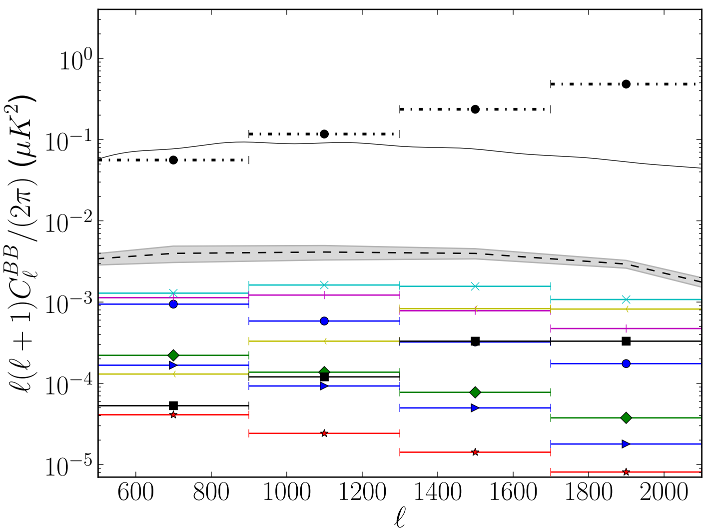

Figure 3.15: **Systematic error simulations** — This is a plot of the simulated systematic instrumental error contributions in the C_ℓ^{BB} power spectrum. The theoretical lensing B-mode (black solid line) and the per bin statistical error (black dashed points) are shown. The individual systematic errors for the pointing model and differential pointing (light blue crosses), the polarization angle (purple pluses), the differential beam size (yellow arrows), the beam ellipticity (black squares), electrical crosstalk (blue arrows), gain drift (red stars), and gain model (green diamonds and blue circles) are plotted. The cumulative error (black dashed line) is also shown. This figure is taken from [38].

is defined as the WMAP-9 ΛCDM model. The error once again includes statistical errors as well as bounds from the systematic errors.

This deflection spectrum result shows evidence of lensing B-modes and rejects the no lensing hypothesis at 4.2σ significance. The C_ℓ^{BB} result can be combined with the C_ℓ^{dd} result by adding the statistical significance of each in quadrature sum. Together the combined significance of the existence of lensing B-modes is at 4.7σ.

The third analysis was a cross correlation between the Polarbear first season data with cosmic infrared background (CIB) data [49]. The CIB measurements trace large scale structures such as galaxy clusters in the universe which are sources of gravitational lensing for the CMB. Hence the CMB polarization lensing signal and CIB are innately correlated. The Polarbear data was cross correlated with the Herschel satellite data. This result also showed evidence for lensing B-modes at the 2.3σ significance.

The three independent analyses of the first season POLARBEAR results all showed the existence of lensing B-modes at $> 2\sigma$ significance. These measurements and significances are expected to improved with further seasons of data and put stronger constraints on CMB B-mode science

3.7 Acknowledgements

Figures 3.1, 3.13. 3.14, and 3.15 are reprints of materials as appears in: The POLARBEAR Collaboration: P. A. R. Ade, Y. Akiba, A. E. Anthony, K. Arnold, M. Atlas, D. Barron, D. Boettger, J. Borrill, S. Chapman, Y. Chinone, M. Dobbs, T. Elleflot, J. Errard, G. Fabbian, C. Feng, D. Flanigan, A. Gilbert, W. Grainger, N. W. Halverson, M. Hasegawa, K. Hattori, M. Hazumi, W. L. Holzapfel, Y. Hori, J. Howard, P. Hyland, Y. Inoue, G. C. Jaehnig, A. H. Jaffe, B. Keating, Z. Kermish, R. Keskitalo, T. Kisner, M. Le Jeune, A. T. Lee, E. M. Leitch, E. Linder, M. Lungu, F. Matsuda, T. Matsumura, X. Meng, N. J. Miller, H. Morii, S. Moyerman, M. J. Myers, M. Navaroli, H. Nishino, A. Orlando, H. Paar, J. Peloton, D. Poletti, E. Quealy, G. Rebeiz, C. L. Reichardt, P. L. Richards, C. Ross, I. Schanning, D. E. Schenck, B. D. Sherwin, A. Shimizu, C. Shimmin, M. Shimon, P. Siritanasak, G. Smecher, H. Spieler, N. Stebor, B. Steinbach, R. Stompor, A. Suzuki, S. Takakura, T. Tomaru, B. Wilson, A. Yadav, O. Zahn. A Measurement of the Cosmic Microwave Background B-mode Polarization Power Spectrum at Sub-degree Scales with POLARBEAR. The Astrophysical Journal, Vol. 794, No 2, pp. 171-192 , October 2014, doi:10.1088/0004-637X/794/2/171. The dissertation author made essential contributions to many aspects of this work especially in the data analysis.

Figures 3.2 (left), 3.3, and 3.5 (right) are reprints of materials as appears in: D. Barron, P. Ade, A. Anthony, K. Arnold, D. Boettger, J. Borrill, S. Chapman, Y. Chinone, M. Dobbs, J. Edwards, J. Errard, G. Fabbian, D. Flanigan, G. Fuller, A. Ghribi, W. Grainger, N. Halverson, M. Hasegawa, K. Hattori, M. Hazumi, W.

Holzapfel, J. Howard, P. Hyland, G. Jaehnig, A. Jaffe, B. Keating, Z. Kermish, R. Keskitalo, T. Kisner, A. T. Lee, M. Le Jeune, E. Linder, M. Lungu, F. Matsuda, T. Matsumura, X. Meng, N. J. Miller, H. Morii, S. Moyerman, M. Meyers, H. Nishino, H. Paar, J. Peloton, E. Quealy, G. Rebeiz, C. L. Reichart, P. L. Richards, C. Ross, A. Shimizu, C. Shimmin, M. Shimon, M. Sholl, P. Siritanasak, H. Spieler, N. Stebor, B. Steinbach, R. Stompor, A. Suzuki, T. Tomaru, C. Tucker, A. Yadav, O. Zahn. The POLARBEAR Cosmic Microwave Background Polarization Experiment. Journal of Low Temperature Physics, Vol. 176, No 5-6, pp. 726-732, September 2014, doi:10.1007/s10909-013-1065-5. The dissertation author made essential contributions to many aspects of this work especially in instrument optical design and deployment.

Figures 3.5 (left) and 3.6 are reprints of materials as appears in: K. Arnold, P. A. R. Ade, A. E. Anthony, D. Barron, D. Boettger, J. Borrill, S. Chapman, Y. Chinone, M. A. Dobbs, J. Errard, G. Fabbian, D. Flanigan, G. Fuller, A. Ghribi, W. Grainger, N. Halverson, M. Hasegawa, K. Hattori, M. Hazumi, W. L. Holzapfel, J. Howard, P. Hyland, A. Jaffe, B. Keating, Z. Kermish, T. Kisner, M. Le Jeune, A. T. Lee, E. Linder, M. Lungu, F. Matsuda, T. Matsumura, N. J. Miller, X. Meng, H. Morii, S. Moyerman, M. J. Myers, H. Nishino, H. Paar, E. Quealy, C. Reichardt, P. L. Richards, C. Ross, A. Shimizu, C. Shimmin, M. Shimon, M. Sholl, P. Siritanasak, H. Speiler, N. Stebor, B. Steinbach, R. Stompor, A. Suzuki, T. Tomaru, C. Tucker, O. Zahn. The bolometric focal plane array of the POLARBEAR CMB experiment. Millimeter, Submillimeter, and Far-Infrared Detectors and Instrumentation for Astronomy VI, Proc SPIE 8452, 84521D, September 24, 2012, doi:10.1117/12.927057. The dissertation author made essential contributions to many aspects of this work especially in instrument optical design and deployment.

Chapter 4

Fourier Transform Spectrometer

4.1 Introduction

Precise and accurate spectral characterization of detectors is a crucial step in any astrophysical experiment. Obtaining this information allows the experimenter to ensure the correct frequency cutoffs are observed, determine the existence of any coupling between the detectors and atmospheric emission lines, and quantify expected amplitudes of astrophysical continuum emission. In addition to these benefits, spectral characterization of detectors is of particular importance when conducting polarization-sensitive observations of the CMB in that it enables the minimization of $T \rightarrow P$ leakage — a systematic error that arises when a polarization signal is extracted from two orthogonally oriented polarization-sensitive detectors.

Characterization of the detectors for POLARBEAR was performed using a Fourier Transform Spectrometer (FTS) that was specially designed for use with the POLARBEAR receiver as it operates in the field. The FTS is a Martin-Puplett interferometer utilizing a blackbody source and mounts direction to the HTT between its primary and secondary reflectors. The FTS has a large throughput in order to fully illuminate multiple pixels simultaneously. The output polarizing grid is continuously rotated to utilize each modulated signal harmonic component separately for different analyses. The parabolic mirror of the FTS is also specially designed to reduce aberrations when coupled to the HTT. The FTS was installed on the HTT in April 2014 and successfully took spectral data across the POLARBEAR focal plane.

This FTS was designed to also be compatible with POLARBEAR-2 and the Simons Array, the next generation receivers of POLARBEAR which will be explained in chapter 5. During fabrication of the Simons Array receivers and focal planes the FTS design was adapted to construct a lab-use FTS for more convenient and frequent testing of detectors and optical components during development in a laboratory setting.

I lead the POLARBEAR FTS project and was in charge of all aspects of the optical design, mechanical development, data taking, and data analysis. All FTS optical components were designed and machined at the University of California, San Diego, and all polarizing wire grids were fabricated in-house using a custom wire gird winder device.

4.2 Fourier Transform Spectrometer

4.2.1 Motivation

As explained in section 3.4.3, one of the largest motivations for detector spectral measurements is to characterize the spectral band center, width, and shape in order to verify that the detector spectral response is well contained within the atmospheric windows. Also because the polarization signal is measured by pair differencing, any spectral band shape mismatch between the detectors in the same pixel will create $T \rightarrow P$ leakage. Therefore spectral characterization of the detectors allows for estimation of the systematic contribution from the atmosphere which can be a dominant systematic in the signal.

Another motivation is that knowledge of the detector spectral response shapes to high accuracy allows for minimization of potential systematics introduced when using different calibration sources. The CMB data is calibrated using various sources such as the atmosphere, point sources, and physical thermal sources. All sources have vastly differing emission spectra that vary within the detector spectral band region. The measured signal is a multiplication of the detector spectra with the source's emission spectra. Therefore if the responses of the detectors are not accurately known, complex systematic errors can be introduced into data due to the differences in the source spectra used for calibration compared to the measured CMB emission spectrum. The FTS is a crucial calibration instrument used to accurately measure the detector spectral responses.

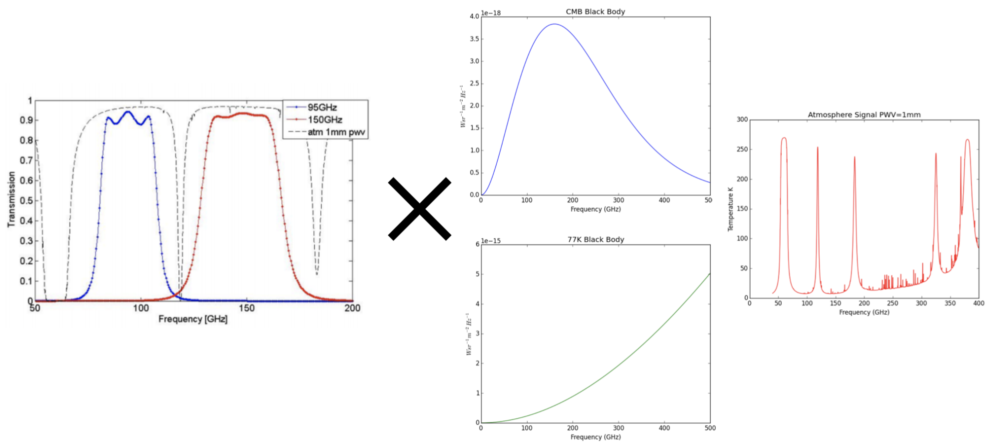

Figure 4.1: **Calibration with emission spectra** — This is an illustration of the different emission spectra of sources potentially used for calibration. The ideal detector spectral bands are shown on the left. The right are emission spectra of the CMB (blue), planet like point source (green), and the atmosphere (red) which are all vastly different. The signal is a multiplication of the band with the emission spectra.

4.2.2 Fourier Transform Spectrometer

An interferogram is the measured interference as a function of the path length difference between two signals within an interferometer. Fourier transform spectroscopy is the technique in which the spectrum of a measured signal is calculated through taking the Fourier transform of the interferogram produced by that signal propagating through a two-beam interferometer to the detector. The interference pattern is given by

$$\begin{aligned} I(k,x) &= \left\langle (\mathbf{E_1} + \mathbf{E_2})^2 \right\rangle_T \\ &= S(k)\left[1 + \cos(\Delta)\right] \end{aligned} \tag{4.1}$$

where $\mathbf{E_1}$ and $\mathbf{E_2}$ are the two interfering waves of the interferometer, the phase difference $\Delta = kx$ is the signal's wavenumber k multiplied by the path length difference x between the two waves, and $S(k)$ is the spectrum. The measured interferogram by a detector $I(x)$ can be written as

$$I(x) = \tilde{I} + \int_0^\infty S(k) \cos(kx)\, dk \tag{4.2}$$

assuming that $I(x)$ is an even function of x. $\tilde{I}$ is a constant offset. Taking the inverse Fourier transform gives

$$S(k) = 2\int_{-\infty}^{\infty} \left(I(x) - \tilde{I}\right) \cos(kx)\, dx, \tag{4.3}$$

and hence it is apparent that the interferogram and spectrum form a Fourier transform pair. The phase difference Δ is introduced into the signal by controlling a movable mirror in one of the two beams ("arms") of the interferometer. In this case the frequency response of the detector determines the shape of the interferogram and allows for calculating the detector spectrum.

4.2.3 Martin-Puplett Interferometer

The POLARBEAR FTS is a Martin-Puplett interferometer [50, 51]. A Martin-Puplett interferometer differs physically from a Michelson interferometer in three ways: the beam-splitters are wire grid polarizers, the mirrors in the two interfering beams are roof mirrors that rotate the polarization of reflected light by 90 degrees, and the output of the interferometer is a polarized signal.

The Martin-Puplett interferometer has two distinct advantages over a standard Michelson interferometer. The first is that the Martin-Puplett interferometer has highly efficient beam-splitting with theoretically no frequency dependence in transmission or reflection due to the wire grid polarizers. The second advantage is that the Martin-Puplett interferometer is a 4 port device with two input and two output ports. The output ports provide complimentary signals in which simple subtraction or continuous modulation by rotating the output polarizer allows for suppression of spurious noise in the signal and unpolarized source. The continuous

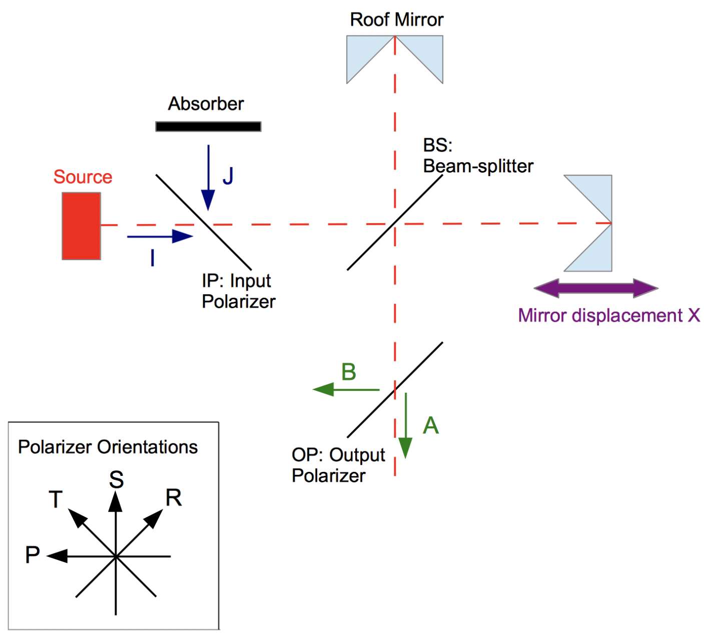

Figure 4.2: **Schematic of Martin-Puplett interferometer** — This is a schematic drawing of a standard Martin-Puplett interferometer with all optical components. I is the input signal from the thermal source and J is a blackbody absorber. A and B are the two output ports of the interferometer.

modulation set-up has some unique characteristics in the output signal as explain in section 4.2.4.

A schematic illustration of a Martin-Puplett interferometer with a source at one input port is shown in Figure 4.2. The POLARBEAR FTS uses a thermal blackbody source that is polarized by the input wire grid polarizer placed in its diverging beam. An input parabolic mirror collimates the radiation from the source and directs it toward the beam-splitter. An identical design output parabolic mirror focuses the output beam and the output rotating wire grid polarizer is placed near the focus. The specific design will be described in section 4.3.1.

4.2.4 Modulation Theory

For POLARBEAR the FTS is primarily used to characterize the spectral response of polarized detectors, and instead of a standard chopper the output polarizer is continuously rotated in order to modulate the signal. Thus the measured signal can be decomposed into various harmonics of the rotation frequency. Using the Jones formalism and the methodology from Martin 1982 [50] as a starting point, the various dependencies on the rotation and polarization angle can be derived.

For the Martin-Puplett interferometer only relative angles between the polarizers and roof mirrors are important. For example the input polarizer and beam-splitter polarizer wire orientations need only to be 45 degrees rotated relative to each other. An overall rotation angle of the whole optical system is unimportant. Therefore the Jones formalism methodology presented by Martin will apply for all generic Martin-Puplett interferometers. For the case of POLARBEAR one last polarizer matrix must be further included in the calculation representing the polarization sensitive axis of the polarized detector.

The calculation through the interferometer to the output port is given by the following matrix calculation:

$$A = R_S(\alpha - \theta(t))T_{OP}R_{OP}(\theta(t))DR_{IP}(45^\circ)I_{IJ}. \tag{4.4}$$

I_{IJ} is the input signal from the two input ports, R_{IP} is the input polarizer, D is the matrix introducing the phase shift between the two arms, $T_{OP}R_{OP}$ represents the transmission through the output polarizer, and R_S is the polarized detector. $\theta(t)$ and α represent the output polarizer angle and detector polarization sensitive angle respectively. $\theta(t)$ has a time dependence and represents the constant modulation. Calculating the signal seen at the detector one obtains

$$A_t A_t^* = A_{DC} + A_{2f} + A_{4f} \tag{4.5}$$

$$\begin{aligned}
A_{DC} &= a_1 + \frac{1}{2}a_2 \cos(2\alpha) + \frac{1}{2}a_3 \sin(2\alpha) = C_{DC} && (4.6)\\
A_{2f} &= a_1 \cos(2\theta(t) - 2\alpha) + a_2 \cos(2\theta(t)) + a_3 \sin(2\theta(t)) \\
&= a_2(\Delta) \cos(2\theta(t)) + C_{2f} && (4.7)\\
A_{4f} &= \frac{1}{2}a_2 \cos(4\theta(t) - 2\alpha) + \frac{1}{2}a_3 \sin(4\theta(t) - 2\alpha) \\
&= \frac{1}{2}a_2(\Delta) \cos(4\theta(t) - 2\alpha) + C_{4f} && (4.8)
\end{aligned}$$

where the signal consists of DC, 2f modulated, and 4f modulated terms. Any terms labeled with C are constant values after demodulation. The a_i terms are given below.

$$a_1 = \frac{1}{4}\left(d_m^2 + d_f^2\right)\left(I_s^2 + J_p^2\right) \tag{4.9}$$

$$a_2 = \frac{1}{2}|d_m||d_f|\left(I_s^2 - J_p^2\right)\cos\left(\Delta\right) \tag{4.10}$$

$$a_3 = \frac{1}{4}\left(d_m^2 - d_f^2\right)\left(I_s^2 + J_p^2\right). \tag{4.11}$$

The interferogram terms of interest are those that only depend on a_2 which contains the Δ dependence. d_m and d_f are the complex propagation coefficients for the moving mirror and fixed mirror arms. They represent the loss in amplitude of the signal as they propagate through the two arms. I and J are the signals from the input ports and the subscripts S and P represent the orthogonal wave amplitude components parallel and perpendicular to the input polarizer wires.

It can be seen that no interferogram is seen in the DC term. The 2f term contains the interferogram signal independent of the detector polarization angle. The 4f signal contains an interferogram signal that depends on the relative angle between the output polarizer angle and detector polarization angle. Hence theoretically even without knowing the relative angle between θ and α the spectrum can be measured using the 2f signal. In a standard Michelson interferometer this separation of signals into different harmonics with different parameter dependencies does not exist. The $4f$ signal with this dependence on α is not measurable in a Michelson interferometer.

4.3 Instrument Design and Hardware

4.3.1 Instrument Design

The POLARBEAR FTS was specifically designed to measure the spectral response of the installed POLARBEAR detectors in the field. Hence the FTS had to be mounted and installed on the HTT with the POLARBEAR receiver in place. Various constraints were put on the FTS design due to this fact. For example, the

FTS had to be relatively light weight, able to withstand environmental conditions in the Atacama Desert in Chile, and capable of correctly optically coupling to the Polarbear receiver.

The FTS design is shown in Figure 4.3. The various component designs are described in the following sections. The FTS was designed to be mounted on top of the HTT lower boom structure at the prime focus located between the primary and secondary reflectors. This was accomplished using a XYZ mounting stage as described in section 4.3.6.

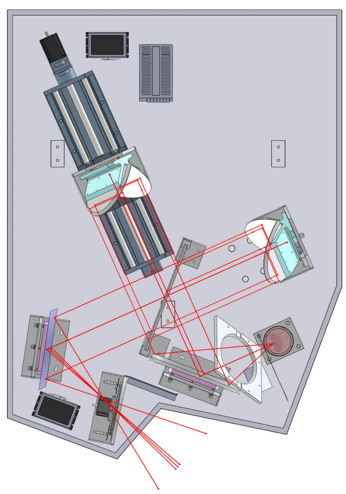

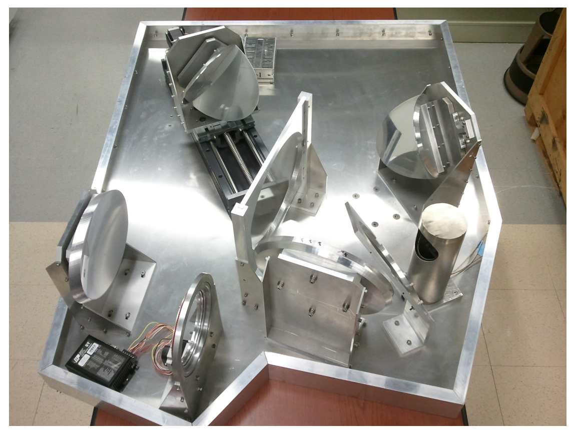

Figure 4.3: **Mechanical design of Polarbear FTS** — The mechanical drawing of the Polarbear FTS is shown on the left, and an image of the completed FTS is shown on the right.

The various optical and physical specifications of the Polarbear FTS are listed in Table 4.1. The FTS is capable of operation in two modes that allow for different spectral resolutions as explained in section 4.3.2.1.

4.3.2 Mirrors

The FTS contains four mirrors of two different types: two roof mirrors and two parabolic mirrors. All the mirrors are made with MIC-6 aluminum and the reflecting surfaces are machined to a surface flatness RMS of less than 25 microns based off the Ruze criterion [42]. The mirrors were further polished to

Table 4.1:: POLARBEAR FTS specifications — The designed specifications of the FTS are listed in this table. The FTS can be used in two different modes that change the interferogram type and frequency resolution in the calculated detector spectrum. Any specifications that don't distinguish between the two modes are common.

Specs	Mode 1 (Mode 2)
Interferogram	Double (Single)
Frequency Resolution	1 GHz (0.5 GHz)
Maximum Frequency	500 GHz
Throughput	15.1 steradian cm^2
Output f-number	$f = 1$
Dimensions	1.3 m $\times$ 1.0 m
Weight	150 lbs

sub-optical quality so visible wavelength lasers could be used to align the various FTS components relative to each other.

4.3.2.1 Roof Mirrors

The roof mirrors consist of two flat aluminum plates intersecting at an angle 90 degrees relative to each other. The angle is maintained using a precision machined 90 degree bracket onto which the aluminum plates can be screwed. Machining tolerances allow for the angle to be constrained to within 0.05 degree error. The bracket further acts as a buffer so exterior stresses from the installed alignment adjustments do not shear the reflecting surfaces. The rims of the two reflecting plates are cut in such a way that in the plane perpendicular to the beam the rim forms a circular 20 cm diameter reflecting area.

The movable roof mirror is positioned on a linear translation stage that is controlled by a motor manufactured by Applied Motion. The mount for this mirror contains a tilt alignment adjustment such that the roof mirror can be adjusted up to $2 - 3$ degrees relative to the vertical direction. The stationary roof mirror mount contains a rotary shear alignment adjustment such that the roof mirror can be rotated up to $2 - 3$ degrees in the plane perpendicular to the beam. These adjustment mechanisms are necessary to ensure that the two roof mirrors are in the same orientation with respect to each other when compared in the plane of the beam-splitter [52].

There are two sets of mounting holes for the stationary roof mirror, one closer to the beam splitter and one farther away. The two positions allow the FTS to operate in two modes. Mode 1 fully extends the stationary beam arm length which puts the maximum constructive interference (“white light fringe") location of the moving mirror approximately midway of the linear stage. A double-sided interferogram can be measured in this mode and the spectrum will have 1 GHz resolution. Mode 2 makes the stationary beam arm length at a minimum. In this case the "white light fringe" location will be near the beam-splitter on one end of the linear stage. A single-sided interferogram can be measured in this mode and the spectrum will have 0.5 GHz resolution.

Mode 2 has higher spectral resolution at the cost of only observing one side of the interferogram. This can be disadvantageous at times because the number of data points is half (less redundant modes) and because single-sided interferograms may be less sensitive to systematics. An asymmetric interferogram is typically a sign of systematic effects such as misaligned optics, reflections, and partial illumination that can be easily observed before calculating the spectrum. Therefore in Polarbear mode 1 is used as the default mode. Theoretically one side of the interferogram is sufficient in order to measure the spectrum in the absence of systematics.

4.3.2.2 Parabolic Mirrors

The Polarbear FTS employs two parabolic mirrors: one to collimate the beam from the source and another to focus the FTS output signal. The two parabolic mirrors have identical conical shapes in order to preserve the f-number in the input and output ports. This shape was designed to act like a small version of the HTT primary reflector.

The HTT telescope primary and secondary reflectors are designed and oriented such that they satisfy the Mizuguchi-Dragone condition [39, 40], thereby minimizing astigmatic aberration as well as limiting cross-polarization at and near the central optical axis of the system. The FTS parabolic mirror is a 65 degree off-axis paraboloid with $f = 1$, consistent with the HTT primary reflector shape, but much smaller with only a 20 cm diameter clear aperture. The FTS parabolic mirror is the 2.5 m HTT primary reflector shrunk proportionally down in all dimensions to a 20 cm reflector.

When the FTS is properly aligned and mounted on the HTT, the output FTS parabolic mirror and HTT secondary reflector together also satisfy the Mizuguchi-Dragone condition. Hence along the central optical axis of the FTS and Polarbear system, the astigmatism will be canceled and cross polarization will be minimized. This orientation is shown in Figure 4.4. But due to the smaller size of the FTS parabolic mirror, the FTS must be placed much closer to the secondary, and the FTS will only couple with a small portion of the focal plane detectors at once. The FTS is placed near the prime focus plane which is a plane that the rays come to an approximate focus (field stop) between the primary and secondary reflectors.

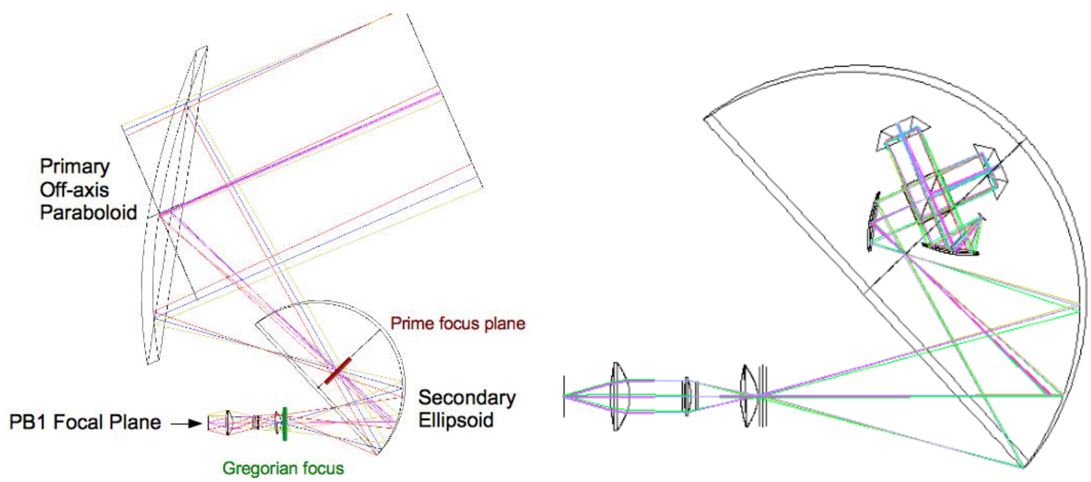

Figure 4.4: **FTS optical coupling to Polarbear** — These are geometric ray traces of the full Polarbear optics (left) and the FTS coupled to the secondary and receiver (right). In both cases the Mizuguchi-Dragone condition is satisfied, but the FTS must be mounted near the prime focus plane in order to fully capture (illuminate) all rays from a particular pixel. The FTS is shown here coupling to 7 pixels at once.

From optical ray tracing simulations it was found that near the central axis of the system, the optical coupling between the receiver and FTS is very efficient. Greater than 95% of the rays are unvignetted and reach the FTS source (reverse time frame). The RMS wavefront error when coupled is found to be less than 1% of one wavelength. This is consistent with the theory and shows that there are minimal aberrations. Theoretically it is expected that the optical coupling efficiency will decrease slightly as a function of distance from the central optical axis, i.e. for pixels located away from the central pixel in the POLARBEAR focal plane the efficiency is lower. From the simulations for the outermost edge pixels greater than 87% of the rays are unvignetted and the RMS wavefront error is less than 25% of one wavelength.

It was found that the FTS parabolic mirror does in fact allow for high optical coupling efficiency for the pixels located in the central region but is limited in effect for the edge pixels. Still this design performs better on average across the focal plane compared to other potential FTS parabolic mirror shapes that do not satisfy the Mizuguchi-Dragone condition. The optical coupling is relatively high even for the focal plane edge pixels in comparison.

4.3.3 Polarizing Grids

The FTS contains three types of polarizing grids: the input grid, beam-splitter grid, and output grid. The necessity to keep the FTS compact in size required for three different grid designs in order to utilize space efficiently. All the grids are strung with 25 micron diameter Tungsten wire at 100 micron spacing. Theoretically wire grids with this specification can produce a polarization efficiency of 99.6% in transmission and 99.2% in reflection for normal incidence unpolarized light [53].

4.3.3.1 Grid Winder

The collimated portion of the FTS instrument is designed to have a 20 cm diameter clear aperture in order to provide large throughput. Grids of large size and unique design are expensive even for millimeter wave applications. Hence a grid winder device was developed for POLARBEAR.

The grid winder device is shown in Figure 4.5. The device is composed of two linear stages and one rotating axel. The frame for the grid to be wound is mounted on the rotating axel and rotated slowly at a constant rate. A Tungsten wire spool is mounted on a vertical linear stage that is synchronized with the motion of the edge of the rotating grid. As the grid rotates, the spool will move vertically in synchronous such that the wire coming from the spool and getting wound on to the grid is always held parallel to the ground. This keeps the tension in the wire constant throughout the winding process by minimizing the angle variation of the wire coming off the spool. The second linear stage controls the spacing of the wire as the grid is wound.

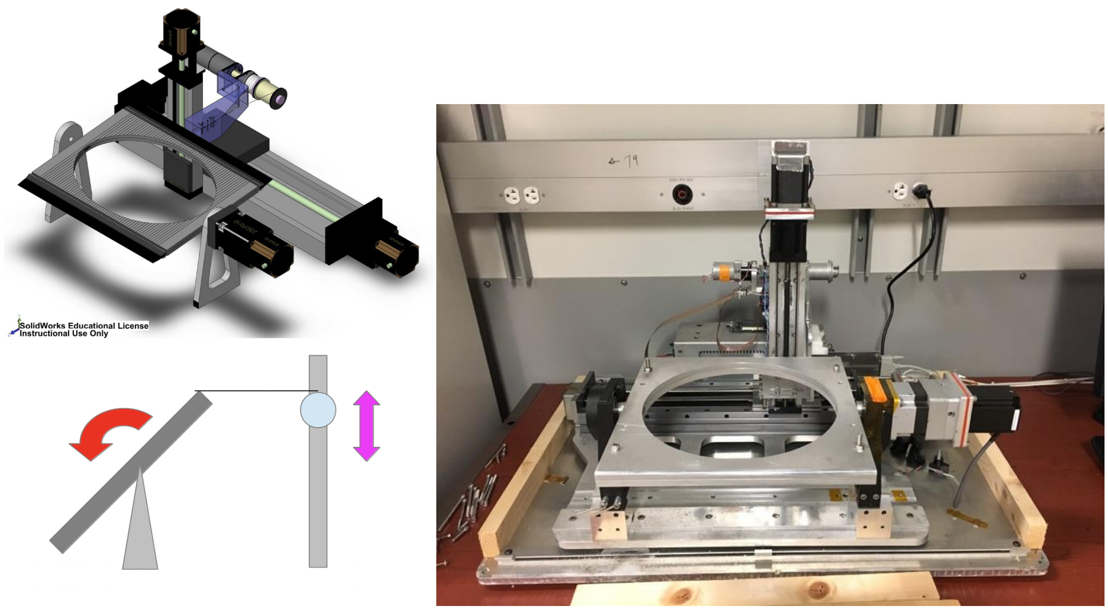

Figure 4.5: **Custom polarizing wire grid winder device design** — The mechanical design (left top) of the custom polarizing wire grid winder device and schematic illustration (left bottom) of the winding procedure are shown. An image of the fabricated grid winder is presented on the right.

A controllable magnetic clutch applies a back tension on the spool as the wire is being spun off it. This is set to create a 45 gram-force constant wire tension. Guide pins are installed to keep the wire between the spool and grid aligned at all times. A small voltage difference is created across two of the pins that are in contact with the wire at all times during the winding. If the wire breaks during the winding process the device will sense an "open circuit" and is programmed to stop. This allows the user to know exactly at what point in time the wire broke so that the winding process can be restarted at that exact location.

The grid winder device allows for consistent spacing of the Tungsten wire with less than 10 micron error in spacing, and the sag in the wire is less than 20 microns for the largest grid sizes. The device is cable of winding up to 37 cm $\times$ 37 cm rectangular grids. In order to create accurate polarizing grids, the grids are wound very slowly and each grid typically takes between 10 and 24 hours depending on the size. One winding process makes two grids of the same design at a time by mounting two grid frames back to back on the axel. Once the winding is complete, epoxy is carefully poured into predesigned grooves in the grid frames that secures the wire onto the grid frames.

4.3.3.2 Beam-splitter and Input Polarizing Grids

The beam-splitter grid is the largest grid in the system and is shown in Figure 4.6. It is rectangular with a 28.3 cm (major axis) by 20 cm (minor axis) clear elliptical aperture. The aperture is designed such that when placing the grid 45 degrees relative to the collimated beam, the clear aperture in that projection is 20 cm in diameter. The beam-splitter wires are oriented in the normal direction to the optical bench.

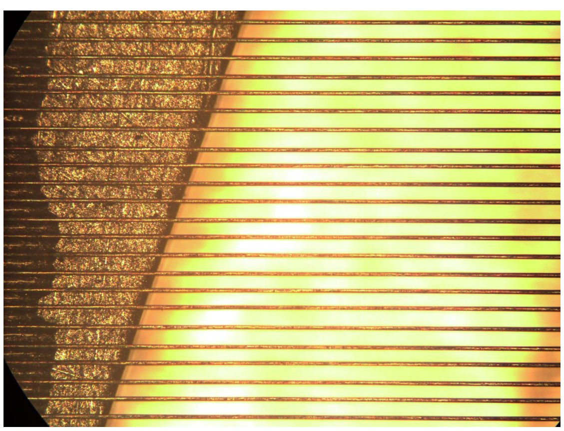

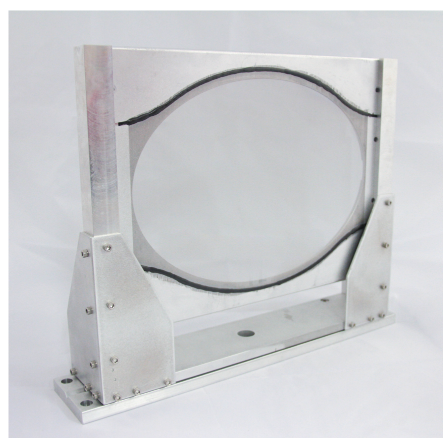

Figure 4.6: **Wire grid polarizer for beam-splitter** — A microscope image of the wire grid wound at 100 micron pitch with 25 micron Tungsten wire is shown on the left. The right is the completed beam-splitter wire grid polarizer.

The input grid is rectangular and has a 13.3 cm (major axis) by 11.2 cm (minor axis) clear elliptical aperture. It is placed in the diverging beam between the source and first parabolic mirror, and tilted relative to the central ray to ensure that the reflected light is terminated at the enclosure walls layered with eccosorb. The input grid is oriented such that in the plane perpendicular to the central ray the projection of the wires are 45 degrees relative to the optical bench.

4.3.3.3 Rotating Output Polarizing Grid

The output grid is circular and has a 12.38 cm diameter clear aperture. It is placed in the converging beam between the second parabolic mirror and FTS output. Similar to the input grid, the output grid is tilted relative to the central ray. The output grid is mounted to a circular bearing that is continuously rotated by a belt drive and another motor from Applied Motion in order to provide the modulation in the output signal.

4.3.4 Source

The FTS uses a S-SHTS/4 ceramic heater source made by Elstein. The radiating area is 60 mm $\times$ 60 mm and can be heated up to 900°C. The source requires 230V input to operate at its nominal temperature. Hence the source was powered using a step-up transformer.

It could easily be seen by eye that the face of heat source had large and complex temperature gradients across it that are most likely due to the positioning of the heated wires within the ceramic itself. Locations where the heated wire existed were much hotter. In order to make the radiating surface much more uniform in temperature, a ceramic adhesive was used to attach another ceramic square plate of a similar size to the radiating area. Even though this had the effect of decreasing the operating temperature of the source slightly, the mitigation of possible systematic effects due to the non-uniform source temperature was determined to be worth the reduction in temperature. The large heater size was motivated by ZEMAX simulations and by requiring that the FTS fully illuminate multiple pixels at once when coupled to POLARBEAR.

4.3.5 Optical Bench and Enclosure

In order to maintain structural strength while minimizing the weight of the full FTS, the optical bench was chosen to be aluminum honeycomb with 3/8 inch cell sizes. The honeycomb panel was custom made by Pacific Panels with fixed and floating screw hole inserts for mounting optical components. The optical bench had to be cut into an irregular 7-sided shape in order to prevent any structural interference with the HTT telescope when mounted near the prime focus plane. Aluminum C channels were placed and screwed in around the entire perimeter of the optical bench.

In order to minimize stray light from the environment entering into the FTS optical path, an aluminum enclosure covered the entire FTS. The enclosure has the same shape as the optical bench footprint and is screwed into the C channel around the perimeter of the optical bench. The inner walls of the enclosure are layered with AN-72 eccosorb in order to minimize reflections inside as well as terminate the reflected light from the polarizers as noted previously. The enclosure has three fans built in to create a constant air flow and reduce possible heating from the source.

4.3.6 XYZ Mounting Stage

In order to optically couple the FTS to the Polarbear receiver, the FTS not only had to be placed in the prime focus of the HTT telescope but also had to be capable of translating around this focus in order to couple with pixels across the Polarbear focal plane. According to optical simulations the FTS had to be able to move ± 10 cm in both X and Y directions within the prime focus plane as well as ± 5 cm in the piston motion perpendicular to this plane to correctly couple to all the pixels in the focal plane. This was accomplished using the XYZ mounting stage as shown in Figure 4.7.

The XYZ mounting stage is a rigid 8020 structure with three translation stages aligned in the directions of the necessary motion. The FTS mounts to the XYZ mounting stage which is mounted on the lower boom structure of the HTT telescope. The stage is remotely operational which allows for automatic scanning

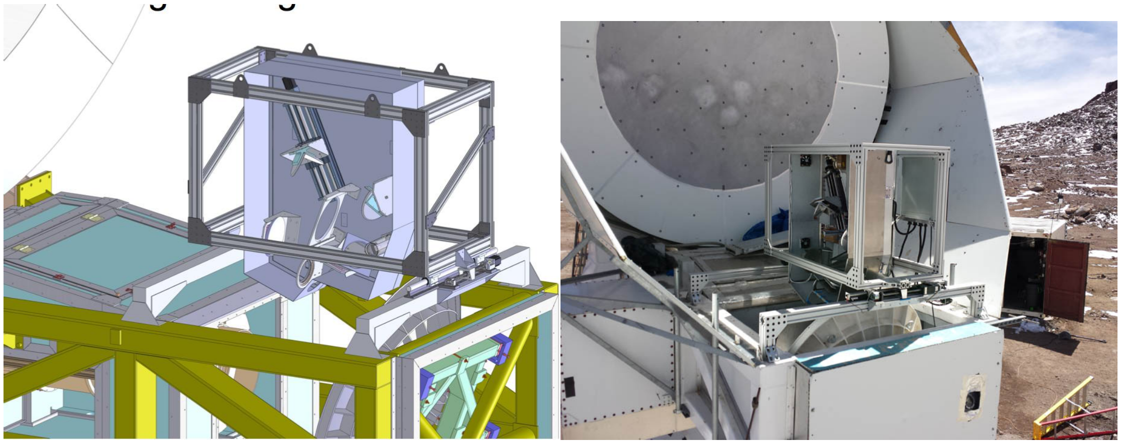

Figure 4.7: **XYZ mounting stage** — The left is a drawing of the XYZ stage mounted on the HTT boom with the FTS mounted. The right is an image of the same set-up with the FTS and XYZ stage physically installed in Chile.

and data taking across the POLARBEAR focal plane.

4.4 Data and Analysis

The FTS was deployed and installed on the HTT in Chile in April 2014 using the XYZ stage. Installation, testing, and full spectral measurements of the POLARBEAR detectors across the focal plane were done through the entire month of April 2014. The FTS successfully took spectral measurements for 69% of the focal plane detectors in this single deployment. Measurements of all focal plane detectors could not be obtained due to various limitations from observational time constraints, temporarily inactive detectors, and temporary unexpected telescope data acquisition noise in certain data runs. The FTS data was also taken near the Bolivian winter season, and hence as a safety precaution observations were stopped when it was snowing and when there were high winds.

4.4.1 Measurements and Data

The FTS was successfully installed near the prime focus plane without interference with any structural components of the HTT. As explained in section 4.3.6, the FTS must be controlled and scanned across the prime focus plane in order to measure spectra across the entire Polarbear focal plane.

It was found that the FTS could fully illuminate $\sim$ 19 pixels at once in one run when placed at one location in the prime focus plane. Thus in order to measure spectral data across the Polarbear focal plane, multiple runs had to be taken with the FTS at different locations in the prime focus plane. Initially a list of XYZ stage coordinate locations that effectively coupled the FTS to the needed pixel locations on the focal plane was determined. Then the XYZ stage and FTS were programmed to automatically scan through these predetermined XYZ stage coordinates and take FTS runs at each location.

Because the FTS signal is much larger in power than the sky signal, the detectors would become saturated under regular conditions. Hence the TES detectors were "over-biased" or configured such that they were less responsive but much less prone to saturate. This is done by setting the TES to operate in a region with smaller dR/dT, and hence the detectors have less response to incoming power compared to the setting for CMB observations. This allowed for the detectors to measure the FTS signal without saturating, but in some detectors non-linear responses to the signal were apparent in the data near the maximum peak of the interferogram. This non-linear effect is expected to introduce negligible systematics in the measured spectra within the main band as will be discussed later.

In order to obtain sufficient signal-to-noise in the measurements, the FTS moving mirror was stepped in 1400 steps across 30 cm of travel and integrated for 2 seconds at each step. Thus each FTS run took $\sim$ 90 minutes. An example of a measured interferogram is shown in Figure 4.8.

When the FTS is installed on the HTT, regular CMB observations cannot be done. In order to limit the amount of CMB "down time", the FTS installment, testing, and measurements were done within a month time span. With this consideration it was determined in advance that obtaining spectra for the entire Polarbear focal plane would be difficult. Therefore the FTS scanning method was differentiated between wafers. The central wafer was scanned most densely with 19 runs. The other 6 wafers were scanned only with 10 runs each. Each run

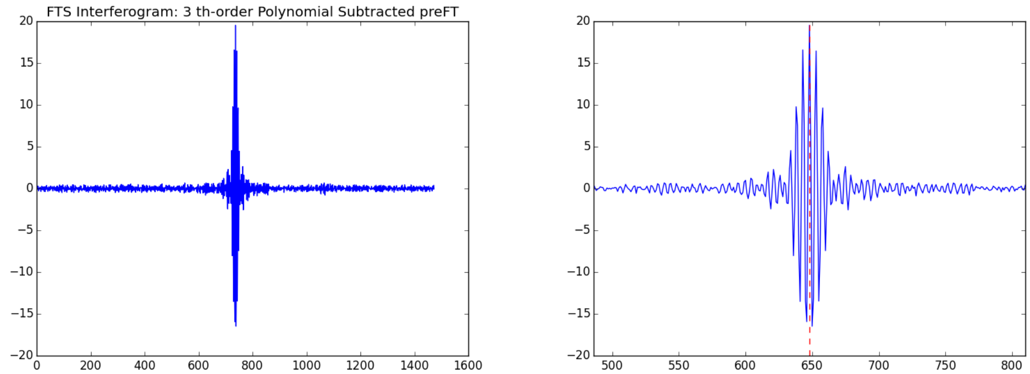

Figure 4.8: **Measured interferogram** — An example of a measured interferogram for one of the POLARBEAR detectors is shown. The full interferogram (left) and the interferogram near the peak (right) is shown.

aims at a different set of pixels within the wafer. Differences in the scan strategy are illustrated in Figure 4.9. With this scan strategy theoretically all the detectors in the central wafer can be measured and $\sim 70\%$ of the detectors in the other 6 wafers can be measured.

A total of 79 different FTS runs coupling to different pixel locations across the POLARBEAR focal plane were done. This scan method across the focal plane allowed for repeated measurements for a large portion of the detectors in order to average out potential systematics effects in the measurements.

4.4.2 Data Analysis and Results

The interferograms taken through the 79 datasets were analyzed, and for detectors that had repeated measurements across datasets the spectra were averaged to improve the signal-to-noise. The spectra were measured with 1 GHz spectral resolution. Sufficient quality detector spectra measurements for 876 detectors ($\sim 69\%$ of the focal plane) were measured. Approximately $\sim 82\%$ of the detectors in the central wafer and $\sim 67\%$ of the detectors in the other 6 wafers were measured. Detector spectra with insufficient signal-to-noise were cut in the analysis. An image of all the measured spectra for the central wafer is shown in Figure 4.10.

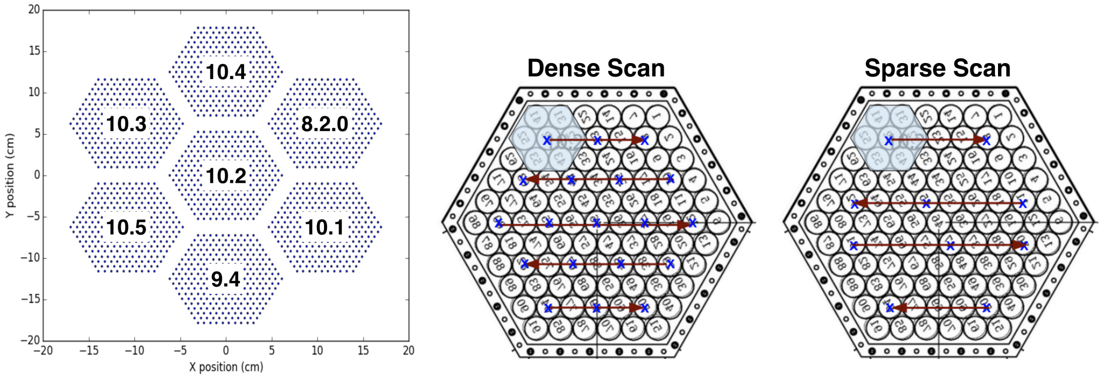

Figure 4.9: **FTS scan strategy** — The left is an image of the POLARBEAR focal plane with wafer IDs labeled. There are a total of 7 wafers. The dense (center) and sparse (right) scan strategies are illustrated. The blue Xs represent the aimed pixels, and the FTS can obtain data for the 19 pixels centered around these aimed pixels per run. The dense scan (19 runs) was used for the central wafer 10.2 and the sparse scan (10 runs) was used for the other 6 wafers. Each run aims at a different set of pixels within the wafer.

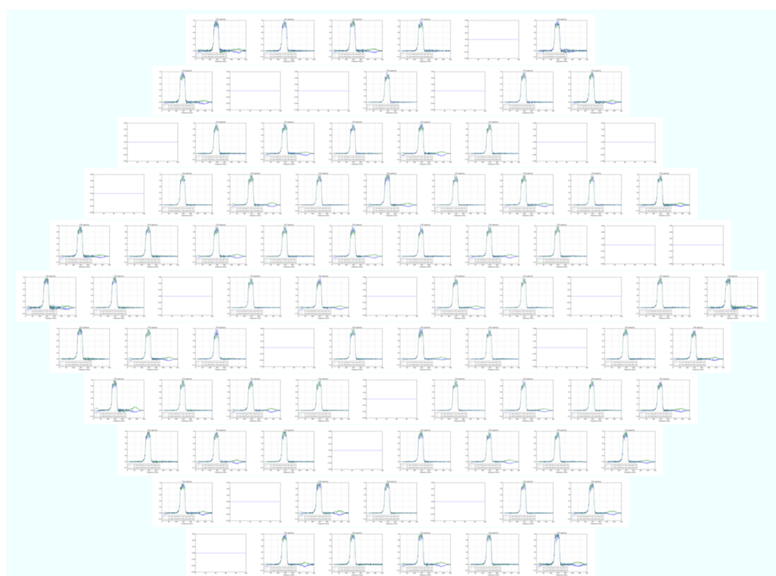

Figure 4.10: **Wafer 10.2 detector spectra** — Layout of the measured detector spectra for the central wafer 10.2 is shown. Each detector is in the correct pixel location on the wafer and each pixel contains spectra for both detectors in its pair.

In POLARBEAR the two orthogonal detectors in one pixel pair are labeled "top" and "bottom" when they are fabricated. For each pixel the top detector's spectrum is peak normalized and then a multiplicative relative gain factor is calculated to normalize its pair's bottom detector spectrum. The relative gain factor is calculated assuming a signal from an atmospheric emission spectra at 1 mm PWV and elevation 60° as a typical observing situation. The gain factor is calculated such that the integrated signal power in the two detectors of a pair are equal. Theoretically this is equivalent in analysis technique to how the relative gain calibration in a pixel would be calibrated if one were to calibrate the detectors using the atmosphere. According to the exact calibration methods and sources chosen for the real CMB data, the emission spectra used in this relative gain factor calculation would need to be adjusted.

The integrated band center and integrated bandwidth distributions per wafer were calculated and are shown in Table 4.2. The integrated band center ν_c and integrated bandwidth $\Delta\nu$ are given by

$$\nu_c = \frac{\int_{\nu_l}^{\nu_r} \nu S(\nu) d\nu}{\int_{\nu_l}^{\nu_r} S(\nu) d\nu}, \quad \Delta\nu = \int_{\nu_l}^{\nu_r} S(\nu) d\nu \tag{4.12}$$

where ν_l and ν_r are the left (rising) and right (setting) edges of the band respectively.

It was found that the average band centers per wafer were very consistent within a wafer but vary on a per wafer basis by a few GHz. Wafer 8.2.0 was found to be slightly lower than the rest. Wafer 10.1 was found to have larger variations within a wafer due to a bimodal distribution of the band centers with two peaks at ~ 140 and ~ 146 GHz. The bandwidths were found to be much more consistent between wafers with a similar spread in each wafer.

The pixel in-band difference was calculated by taking the difference in spectra (top minus bottom) between pixel pairs and measuring the average and standard deviation of the differenced spectra values within the band. By default in the pair differencing for CMB observations, the top minus the bottom signal is used as well. Table 4.2 shows the wafer averages of these value.

It was found that the pixel pair in-band differences were very small with

Table 4.2:: Detector spectral response statistics — The measured and calculated detector spectral response statistics are shown. The number of measured detectors, integrated band center, and integrated bandwidth values are given per wafer. The average (AVG) and standard deviation (STD) of the distribution per wafer were calculated for the band center and bandwidth. The wafer average value of the pixel pair in-band difference average (AVG) and standard deviation (STD) values are also shown.

		Band Center (GHz)		Bandwidth (GHz)		Pixel In-band Diff	
Wafer	# Detectors	AVG	STD	AVG	STD	AVG	STD
8.2.0	106	136.872	0.691	30.435	1.825	-0.0298	0.0588
9.4	107	146.896	0.525	32.756	1.553	-0.0046	0.0624
10.1	114	142.081	2.520	31.814	1.840	-0.0070	0.0618
10.2	149	143.472	0.547	32.576	1.113	-0.0001	0.0414
10.3	133	148.734	0.621	31.026	1.854	0.0054	0.0615
10.4	154	143.981	0.505	32.159	1.218	0.0070	0.0438
10.5	113	145.455	0.363	31.819	1.299	0.0090	0.0414

averages $< 1\%$ in amplitude except for wafer 8.2.0 that had $\sim 3\%$ differences. In all cases the fluctuations (standard deviation) in the differences seem to average out across the band. Example pixel pair spectra and their difference is shown in Figure 4.11.

The averaged spectra per wafer were also calculated. These are shown in Figures 4.12, 4.13, 4.14, and 4.15. It can be seen in Figure 4.12 that some detectors show a "bump" in the spectrum at ~ 300 GHz. This effect is due to the expected non-linear response when high power is incident on the detector. Because the detectors are much more near saturation when making FTS measurements, non-linear responses become more apparent with more incident power.

Due to this effect the peak of the interferogram is slightly decreased. This reduction in the interferogram peak magnitude can be analytically modeled to show that it creates a bump in the spectrum at approximately twice the band center value. This effect was also observable in the data because this effect was only apparent in detectors that the polarization sensitive angle was more co-aligned with the FTS beam-splitter orientation. This situation creates more incident power on these detectors and the non-linear response is more apparent. But this effect is expected to have negligible effect within the band.

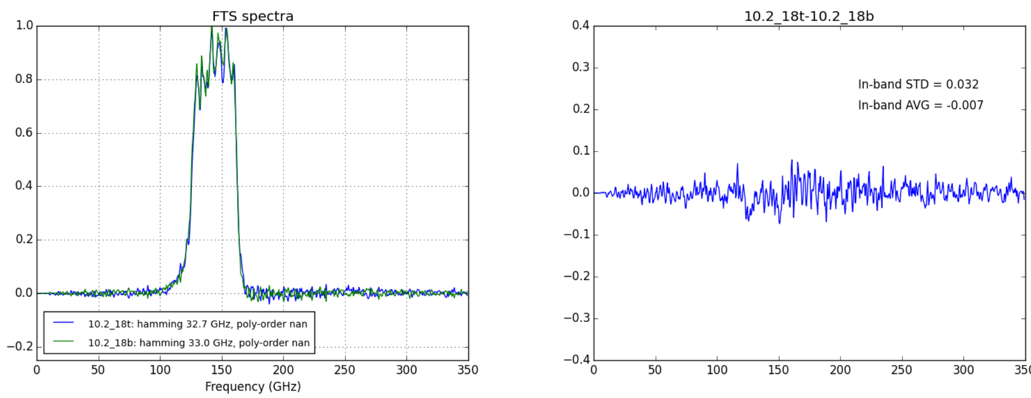

Figure 4.11: **Measured pixel pair spectral difference** — An example of the spectra for one pixel on wafer 10.2 is shown on the left. The spectra for the top and bottom detectors are over-plotted. The differenced spectra is shown on the right. The average in-band difference for this pixel is -0.007.

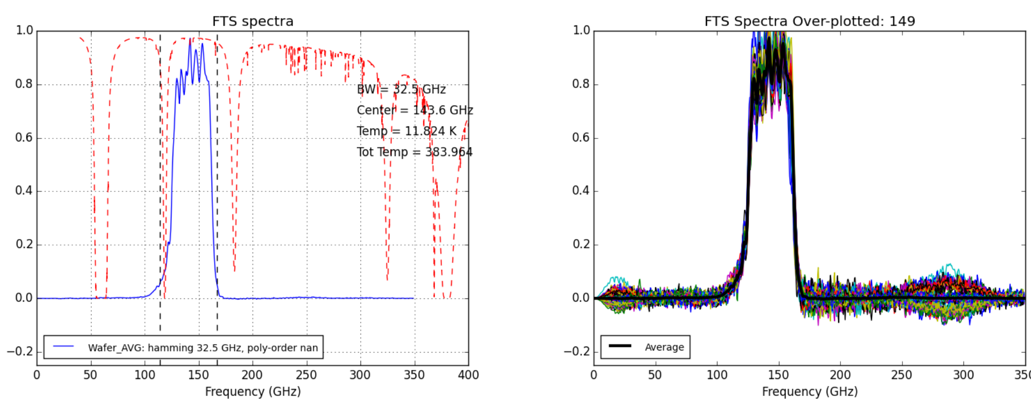

Figure 4.12: **Wafer 10.2 averaged spectrum** — The wafer averaged spectrum for wafer 10.2 is shown (left). All the spectra for wafer 10.2 over-plotted are also shown (right). The averaged spectrum is over-plotted as a thick black line.

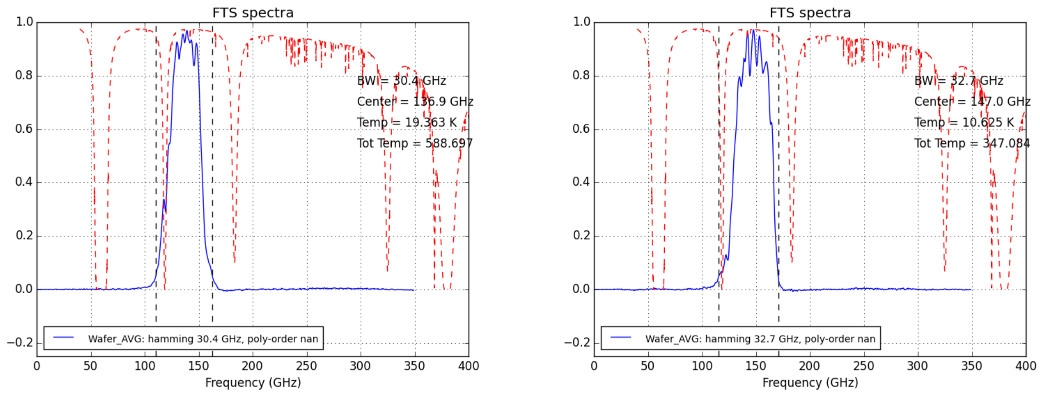

Figure 4.13: **Wafer 8.2.0 and 9.4 averaged spectrum** — The wafer averaged spectrum for wafer 8.2.0 (left) and 9.4 (right) are shown.

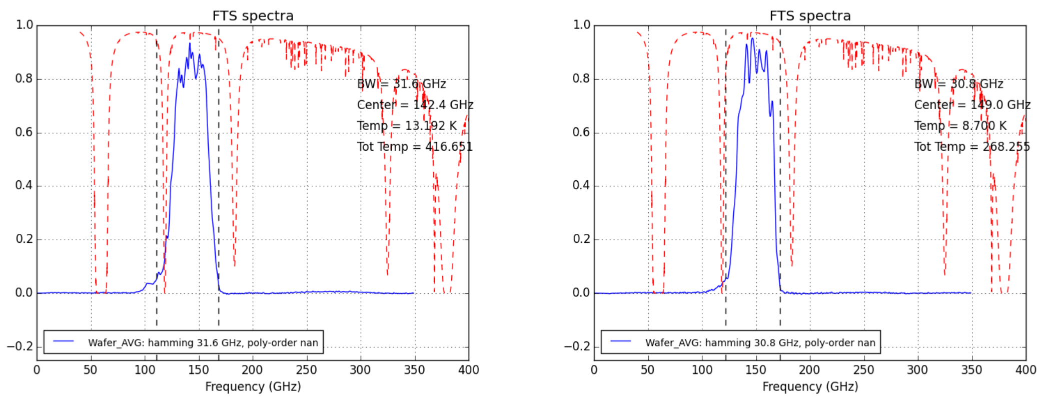

Figure 4.14: **Wafer 10.1 and 10.3 averaged spectrum** — The wafer averaged spectrum for wafer 10.1 (left) and 10.3 (right) are shown.

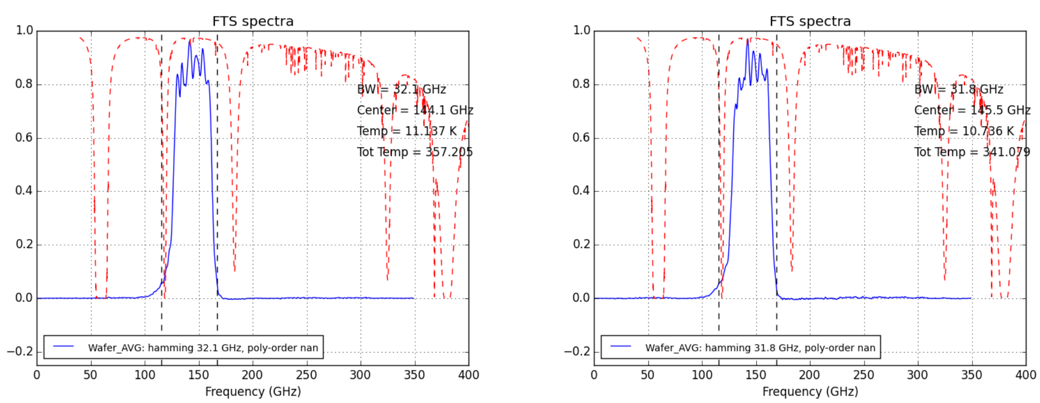

Figure 4.15: **Wafer 10.4 and 10.5 averaged spectrum** — The wafer averaged spectrum for wafer 10.4 (left) and 10.5 (right) are shown.

Table 4.3:: Detector spectral response fractional errors — The estimated statistical and systematic fractional errors in the spectral measurements for each wafer are shown. The average error value in all detectors per wafer is shown for each. These are measured errors (noise) across all frequency bins measured in each spectra with the spectra normalized as explained previously.

Wafer	# Detectors	Statistical Error	Systematic Error
8.2.0	106	0.0181	0.0330
9.4	107	0.0189	0.0475
10.1	114	0.0200	0.0449
10.2	149	0.0167	0.0405
10.3	133	0.0196	0.0487
10.4	154	0.0163	0.0344
10.5	113	0.0212	0.0354

The statistical and systematic errors per wafer are summarized in Table 4.3. All errors are fractional errors relative to the peak value of each spectra that are normalized as explained previously. The systematic error includes spectral errors due to temporal variations and due to the alignment of the FTS with the POLARBEAR instrument, and was conservatively estimated to be $3.3 - 4.9\%$ according to the wafer. Of this the temporal variation error, that was measured across a timespan of 6 hours, was estimated to be $\leq 2.25\%$.

The final spectra for each detector across the focal plane were measured to a statistical precision on average with only $1.6 - 2.1\%$ spectral error according to the wafer. The wafer averaged spectra all have statistical errors of $< 0.34\%$. The in-band differences between pixel pairs were found to be on average small $< 1\%$ for all wafers except wafer 8.2.0. Wafer 8.2.0 is expected to have the least sensitivity due to the lower band center that makes the band have larger contamination from the oxygen line emission from the atmosphere. The larger in-band difference in wafer 8.2.0 may also introduce larger $T \to P$ leakage as well.

The POLARBEAR FTS was able to couple efficiently across the entire focal plane and successfully measured high precision detector spectra for $\sim 69\%$ of the detector array directly in the field.

4.5 Future Application

POLARBEAR-2 and the Simons Array, as will be described in chapter 5, use the same HTT design coupled to each new generation receiver. The POLARBEAR FTS optical design is highly driven by the primary and secondary reflectors, and hence the FTS is compatible with POLARBEAR-2 and Simons Array as well. As for POLARBEAR, described in section 4.3.2.2, the optical coupling efficiency decreases slightly as a function of increased distance from the optical central axis. For the larger focal plane of POLARBEAR-2 this effect is larger but from optical ray tracing simulations it is expected that greater than 76% of the rays are unvignetted on average for the outermost POLARBEAR-2 pixels. Therefore the FTS is compatible with the POLARBEAR-2 receiver as well.

Another characteristic of the FTS that has merits for POLARBEAR-2 is the continuous modulation by the output polarizing grid. As explained in Section 4.2.4, the 4f component interferogram is dependent on the relative angle between the output polarizer and detector polarization sensitive axis. POLARBEAR-2 uses very broadband sinuous antennas that are known to have a polarization angle wobble [54]. Hence the 4f component has the potential of extracting the spectral response of the detectors as a function of this polarization angle wobble as well.

4.6 Lab-use FTS

In addition to the FTS described above constructed for detector measurements in the field, a lab-use FTS was designed that will enable characterization of detectors and other optical components before they are deployed to the telescope site in Chile. One such FTS was built and has been used in preliminary testing. The construction of an additional two is underway to allow simultaneous testing of Simons Array components at multiple institutions.

The design of the lab-use FTS was much less constrained as it was not limited by the HTT's optics and mechanical structure. Nonetheless, in constructing this device the design of many components was carried over from the original POLARBEAR FTS following its success in the field. Figure 4.16 shows a mehanical

Table 4.4:: **Lab-use FTS specifications** — The designed specifications of the lab-use FTS are listed in this table. Any specifications that don't distinguish between the two modes are common.

Specs	Mode 1 (Mode 2)
Interferogram	Double (Single)
Frequency Resolution	1 GHz (0.5 GHz)
Maximum Frequency	500 GHz
Throughput	4.87 steradian cm^2
Output f-number	$f = 2$
Dimensions	1.4 m $\times$ 1.0 m
Weight	175 lbs

model as well as a photo of the final assembled FTS with its design specifications in Table 4.4.

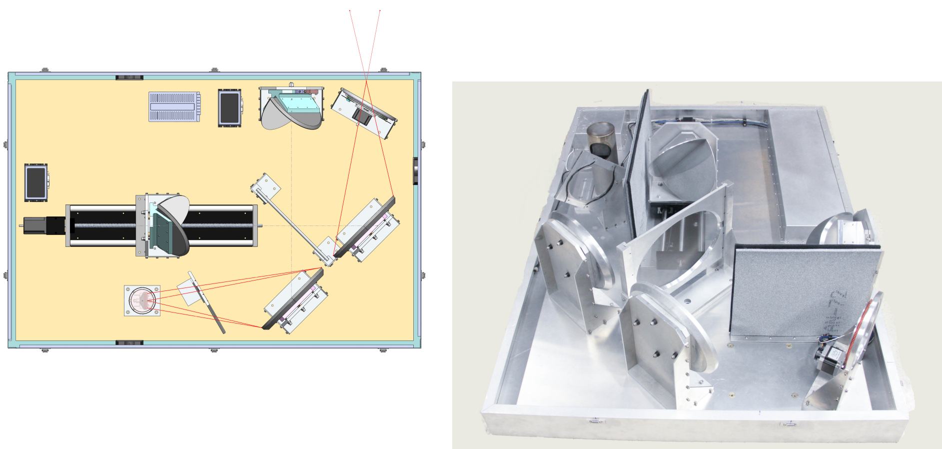

Figure 4.16: **Mechanical design of lab-use FTS** — The mechanical drawing (left) of the lab-use FTS and image of the fabricated lab-use FTS (right) are shown.

Three main changes were made to the to the POLARBEAR FTS when creating one for the lab: the parabolic mirror design, the layout of the components, and the linear translation stage.

The two parabolic mirrors (collimating input mirror and focusing output mirror) used in the lab-use FTS are identical to one another but differ from those used in the original FTS because there is no longer a need for this to emulate the HTT primary mirror. Thus the new mirrors have an f-number of 2. The design of these mirrors was also modified so that they are 90 degree off-axis paraboloids rather than 65 degrees.

The change in output parabolic mirror shape and f-number allowed for the FTS components to be laid out in a more convenient way compared to the irregular POLARBEAR FTS layout that was required for coupling on the HTT. As seen in the photo, the final lab-use device is rectangular, allowing for easier coupling to a variety of test cryostats and simpler fabrication of the optical bench and enclosure. This layout also allowed the total path length within the FTS to become slightly shorter as well which minimizes spillover within the FTS.

Finally, the translation stage used in the original POLARBEAR FTS is a different model than that used for the one in the lab. The new FTS design employs a translation stage manufactured by LinTech which has a slightly longer travel distance than the previously used model.

Initial tests of the lab-use FTS were performed using the POLARBEAR-2 receiver in a laboratory setting. An elliptical mirror was machined to serve as the optical coupling between the FTS output and the receiver. This preliminary test was successful in producing repeatable spectra of POLARBEAR-2 type detectors. This demonstrated the functionality of the lab-use FTS and its utility in characterizing future components of the Simons Array.

4.7 Conclusions

The POLARBEAR FTS was designed to be installed on the HTT and to specifically couple to the POLARBEAR, POLARBEAR-2, and Simons Array receivers in the field. This was accomplished with a custom output parabolic mirror within the FTS to satisfy the Mizuguchi-Dragone condition when coupling to the telescope optics. The FTS was also mechanically designed to be compact, light weight, and robust to the harsh environment in Chile.

The FTS was fully fabricated and deployed in April 2014. The FTS was installed on the HTT and successfully took detector spectra for 69% of the detectors (876 detectors) in the POLARBEAR focal plane in an efficient manner. High precision spectra were measured with 1 GHz spectral resolution, and quantified the spectral in-band difference between pixel pairs that can introduce $T \rightarrow P$ systematics. This is one of the largest detector spectra datasets for characterizing a CMB instrument in the field.

The successful FTS run also proved that the POLARBEAR FTS design does in fact optically couple effectively with the HTT and receiver as designed, and is expected to perform well for future receivers. The POLARBEAR FTS is planned to be used for the POLARBEAR-2 and Simons Array receivers as well to measure spectra in the field after deployment.

4.8 Acknowledgements

This chapter includes material in preparation for publication for: F. Matsuda and The POLARBEAR Collaboration. Spectroscopic Characterization of the POLARBEAR Instrument. In preparation. The dissertation author is the first author of this material in preparation and lead this project.

Chapter 5

The Simons Array

POLARBEAR-2 and the Simons Array are the next generation installments of the POLARBEAR experiment. POLARBEAR-2 is an upgraded receiver that will be installed on a HTT type telescope in late 2017. POLARBEAR-2 will have 7,588 detectors and observe at 95 and 150 GHz. POLARBEAR-2 is part of the Simons Array that will consist of three HTT type telescopes each with a POLARBEAR-2 type receiver. Each receiver contains multi-chroic detector arrays with a combined total of 22,764 detectors in Simons Array. Simons Array will observe at 4 frequencies of light: 95, 150, 220, and 280 GHz. The three receivers will start observations incrementally between 2017 to late 2018, and obtain unprecedented sensitivities in measuring the CMB B-modes to put further tight constraints on inflationary cosmology.

5.1 POLARBEAR-2 Experiment

In order to measure the primordial signal potentially at a very low r value, further improvements in sensitivity are required and respective technological advancements are needed. The POLARBEAR-2 receiver is an upgraded instrument for such precision CMB polarization measurements. POLARBEAR-2 will be installed on a second HTT type telescope along side the current HTT with the POLARBEAR receiver, and is currently planned to deploy in late 2017. POLARBEAR-2 will have far superior sensitivity and advanced refractive, detector, and readout technological capabilities compared to POLARBEAR. The design and photograph of the POLARBEAR-2 receiver in development are shown in Figure 5.1.

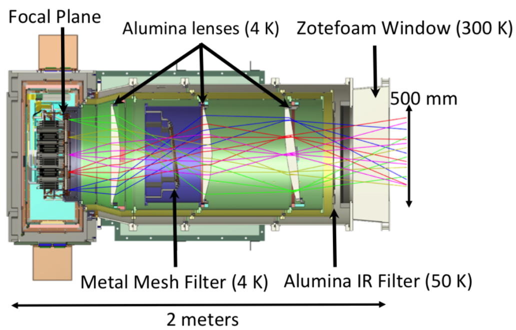

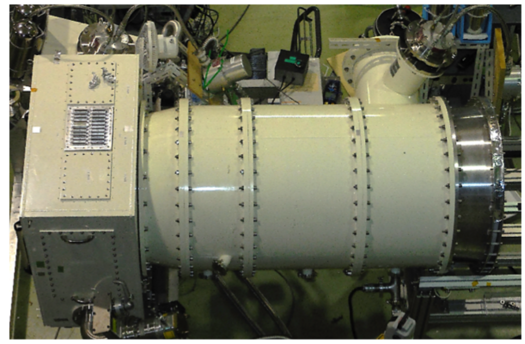

Figure 5.1: **POLARBEAR-2 receiver design** — The mechanical design (left) and image (right) of the POLARBEAR-2 receiver currently in development is shown. This figure is taken from [55].

5.1.1 Optics Design

The POLARBEAR-2 receiver contains 7,588 detectors or ~ 6 times as many detectors than POLARBEAR, and will observe at 95 and 150 GHz. The sky resolution of POLARBEAR-2 is estimated to be 5.2 and 3.5 arcmin FWHM for 95 and 150 GHz respectively. Each spatial pixel contains two orthogonally oriented polarization sensitive antennas for each frequency. Therefore each spatial pixel contains 4 detectors. A larger focal plane area to fit this larger number of detectors requires a larger DLFOV while sustaining optical performance across a larger frequency range to incorporate the passbands at two different observational frequencies. This requires an upgraded re-imaging optics design that will couple to the HTT reflector designs inherited from POLARBEAR.

The basic optical design concepts are similar to that of the POLARBEAR receiver except that the DLFOV is significantly increased using the re-imaging optics for POLARBEAR-2. The re-imaging optics are designed to couple to the off-axis Gregorian-Dragone dual reflectors of the HTT, increase the DLFOV, create a flat and telecentric focal plane, and create a compact and cryogenic Lyot stop. Due to the requirement of a much larger focal plane, the throughput of the optical system must be significantly increased and requires larger optical components and receiver system. One large constraint on the POLARBEAR-2 design was that the receiver must fit within the structural framework or boom of the HTT design. For the POLARBEAR receiver this was not a limitation due to the relatively smaller instrument size, but POLARBEAR-2 is a much tighter fit. This creates strong constraints on the optical design because larger throughput typically requires larger and longer optics in general.

The POLARBEAR-2 receiver contains three conically shaped alumina lenses each 50 cm in diameter with an index of refraction of 3.15. The lenses are named in the same manner as the POLARBEAR re-imaging lenses. The three lenses are designed to create a 36 cm diameter focal plane and 18 cm diameter Lyot stop. As can be seen in Figure 5.1, the Lyot stop is slightly further away from the aperture lens relative to POLARBEAR, and tilted by 7° similar to the Field lens. Due to the much higher refractive index of alumina compared to that of UHMWPE, the lenses have innately much higher focusing power and are capable of much faster optics than POLARBEAR.

With higher focusing power re-imaging optics, the DLFOV of POLARBEAR-2 is circular with 4.5 degrees diameter at 150 GHz, which is ~ 2.5 times larger in angular area than that of the POLARBEAR FOV, and ~ 1.5 times larger in angular area than that of the dual reflector system's DLFOV. This extended DLFOV allows for coupling to a much larger focal plane area and installing ~ 3 times as many spatial pixels. The increased DLFOV for POLARBEAR-2 is shown in Figure 5.2. As can be seen from equation 2.8, for the same aberrations the Strehl ratio increases at lower frequencies, and hence by definition the DLFOV for 95 GHz should be larger. But realistically the FOVs for both 95 and 150 GHz are the same due to vignetting by the finite size of the optical components.

Even though the DLFOV is not limited by the addition of the 95 GHz channels, the optical clearances within the design must be more carefully assessed. The effects of diffraction off optical aperture edges are much more severe at 95 GHz due to faster beam spreading compared to 150 GHz. This idea can be conceptualized using Gaussian beam optics, and will be explained in more detail in section 6.2.2. This consideration creates a need to increase the optical clearances beyond the

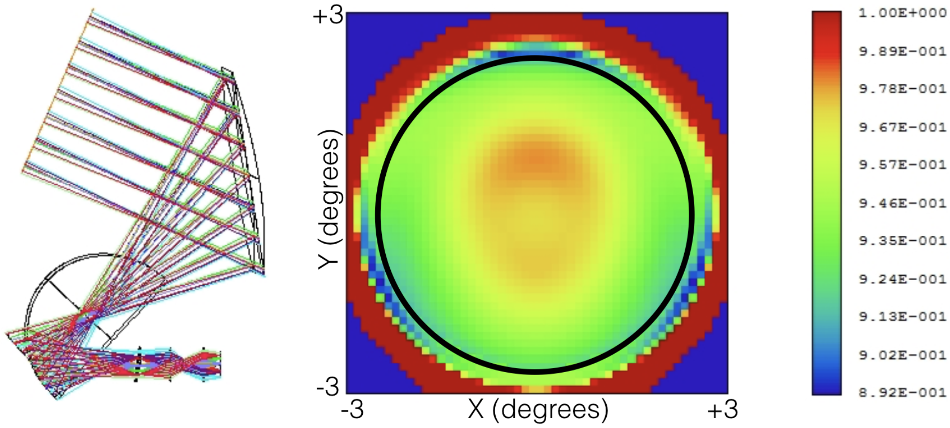

Figure 5.2: **DLFOV for POLARBEAR-2** — A geometric ray trace (left) and the 150 GHz 2D Strehl ratio map as a function of FOV (right) is shown for the POLARBEAR-2 design. The black solid circle represents the used FOV for POLARBEAR-2. The "high" Strehl ratio (red) ring beyond the circle represents vignetting. This region is not physically usable because most of the rays are vignetted and do not propagate to the sky. A "high" Strehl ratio is calculated by ZEMAX due to small wavefront errors in the small portion of rays that are not vignetted.

outermost geometric ray at each optical surface. For POLARBEAR-2 the design included $2 - 5$ cm of extra radii clearance at each surface to minimize diffraction effects.

5.1.2 Instrument

Similar to the POLARBEAR receiver, the POLARBEAR-2 receiver is also cryogenically cooled to lower the noise in the TES detectors and minimize loading from the lenses and filters within the receiver. Due to the significantly larger volume of the POLARBEAR-2 receiver, two PTCs are used to cool the entire optics to 4 K: one for the focal plane backend and a second for the optics tube. The detectors are further cooled to 250 mK using a similar closed cycle three-stage Helium sorption refrigerator.

With this cryogenic environment the TES detectors are once again limited by photon shot noise. Therefore in order to increase the sensitivity for CMB measurements, increasing the number of detectors is fundamentally needed. This has been a trend in the CMB field as a whole. Also due to the known large foreground contaminations from dust and synchrotron noise, observations of the sky at multiple frequencies has become much more critical in order to distinguish the small CMB polarization signal. The POLARBEAR-2 receiver achieves both of these goals using TES coupled sinuous antenna technology.

Unlike the slotted dipole antenna used in POLARBEAR, the sinuous antenna is a log-periodic design that makes it very broad-band and sensitive across a wide range of frequencies. It also contains sensitivity to the two orthogonal linear polarizations, and when used in combination with a lenslet the antenna has a high gain ideal for coupling to telescopes. An image of the sinuous antennas used in POLARBEAR-2 is shown in Figure 5.3. Each sinuous antenna is coupled to 4 TES detectors: 2 orthogonal polarizations for each frequency. There are band defining filters on the detector array that make the spectral responses of the detectors with band centers at 95 and 150 GHz each with passbands approximately $30 - 40$ GHz wide. Ideal theoretical spectral bands for the two frequencies are shown in Figure 5.3 as well.

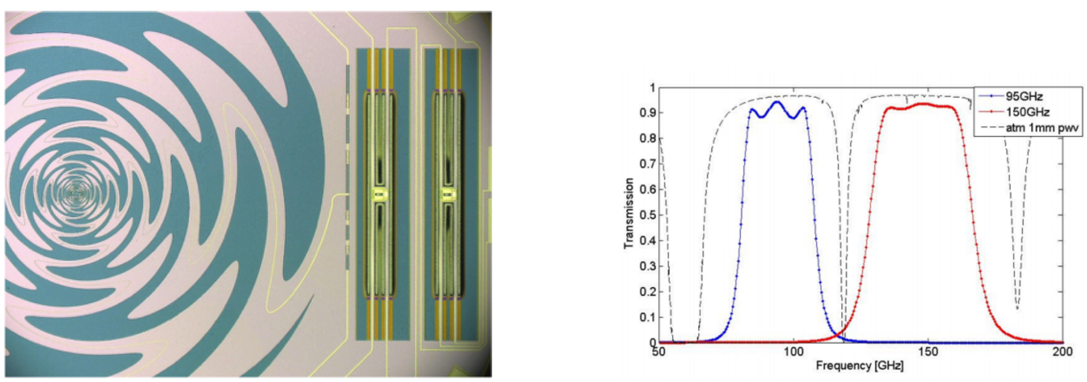

Figure 5.3: **Sinuous antenna design and detector spectral response** — An image of a fabricated sinuous antenna with band defining filters is shown on the left. This figure is taken from [55]. The analytically calculated ideal spectral response bands center at 95 and 150 GHz are shown on the right.

Similar to POLARBEAR, the focal plane consists of 7 hexagonal wafer detector arrays of larger size each with 271 spatial pixels. POLARBEAR-2 in total will have 7,588 detectors including both frequencies. The sinous antennas are coupled to the rest of the optics using AR coated lenslets made of alumina. A picture of a fully assembled wafer array as well as an illustration of the complete focal plane assembly is shown in Figure 5.4.

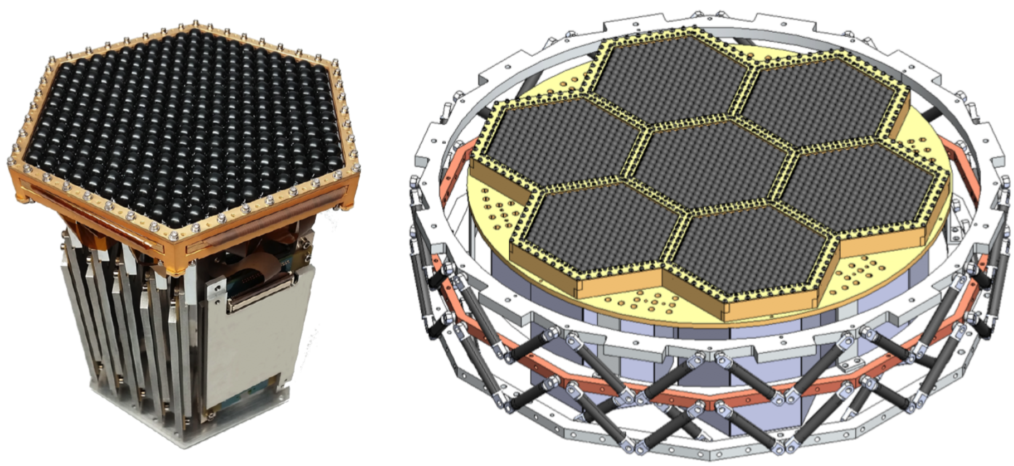

Figure 5.4: **POLARBEAR-2 focal plane** — An image of one fully assembled POLARBEAR-2 detector array wafer is shown (left). The AR coated lenslet array is installed above the detector array and LC board readout components are installed below. This figure is taken from [55]. The mechanical design of the full POLARBEAR-2 focal plane is shown as well (right).

The POLARBEAR-2 receiver is currently in development and is scheduled to deploy in late 2017 to Chile. The completed receiver will be mounted on a second HTT type telescope that has already been built next to the current POLARBEAR experiment.

5.2 Simons Array Telescopes

The POLARBEAR-2 experiment will be further expanded to the Simons Array experiment. Simons Array will consist of three POLARBEAR-2 type receivers installed on three HTT type telescopes in Chile at the same site of POLARBEAR. In order to have better foreground removal capabilities, Simons Array will observe at 4 frequencies of light: 95, 150, 220, and 280 GHz. Simons Array will have a total of 22,764 detectors in three instruments. The POLARBEAR-2 instrument is the first installment of the Simons Array and two more instruments with similar technology and caliber will follow. The second and third receivers will use very similar cryogenic, detector, and readout technologies to POLARBEAR-2 but will have a further improved optical design in order to have better optical performance at the higher frequency channels as well. The Simons Array optics design will be discussed in detail in section 6.2.

The second receiver will observe at 95 and 150 GHz similar to POLARBEAR-2, and will be installed in early 2018 on a third HTT type telescope that is currently being assembled in Chile. The third receiver will observe at 220 and 280 GHz, and will be installed on the current HTT telescope replacing the POLARBEAR receiver in late 2018.

As explained in Section 3.2.2, the POLARBEAR site allows for potential observation of 80% of the CMB sky above an elevation of 30°. The Simons Array will observe large patches of CMB sky for three years at the Chilean location. With the three instruments and vastly increased number of detectors across many frequencies, Simons Array will achieve very high sensitivities to the CMB polarization signal and characterize the foreground contamination to high precision.

Figure 5.5: **Simons Array Chilean site** — This is an image of the Simons Array site in Chile. The original HTT (center) and the two new HTT type telescopes in construction can be seen. The neighboring ACT experiment can be seen in the background as well. This figure is taken from [55].

5.3 Simons Array Science

The main science goals of the Simons Array are similar to that of the POLARBEAR experiment. Simons Array will continue to measure the CMB polarization signal focusing on the B-mode signal from inflation and gravitational lensing. After three years of observation and foreground removal, the Simons Array is forecasted to achieve sensitivities that will put strong constraints on the tensor-to-scalar ratio r, the sum of the neutrino masses, and the spectral index n_s of the inflation potential. A forecasted sensitivity plot of the Simons Array is shown in Figure 5.6.

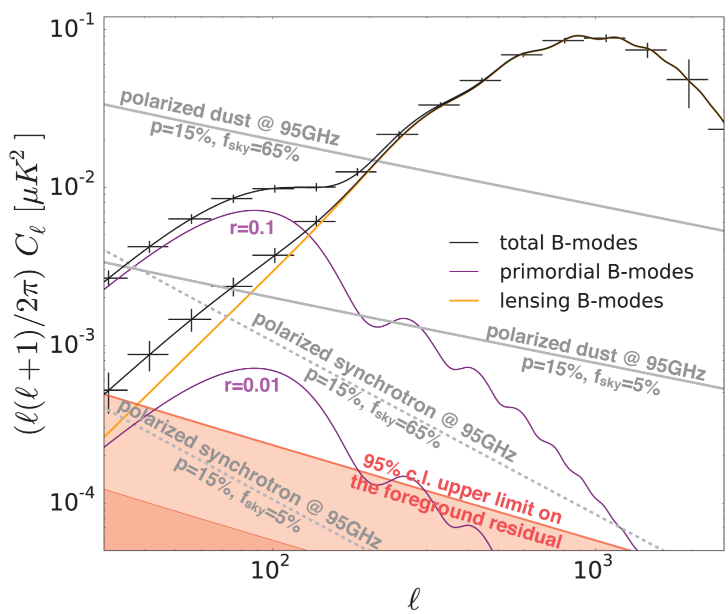

Figure 5.6: **Simons Array sensitivity** — The forecasted sensitivities of the Simons Array is shown. Theoretical B-mode power spectra with the primordial signal at r = 0.1 and r = 0.01 (purple) and the lensing signal (orange) are plotted. Binned error bars from three years of observation with $f_{sky} = 0.65$ are over-plotted. This figure is taken from [55].

Simons Array will achieve sensitivities to measure the tensor-to-scalar ratio r amplitude down to $\sigma(r = 0.1) = 0.006$. The current upper limit on r by other CMB experiments is $r < 0.09$ [20]. Simons Array will achieve sensitivities that are superior to the current limits by an order of magnitude or more. Many inflationary models predict that $r > 0.01$ and hence the Simons Array is well suited to measure the primordial signal if it exists. Even if the signal is not detected, a large subset of inflationary models will be ruled out and still provide great input to cosmology. Through characterizing the E-mode spectrum with high precision to high ℓ, the Simons Array will also be able to constrain the spectral index n_s to $\sigma(n_s) = 0.0015$. The tight constraint on both r and n_s will allow the Simons Array to give great insight to the nature of inflation.

The Simons Array small angular scale measurements will constrain the sum of the neutrino masses to $\sigma(\sum m_\nu) = 40$ meV. This sensitivity is much better than any published cosmological upper limit by combined data sets using Planck, baryonic acoustic oscillation, Lyman-α survey, and dark energy survey data claiming upper limits of $120 - 230$ meV [6, 56, 57]. Simons Array will provide insight to possibly differentiating between the normal and inverted mass hierarchies in the Standard Model.

5.4 Systematics Estimation

As sensitivities are increased in CMB experiments in order to measure faint CMB polarization signals with high statistical precision, assessment and minimization of systematic errors is becoming evermore crucial in the data analysis. A misestimation of systematic errors in the data can potentially lead to false CMB polarization signals and misinterpretations of the final results.

In a complex optical system with forefront technologies such as the Simons Array, there are potentially many sources of systematics that can lead to large systematic errors in the final CMB spectra if not carefully considered. Of the systematics, instrumental systematics are studied in detail because they contaminate the polarization data directly and can potentially cause errors that are orders of magnitude larger than the CMB signal. Instrumental polarization systematics due to the optics were discussed in section 2.3.1, but in general instrumental polarization or $T \rightarrow P$ leakage systematics can also be caused by many other aspects of the instrument and data analysis.

Similar to Polarbear, in Simons Array the polarization signal is extracted from two orthogonal polarization sensitive detectors in one pixel as explained in 3.4.2. Pair differencing is a useful technique in measuring a linear polarization signal but needs to be done with care because optical and detector non-idealities can introduce systematics.

5.4.1 Differential Beam Systematics

In pair differencing analysis, systematics can be introduced into the polarization signal if there are any non-idealities that are different between the two detectors in one spatial pixel. One type of systematic in this category is called differential beam systematics. Differential beam systematics arise due to the differences between the sky beams of the two detectors in one pixel, and primarily introduce instrumental polarization leakage into the measurement.

Each detector in one spatial pixel will have its own sky beam. Ideally the two beams will be identical in shape and power on the sky, and hence taking the difference in the measured TOD from each detector will give the exact polarization signal measured by the overlapping beam on the sky. But typically the two sky beams will not be identical in shape and power due to detector characteristics and optical design effects. Therefore each detector will not be looking at the exact same region of the sky defined by each respective beam. This difference primarily introduces instrumental polarization leakage because some temperature signal residual will be left in the pair differenced signal due to incomplete temperature subtraction between the detectors.

Instrumental polarization must be dealt with carefully because the temperature power is more than four orders of magnitude larger than the B-mode power. Thus even a small fraction of residual temperature power leakage will contaminate the B-mode power spectrum and can easily dominate the primordial signal if not accounted for in the data analysis.

Many of these systematics can be mitigated by the scan strategy and sky rotation as explained in section 3.2.2. In terms of differential beam systematics, by observing the CMB patches at many angles the beam asymmetries can effectively be averaged out and mitigate the leakage. Theoretically differential beam systematics can introduce cross polarization systematics as well, but the instrumental polarization is far more dominant. Only leading order terms of each type of instrumental systematic will be considered in this section.

The analytical formalism for calculating the differential beam systematics from Shimon et al. 2008 [58] and Miller et al. 2009 [59, 60] is used. A qualitative explanation will be given in this section, and generalized forms of the equations from Shimon et al. for leakage into C_ℓ^{BB} will be used as the starting point. The analytical formalism can be calculated assuming a 2D Gaussian main beam profile for each detector. The differential beam systematics can then be further classified according to the shape of the residual leakage after subtracting the two beams. There are monopole, dipole, and quadruple terms of interest.

The monopole term is called differential beam size. This is instrumental polarization arising from a difference in the Gaussian beam sizes σ_1 and σ_2 of the two detectors. The subscripts 1 and 2 will represent each detector in a pixel pair. Differential beam size can be parameterized by the differential beam size μ and average beam size σ given by

$$\mu = \frac{\sigma_1 - \sigma_2}{\sigma_1 + \sigma_2}, \quad \sigma = \frac{\sigma_1 + \sigma_2}{2}. \tag{5.1}$$

Thus the leading order leakage term ΔC_ℓ^{BB} can be written as

$$\Delta C_\ell^{BB} = \frac{1}{4}\left[(\ell\sigma_1)^2 - (\ell\sigma_2)^2\right]^2 C_\ell^{TT} \star f_1 = 4\mu^2\ell^4\sigma^4 C_\ell^{TT} \star f_1 \tag{5.2}$$

where the f_i parameter is the scan strategy as given in Shimon et al. [58], and the star represents a convolution. The f_i parameters represent how much the leakage is mitigated, and will range in value from $0-1$ with 0 being full mitigation from a perfect scan strategy and 1 being no mitigation at all.

The dipole term is called differential pointing. This is the leakage arising from the difference in the Gaussian main beam centroid positions of the two detectors. The sky positions of the two beams $\boldsymbol{\rho}_1 = (\rho_1, \theta_1)$ and $\boldsymbol{\rho}_1 = (\rho_2, \theta_2)$ are given in polar coordinates and will depend on the physical focal plane orientation of the instrument projected onto the sky. The differential pointing parameter is $\boldsymbol{\rho} = \boldsymbol{\rho}_1 - \boldsymbol{\rho}_2$. The leakage is given by

$$\Delta C_\ell^{BB} = {}_2\tilde{s}_\theta^2 C_\ell^{TT} + {}_1\tilde{s}_\theta^2 C_\ell^{TT} \star f_2 \tag{5.3}$$

where

$$ {}_1\tilde{s}_\theta \equiv J_1\left(\ell\rho_1\right)\sin\theta_1 - J_1\left(\ell\rho_2\right)\sin\theta_2 \tag{5.4} $$

$$ {}_2\tilde{s}_\theta \equiv J_2\left(\ell\rho_1\right)\sin 2\theta_1 - J_2\left(\ell\rho_2\right)\sin 2\theta_2 \tag{5.5} $$

and the J_i are Bessel functions of the first kind. Unlike the differential beam size, differential pointing has a term that cannot be mitigated by the scan strategy.

The quadrupole terms is called differential ellipticity. This is a leakage term arising from differences in the ellipticities of the detector beams. The beam ellipticities are parameterized by the ellipticity

$$ e = \frac{\sigma_x - \sigma_y}{\sigma_x + \sigma_y} \tag{5.6} $$

and ψ which is the angle between the polarization sensitive axis and ellipse major axis for each detector. Here σ_x and σ_y are the beam sizes in the x and y axes respectively. The differential ellipticity parameter is given by

$$ \epsilon = \frac{e_1 - e_2}{e_1 + e_2}. \tag{5.7} $$

Not only the magnitudes of the ellipticities but the relative orientations also matter and create leakages. The leakage is given by

$$ \Delta C_\ell^{BB} = \tilde{s}_\psi^2 C_\ell^{TT} \tag{5.8} $$

where

$$ \tilde{s}_\psi = I_1\left(z_1\right)\sin 2\psi_1 - I_1\left(z_2\right)\sin 2\psi_2. \tag{5.9} $$

Here $z = \left(\sigma\ell\right)^2 e$ and I_i is the modified Bessel function of the first kind. Unlike the monopole and dipole, the quadrupole term cannot be mitigated by the scan strategy.

Another differential beam systematic that is not classified above is the differential gain. This systematic is not a beam shape feature but a difference in the relative gains g_1 and g_2, or in other words differences in the sky powers of the beams of the two detectors. The differential gain g and the differential gain fraction γ are given by

$$ g = g_1 - g_2, \quad \gamma = \frac{g_1 - g_2}{g_1 + g_2}. \tag{5.10} $$

Thus the leakage is

$$\Delta C_\ell^{BB} = g^2 C_\ell^{TT} \star f_1 \tag{5.11}$$

This will leak the temperature signal directly into the polarization signal if the relative gains are not correctly calibrated between the two detectors.

5.4.2 Design Criteria

The need to minimize systematic errors below the statistical error is ever-more important in achieving high sensitivity CMB measurements. An instrument must be designed such that these systematics are controllable and low. Therefore design criteria need to be estimated beforehand as a guideline for an instrument design. These design criteria are then used as a benchmark or upper limit in the instrument development to assure that the systematic error from these effects are lower than the expected statistical error of the experiments.

The differential beam systematics are primarily caused by the detector and optical design of the instrument. The detector's directivity or beam profile is determined by the antenna and lenslet coupling. This detector beam will propagate to the sky through the optics, and hence if there are any beam asymmetries and non-idealities that differ in the original detector beams these will create differential beam systematics. Furthermore the refractive and reflective optics design itself will further create beam differences because orthogonal polarization states propagate differently through an optical system. Hence these systematics must be controlled both in the detector and optical design.

The analytical models of the differential beam systematics can be used to determine the design criteria for the Polarbear-2 and Simons Array based off the forecasted sensitivities of both experiments. For the monopole, dipole, and quadrupole leakages the design criteria are calculated requiring that the systematic leakage of each is below each instrument's statistical error across all ℓ. For the differential gain the design criterion is calculated requiring that the systematic leakage is below each instrument's statistical error at $\ell \sim 100$ which is around the primordial peak. Also the scan strategy is assumed to be completely unideal $f_i = 1$ when determining the design criteria. Realistically $f_i < 1$ for any scan

Table 5.1:: Differential beam systematics design criteria — This is a table of the design criteria for each differential beam systematic calculated based off the analytical model. The instruments must be designed and built to be better (smaller in value) than these specifications.

	POLARBEAR-2		Simons Array	
Systematic	150 GHz	95 GHz	150 GHz	95 GHz
Differential Beam size (μ)	0.474%	0.215%	0.337%	0.153%
Differential pointing (ρ)	0.877"	0.877"	0.582"	0.582"
Differential ellipticity ($\bar{e}\sin 2\psi$)	0.948%	0.430%	0.674%	0.305%
Differential Gain (γ)	0.019%	0.019%	0.017%	0.017%

strategy chosen and hence the criteria will be conservative. The determined design criteria are given in Table 5.1. The calculated leakages from the determined criteria compared to the statistical error are shown in Figure 5.7.

For the differential beam size and differential ellipticity, the nominal beam size of 3.5' (5.2') was assumed for the average beam size at 150 (95) GHz. For the differential gain the relative gain of one of the detectors in one pixel was assumed to be normalized to $g_1 = 1$.

For differential pointing in order to assign a differential pointing amplitude criterion for each pixel, the origin of the polar coordinate system was chosen to be at the average location of the detectors in one pixel. Hence $\theta_2 = \theta_1 + \pi$ and $\rho_1 = \rho_2 \to \rho = 2\rho_1$. In order to provide a conservative criterion $\theta_1 = \frac{\pi}{2}$ was chosen to maximize the leakage. Therefore equation 5.3 simplifies to

$$\Delta C_\ell^{BB} = 4J_1^2\left(\ell\rho_1\right)\sin^2\theta_1 C_\ell^{TT} = 4J_1^2\left(\ell\rho_1\right)C_\ell^{TT}. \tag{5.12}$$

Because this equation cannot be solved for ρ, the leading order term in $J_1(\ell\rho_1)$ was used as an initial guess and ρ was determined iteratively.

Due to the complexity in the differential ellipticity model, some reasonable assumptions were made to calculate the criterion for a combination of the parameters. According to the detector fabrication team, for sinuous antenna coupled detectors the differential ellipticity ϵ and the angle between the two detectors $\Delta\psi$ are very controllable due to the characteristics of the antenna itself. Hence it can

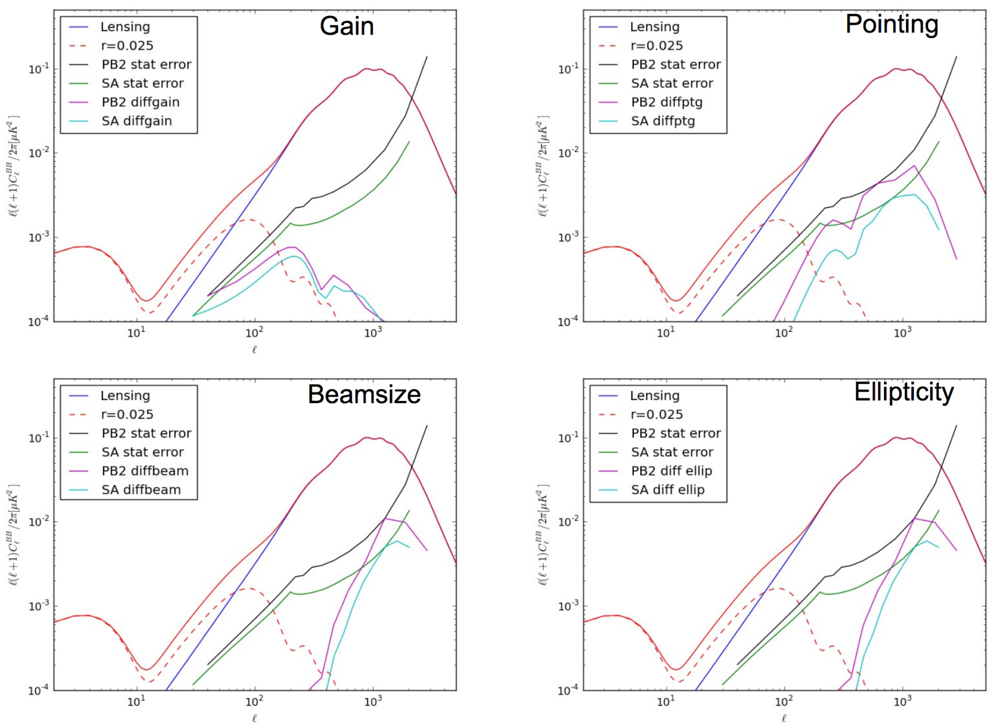

Figure 5.7: ΔC_ℓ^{BB} **leakages** — These are plots of the ΔC_ℓ^{BB} leakages for each systematic with the designed criteria values in Table 5.1. The cases for POLARBEAR-2 leakage (magenta) and Simons Array leakages (cyan) are shown. The theoretical C_ℓ^{BB} signal (red), POLARBEAR-2 statistical error (black), and Simons Array statistical error (green) are over-plotted. The leakages are binned according to the binning of the statistical errors.

be reasonably assumed that

$$\epsilon \ll 1 \;\rightarrow\; e_1 \approx e_2 \approx \bar{e} \equiv \frac{e_1 + e_2}{2} \tag{5.13}$$

and that

$$\psi_2 = \psi_1 + \Delta\psi,\;\; \Delta\psi = \frac{\pi}{2} + \delta,\;\; \delta \ll 1. \tag{5.14}$$

Now taking only the leading order term in $I_1(z) = \frac{z}{2} + O(z^3)$, $\tilde{s}_\psi$ can be approximated as

$$\tilde{s}_\psi \approx I_1(\bar{z})\left(2\sin 2\psi_1 + \sin 2\delta + O\left(\delta^2\right)\right) \tag{5.15}$$

$$\approx \bar{z}\sin 2\psi_1 \quad (z \ll 1, \delta \ll 1) \tag{5.16}$$

$$= (\sigma\ell)^2\,\bar{e}\sin 2\psi_1. \tag{5.17}$$

Therefore equation 5.8 can be simplified to

$$\Delta C_\ell^{BB} \approx (\sigma\ell)^4 \left(\bar{e}\sin 2\psi_1\right)^2 C_\ell^{TT}. \tag{5.18}$$

Hence the criterion was determined for the parameter combination $\bar{e}\sin 2\psi_1$ which includes both the ellipticity and elliptical orientation of the beam.

With the criteria in Table 5.1 the differential beam systematic leakages are guaranteed to be below the forecasted POLARBEAR-2 and Simons Array sensitivities across all ranges of ℓ of interest for cosmology. With an optimized scan strategy the leakages from differential beam size, pointing, and gain will be significantly decreased. The differential ellipticity is the only leakage that will not be mitigated by the scan strategy and can be considered the most stringent. Ideally each receiver should be designed and developed such that each of these systematics will be minimized further in order to be able to obtain the forecasted sensitivities because these systematics will add along with other systematic errors not discussed in this section. It is crucial that these systematics are controlled in the design to ensure POLARBEAR-2 and the Simons Array will be able to obtain the expected sensitivities and cosmological results.

5.5 Acknowledgements

Figures 5.1, 5.3 (left), 5.4, 5.5, and 5.6 are reprints of materials as appears in: N. Stebor, P. Ade, Y. Akiba, C. Aleman, K. Arnold, C. Baccigalupi, B. Barch, D. Barron, S. Beckman, A. Bender, D. Boettger, J. Borrill, S. Chapman, Y. Chinone, A. Cukierman, T. de Haan, M. Dobbs, A. Ducout, R. Dunner, T. Elleflot, J. Errard, G. Fabbian, S. Feeney, C. Feng, T. Fujino, G. Fuller, A. J. Gilbert, N. Goeckner-Wald, J. Groh, G. Hall, N. Halverson, T. Hamada, M. Hasegawa, K. Hattori. M. Hazumi, C. Hill, W. L. Holzapfel, Y. Hori, L. Howe, Y. Inoue, F. Irie, G. Jaehnig, A. Jaffe, O. Jeong, N. Katayama, J. P. Kaufman, K. Kazemzadeh, B. G. Keating, Z. Kermish, R. Keskitalo, T. Kisner, A. Kusaka, M. Le Jeune, A. T. Lee, D. Leon, E. V. Linder, L. Lowry, F. Matsuda, T. Matsumura, N. Miller, J. Montgomery, M. Navaroli, H. Nishino, H. Paar, J. Peloton, D. Poletti, G. Puglisi, C. R. Raum, G. M. Rebeiz, C. L. Reichardt, P. L. Richards, C. Ross, K. M. Rotermund,

Y. Segawa, B. D. Sherwin, I. Shirley, P. Siritanasak, L. Steinmetz, R. Stompor, A. Suzuki, O. Tajima, S. Takada, S. Takatori, G. P. Teply, A. Tikhomirov, T. Tomaru, B. Westbrook, N. Whitehorn, A. Zahn, O. Zahn. The Simons Array CMB polarization experiment. Millimeter, Submillimeter, and Far-Infrared Detectors and Instrumentation for Astronomy VIII, Proc SPIE 9914, 99141H, July 20, 2016, doi:10.1117/12.2233103. The dissertation author made essential contributions to many aspects of this work especially in instrument optical design and development.

Chapter 6

The Simons Array Optics

In order to improve CMB sensitivity, various considerations and studies were done on the Simons Array optical design. This chapter will discuss two large optical considerations that I studied in great detail. The theoretical placement of a polarization modulator (half-wave plate) in the optical design and its cross polarization effects are discussed in section 6.1. An optical redesign of the second and third Simons Array receivers to improve sensitivity at the highest 280 GHz frequency is discussed in section 6.2.

6.1 Mizuguchi-Dragone Condition Breaking

Gregorian-Dragone off-axis dual reflector design telescopes are very commonly used is the CMB field today, and are becoming evermore important for measuring polarized signals. By satisfying the Mizuguchi-Dragone condition, these designs are guaranteed to have a large DLFOV with low aberration and low cross polarization systematics. This allows for a large number of detectors to be used in one telescope while minimizing possible polarization systematics.

Even if the reflector shapes and alignment satisfy the Mizuguchi-Dragone condition it is found that the condition can be broken by introducing a refractive optical element between the two reflectors that rotates the polarization. A half-wave plate is such an element that can break the condition. It is found that a half-wave plate will increase the cross polarization but theoretically keep the aberrations low. The cross polarization effect of such an optical element must be assessed and weighed with the potential advantage that the prime focus plane between the reflectors is a localized field stop that allows for a small aperture element.

6.1.1 Mizuguchi-Dragone Condition

A series of papers by Dragone [39, 61, 62] describe the Dragone reflective optical designs that achieve high throughput and DLFOV by significantly reducing aberrations as well as cross polarization. As stated previously, symmetric optical designs have ideal optical properties due to their high symmetry. In the case of a paraboloid, an on-axis paraboloid has no astigmatism due to circular symmetry. From Ludwig's third definition [63] one can see that this same symmetry leads to low cross polarization when a feed is placed at the focus. Off-axis paraboloids lose this symmetry but have the advantage of no blockage of the FOV. The analytical expression showing the increase in cross polarization dependent on the off-axis angle for parabolic reflectors is shown in Chu and Turrin 1973 [64].

Through geometric optics Dragone shows that a series of correctly shaped and placed confocal reflectors can be made optically equivalent to a single reflector [39]. This is possible for any number of reflectors and the equivalent reflector does not need to be of any specific conical shape. For the case of most interest to CMB telescopes, a combination of multiple reflectors can be arranged to be equivalent to an on-axis paraboloid with its ideal symmetries. Hence a Dragone designs allows off-axis multi-reflector systems to have low astigmatic aberrations and low cross polarization similar to an on-axis parabolic reflector if designed in this manner.

Dragone further showed that in a Dragone design astigmatism is not only eliminated along the optical center but also minimized for small displacements along the center which increases the DLFOV [61]. By adding deformations into the reflectors coma aberration can also be cancelled further increasing performance [62]. These modifications can be made to both Cassegrain and Gregorian designs.

The Gregorian-Dragone optical design with an off-axis parabolic primary and elliptical secondary minimizes cross polarization due to equivalence with an on-axis parabolic reflector. Any cross polarization introduced into the system due to the asymmetries of an off-axis parabolic reflector are cancelled by a correctly shaped and positioned elliptical secondary. According to Dragone's theory the combination of two reflections of nonzero angles of incidence can ensure perfect symmetry at the end. Theoretically this same procedure can be applied to any number of reflectors in series.

Slightly before Dragone, Mizuguchi et al. published results specific to the Gregorian off-axis parabolic dual reflector design. The condition in which a parabolic primary and elliptical secondary combination acts like an equivalent on-axis parabola with low cross polarization is given by [40]

$$\tan\alpha = \frac{(1-e^2)\sin\beta}{(1+e^2)\cos\beta - 2e} \tag{6.1}$$

where α is the angle between the feed axis and secondary rotation axis, β is the angle between the rotation axis of the secondary and primary, and e is the eccentricity of the secondary. This is called the Mizuguchi-Dragone condition (also stated as the Mizuguchi criteria). Mizuguchi was the first to quantitatively describe this cross polarization canceling condition for the off-axis parabolic dual reflector system. Dragone generalized this theory to any multi-reflector system and also extended the analysis to show that aberrations (specifically astigmatism) are also cancelled by the same condition. If the off-axis dual reflector system satisfies this equation then the cross polarization and astigmatism are eliminated along the optical center and also minimized for small displacements from it.

Many telescopes are of the Gregorian-Dragone design with the Mizuguchi-Dragone condition satisfied. As explained in section 3.3, Polarbear is an off-axis Gregorian-Dragone telescope design combined with further refractive optics to further correct for aberrations. The reflective optics consists of a 2.5 m diameter 65 degree off-axis parabolic primary reflector coupled to an over-sized elliptical secondary reflector.

Another commonly used class of a Dragone design telescope is the crossed Dragone design. The crossed Dragone design consists of an off-axis parabolic primary with a concave hyperbolic secondary with the Mizuguchi-Dragone condition satisfied. The crossed Dragone design has the advantages of compact design and typically lower aberrations compared to the Gregorian-Dragone design [65]. But has disadvantages in having more complex far side-lobe scattering [66] and difficulty in making low f-number designs due to vignetting effects.

6.1.2 Mizuguchi-Dragone Breaking

By design the HTT satisfies the Mizuguchi-Dragone condition but under certain circumstances this condition may be violated even if the shapes and orientations of the reflectors are not altered from their original design. Any optical element placed between the primary and secondary that can rotate polarization can be shown to violate the condition. This violation can be called Mizuguchi-Dragone breaking.

6.1.2.1 Half-Wave Plate at Primary Focus

A half-wave plate (HWP) is an optical element that can rotate the linear polarization state of light transmitted through it. HWPs are typically made of birefringent materials that have different indices of refraction along different polarization axes. The differences in indices of refraction between orthogonal polarization components create phase differences in the transmitted light. A HWP rotates linear polarization according to the angle between the incoming light's polarization axis and the crystal optical axis.

Because the CMB is partially linearly polarized, a HWP allows for controlled rotation of the incoming polarized CMB signal. This controlled rotation mitigates many systematic effects in the detectors and optics similar to sky rotation in the dataset. For the case of a continuously rotating HWP, the incoming signal can be modulated. This allows for not only systematic mitigation but also lowering the 1/f knee and measuring Q and U from one detector alone. A continuously rotating HWP has been implemented for Polarbear from third season observations onward.

Due to size and spatial constraints, for Polarbear a rotating HWP is placed near the prime focus of the HTT, the focus point between the primary and secondary. At prime focus all rays for pixels across the focal plane come to an approximate focus. Realistically only the rays for the central pixel located at the optical center will come to a near perfect focus. The further a pixel is placed away from the optical center (i.e. radially located further from the center of the focal plane) the larger the focus footprint will be at prime focus. The prime focus plane will still contain all the rays for all pixels localized within a small area, and is optimal in location to place a small aperture optical element. For POLARBEAR all (-10dB) rays are contained within a 18 cm diameter area in the prime focus plane as evident in Figure 6.1.

A HWP is also planned to be used for POLARBEAR-2 and Simons Array. One proposed location is at the prime focus due to similar spatial reasons as POLARBEAR. Another proposed location is near the Gregorian focus in front of the receiver itself. The prime focus for POLARBEAR-2 is larger in area than for POLARBEAR but similarly rays from all the pixels will be localized and contained in a relatively small area as shown in Figure 6.1. The necessary HWP size is much smaller ($\sim$ 35 cm) at the prime focus compared to the Gregorian focus ($\sim$ 45 cm). Therefore a HWP at prime focus once again has an advantage in minimizing its size but will violate the Mizuguchi-Dragone condition while near the Gregorian focus it will not violate the condition.

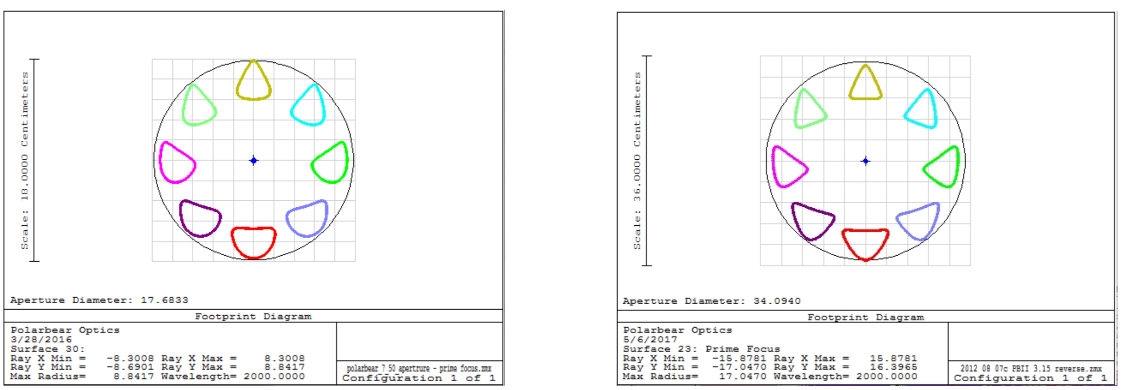

Figure 6.1: **Prime focus rays** — Footprint diagrams at the prime focus plane for POLARBEAR (left) and POLARBEAR-2 (right) are shown. The footprint is the outline of all the rays that are not vignetted in the system. The center and edge pixel rays are plotted in various colors within the circular aperture of $\sim$ 18 cm and $\sim$ 34 cm for POLARBEAR and POLARBEAR-2 respectively.

Qualitatively one can see that this type of polarization rotating optical element at prime focus will in fact violate the Mizuguchi-Dragone condition. When considering each individual polarized geometric ray the exact combination of two reflections of nonzero angles of incidence off two designed surfaces (primary and secondary) ensures the cancellation of aberrations and cross polarization. Even though the ray path is essentially unaltered by a thin and ideal HWP, the polarization state is altered and one would not expect to have cross polarization cancellation to occur between the two reflectors. The polarization state after the HWP is now dependent on an external parameter, the angle between the polarization state and the optical axis of the HWP.

In the following section the situation where a half-wave plate placed near the prime focus will be considered and shown that this will produce Mizuguchi-Dragone breaking.

6.1.2.2 Aberration Cancellation

Even though a thin and ideal HWP at prime focus is expected to produce Mizuguchi-Dragone breaking and increase cross polarization, the aberration cancellation in a Gregorian-Dragone design should not degrade significantly. In the geometric ray trace framework, the introduction of any flat refractive element between the two reflectors will theoretically make the optics slower, but this can be compensated by moving the secondary and receiver together slightly further out in the direction perpendicular to the surface plane of the optical element.

Through ray tracing simulations, It has been calculated that the Strehl ratios can in fact be recovered even with an ideal HWP at prime focus with this method. This is shown in Figure 6.2. The result compares the Strehl ratios of the POLARBEAR-2 without and with a prime focus HWP cases. The Strehl ratio comparison is done within the DLFOV of POLARBEAR-2. The with HWP case is compensated by pulling the secondary and receiver away from the primary by 7.9 mm in the direction perpendicular to the HWP plane. With this compensation the Strehl ratios are recovered to within $< 0.1\%$. Without compensation the Strehl ratio with a HWP at 150 GHz was found to decrease by up to 0.28 in value to become not diffraction limited, but this effect is not specific to a HWP and will

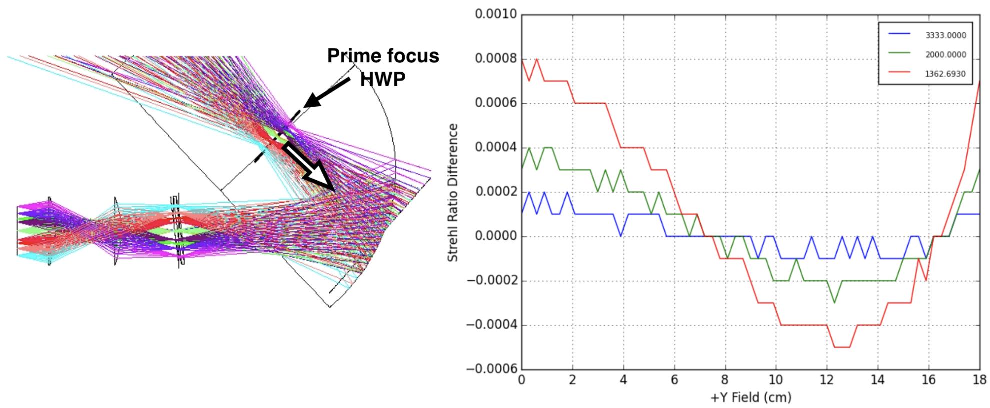

Figure 6.2: **Aberration cancellation with HWP and compensation** — A ray trace diagram for the POLARBEAR-2 design with a prime focus HWP is shown (left). The difference in the Strehl ratio as a function of focal plane position between the POLARBEAR-2 design without and with the HWP is shown (right). The secondary and receiver compensation is performed in the with HWP case. The direction of the compensation is shown with the white arrow. The plot shows Strehl ratios differences for 95 (blue), 150 (green), and 220 (red) GHz.

occur for any refractive flat element at the prime focus.

But it must be noted that this analysis assumes an ideal and perfectly flat HWP at prime focus, and ignores any effects arising from the material properties of the HWP. Thus complex electromagnetic effects due to the material properties of the HWP can potentially cause degradation in the Strehl ratio and other irregular diffraction effects. But to the extent that the geometric ray tracing framework is accurate ($\frac{\lambda}{D} << 1$), it can be expected that the aberration cancelations will not degrade significantly even with a HWP at prime focus.

6.1.3 Mueller Matrix Modeling

Mizuguchi-Dragone breaking can be simplistically modeled using the Mueller matrix formalism. One can define the most generic model for the reflectors without any knowledge of their optical properties and shapes.

$$P = \begin{bmatrix} p_i & p_{qi} & p_{ui} & 0 \\ p_{iq} & p_q & p_{uq} & 0 \\ p_{iu} & p_{qu} & p_u & 0 \\ 0 & 0 & 0 & 1 \end{bmatrix}, \qquad S = \begin{bmatrix} s_i & s_{qi} & s_{ui} & 0 \\ s_{iq} & s_q & s_{uq} & 0 \\ s_{iu} & s_{qu} & s_u & 0 \\ 0 & 0 & 0 & 1 \end{bmatrix}. \tag{6.2}$$

P is the Mueller matrix of the primary and S is the Mueller matrix of the secondary. The i, q, and u indices represent the corresponding I, Q, and U Stokes parameter components. Any combination of the indices represents mixing of those signal components. The circular polarization component V is ignored for the CMB application. An ideal HWP disregarding any material properties is given by

$$H = \begin{bmatrix} 1 & 0 & 0 & 0 \\ 0 & 1 & 0 & 0 \\ 0 & 0 & -1 & 0 \\ 0 & 0 & 0 & -1 \end{bmatrix}. \tag{6.3}$$

A rotated HWP by angle α is just given by

$$H(\alpha) = R(-\alpha)HR(\alpha) = \begin{bmatrix} 1 & 0 & 0 & 0 \\ 0 & \cos(4\alpha) & \sin(4\alpha) & 0 \\ 0 & \sin(4\alpha) & -\cos(4\alpha) & 0 \\ 0 & 0 & 0 & -1 \end{bmatrix} \tag{6.4}$$

where R is just the standard rotation matrix

$$R(\alpha) = \begin{bmatrix} 1 & 0 & 0 & 0 \\ 0 & \cos(2\alpha) & \sin(2\alpha) & 0 \\ 0 & -\sin(2\alpha) & \cos(2\alpha) & 0 \\ 0 & 0 & 0 & 1 \end{bmatrix}. \tag{6.5}$$

The CMB signal of interest should theoretically have no circularly polarized component so the incoming signal D can be assumed to take the form

$$D = \begin{bmatrix} I \\ Q \\ U \\ 0 \end{bmatrix}. \tag{6.6}$$

In the ideal case where there is no instrumental polarization or cross polarization, then all off-diagonal terms in P and S go to zero. Assuming energy is not lost at each surface, P and S can be treated as the identity matrix. The HWP modulated signal becomes

$$D_{Ideal} = SH(\alpha)PD = \begin{bmatrix} I \\ Q\cos(4\alpha) + U\sin(4\alpha) \\ Q\sin(4\alpha) - U\cos(4\alpha) \\ 0 \end{bmatrix}. \tag{6.7}$$

Here it can be seen that the Q and U signals are modulated into different phases of the 4f harmonic at the original Q and U orientations as expected. The standard demodulation technique will allow for recovering the Q and U signals separately.

Now assuming there is cross polarization and instrumental polarization but no HWP in the system, then one obtains the results

$$\begin{aligned} D_{No\ HWP} &= SPD \\ &= \begin{bmatrix} I(p_i s_i + p_{iq}s_{qi} + p_{iu}s_{ui}) + Q(p_q s_{qi} + p_{qi}s_i + p_{qu}s_{ui}) \\ + U(p_u s_{ui} + p_{ui}s_i + p_{uq}s_{qi}) \\ I(p_i s_{iq} + p_{iq}s_q + p_{iu}s_{uq}) + Q(p_q s_q + p_{qi}s_{iq} + p_{qu}s_{uq}) \\ + U(p_u s_{uq} + p_{ui}s_{iq} + p_{uq}s_q) \\ I(p_i s_{iu} + p_{iq}s_{qu} + p_{iu}s_u) + Q(p_q s_{qu} + p_{qi}s_{iu} + p_{qu}s_u) \\ + U(p_u s_u + p_{ui}s_{iu} + p_{uq}s_{qu}) \\ 0 \end{bmatrix}. \end{aligned} \tag{6.8}$$

From this result a simplified model of the Mizuguchi-Dragone condition in the Mueller formalism can be obtained. If by definition a Mizuguchi-Dragone condition satisfying dual reflector system suppresses cross polarization at the optical center due to cancellation between the primary and secondary (i.e. the Q and U signals are not mixed by cross polarization terms), then it must be that

$$\begin{aligned} p_u s_{uq} + p_{uq}s_q &= 0 \\ p_q s_{qu} + p_{qu}s_u &= 0. \end{aligned} \tag{6.9}$$

In this simple Mueller model this would represent the Mizuguchi-Dragone condition. It can be seen that the primary $Q \leftrightarrow U$ term is canceling the secondary $Q \leftrightarrow U$ term as expected from the Mizuguchi-Dragone condition.

Now assuming there is a HWP in the system between the primary and secondary, the results become

$$\begin{aligned} D_{HWP} &= SH(\alpha)PD \\ &= \begin{bmatrix} \begin{gathered} s_i(Ip_i + Qp_{qi} + Up_{ui}) \\ + (I(p_{iq}s_{qi} - p_{iu}s_{ui}) + Q(p_q s_{qi} - p_{qu}s_{ui}) + U(-p_u s_{ui} + p_{uq}s_{qi}))\cos(4\alpha) \\ + (I(p_{iq}s_{ui} + p_{iu}s_{qi}) + Q(p_q s_{ui} + p_{qu}s_{qi}) + U(p_u s_{qi} + p_{uq}s_{ui}))\sin(4\alpha) \end{gathered} \\ \begin{gathered} s_{iq}(Ip_i + Qp_{qi} + Up_{ui}) \\ + (I(p_{iq}s_q - p_{iu}s_{uq}) + Q(p_q s_q - p_{qu}s_{uq}) + U(-p_u s_{uq} + p_{uq}s_q))\cos(4\alpha) \\ + (I(p_{iq}s_{uq} + p_{iu}s_q) + Q(p_q s_{uq} + p_{qu}s_q) + U(p_u s_q + p_{uq}s_{uq}))\sin(4\alpha) \end{gathered} \\ \begin{gathered} s_{iu}(Ip_i + Qp_{qi} + Up_{ui}) \\ + (I(p_{iq}s_{qu} - p_{iu}s_u) + Q(p_q s_{qu} - p_{qu}s_u) + U(-p_u s_u + p_{uq}s_{qu}))\cos(4\alpha) \\ + (I(p_{iq}s_u + p_{iu}s_{qu}) + Q(p_q s_u + p_{qu}s_{qu}) + U(p_u s_{qu} + p_{uq}s_u))\sin(4\alpha) \end{gathered} \\ 0 \end{bmatrix}. \end{aligned} \tag{6.10}$$

The terms of particular interest are

$$\begin{aligned} U(-p_u s_{uq} + p_{uq}s_q)\cos(4\alpha) \\ Q(p_{qu}s_q + p_q s_{uq})\sin(4\alpha) \\ Q(p_q s_{qu} - p_{qu}s_u)\cos(4\alpha) \\ U(p_u s_{qu} + p_{uq}s_u)\sin(4\alpha) \end{aligned} \tag{6.11}$$

The cross polarization terms from both the primary and secondary are modulated into the 4f harmonic at first order and will be observed even after demodulation. Hence the recovered Q and U signals will contain cross polarization terms. One interesting point is that the secondary cross polarization terms are modulated into the signal despite the fact that the secondary is located optically after the HWP (forward time).

One can see by simple comparison that the Mueller model Mizuguchi-Dragone condition does not match any of the above 4 equations. Hence it cannot be expected that any of these cross polarization terms will vanish unlike the case where no HWP exists. Therefore it can be concluded that a HWP between the primary and secondary reflectors will in fact violate the Mizuguchi-Dragone condition and show Mizuguchi-Dragone breaking.

This Mueller model is simplified and will not capture all the exact details but is a theoretically correct illustration of the effect. The true effect of Mizuguchi-Dragone breaking is complex and like any optical systematic is difficult to analytically calculate exactly. Physical optics simulations are required to asses the details.

From this simple model one can see that for POLARBEAR and the Simons Array Mizuguchi-Dragone breaking will occur with the introduction of the HWP at prime focus. Therefore the cross polarization systematic leakages in the B-mode spectrum must be assessed when this occurs. Even though the prime focus HWP allows for minimizing the required optical aperture size, placing a larger HWP at the Gregorian focus may be required to lower cross polarization systematics.

In order to estimate the impact of the cross polarization due to Mizuguchi-Dragone breaking on the measured C_ℓ^{BB} spectrum, the effects of the cross polarization in the Mueller matrix need to be propagated to the power spectrum through simulated CMB maps.

6.1.4 Mueller Beam Matrix

The Mueller beam matrix is defined as

$$M = \{m_{ij}\} = \begin{bmatrix} m_{II} & m_{IQ} & m_{IU} & m_{IV} \\ m_{QI} & m_{QQ} & m_{QU} & m_{QV} \\ m_{UI} & m_{UQ} & m_{UU} & m_{UV} \\ m_{VI} & m_{VQ} & m_{VU} & m_{VV} \end{bmatrix} \tag{6.12}$$

where the indices $i, j = \{I, Q, U, V\}$ which represent the standard Stokes parameters. Hence the diagonal elements in M represent the polarization beams for each Stokes parameter, and the off-diagonal elements represent the leakage or mixing beams between the different polarization states. For example, m_{QU} represents how much the U polarization signal leaks into the Q polarization signal, and m_{QI} represents how much the I intensity signal leaks into the Q polarization signal. Using standard optics terminology, instrumental polarization are the off-diagonal m_{iI} elements and cross polarization are the m_{QU}, m_{QV}, m_{UV} (and counterpart) elements. Typically the mueller element pairs with the reversed indices are equivalent in beam shape and pattern with possibly only an overall multiplicative negative sign. For example m_{QU} and m_{UQ} will typically have the same beam shape and absolute magnitude, but one will be the negative of the other. The measured signals are just given by

$$D' = MD = \begin{bmatrix} m_{II}I + m_{IQ}Q + m_{IU}U \\ m_{QI}I + m_{QQ}Q + m_{QU}U \\ m_{UQ}I + m_{UQ}Q + m_{UU}U \\ m_{VI}I + m_{VQ}Q + m_{VU}U \end{bmatrix}. \tag{6.13}$$

One can see that the measured Q and U signals each have instrumental polarization terms leaking unpolarized signal into the polarized signal, a beam convoluted polarization signal, and the cross polarization signal mixing Q and U.

This Mueller beam matrix can be used to simulate contaminated I, Q, U, V maps in order to estimate the level of contamination in map space due to an optical system. For the case of CMB polarization simulations, one can take the theoretical CMB polarization maps simulated from ideal polarization spectra and mathematically add in the contamination. If the theoretical CMB polarization maps are given by Q_{map}, U_{map} then the contaminated maps Q'_{map}, U'_{map} can be calculated in the following way

$$Q'_{map} = m_{QQ} \star Q_{map} + m_{QU} \star U_{map}, \quad U'_{map} = m_{UU} \star U_{map} + m_{UQ} \star Q_{map} \tag{6.14}$$

$$Q'_{map} = m_{QQ} \star Q_{map} + m_{QI} \star I_{map}, \quad U'_{map} = m_{UU} \star U + m_{UI} \star I_{map} \tag{6.15}$$

where the components for the cross polarization and instrumental polarization have been separated out. The star represents a convolution. This study solely focuses on cross polarization and hence will assume the instrumental polarization can be analyzed completely independently from the cross polarization analysis. From these equations one can calculate Q'_{map} and U'_{map} with the cross polarization contamination using simulations of I, Q, and U maps.

6.1.5 Physical Optics Calculations

Using physical optics simulations of different polarization states M can be calculated. Now the Mueller beam matrix M represents the transfer matrix of the optics system of interest. S is the input signal Stokes vector and S' is the output signal Stokes vector. If the simple input polarization states are defined in terms of the Stokes vectors, X and Y polarized input light are given by

$$S_X = \begin{bmatrix} 1 \\ 1 \\ 0 \\ 0 \end{bmatrix}, \quad S_Y = \begin{bmatrix} 1 \\ -1 \\ 0 \\ 0 \end{bmatrix}. \tag{6.16}$$

45 and 135 degrees polarized light are given by

$$S_{45} = \begin{bmatrix} 1 \\ 0 \\ 1 \\ 0 \end{bmatrix}, \quad S_{135} = \begin{bmatrix} 1 \\ 0 \\ -1 \\ 0 \end{bmatrix} \tag{6.17}$$

and right and left circularly polarized light are

$$S_{RC} = \begin{bmatrix} 1 \\ 0 \\ 0 \\ 1 \end{bmatrix}, \quad S_{LC} = \begin{bmatrix} 1 \\ 0 \\ 0 \\ -1 \end{bmatrix}. \tag{6.18}$$

Propagating the inputs through the optical system M, one obtains the following:

$$S' = \begin{bmatrix} I' \\ Q' \\ U' \\ V' \end{bmatrix} = MS \tag{6.19}$$

$$S'_{X,i} = m_{iI} + m_{iQ}, \quad S'_{Y,i} = m_{iI} - m_{iQ} \tag{6.20}$$

$$S'_{45,i} = m_{iI} + m_{iU}, \quad S'_{135,i} = m_{iI} - m_{iU} \tag{6.21}$$

$$S'_{RC,i} = m_{iI} + m_{iV}, \quad S'_{LC,i} = m_{iI} - m_{iV}. \tag{6.22}$$

In S' the index i represents the I, Q, U, V vector components (e.g. $S'_{X,Q} = Q'_X$). Solving these equations for each mueller beam matrix element:

$$m_{iI} = \frac{1}{2}\left(S'_{X,i} + S'_{Y,i}\right) = \frac{1}{2}\left(S'_{45,i} + S'_{135,i}\right) = \frac{1}{2}\left(S'_{RC,i} + S'_{LC,i}\right) \tag{6.23}$$

$$m_{iQ} = \frac{1}{2}\left(S'_{X,i} - S'_{Y,i}\right) \tag{6.24}$$

$$m_{iU} = \frac{1}{2}\left(S'_{45,i} - S'_{135,i}\right) \tag{6.25}$$

$$m_{iV} = \frac{1}{2}\left(S'_{RC,i} - S'_{LC,i}\right). \tag{6.26}$$

Hence by simulating X, Y, 45°, 135°, right circular, and left circular polarization beams propagating through an optical system represented by M, one can fully calculate the Mueller beam matrix of the optical system of interest by addition and subtraction of the E-field outputs from each type of simulation. For example, to calculate the m_{UQ} element one needs

$$m_{UQ} = \frac{1}{2}\left(S'_{X,U} - S'_{Y,U}\right). \tag{6.27}$$

So from the X and Y polarization input feed simulations one would take the output E-fields of each simulation, calculate the U stokes beam map for each and subtract the Y polarization simulation from the X polarization simulation to calculate m_{UQ}. Similarly each element of M can be calculated to obtain the full Mueller beam matrix of the optical system of interest and quantify the level of instrumental and cross polarization the optics create. These simulations typically need to be calculated using commercial physical optics simulation software such as GRASP and QUAST [67].

6.1.6 Physical Optics Simulations

Due to the increasing complexity of current telescope designs, optical performances of such designs are impossible to assess with analytical calculations alone. Full physical optics simulations are needed in order to estimate the full effects of diffraction in reflective and refractive optical designs. GRASP and QUAST add-on [67] are commercial physical optics simulation software currently most commonly used to simulate optical performances of telescopes and receivers across various wavelengths.

6.1.6.1 POLARBEAR-2 Physical Optics

As an example calculation using GRASP and QUAST, the Mueller beam matrix for the POLARBEAR-2 optics can be determined using the procedure in section 6.1.5. The POLARBEAR-2 optical design can be modeled only using the reflectors, re-imaging lenses, Lyot stop, and feeds at the focal plane. Running physical optics simulations through this POLARBEAR-2 model with feed inputs of X, Y, 45°, 135°, right circular, and left circular polarization, the full Mueller beam matrix for POLARBEAR-2 can be calculated. Physical optics are done in the reverse time frame with emitting feeds at the focal plane.

The resulting Mueller beam matrix for the center pixel is shown in Figure 6.3. For CMB applications circular polarization is not measured in many experiments and not expected from CMB. Thus the Stokes V related components are not necessary for this study. It can be seen that the off-diagonal Mueller elements such as m_{QU} and m_{UQ} are the same beam pattern but with one the negative of the other. This pattern is similar for the rest of the off-diagonal elements. The absolute value is taken for converting to dB units.

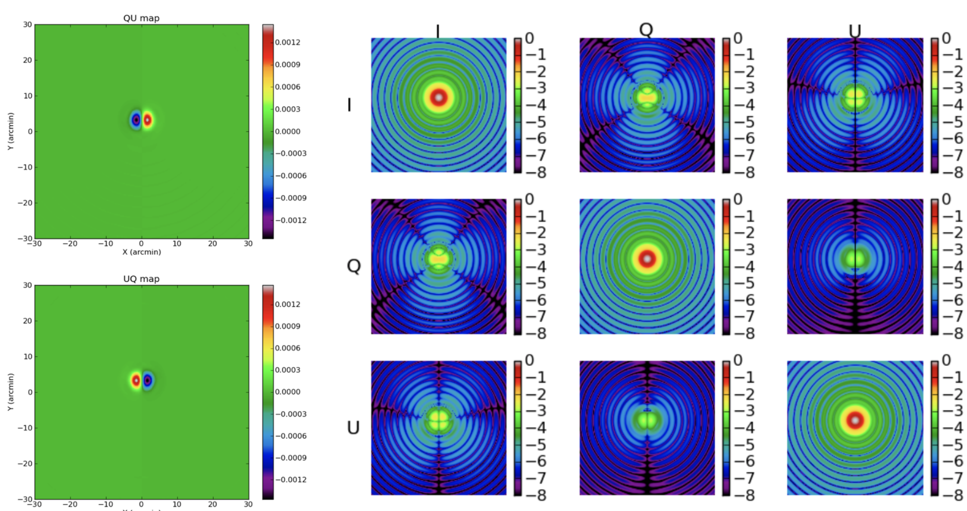

Figure 6.3: **POLARBEAR-2 Mueller matrix simulations** — Plots of the calculated m_{QU} and m_{UQ} center pixel beams using the GRASP physical optics model for POLARBEAR-2 is shown (left). The calculated Mueller beam matrix for the center pixel is also shown (right). The Stokes V related elements are not shown. The Mueller beams are in absolute units of dB/10.

This set of simulations must be calculated for every pixel and frequency of interest separately. Due to potentially long computation times required, simulating every pixel on the focal plane is difficult and usually only specific positions are calculated. Typically as a comparison the center and edge pixels are simulated because the center pixel should be the most ideal and the edge pixel should contain the most aberrations. Examples of the m_{II} and m_{QU} beams for the center and edges are shown in Figure 6.4.

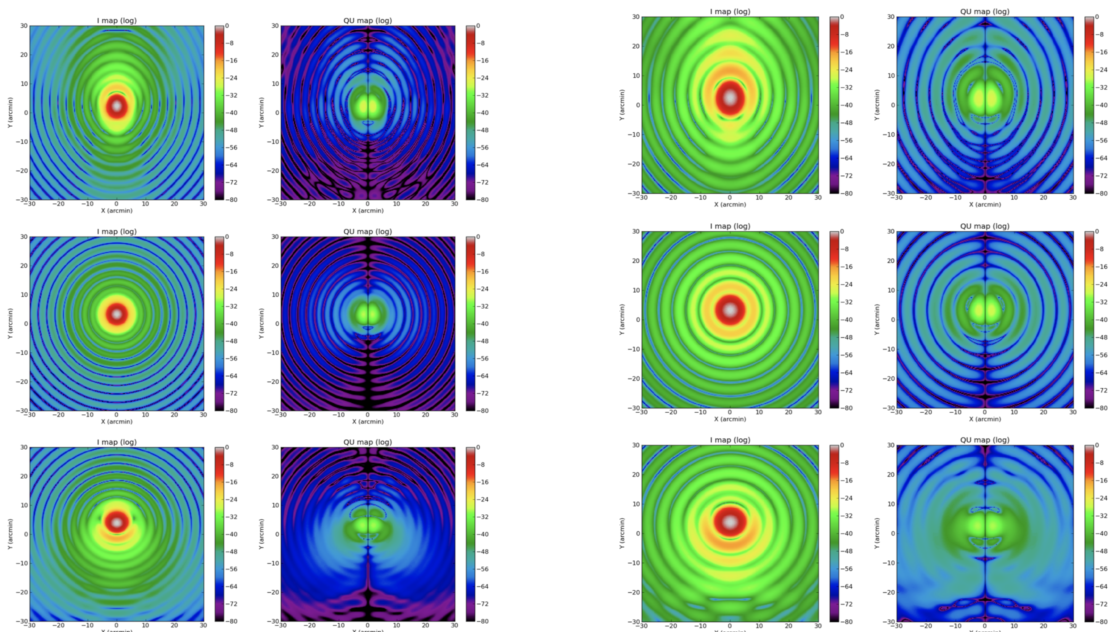

Figure 6.4: **POLARBEAR-2 physical optics simulations** — GRASP simulation results for m_{II} (first column) and m_{QU} (second column) are shown for the center and ±Y edge FOV pixels at 150 (left) and 95 GHz (right). The rows in order from top to bottom are the +Y edge FOV, center FOV, and -Y edge FOV simulations. All beams are in units of dB.

In this way the Mueller beam matrix elements for a specific optical system can be calculated using physical optics simulations. The physical optics simulations incorporate complex diffraction and aberration effects that allows for determining the beam shapes to high accuracy for a specific optical design.

6.1.6.2 Mizuguchi-Dragone Breaking Physical Optics

Because Mizuguchi-Dragone breaking is a direct consequence of the HWP in the dual reflector design, only physical optics simulations of the HTT dual reflectors will be used. The feeds will be placed at positions in the Gregorian focus corresponding to specific focal plane (FOV) pixel positions. With this the Mizuguchi-Dragone breaking analysis is applicable to POLARBEAR-2 and all the Simons Array which will have multiple re-imaging optics designs. The main focus of this study is the cross polarization systematic, and hence the m_{QU} and m_{UQ} elements will be primarily used.

Because there are no re-imaging optics in these simulations the calculated beam shapes contain greater levels of aberrations across the focal plane than in a full POLARBEAR-2 or Simons Array optical design. Therefore this study will produce a conservative estimate of the cross polarization systematics due to Mizuguchi-Dragone breaking. Typically re-imaging optics will create more ideal beam shapes which will decrease the cross polarization systematic. It must be noted that any cross polarization effects from the re-imaging optics will be ignored in this study, but cross polarization from re-imaging optics are expected to be smaller than those from the reflective optics.

Simulated m_{QU} beams from the HTT off-axis Gregorian-Dragone dual reflector design without the HWP is shown in Figure 6.5. It can be seen that the beams are all dipole like. The center has a low cross polarization amplitude of 0.06% as expected. At the edges of FOV the amplitudes increase to $\sim 4.5\%$ at the highest.

The Mueller matrix beams for Mizuguchi-Dragone breaking were calculated from GRASP simulations of the dual reflector system combined with a custom HWP simulator code developed by Satoru Takakura to simulate a HWP at prime focus. The particular 19 physical optics simulation results that incorporate the HWP simulator were provided by Satoru Takakura, a POLARBEAR collaborator. Details on the simulations can be found in [68].

Simulated m_{QU} beams from the HTT design with a prime focus HWP are shown in Figure 6.6. It can be seen that the center pixel is now a quadrupole with

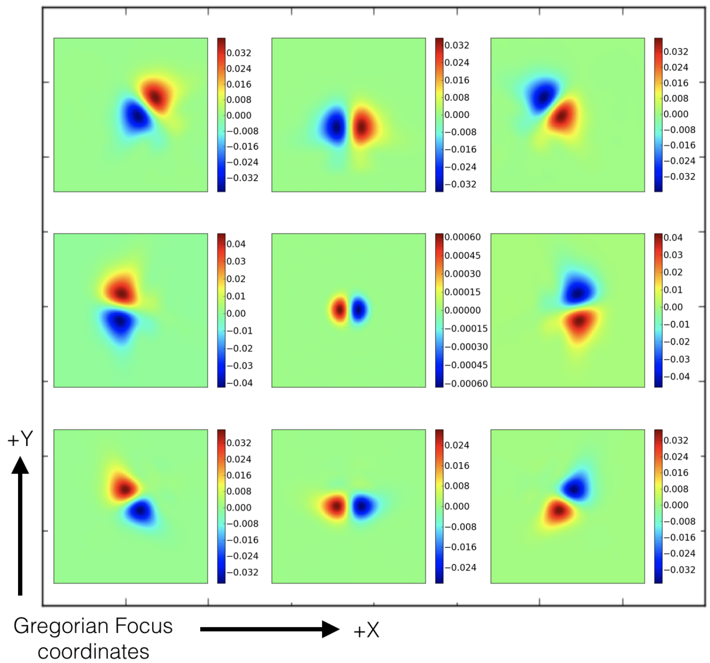

Figure 6.5: **HTT dual reflector physical optics simulations** — The dual reflector design m_{QU} beam for the center and edge FOV locations for POLARBEAR-2 and Simons Array are shown. The sky m_{QU} beams are placed in the plot according to the corresponding feed location at Gregorian focus. All individual sky beams are plotted on 24'×24' grids.

the edge pixels still dipole like. The beam shapes seem to be more skewed as well due to the HWP. The cross polarization amplitude has increased significantly with 0.6% at the center FOV and as large as $16-20\%$ for the edge FOV. This level of cross polarization is similar in amplitude to the expected cross polarization from the off-axis parabolic primary alone. Consistent with the theory, the Mizuguchi-Dragone condition seems to be broken by the HWP placed at the prime focus. These irregular beam shapes and higher cross polarization amplitudes need to be assess in terms of the increased leakage in the B-mode power spectrum.

6.1.7 Cross Polarization Map Simulations

Q and U CMB maps can be simulated using CAMB [17] derived power spectra for various cases. In order to quantify the leakage into C_ℓ^{BB} due to cross polarization only, Q and U CMB maps that only have theoretical C_ℓ^{TT}, C_ℓ^{TE}, and

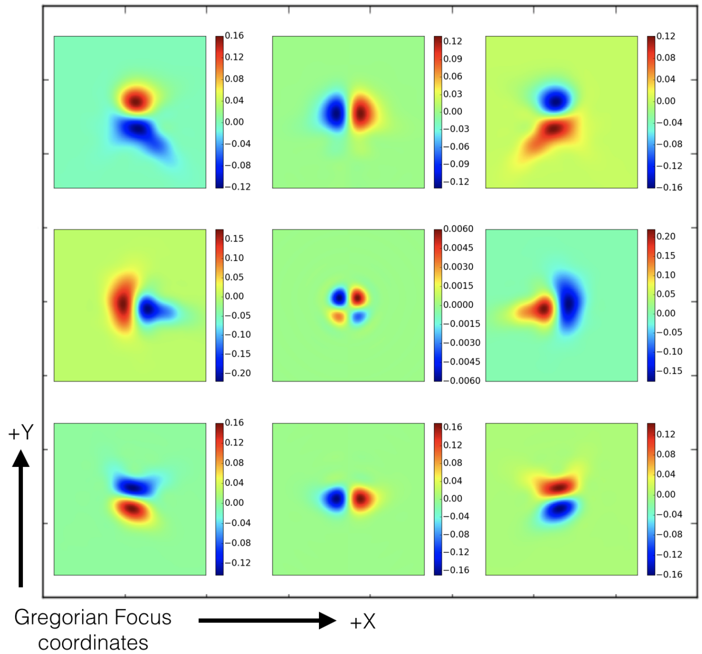

Figure 6.6: **HTT with prime focus HWP physical optics simulations** — The dual reflector design with a prime focus HWP case m_{QU} beam for the center and edge FOV locations for POLARBEAR-2 and Simons Array are shown. The sky m_{QU} beams are placed in the plot according to the corresponding feed location at Gregorian focus. All individual sky beams are plotted on 24'×24' grids.

C_ℓ^{EE} signals and null C_ℓ^{BB} were simulated. The simulated Q and U maps are convolved with the various physical optics derived Mueller beams matrices and Q' and U' maps were calculated from equations 6.14.

The derived Q' and U' maps are propagated through the POLARBEAR analysis pipeline and power spectra are calculated based off the MASTER method [69]. Because the initial Q and U maps are simulations without C_ℓ^{BB} signal, any resulting B-mode signal is the effect of the cross polarization due to Mizuguchi-Dragone breaking.

6.1.8 Mitigation Estimation

The cross polarization systematic like any other systematic can be mitigated to a certain degree by sky rotation as well as focal plane pixel averaging. These mitigation effects are also simulated in this method.

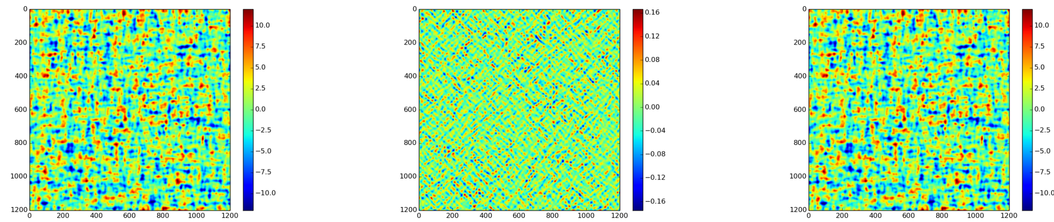

Figure 6.7: **Cross polarization contaminated Q and U maps** — Simulated null C_ℓ^{BB} Q map without cross polarization (left), a convolved $m_{uq}U$ map (middle), and calculated Q' map are shown. The amplitude of the cross polarization signal is typically more than an order of magnitude smaller and difficult to see in map space.

6.1.8.1 Sky Rotation Mitigation

In a real CMB observation, the Mueller matrix beam is fixed relative to the instrument's orientation. As the CMB patch on the sky is observed across time, the patch orientation will rotate relative to the instrument's Mueller matrix beam. Repeated measurements of the patch at different relative instrument orientations allow for sky rotation mitigation of various systematics. This sky rotation is represented by the attack (parallactic) angle distribution during observations for a particular patch. The parallactic angle is the angle between the horizontal and equatorial coordinate systems at any point in time. This attack angle distribution is dependent on the scan strategy being used, and with a wider and more uniform distribution of attack angles a larger sky rotation mitigation effect can be expected.

In simulations, sky rotation mitigation can be estimated by spatially rotating the Mueller matrix beam relative to the simulated Q and U maps before convolution. By averaging multiple Q' and U' maps each with different rotation angle Mueller matrix beam convolutions the effect of sky rotation can be simulated. To estimate the sky rotation mitigation characteristic of a Polarbear like observation, the various rotation angles must mimic the attack angles of the Polarbear scan strategy on a particular patch. In order to shorten the computation time to a tractable length, rotation angles had to be carefully chosen to approximately represent the real attack angle distribution found from the Polarbear scan strategy. The simulated rotation angle distribution is shown in Figure 6.8. Therefore this limited simulation should underestimate the sky rotation mitigation and be a conservative estimate.

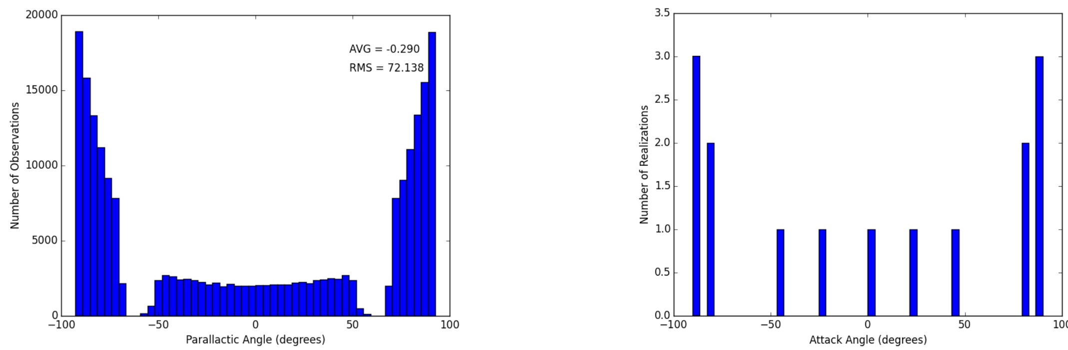

Figure 6.8: **Sky rotation mitigation estimate** — The right is a histogram of attack (parallactic) angles taken from simulated pointing of a realistic POLARBEAR 10-day scan strategy. The left is the histogram of Mueller matrix beam rotation angles used in the sky rotation mitigation simulation. Rotation angles and their frequencies were chosen to represent a similar shape to the realistic attack angles.

6.1.8.2 Focal Plane Averaging Mitigation

Focal plane averaging mitigation can be estimated by implementing pixel specific Mueller matrix beams for each pixel in the focal plane within the simulation. The simulation pipeline simulates TODs for each pixel based off the scan strategy pointing information and picking out the Q' and U' value from the simulated maps according to the pixel pointing. Therefore theoretically focal plane averaging can be estimated by using specific Q' and U' maps derived from the pixel specific Mueller matrix beams for every individual pixel in the focal plane.

As outlined in section 6.1.5, physical optics simulations for pixels across the entire focal plane are very time consuming. Calculating Q' and U' maps for each pixel separately and running them through the analysis pipeline is further time consuming. Therefore in order to simplify the procedure, interpolation-based wafer specific Mueller beam matrices calculated from physical optics simulations were used.

An interpolation of the dipole amplitudes as a function of focal plane position was calculated based off physical optics simulations for 19 pixels approximately evenly spread out across the focal plane. Then the interpolated dipole amplitudes were averaged across each wafer to produce an interpolation-based wafer average dipole amplitude value characteristic of each wafer.

The Mueller matrix beam shapes of the focal plane center pixel and outermost edge pixels were used. The cross polarization contamination increases with distance away from the optical axis and the Mueller matrix beam shapes also tend to get more skewed analogously. Therefore the outermost edge pixels represent the largest contribution to the cross polarization contamination in terms of both amplitude and beam shape. By taking the beam shapes from the outermost edge pixels and rescaling their amplitudes based off the interpolation-based wafer average amplitude, one can obtain Mueller matrix beams that represent each wafer's average. These Mueller matrix beams are conservative in estimate because the worst-case beam shape is assumed in each wafer. The wafer averaged Mueller matrix beams are shown in Figure 6.9.

Now the effect of focal plane averaging can be estimated by calculating Q' and U' maps specific to each wafer and simulating TODs for all pixels by grouping them by wafer. From the simulations it can be seen that the Mueller matrix beam rotates once every 180 degrees azimuthally around the center pixel. Therefore the focal plane averaging across all focal plane pixels should theoretically contain many orientations of the dipole like beam, and have a large mitigation effect. It is expected that the mitigation effect will be underestimated in this simulation because only 7 different Mueller matrix beam simulations at chosen locations are used and will once again be a conservative estimate.

6.1.9 Power Spectra Leakage Estimation

The results of propagating the Mizuguchi-Dragone breaking cross polarization Mueller matrix beams with mitigation through the analysis pipeline are shown in Figure 6.10. Four cases were simulated for Polarbear-2 and Simons Array:

1. Edge pixel Mueller matrix beam ($\sim 17\%$ dipole)

2. Edge pixel Mueller matrix beam scaled to 6 outer wafer average amplitude

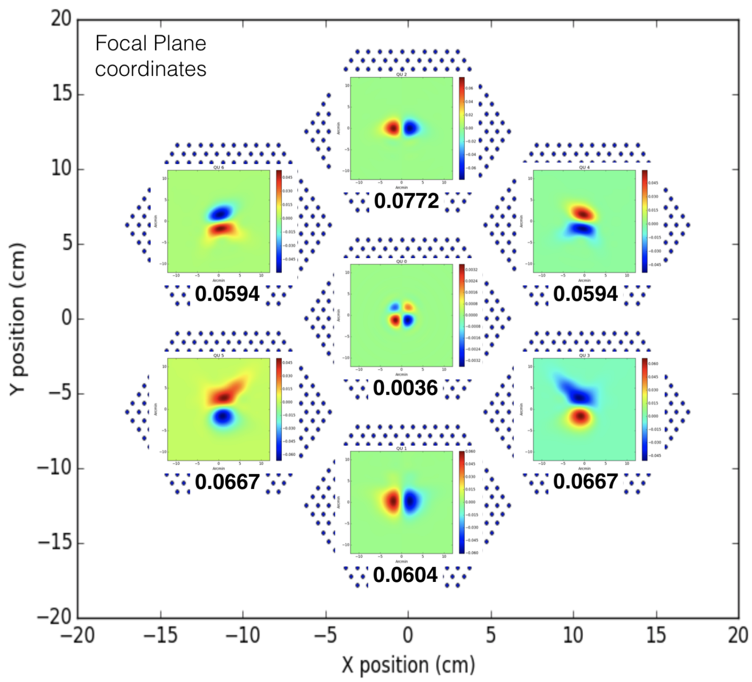

Figure 6.9: **Focal Plane Averaged Mueller Matrix Beams** — Estimated POLARBEAR-2 focal plane wafer averaged Mueller matrix beams are shown. Interpolation-based wafer averaged mueller beam amplitudes are shown below each beam plot. The Mueller matrix beams have been scaled in amplitude to match the wafer averaged values. Between the Gregorian focus plane and focal plane the field locations flip in X and Y optically.

(∼ 6% dipole)

3. Full 7 wafer Mueller matrix beams with interpolation-based focal plane averaging scaling

4. Full 7 wafer Mueller matrix beams with interpolation-based focal plane averaging scaling and sky rotation

The four cases are listed in order from maximum to minimum leakage. C_ℓ^{BB} leakage for case 3 is shown separately in Figure 6.11, and C_ℓ^{BB} leakage for case 4 is shown separately in Figure 6.12.

From Figure 6.10, it can be seen that the C_ℓ^{BB} leakage due to Mizuguchi-Dragone breaking has a C_ℓ^{EE} spectrum like shape because it converts the E-mode signal into B-modes. As expected the worse leakage is seen for the leakage due

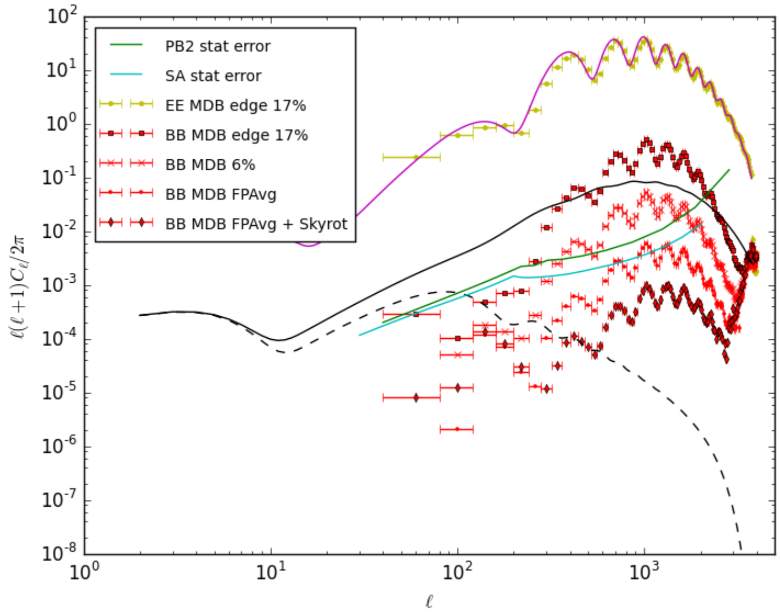

Figure 6.10: C_ℓ^{BB} **leakages from Mizuguchi-Dragone Breaking** — The C_ℓ^{BB} leakage spectra due to Mizuguchi-Dragone breaking are shown. Leakage spectra from case 1 (red squares), case 2 (red crosses), case 3 (red dots), and case 4 (red diamonds) are plotted. Theoretical C_ℓ^{EE}, primordial C_ℓ^{BB} (r=0.01), and lensed C_ℓ^{BB} spectra are also plotted. The POLARBEAR-2 and Simons Array estimated statistical errors are plotted in green and cyan respectively.

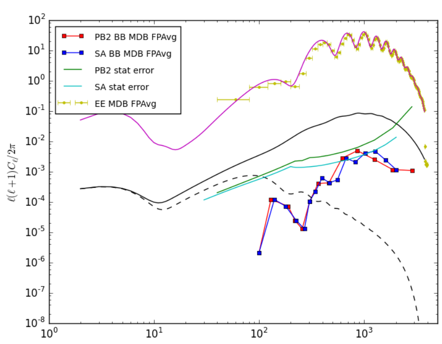

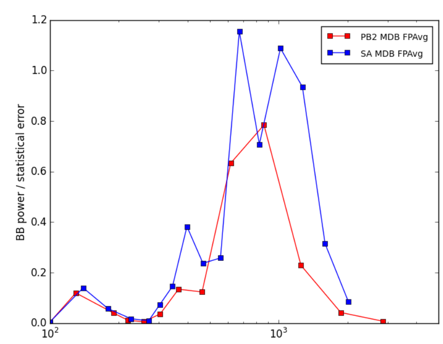

Figure 6.11: C_ℓ^{BB} **leakage with focal plane averaging mitigation** — The case 3 C_ℓ^{BB} leakage spectra due to Mizuguchi-Dragone breaking with focal plane averaging mitigation are shown (left). The leakage spectra are binned according to the statistical error bins. The C_ℓ^{BB} leakages divided by the POLARBEAR-2 and Simons Array statistical error are shown for comparison (right).

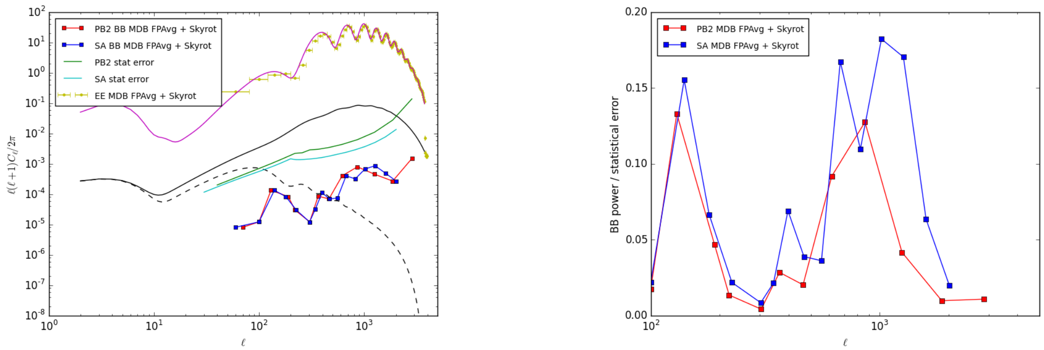

Figure 6.12: **C_ℓ^{BB} leakage with focal plane averaging and sky rotation mitigation** — The case 4 C_ℓ^{BB} leakage spectra due to Mizuguchi-Dragone breaking with focal plane averaging and sky rotation mitigation are shown (left). The leakage spectra are binned according to the statistical error bins. The C_ℓ^{BB} leakages divided by the Polarbear-2 and Simons Array statistical error are shown for comparison (right).

to the edge pixel Mueller matrix beam with no mitigation (case 1). This results in a C_ℓ^{BB} leakage approximately an order of magnitude larger than the lensing B-mode peak and two orders of magnitude larger than the Polarbear-2 statistical error. Case 2 has leakage that is below the lensing B-mode peak but still an order of magnitude larger than the Polarbear-2 statistical error. This case is approximately equal to observing with only one of the outer 6 wafers, and shows that wafer averaging from one of these wafers is potentially not sufficient.

Leakages smaller than or equal to the statistical error are only achievable with full focal plane averaging and sky rotation mitigation or else the leakage due to Mizuguchi-Dragone breaking dominates the B-mode signal. From Figures 6.11 and 6.12, it can be seen that with full focal plane averaging the C_ℓ^{BB} leakage becomes approximately equivalent to the Polarbear-2 and Simons Array statistical errors. Further adding the sky rotation mitigation, the leakage becomes approximately an order of magnitude lower than the Polarbear-2 statistical error and a factor of ~ 5 lower than the Simons Array statistical error across all ℓ. As noted previously the estimated mitigation from from focal plane averaging and sky rotation are conservative and underestimated. Hence in real observations it is expected that the two mitigation effects will be larger.

It is found that the C_ℓ^{BB} leakage due to Mizuguchi-Dragone condition breaking is a cross polarization systematic that is not negligible on a per bolometer (pixel) basis. The leakage can dominate the theoretical lensing B-mode signal and become problematic for the primordial B-mode signal as well if not correctly accounted for. But it is shown that the systematic can be highly suppressed by full focal plane averaging and sky rotation to levels lower than the estimated statistical error even from this conservative simulation.

The edge pixel case without Mizuguchi-Dragone breaking was also simulated as comparison as shown in Figure 6.13. It can be seen that for the edge

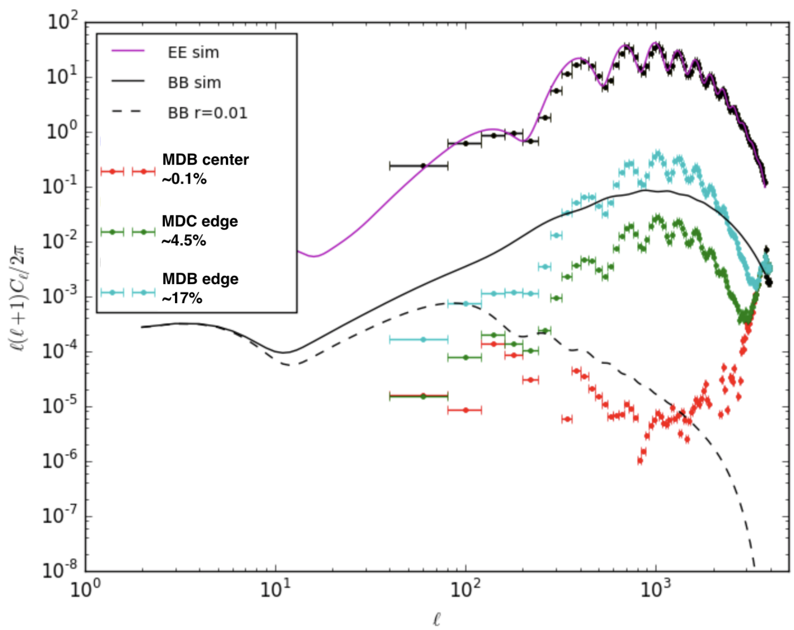

Figure 6.13: C_ℓ^{BB} **leakage comparisons** — The C_ℓ^{BB} leakage spectra due to Mizuguchi-Dragone breaking for the center (red) and edge (cyan) pixels are shown. The leakage for the same edge pixel without Mizuguchi-Dragone breaking is also plotted (green).

pixel, which is the worst leakage pixel, that without a HWP the C_ℓ^{BB} leakage is more than an order of magnitude lower than the with HWP case, and also subdominant to the lensing B-mode peak. The leakage due to the center pixel at an amplitude of $\sim 0.1\%$ is completely negligible in comparison and found to be not problematic for both without and with HWP cases. The cross polarization leakage is dominated by the 6 outer wafer pixels.

Hence for the Mizuguchi-Dragone condition satisfying case, the cross polarization is expected to be smaller than the theoretical B-mode signal across the entire focal plane. This will further decrease with focal plane averaging and sky rotation mitigation to levels much smaller than the Mizuguchi-Dragone breaking case.

Even though the effects of Mizuguchi-Dragone breaking are found to be suppressible through mitigation, this level of cross polarization systematic is concerning. For the Polarbear-2 and Simons Array, a HWP at the prime focus has the advantage of reducing the size of the HWP by $\sim 20\%$, but it can potentially increase the per pixel cross polarization B-mode leakage by more than an order of magnitude. Placing the HWP at Gregorian focus will theoretically not violate the Mizuguchi-Dragone condition, and is preferred in terms of minimizing the cross polarization leakage even at the cost of necessitating a larger HWP.

Polarbear-2 and the Simons Array are planned to use a HWP at the Gregorian focus due to these considerations. A HWP at prime focus can in fact be used as a back-up location, but focal plane averaging and sky rotation mitigation must be carefully implemented to lower the cross polarization systematics to a sufficient level.

6.2 SA Receiver Optics Design

With evermore observational evidence of foreground contamination from dust and other astronomical sources in the measured polarization signal, measuring contamination directly for removal is becoming more important in CMB experiments. Current and future generation CMB experiments are implementing observations across multiple frequencies in order to obtain sensitivity to both CMB and foregrounds. This requires an expansion of the instrument to observe a wider range of frequencies and improvements not only to technology but the optical design as well.

From Polarbear to Polarbear-2 the observational frequency was expanded to 95 and 150 GHz. In upgrading to the Simons Array the observational frequency range will be increased to include 95, 150, 220, and 280 GHz observational bands.

6.2.1 Technological Frequency Expansion

Various technological upgrades must be made in order to be able to observe at multiple frequencies. The first being broad-band detector technology. As explained in section 5.1.2, unlike the POLARBEAR slotted dipole antenna detectors, the POLARBEAR-2 and Simons Array sinuous antenna detectors are much more broad-band due to the characteristic log-periodic antenna design. This allows for observation across a large frequency range. Combined with band defining filters the detectors will become sensitive to various observational frequencies bands. For Simons Array due to the limitations by the atmospheric emission, the bands are controlled and defined to be contained within the atmospheric windows. But theoretically multiple bands can be defined such that the bands overlap as discussed for satellite experiments [70].

A second essential upgrade is to the AR coating technology. AR coatings are coatings on any refractive optical element in order to reduce losses due to reflection when light propagates between interfaces of different indices of refraction. Thus the transmission efficiency through a refractive element is substantially increased. The AR coating materials are chosen such that the difference in the index of refraction at each interface is minimized analogous to impedance matching. The thicknesses of the coatings are chosen such that they create constructive and destructive interference between coating layers to maximize the transmission. Therefore it is common to use multiple layers in order to create an efficient AR coating.

To observe across a larger range in frequency, the AR coatings usually must use more layers of differing material in order to increase transmission across the entire range of interest. The AR coatings must be applied to all refractive optical elements including lenses, lenslets, filters, and receiver windows. Creating multi-layer AR coatings are difficult and hence an expansion of the observational frequency range requires development of the coating technique.

There are many other improvements that must be made to expand the frequency range. The needed improvements that relate more directly to the optical design will be discussed in the next section.

6.2.2 Optical Design Frequency Expansion

In expanding the observational range to include lower frequencies, optical clearances within the design must be assessed carefully in order to reduce diffraction effects. The optical clearances are an added extra margin in radii or overall aperture size beyond the outermost geometric ray at each optical surface. For example, in a single lens system if the geometric ray used area of the lens surface extends to a radius of 10 cm, then with an optical clearance of 2 cm the lens would need to have a radius of 12 cm. This is needed because the effects of diffraction off optical aperture edges are much more severe at lower frequencies compared to higher frequencies. This is due to the longer characteristic wavelength as well as faster beam spreading at lower frequency.

This idea can be conceptualized using Gaussian beam optics. Based off equation 2.5, it can be seen that for the same beam waist the propagating beam size increases more quickly for lower frequencies. If a broad-band antenna is used in combination with a lenslet, the beam waist can be approximately the same size across each frequency at the focal plane. Hence the lower frequencies beams will be comparatively larger as they propagate through the optics and will theoretically be truncated at higher power at each optical aperture. The effects of diffraction scale with the power level at truncation analogous to the case illustrated in Figure 2.2. Thus the lower frequency detectors will be much more prone to diffraction ringing and spillover at each optical element.

In order to minimize the diffraction ringing and spillover effects for lower frequencies detectors more optical clearance must be given in the design. Because geometric rays do not account for diffraction or beam spreading effects, it is typical to design in anywhere between $1-5$ cm of extra radii at each optical element. The needed clearance will differ at every optical element and depend on the optical design itself, how much spillover the detectors can tolerate, and the frequencies of observation. Determining the extra margin is a complex problem that usually must be calculated through physical optics simulations of the entire optical design, and is difficult to analytically estimate in most cases. For POLARBEAR-2 with the inclusion of the 95 GHz detectors, much more margin was given for the design of each optical aperture with up to 5 cm for the Field lens.

In expanding the observational range to higher frequencies the DLFOV becomes the determining factor in an optical design. The Strehl ratio given by equation 2.8 decreases for higher frequencies at constant RMS wavefront error δ. Qualitatively this is because the effects of diffraction are smaller for higher frequencies. In terms of the instrument sky beam, the beam size of the higher frequency detectors are smaller which can also be observed in the size of the Airy pattern from equation 2.3. Therefore for the same amount of aberration the Strehl ratio decreases at higher frequencies because the Strehl ratio is a measure of the amplitude of aberrations relative to the effects of diffraction.

The Strehl ratio determines the size of the DLFOV which defines the FOV where the aberrations are subdominant to the diffraction effects. Hence the DLFOV size decreases for higher frequencies in the same optical design. Ideally the entire focal plane of detectors should be diffraction-limited so the number of detectors will become more limited at higher frequencies. Hence any optical design must be designed such that any DLFOV size requirement is met at the highest frequency. For Simons Array the expansion to higher frequencies with the same focal plane size requires an improvement in the DLFOV.

6.2.3 Redesign Motivation

The POLARBEAR-2 optics were initially designed primarily for optimal performance at 95 and 150 GHz, but also with possible use at 220 GHz. Because the Simons Array receivers were decided to span 95, 150, 220, and 280 GHz detectors, the original POLARBEAR-2 design was insufficient and required an upgraded optical design for improved optical performance across all frequencies. Therefore the second 95/150 GHz receiver and third 220/280 GHz receiver optical designs were modified to accommodate this.

The original Polarbear-2 optical design Strehl ratios across all frequencies are shown in Figure 6.14. It can be seen that for 95, 150, and 220 GHz, the entire 36 cm diameter focal plane is diffraction limited. But at 280 GHz the diffraction limited focal plane area is reduced to a 30 cm minor (X) and 35 cm major (Y) axes ellipse which is $\sim$ 19% smaller in area. This equates to a 4.5 degrees diameter DLFOV at 95, 150, and 220 GHz, and a 3.8 degrees minor (X) and 4.4 degrees major (Y) DLFOV at 280 GHz. Therefore it was determined that the

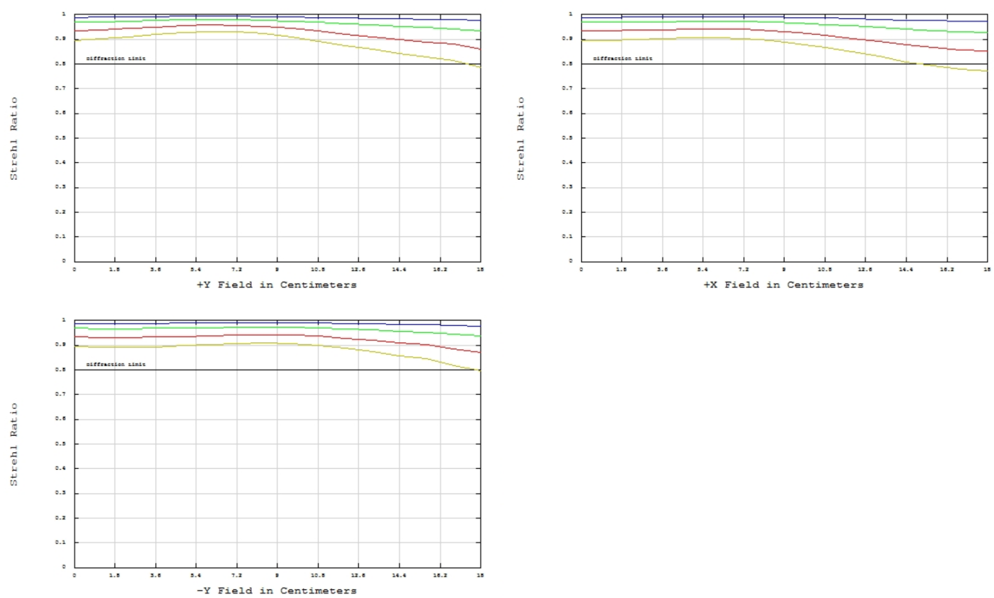

Figure 6.14: **Polarbear-2 Strehl ratio** — The Polarbear-2 Strehl ratios as a function of focal plane position in +Y (top left), -Y (bottom left), and +X (top right) are shown. The Polarbear-2 design is symmetric in ±X. The Strehl ratios for 95 (blue), 150 (green), 220 (red), and 280 (yellow) are shown. The diffraction limited line is plotted in black.

Simons Array receiver design must be improved to maximize the DLFOV for 280 GHz detectors as well. The original Polarbear-2 optical design is summarized in Figure 6.15, Table 6.1, and Table 6.2.

Alumina material, used for the refractive lenses, is made by packing and solidifying alumina powder. In the fabrication process of block alumina for the second and third Simons Array receivers, it was found that there was a large dependency of the index of refraction of the alumina to the batch it was made from. Therefore the batch of alumina purchased for these two receivers had a

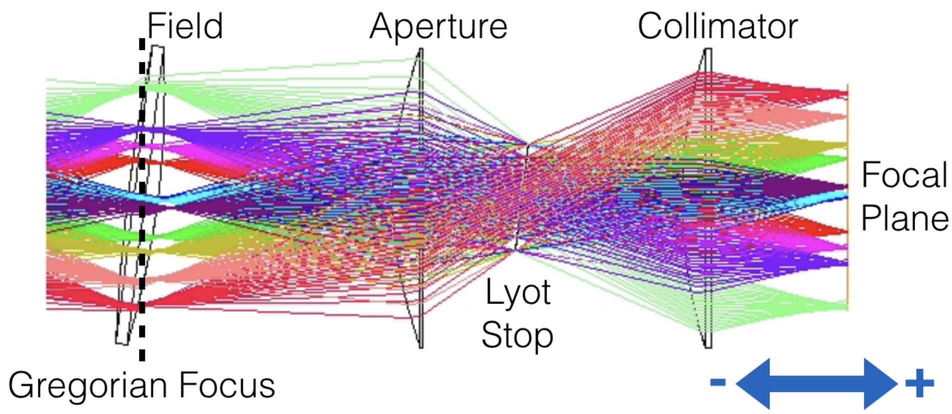

Figure 6.15: **POLARBEAR-2 re-imaging optics** — The POLARBEAR-2 re-imaging optics designs with labels for the Gregorian focus, lenses, Lyot stop, and focal plane is shown. Toward the secondary or sky-side is defined as negative and away from the secondary or focal plane side is defined as positive.

Table 6.1:: **POLARBEAR-2 re-imaging lenses** — The shapes of the re-imaging lenses for the POLARBEAR-2 design are shown. The lens center thickness, radius of curvature, and conic value for both surfaces are shown. Surface 1 (2) are the sky-side (focal plane side) surfaces of each lens.

		Surface 1		Surface 2	
Lens	Thickness (cm)	Radius (cm)	Conic	Radius (cm)	Conic
Collimator	5.000	82.637	0.000	Infinity	0.000
Aperture	5.000	63.233	-2.873	Infinity	0.000
Field	5.000	316.252	-10.026	136.683	-10.258

Table 6.2:: **POLARBEAR-2 optical element positions** — The positions of the focal plane, three lenses, and Lyot stop are shown. The positions are measured from to the Gregorian focus of the telescope to the sky-side surface 1 of each element in units of centimeters. The Field lens is placed approximately centered on the Gregorian and hence the sky-side surface 1 is in front of the Gregorian focus. Positive (negative) is defined as away from (toward) the secondary.

FP	Collimator	Lyot Stop	Aperture	Field
117.804	90.145	63.427	41.834	-2.299

slightly lower index of 3.1048 compared to the designed 3.15.

Theoretically a lower index of refraction decreases the focusing power of all the lenses and makes the optics slightly slower. This will significantly decrease the Strehl ratios to make the optics not diffraction limited even for 150 GHz. To a certain degree a lower index of refraction of all the lenses can be accounted for by pulling (pistoning) the entire receiver away from the secondary reflector. This is shown in Figure 6.16. In this case the indices of refraction of all the lenses are lowered to 3.1048 and the receiver is pulled away from the secondary by 1.707 cm. With this the Strehl ratios at all frequencies can be recovered above the diffraction

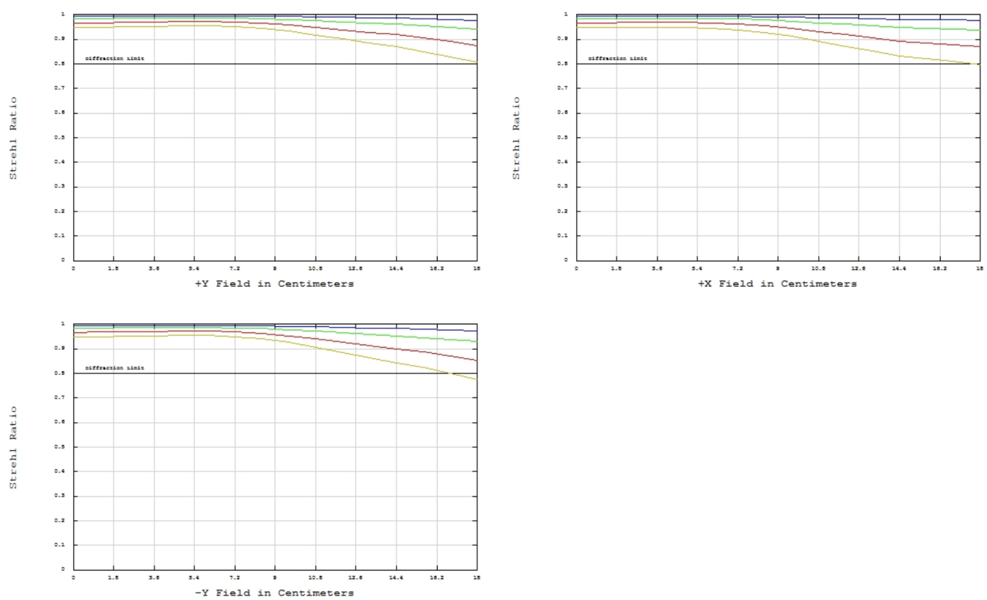

Figure 6.16: **POLARBEAR-2 with lower index and piston compensation** — Strehl ratios are shown for the 3.1048 index POLARBEAR-2 design with 1.707 cm piston away from the secondary used to recover Strehl values.

limit and slightly improve but 280 GHz is still not fully diffraction limited across the focal plane. But it was found that there is a noticeable degradation of the image at the Lyot stop as well as increased non-telecentricity of the optical focal plane. Pistoning cannot fix the issue entirely because each lens is curved and unique in shape.

A degradation of the Lyot image is apparent (in the forward time frame) as a variation of the geometric ray footprint image or illumination pattern on the primary as a function of FOV location. This can be seen in Figure 6.17. It was found that there was $\sim$ 6 cm more variation and difference in the illumination pattern from pixels on opposite sides of the focal plane compared to the original design. The illumination pattern between pixels are less overlapping on the primary and points to a noticeable degradation in the Lyot image. This creates larger variations in the beam shapes on the sky as a function of FOV position due to larger primary illumination pattern differences. The illumination pattern can change in size and become asymmetric which creates asymmetric sky beams.

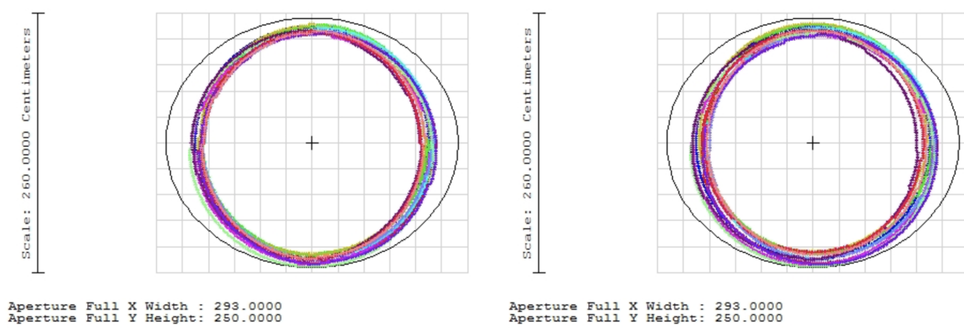

Figure 6.17: **Primary footprint variation** — The illumination pattern (footprint) on the primary for pixels across the focal are shown for the POLARBEAR-2 original (left) and the lower index with piston compensation (right) optics. The illumination variation increases by $\sim$ 6 cm in the lower index design and represents a Lyot image degradation.

It was also found that the telecentricity of the focal plane was worse compared to the original design as well. On average across the focal plane the telecentricity was worse by $\sim 0.6°$ with some locations of the focal plane being $> 1.0°$ worse. For these extreme position this is $\sim$ 60% more non-telecentric. This is shown in Figure 6.18. In the case of using flat focal plane detectors, higher degrees of optical non-telecentricity create differences in the beam truncation at the Lyot stop as a function of FOV. The original POLARBEAR-2 design is not completely telecentric and the lower index makes this noticeably worse.

In an ideal system with a telecentric optical focal plane, the Lyot stop will truncate each detector beam at the same power symmetrically. If the telecentricity across the optical focal plane deviates from normal incidence, then the beams of

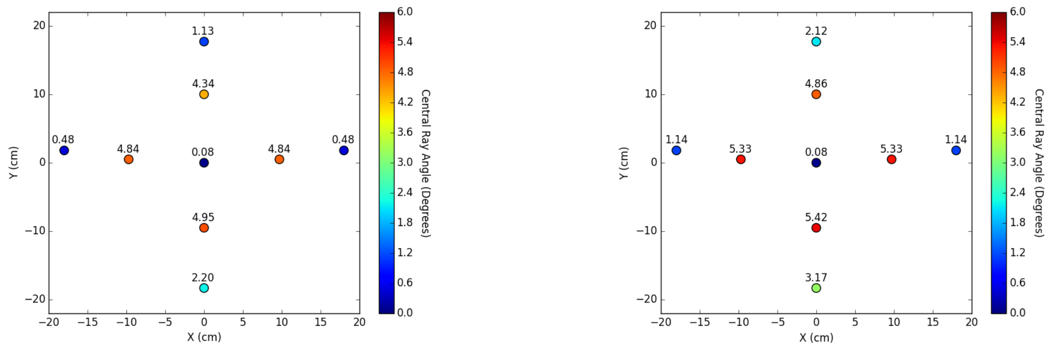

Figure 6.18: **Telecentricity at focal plane** — The degree of telecentricity at the focal plane for the POLARBEAR-2 original (left) and low index with piston compensation (right) optics is shown. The plot shows the deviation from normal incidence (in degrees) of the chief ray at the focal plane.

the detectors placed at focal plane locations where it does deviate will be truncated asymmetrically. Asymmetric truncation creates an asymmetric beam propagating through the optical system and asymmetric beams on the sky.

Thus degradation of the Lyot image and increased non-telecentricity are two different optical characteristics that have similar effects of making larger variations in beam shape across the FOV. The two in combination can potentially cause a complex relation between the sky beam shape and FOV position. The combined complex effect is difficult to assess analytically and can only be calculated through full physical optics simulations.

Focal plane piston is defined as the amount of change in the distance between the focal plane and the telescope Gregorian focus. In many cases allowing the focal plane piston to be free allows for greater freedom in the design. Typically shorter optical systems are more constraining due to necessitating higher focusing power lenses with more curvature.

In the case of POLARBEAR-2 there is a strong limitation due to the HTT structure. The volume of free space in the lower boom in which the receiver resides is limited especially toward the backside of the receiver due to structural support beams. Due to the large mechanical size of the POLARBEAR-2 receiver, extensions in length are not preferred and pistoning the entire receiver away from the secondary is severely limited to < 5 cm. It is preferential to leave as much space possible behind the receiver when considering the need for access, cable routing, and optical adjustments when aligning the receiver to the reflectors.

The Simons Array receivers include a HWP in front of each receiver for mitigation of systematics. HWPs are very high index sapphire flat plates that effectively slow down the optics at that location and require pistoning of the receiver to recover Strehl. It is estimated that the HWP (with filters) will possibly require up to ~ 1.5 cm of piston. Also the receiver window may be replaced with a higher index polyethylene window to reduce scattering for high frequency observations. A higher index window will also potentially need up to ~ 1 cm pistoning for correction. With these possibilities in mind, leaving as much space behind the receiver is preferential and using 1.707 cm of receiver piston for the lower index alumina is not ideal.

With these considerations, an optical redesign or modifications for the second and third Simons Array receivers was necessitated. In the redesign the lower index alumina had to be used, and the optical modifications were required to be minimal in the sense that any modified optical design must fit within the current POLARBEAR-2 receiver mechanical design. Therefore the redesign modifications were limited to reshaping of the Collimator lens, and modifications to the lens and Lyot stop positions. The Collimator redesign was chosen based off the fact that the the collimator lens was the only spherical lens and had a relatively high curvature. It was expected that modifications to the Collimator lens would comparatively be the most beneficial out of the three lenses.

6.2.4 Optical Criteria

It was required that any optical redesign should produce a new optical design that not only increases the DLFOV for 280 GHz but also sustains optical performance levels of the original POLARBEAR-2 design. Hence the optical redesign was based off 9 different optical criteria. These criteria are focal plane piston, Strehl ratio, focal plane telecentricity, Lyot image, primary illumination size, detector f-number, focal plane plate scale, Aperture lens clearance, and Collimator lens clearance.

The focal plane piston, Strehl ratio, focal plane telecentricity, and Lyot image are as explained in section 6.2.3. It was found that the focal plane within the receiver could be mechanically moved back ~ 1 cm without interference with the cryogenic shells. This allows the optical length to slightly increase without having to piston the entire receiver back in the lower boom. Hence the focal plane pistoning was required to be ≤ 1 cm.

The new design is required to enhance the 280 GHz DLFOV to span close to the entire 4.5 degree diameter FOV of the instrument. The focal plane telecentricity and Lyot image quality are required to be also similar to that of the POLARBEAR-2 design. The telecentricity will be calculated from taking the average difference in incident angles of the chief rays across the FOV compared to the POLARBEAR-2 design. The Lyot stop image quality will be evaluated as the variation of the primary illumination footprint across the FOV. The maximum variation or spread of the footprints was used as the comparison criteria.

The primary illumination size for the center pixel was also used as a criteria. The illumination size was approximated by the geometric ray footprint on the primary. A decrease in illumination size equates to a degradation in sky resolution and thus it was required that the primary illumination size does not significantly change compared to POLARBEAR-2.

Detector f-number and the focal plane plate scale are related optical characteristics. The detector f-number is just the optical f-number at the focal plane. Because POLARBEAR-2 is designed such that the optical design and sinuous antenna detectors couple efficiently, it was required that the f-number at the focal plane also stays approximately the same at $f \sim 1.8$ in the new design using the same detector technology. The plate scale relates the angular separation of the FOV to the spatial separation on the focal plane. Hence it is a measure of the angular FOV per focal plane size. In this case the focal plane size must remain the same as POLARBEAR-2 at 36 cm in diameter. Thus the 4.5 degree diameter FOV must approximately couple to this size. The focal plane size scales as the detector f-number and hence requiring a similar f-number approximately equates to a similar plate scale.

The Aperture and Collimator lens clearances are as explained in section 6.2.2 and is important for the lower frequency of 95 GHz for the second receiver. The Field lens clearances in the POLARBEAR-2 design were taken very conservatively with an extra 5 cm radii because the Field lens is placed approximately at the telescope Gregorian focus. The diffraction ringing at optical foci are the strongest and hence extra clearance was designed. Limiting the piston motion of the focal plane naturally keeps the Field lens clearance under control because the Gregorian focus field stop does not change in size.

Because the f-number of the POLARBEAR-2 system is approximately the same at Gregorian and focal plane focus, it is expected that field and aperture stop locations will be smaller in size than intermediate locations where the rays are diverging or converging. There was a mechanical limitation in the size of the lenses to 50 cm diameter. The diffraction ringing will be lower in power but the ray footprints will be larger at the Aperture and Collimator lenses which are not at an aperture or field stop. Hence in optimizing the POLARBEAR-2 design the optical clearances for the Aperture and Collimator lenses were chosen to be approximately only an extra 2 cm in radii. The clearances at the Aperture and Collimator are much more stringent and was also used as a design criteria.

6.2.5 Optical Redesign

The optical redesign optimization was performed using the optical design software ZEMAX using geometric ray tracing. The alumina index was assumed to be the lower index 3.1048 in the redesign for all lenses as well. A custom merit function optimizing the above 9 design criteria was created, and the optimization minimized the geometric ray spot size across the focal plane for a forward time ray trace model with the Collimator lens radius, conic, thickness, and all lens and Lyot stop positions as variables. A table comparing the values of the design criteria for various cases can be found in Tables 6.3 and 6.4. The three compared cases are the original POLARBEAR-2 design, the POLARBEAR-2 design with the lower index 3.1048 and piston compensation, and the new Simons Array redesign.

It can be seen that the POLARBEAR-2 design with a lower index of refraction

Table 6.3:: Optical design criteria comparison #1 — A table comparing the values for the focal plane piston, diffraction limited focal plane area (at 280 GHz), focal plane telecentricity, primary spread (Lyot image performance), and primary illumination size are shown for the POLARBEAR-2 design, POLARBEAR-2 design with lower index and piston (labeled "lower index"), and the new Simons Array redesign. For the telecentricity average difference, a positive value means less telecentricity compared to POLARBEAR-2.

Model	FP Piston (cm)	DL Area (cm^2)	Telecentricity AVG Diff (°)	Primary Spread (cm)	Primary Size (cm)
POLARBEAR-2	-	3298.67	-	13.126	232.734
Lower Index	+1.707	3887.47	+0.583	19.121	232.734
Redesign	+1.004	3854.67	+0.165	13.231	234.711

Table 6.4:: Optical design criteria comparison #2 — A table comparing the values for the detector f-number, focal plane plate scale, Aperture lens clearance, and Collimator lens clearance are shown for the POLARBEAR-2 design, POLARBEAR-2 design with lower index and piston (labeled "lower index"), and the new Simons Array redesign. The focal plane plate scale here is the size of the focal plane at a constant 4.5 degree diameter FOV.

Model	Detector f-number	FP Plate Scale (cm)	Aperture Edge Ray (cm)	Collimator Edge Ray (cm)
POLARBEAR-2	1.792	35.965	23.056	22.430
Lower Index	1.810	36.501	23.373	22.352
Redesign	1.788	35.726	23.609	23.187

Table 6.5:: Collimator lens redesign — The changes to the Collimator (plano-convex) lens compared to the POLARBEAR-2 design are shown. The values for the center thickness of the lens, radius of curvature, and conic constant are listed. The flat side of the lens was unchanged.

Model	Thickness (cm)	Radius (cm)	Conic
POLARBEAR-2	5.000	82.637	0.000
Redesign	4.464	79.986	-0.3898

Table 6.6:: Optical element position redesign — The relative changes in positions of all the optical elements are shown for the new redesign. All relative positions are in cm with positive directions away from the Gregorian focus and secondary.

Model	FP Piston	Collimator	Lyot Stop	Aperture	Field
Redesign	+1.004	-0.166	+0.787	-0.533	+0.215

and piston compensation has a larger diffraction limited focal plane area for 280 GHz but does much worse in terms of focal plane piston, telecentricity, and Lyot image compared to the POLARBEAR-2 design. In the particular case for this lower index design the focal plane piston is moving the entire refractive optics away from the secondary while keeping relative distances between refractive elements and the focal plane constant.

The new Simons Array optical redesign consists of a slightly more curved Collimator lens with an elliptical surface. The thickness is also reduced by $\sim 10\%$. The relative distance between all the lenses, Lyot stop, focal plane were moved from 1.66 mm up to $\sim$ 1 cm. These adjustments are small enough to not necessitate any changes to the POLARBEAR-2 mechanical design. In total the focal plane was moved away from the Gregorian focus by 1.004 cm. The redesign values are summarized in Tables 6.5 and 6.6.

The new redesign has a $\sim 16\%$ larger diffraction limited focal plane area compared to POLARBEAR-2 at 280 GHz. The Strehl ratios across the focal plane are on average larger in the new redesign for all frequencies as shown in Figures 6.19 and 6.20. The new redesign also sustains other design criteria to the level approximately of the POLARBEAR-2 design as well except for slightly reducing the clearances by 5.5 mm and 7.6 mm for the Aperture and Collimator lenses

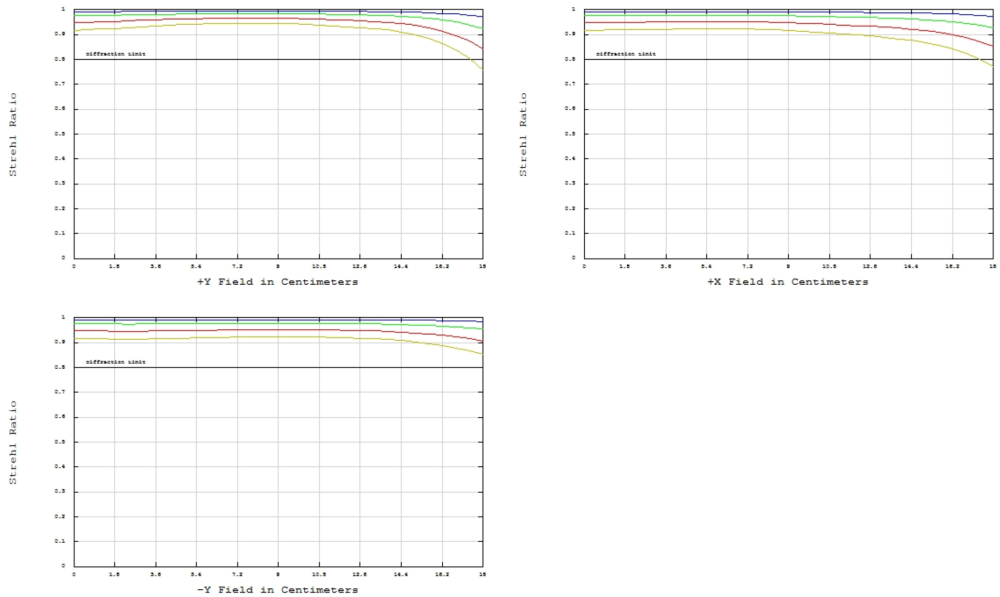

Figure 6.19: **Simons Array redesign Strehl ratios** — The Strehl ratios as a function of the focal plane position is shown for the redesign.

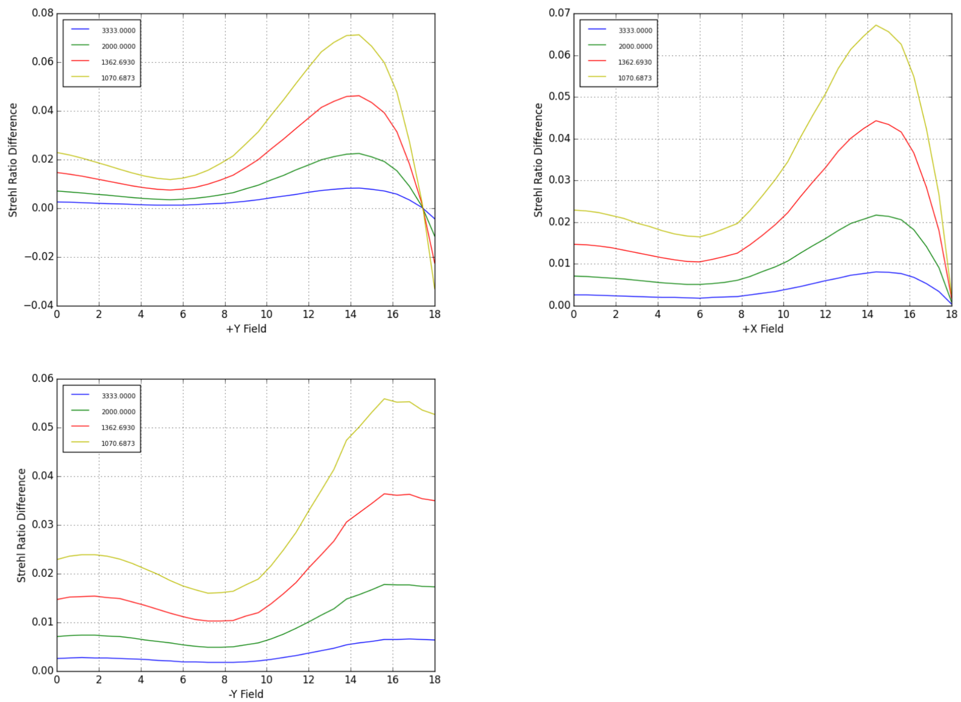

Figure 6.20: **Strehl comparison: POLARBEAR-2 and redesign** — The difference in Strehl ratio values as a function of focal plane position between Simons Array redesign and POLARBEAR-2 is shown. The difference is the redesign values minus the POLARBEAR-2 values.

respectively. From ZEMAX physical optics simulations it was found that this reduction in the clearances equated only to a 0.12% and 2.20% larger spillover at 95 GHz at the Aperture and Collimator lens apertures for the extreme edge pixel where the effect is expected to be the largest. This spillover increase is found to be sufficiently small because the lenses are contained in a 4 K environment. Results from the simulation are shown in Figure 6.21.

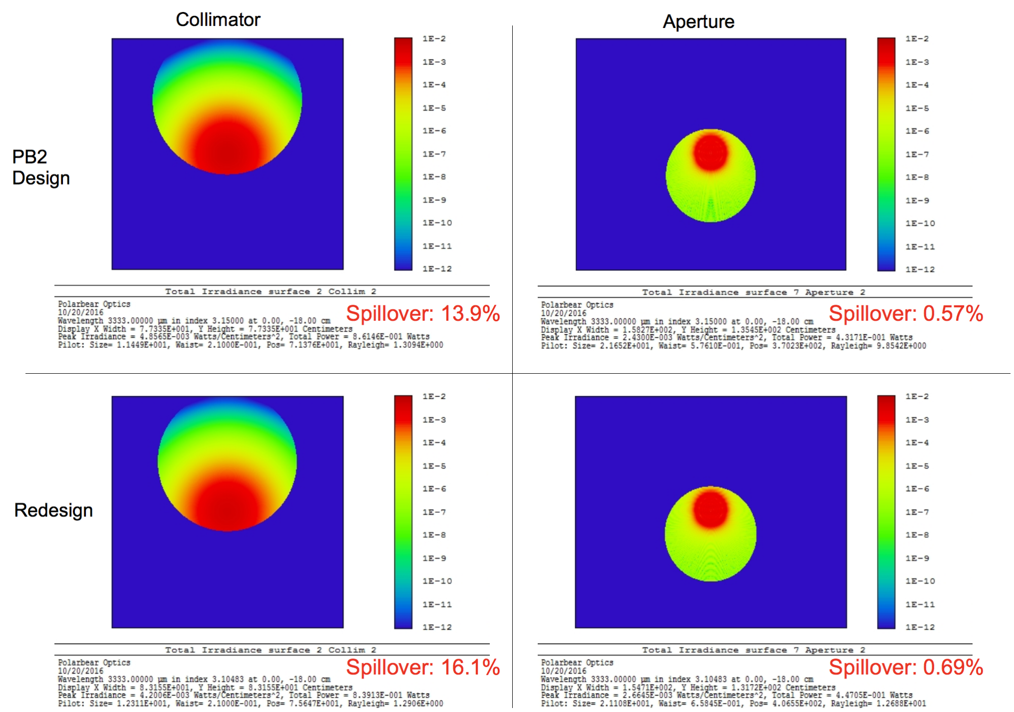

Figure 6.21: **Physical optics simulation of Aperture and Collimator lens spillover** — The spillover plots for the POLARBEAR-2 (top row) and redesign (bottom row) are shown. Physical optics simulations at 95 GHz are shown at the Aperture (right) and Collimator lenses (left) with the spillover value in red.

The diffraction ringing power increase due to the smaller clearance on the Aperture lens was found to be negligible. For the Collimator lens there was $\sim 3.7\%$ increase in total power from the diffraction ringing in the main beam at the Lyot aperture for this edge pixel, but this was also found to be a negligible effect in the beams and spillover at subsequent surfaces (reverse time) and at the sky. This is predominantly due to the fact that the Lyot stop diffraction effect right after the Collimator lens largely dominates over the ringing caused by the Collimator lens at 95 GHz. The Lyot stop truncates approximately half the beam power at 95 GHz. Hence the Lyot diffraction effects are >3 times larger in power.

The focal plane size at a 4.5 degree diameter FOV was found to be 2.39 mm smaller for the redesign compared to POLARBEAR-2 but this effect is optically very small because it is smaller in size than one pixel spacing. The diffraction limited focal plane area for 280 GHz is in fact larger in area than POLARBEAR-2 and hence the number of diffraction limited detectors at 280 GHz is far larger for the new redesign. For the other three frequencies the diffraction limited area extends beyond the physical focal plane size and therefore is no issue. This just means that the DLFOV for the lower frequencies is slightly larger than 4.5 degree diameter FOV by a very small amount.

The true effect of the focal plane telecentricity in relation to the Lyot stop image quality cannot be assess by geometric ray tracing alone and requires physical optics simulations. Thus ZEMAX physical optics simulations were used to assess the impact on the Lyot truncation from the telecentricity and Lyot image. Ideally the Lyot stop should truncate each beam across the focal plane symmetrically.

It was found that the Lyot truncation at 95 GHz for the center pixel was found to be approximately similar between the new Simons Array redesign and the POLARBEAR-2 design. The Lyot truncation for pixels located at focal plane radii of ~ 9 cm were slightly more asymmetric in the redesign, but the truncation level only was $\sim 1\%$ more asymmetric and very small. For the pixels at the far edges of the focal plane, it was found that the redesign truncated more symmetrically than the POLARBEAR-2 design. These results can be seen in Figure 6.22. Therefore it was found that the telecentricity being very slightly worse ($+0.165°$) in the redesign has only a small impact when combined with the good Lyot image quality.

Overall the new Simons Array optical redesign has Strehl ratios $1-7\%$ higher across the focal plane compared to POLARBEAR-2 for all frequencies. The DLFOV is also increased $\sim 16\%$ at 280 GHz. This equates to a similar 4.5 degrees diameter DLFOV at 95, 150, and 220 GHz, but a larger 4.2 degrees minor (X) and 4.5 degrees major (Y) DLFOV at 280 GHz. Even though the clearances for the Aperture and Collimator lenses are slightly smaller, the increased diffraction effect

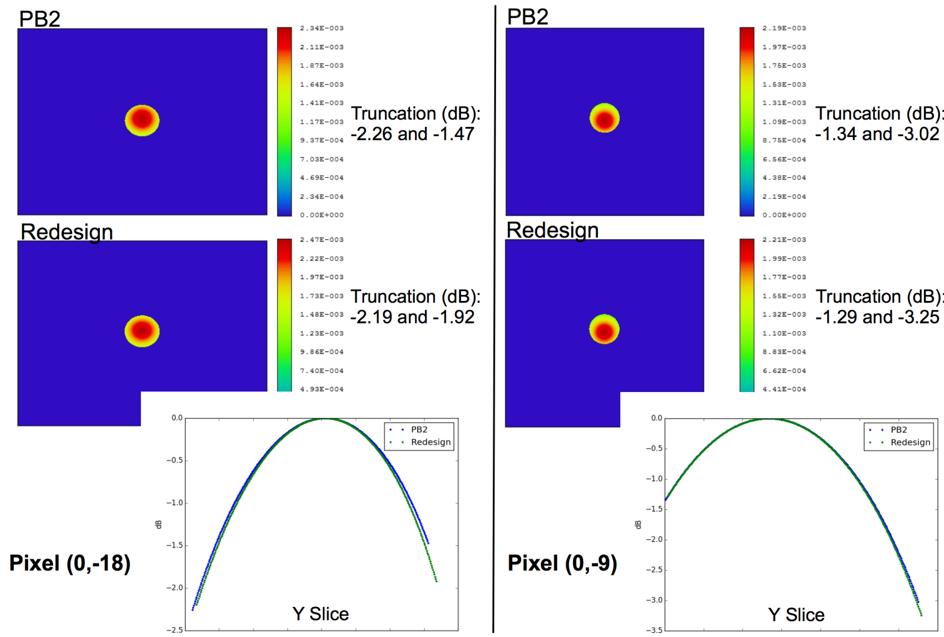

Figure 6.22: **Physical optics simulations of Lyot stop** — Plots of the beam truncation at Lyot stop at 95 GHz are shown for POLARBEAR-2 (top row) and new redesign (bottom row). The results for the pixels located -18 cm (left) and -9 cm (right) in Y from the focal plane center are shown. The Y -18 cm pixel is the edge most focal plane pixel. Y slices of the simulated beams are also plotted, and the truncation values are written.

was determined to be small even for the extreme edge pixels where the effect is greatest. The focal plane piston was increased $\sim$ 1 cm in length but this motion is mechanically possible within the receiver and does not require any motion of the entire receiver.

This new optical redesign enhances the optical performance for high frequency observations compared to POLARBEAR-2 while accommodating for the lower alumina index and sustaining the optical performance levels of the other design criteria across all four frequencies. This new redesign is an improved design over POLARBEAR-2 in terms of DLFOV and is planned to be implemented for the second and third Simons Array receivers in order to improve sky sensitivities substantially.

Chapter 7

Future CMB Research

7.1 Current CMB Measurements

Due to the faint CMB polarization B-mode signal, for a long time only upper limits had been measured by countless CMB experiments. Just recently since 2014, various experiments including POLARBEAR published results on measurements of the B-mode spectrum, and have proved that current generation experiments are technologically sensitive enough to detect B-modes from the CMB. A plot of the past and current B-mode measurements is shown in Figure 7.1

Only the lensing B-modes have currently been measured by multiple experiments observing various patches of the CMB sky. The current best upper limit on the primordial signal and tensor-to-scalar ratio r is given by the BICEP and Keck Array experiment in combination with Planck and WMAP data [20] at $r < 0.09$ at the 95% confidence level. This measurement was largely limited by the foreground dust contamination of which the physics is still not understood in detail.

Current estimates of the foreground contamination rely heavily on the Planck 353 GHz full sky maps, but because many of the dust models are to an extent unproven, direct measurements have become much more important to characterize the foregrounds. The recent B-mode measurements have put greater focus in measuring foregrounds as well by expanding the observation frequencies to multiple bands.

Next generations experiments such as the Simons Array, SPT-3G [71], Ad-

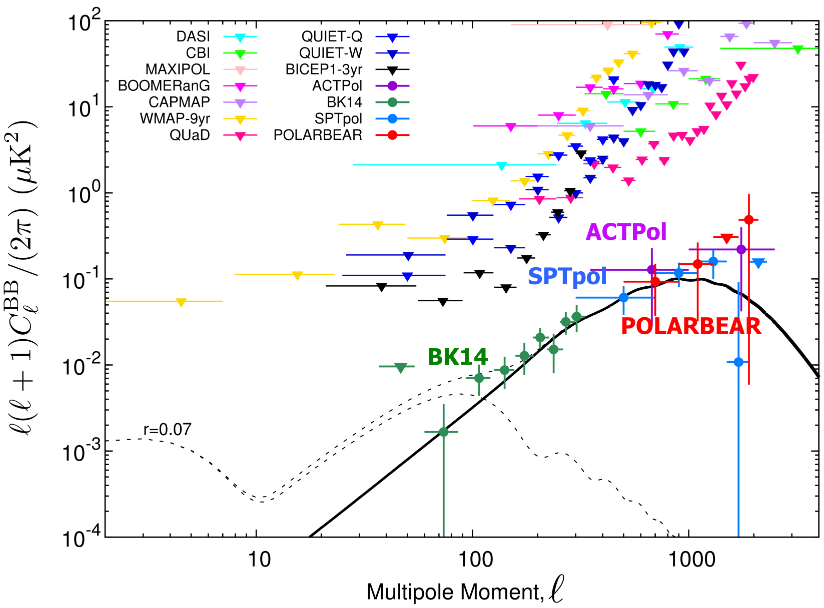

Figure 7.1: **Current CMB B-mode power spectrum measurements** — The published measurements of the C_ℓ^{BB} spectrum as of May 2017 are shown [38, 21, 24, 23]. The upper limits published by CMB experiments before 2014 are also plotted. This plot is provided by Yuji Chinone.

vACT [72], CLASS [73], and BICEP3 [74] have recently started or are planned to start full observations within the next few years. Many of these experiments observe at multiple frequencies similar to Simons Array in order to measure the CMB polarization and foregrounds at high sensitivities. The CMB field as a whole has evolved to observing with large numbers of detectors to improve sensitivities and these generations have orders of 10^4 detectors. These experiments are all expected to greatly constrain cosmology for measuring parameters such as r, $\sum_\nu m_\nu$, and N_{eff}. Further generation experiments have already started with the aim to further understand the physics of the current universe.

7.2 Simons Observatory

Simons Observatory is a 2016 newly funded experiment and collaboration between CMB experiments in Chile including Simons Array and ACT, and is pursuing further CMB science and technological development toward next generation experiments. The experiment is in the early development stages of designing and proposing new potential ground-based telescopes that range from 1 m scale small aperture telescopes to a few meter scale large aperture telescopes. In the next few years, Simons Observatory is aiming to develop a combination of these telescopes that will observe the sky across many frequencies with close to an order of 10^5 detectors. Simons Observatory will achieve improved sensitivities at high sky resolutions that are currently technologically difficult to obtain with satellite missions. Simons Observatory will be the next generation of current ground-based CMB telescopes, and is planned to lead into the future CMB Stage-4 experiment.

7.3 Future Outlook

The CMB field is continuously advancing, and preparation for future experiments have already started. Two of the largest and most promising potential future instruments are the CMB Stage-4 and LiteBIRD experiments.

CMB Stage-4 is expected to be the one of largest goals of the ground-based CMB community as a whole, and is expected to make definitive statements for cosmology through pursuing ultimate limits on sensitivities from the ground [75]. Current generation experiments and Simons Observatory are all leading into CMB Stage-4 through collaborative efforts between the various groups. CMB Stage-4 is targeted to reach sensitivities of $\sigma(r) = 0.0005$, $\sigma(\sum_\nu m_\nu) = 15$ meV, and $\sigma(N_{eff}) = 0.027$ which will require on the order of 10^6 detectors. CMB Stage-4 can potentially put constraints on the tensor spectral index parameter n_t. CMB Stage-4 is planned to start development in 2020.

LiteBIRD is a proposed international CMB polarization satellite experiment in development, lead by JAXA [70]. The instrument will orbit at the L2 Lagrange point and observe the full CMB sky for 3 years. The Simons Array receivers are pathfinders for LiteBIRD because the same multi-chroic detector technologies are planned to be used. LiteBIRD can accommodate up to 15 frequency bands covering the range from 40 to 235 GHz in the Low-Frequency Telescope (LFT) and from 280 to 402 GHz in the High- Frequency Telescope (HFT) which are installed side-by-side. This satellite is expected to reach sensitivities for $\sigma(r) = 0.001$, and be able to measure deep full sky CMB and foreground maps across frequencies ranges wider than any CMB instrument on the ground. The satellite is aimed to deploy in the late 2020s.

The CMB field is constantly evolving with current experiments such as the POLARBEAR and Simons Array starting a new era in direct CMB polarization measurements. The B-mode measurements will continue to improve in the coming decade, and these measurements have great promise in uncovering the physics of the current universe and the inflationary ΛCDM cosmological model.

7.4 Acknowledgements

Figure 7.1 was provided by Yuji Chinone. The dissertation author made essential contributions to many aspects of this work.

References

[1] Dodelson, S., [*Modern cosmology*], Academic press (2003).

[2] Lachièze-Rey, M. and Luminet, J.-P., "Cosmic topology," *Physics Reports* **254**(3), 135 – 214 (1995).

[3] Hubble, E., "A relation between distance and radial velocity among extra-galactic nebulae," *Proceedings of the National Academy of Sciences* **15**(3), 168–173 (1929).

[4] Alpher, R. A., Bethe, H., and Gamow, G., "The origin of chemical elements," *Physical Review* **73**(7), 803 (1948).

[5] Dicke, R. H., Peebles, P. J. E., Roll, P. G., and Wilkinson, D. T., "Cosmic black-body radiation.," *The Astrophysical Journal* **142**, 414–419 (1965).

[6] Planck Collaboration, Ade, P. A. R., Aghanim, N., Arnaud, M., Ashdown, M., Aumont, J., Baccigalupi, C., Banday, A. J., Barreiro, R. B., Bartlett, J. G., Bartolo, N., Battaner, E., Battye, R., Benabed, K., Benoît, A., Benoit-Lévy, A., Bernard, J.-P., Bersanelli, M., Bielewicz, P., Bock, J. J., Bonaldi, A., Bonavera, L., Bond, J. R., Borrill, J., Bouchet, F. R., Boulanger, F., Bucher, M., Burigana, C., Butler, R. C., Calabrese, E., Cardoso, J.-F., Catalano, A., Challinor, A., Chamballu, A., Chary, R.-R., Chiang, H. C., Chluba, J., Christensen, P. R., Church, S., Clements, D. L., Colombi, S., Colombo, L. P. L., Combet, C., Coulais, A., Crill, B. P., Curto, A., Cuttaia, F., Danese, L., Davies, R. D., Davis, R. J., de Bernardis, P., de Rosa, A., de Zotti, G., Delabrouille, J., Désert, F.-X., Di Valentino, E., Dickinson, C., Diego, J. M., Dolag, K., Dole, H., Donzelli, S., Doré, O., Douspis, M., Ducout, A., Dunkley, J., Dupac, X., Efstathiou, G., Elsner, F., Enßlin, T. A., Eriksen, H. K., Farhang, M., Fergusson, J., Finelli, F., Forni, O., Frailis, M., Fraisse, A. A., Franceschi, E., Frejsel, A., Galeotta, S., Galli, S., Ganga, K., Gauthier, C., Gerbino, M., Ghosh, T., Giard, M., Giraud-Héraud, Y., Giusarma, E., Gjerløw, E., González-Nuevo, J., Górski, K. M., Gratton, S., Gregorio, A., Gruppuso, A., Gudmundsson, J. E., Hamann, J., Hansen, F. K., Hanson, D., Harrison, D. L., Helou, G., Henrot-Versillé, S., Hernández-Monteagudo, C., Herranz, D., Hildebrandt, S. R., Hivon, E., Hobson, M., Holmes, W. A., Horn-

strup, A., Hovest, W., Huang, Z., Huffenberger, K. M., Hurier, G., Jaffe, A. H., Jaffe, T. R., Jones, W. C., Juvela, M., Keihänen, E., Keskitalo, R., Kisner, T. S., Kneissl, R., Knoche, J., Knox, L., Kunz, M., Kurki-Suonio, H., Lagache, G., Lähteenmäki, A., Lamarre, J.-M., Lasenby, A., Lattanzi, M., Lawrence, C. R., Leahy, J. P., Leonardi, R., Lesgourgues, J., Levrier, F., Lewis, A., Liguori, M., Lilje, P. B., Linden-Vørnle, M., López-Caniego, M., Lubin, P. M., Macías-Pérez, J. F., Maggio, G., Maino, D., Mandolesi, N., Mangilli, A., Marchini, A., Maris, M., Martin, P. G., Martinelli, M., Martínez-González, E., Masi, S., Matarrese, S., McGehee, P., Meinhold, P. R., Melchiorri, A., Melin, J.-B., Mendes, L., Mennella, A., Migliaccio, M., Millea, M., Mitra, S., Miville-Deschênes, M.-A., Moneti, A., Montier, L., Morgante, G., Mortlock, D., Moss, A., Munshi, D., Murphy, J. A., Naselsky, P., Nati, F., Natoli, P., Netterfield, C. B., Nørgaard-Nielsen, H. U., Noviello, F., Novikov, D., Novikov, I., Oxborrow, C. A., Paci, F., Pagano, L., Pajot, F., Paladini, R., Paoletti, D., Partridge, B., Pasian, F., Patanchon, G., Pearson, T. J., Perdereau, O., Perotto, L., Perrotta, F., Pettorino, V., Piacentini, F., Piat, M., Pierpaoli, E., Pietrobon, D., Plaszczynski, S., Pointecouteau, E., Polenta, G., Popa, L., Pratt, G. W., Prézeau, G., Prunet, S., Puget, J.-L., Rachen, J. P., Reach, W. T., Rebolo, R., Reinecke, M., Remazeilles, M., Renault, C., Renzi, A., Ristorcelli, I., Rocha, G., Rosset, C., Rossetti, M., Roudier, G., Rouillé d'Orfeuil, B., Rowan-Robinson, M., Rubiño-Martín, J. A., Rusholme, B., Said, N., Salvatelli, V., Salvati, L., Sandri, M., Santos, D., Savelainen, M., Savini, G., Scott, D., Seiffert, M. D., Serra, P., Shellard, E. P. S., Spencer, L. D., Spinelli, M., Stolyarov, V., Stompor, R., Sudiwala, R., Sunyaev, R., Sutton, D., Suur-Uski, A.-S., Sygnet, J.-F., Tauber, J. A., Terenzi, L., Toffolatti, L., Tomasi, M., Tristram, M., Trombetti, T., Tucci, M., Tuovinen, J., Türler, M., Umana, G., Valenziano, L., Valiviita, J., Van Tent, F., Vielva, P., Villa, F., Wade, L. A., Wandelt, B. D., Wehus, I. K., White, M., White, S. D. M., Wilkinson, A., Yvon, D., Zacchei, A., and Zonca, A., "Planck 2015 results - xiii. cosmological parameters," *A&A* **594**, A13 (2016).

[7] Penzias, A. A. and Wilson, R. W., "A measurement of excess antenna temperature at 4080 mc/s.," *The Astrophysical Journal* **142**, 419–421 (1965).

[8] Gamow, G. et al., "The evolution of the universe," *Nature* **162**(4122), 680–682 (1948).

[9] Smoot, G. F., Bennett, C. L., Kogut, A., Wright, E. L., Aymon, J., Boggess, N. W., Cheng, E. S., de Amici, G., Gulkis, S., Hauser, M. G., Hinshaw, G., Jackson, P. D., Janssen, M., Kaita, E., Kelsall, T., Keegstra, P., Lineweaver, C., Loewenstein, K., Lubin, P., Mather, J., Meyer, S. S., Moseley, S. H., Murdock, T., Rokke, L., Silverberg, R. F., Tenorio, L., Weiss, R., and Wilkinson, D. T., "Structure in the COBE differential microwave radiometer first-year maps," *ApJL* **396**, L1–L5 (Sept. 1992).

[10] Mather, J. C., Cheng, E. S., Cottingham, D. A., Eplee, Jr., R. E., Fixsen, D. J., Hewagama, T., Isaacman, R. B., Jensen, K. A., Meyer, S. S., Noerdlinger, P. D., Read, S. M., Rosen, L. P., Shafer, R. A., Wright, E. L., Bennett, C. L., Boggess, N. W., Hauser, M. G., Kelsall, T., Moseley, Jr., S. H., Silverberg, R. F., Smoot, G. F., Weiss, R., and Wilkinson, D. T., "Measurement of the cosmic microwave background spectrum by the COBE FIRAS instrument," *ApJ* **420**, 439–444 (Jan. 1994).

[11] Fixsen, D. J. and Mather, J. C., "The spectral results of the far-infrared absolute spectrophotometer instrument on cobe," *The Astrophysical Journal* **581**(2), 817 (2002).

[12] Bennett, C. L., Larson, D., Weiland, J. L., Jarosik, N., Hinshaw, G., Odegard, N., Smith, K. M., Hill, R. S., Gold, B., Halpern, M., Komatsu, E., Nolta, M. R., Page, L., Spergel, D. N., Wollack, E., Dunkley, J., Kogut, A., Limon, M., Meyer, S. S., Tucker, G. S., and Wright, E. L., "Nine-year wilkinson microwave anisotropy probe (wmap) observations: Final maps and results," *The Astrophysical Journal Supplement Series* **208**(2), 20 (2013).

[13] Planck Collaboration, Adam, R., Ade, P. A. R., Aghanim, N., Akrami, Y., Alves, M. I. R., Argüeso, F., Arnaud, M., Arroja, F., Ashdown, M., and et al., "Planck 2015 results. I. Overview of products and scientific results," *A&A* **594**, A1 (Sept. 2016).

[14] Story, K. T., Reichardt, C. L., Hou, Z., Keisler, R., Aird, K. A., Benson, B. A., Bleem, L. E., Carlstrom, J. E., Chang, C. L., Cho, H.-M., Crawford, T. M., Crites, A. T., de Haan, T., Dobbs, M. A., Dudley, J., Follin, B., George, E. M., Halverson, N. W., Holder, G. P., Holzapfel, W. L., Hoover, S., Hrubes, J. D., Joy, M., Knox, L., Lee, A. T., Leitch, E. M., Lueker, M., Luong-Van, D., McMahon, J. J., Mehl, J., Meyer, S. S., Millea, M., Mohr, J. J., Montroy, T. E., Padin, S., Plagge, T., Pryke, C., Ruhl, J. E., Sayre, J. T., Schaffer, K. K., Shaw, L., Shirokoff, E., Spieler, H. G., Staniszewski, Z., Stark, A. A., van Engelen, A., Vanderlinde, K., Vieira, J. D., Williamson, R., and Zahn, O., "A measurement of the cosmic microwave background damping tail from the 2500-square-degree spt-sz survey," *The Astrophysical Journal* **779**(1), 86 (2013).

[15] Das, S., Marriage, T., Ade, P., Aguirre, P., Amiri, M., Appel, J., Barrientos, L., Battistelli, E., Bond, J., Brown, B., Burger, B., Chervenak, J., Devlin, M., Dicker, S., Doriese, W., Dunkley, J., Dünner, R., Essinger-Hileman, T., Fisher, R., Fowler, J., Hajian, A., Halpern, M., Hasselfield, M., Hernndez-Monteagudo, C., Hilton, G., Hilton, M., Hincks, A., Hlozek, R., Huffenberger, K., Hughes, D., Hughes, J., Infante, L., Irwin, K., Juin, J., Kaul, M., Klein, J., Kosowsky, A., Lau, J., Limon, M., Lin, Y., Lupton, R., Marsden, D.,

Martocci, K., Mauskopf, P., Menanteau, F., Moodley, K., Moseley, H., Netterfield, C., Niemack, M., Nolta, M., Page, L., Parker, L., Partridge, B., Reid, B., Sehgal, N., Sherwin, B., Sievers, J., Spergel, D., Staggs, S., Swetz, D., Switzer, E., Thornton, R., Trac, H., Tucker, C., Warne, R., Wollack, E., and Zhao, Y., "The atacama cosmology telescope: A measurement of the cosmic microwave background power spectrum at 148 and 218 ghz from the 2008 southern survey," *Astrophysical Journal* **729** (3 2011).

[16] Fixsen, D. J., "The temperature of the cosmic microwave background," *The Astrophysical Journal* **707**(2), 916 (2009).

[17] Lewis, A., Challinor, A., and Lasenby, A., "Efficient computation of cosmic microwave background anisotropies in closed friedmann-robertson-walker models," *The Astrophysical Journal* **538**(2), 473 (2000).

[18] Sachs, R. K. and Wolfe, A. M., "Perturbations of a Cosmological Model and Angular Variations of the Microwave Background," *ApJ* **147**, 73 (Jan. 1967).

[19] Nagy, J. M., Ade, P. A. R., Amiri, M., Benton, S. J., Bergman, A. S., Bock, J. J., Bond, J. R., Bryan, S. A., Chiang, H. C., Contaldi, C. R., Dore, O., Duivenvoorden, A. J., Eriksen, H. K., Farhang, M., Filippini, J. P., Fissel, L. M., Fraisse, A. A., Freese, K., Galloway, M., Gambrel, A. E., Gandilo, N. N., Ganga, K., Gudmundsson, J. E., Halpern, M., Hartley, J., Hasselfield, M., Hilton, G., Holmes, W., Hristov, V. V., Huang, Z., Irwin, K. D., Jones, W. C., Kuo, C. L., Kermish, Z. D., Li, S., Mason, P. V., Megerian, K., Moncelsi, L., Morford, T. A., Netterfield, C. B., Nolta, M., Padilla, I. L., Racine, B., Rahlin, A. S., Reintsema, C., Ruhl, J. E., Runyan, M. C., Ruud, T. M., Shariff, J. A., Soler, J. D., Song, X., Trangsrud, A., Tucker, C., Tucker, R. S., Turner, A. D., van der List, J. F., Weber, A. C., Wehus, I. K., Wiebe, D. V., and Young, E. Y., "A New Limit on CMB Circular Polarization from SPIDER," *ArXiv e-prints* (Apr. 2017).

[20] Ade, P. A. R., Ahmed, Z., Aikin, R. W., Alexander, K. D., Barkats, D., Benton, S. J., Bischoff, C. A., Bock, J. J., Bowens-Rubin, R., Brevik, J. A., Buder, I., Bullock, E., Buza, V., Connors, J., Crill, B. P., Duband, L., Dvorkin, C., Filippini, J. P., Fliescher, S., Grayson, J., Halpern, M., Harrison, S., Hilton, G. C., Hui, H., Irwin, K. D., Karkare, K. S., Karpel, E., Kaufman, J. P., Keating, B. G., Kefeli, S., Kernasovskiy, S. A., Kovac, J. M., Kuo, C. L., Leitch, E. M., Lueker, M., Megerian, K. G., Netterfield, C. B., Nguyen, H. T., O'Brient, R., Ogburn, R. W., Orlando, A., Pryke, C., Richter, S., Schwarz, R., Sheehy, C. D., Staniszewski, Z. K., Steinbach, B., Sudiwala, R. V., Teply, G. P., Thompson, K. L., Tolan, J. E., Tucker, C., Turner, A. D., Vieregg, A. G., Weber, A. C., Wiebe, D. V., Willmert, J., Wong, C. L., Wu, W. L. K., and Yoon, K. W., "Improved constraints on cosmology and foregrounds from

bicep2 and keck array cosmic microwave background data with inclusion of 95 ghz band," *Phys. Rev. Lett.* **116**, 031302 (Jan 2016).

[21] BICEP2 and Keck Array Collaborations, Ade, P. A. R., Ahmed, Z., Aikin, R. W., Alexander, K. D., Barkats, D., Benton, S. J., Bischoff, C. A., Bock, J. J., Brevik, J. A., Buder, I., Bullock, E., Buza, V., Connors, J., Crill, B. P., Dowell, C. D., Dvorkin, C., Duband, L., Filippini, J. P., Fliescher, S., Golwala, S. R., Halpern, M., Harrison, S., Hasselfield, M., Hildebrandt, S. R., Hilton, G. C., Hristov, V. V., Hui, H., Irwin, K. D., Karkare, K. S., Kaufman, J. P., Keating, B. G., Kefeli, S., Kernasovskiy, S. A., Kovac, J. M., Kuo, C. L., Leitch, E. M., Lueker, M., Mason, P., Megerian, K. G., Netterfield, C. B., Nguyen, H. T., O'Brient, R., Ogburn, IV, R. W., Orlando, A., Pryke, C., Reintsema, C. D., Richter, S., Schwarz, R., Sheehy, C. D., Staniszewski, Z. K., Sudiwala, R. V., Teply, G. P., Thompson, K. L., Tolan, J. E., Turner, A. D., Vieregg, A. G., Weber, A. C., Willmert, J., Wong, C. L., and Yoon, K. W., "BICEP2/Keck Array V: Measurements of B-mode Polarization at Degree Angular Scales and 150 GHz by the Keck Array," *ApJ* **811**, 126 (Oct. 2015).

[22] Crites, A. T., Henning, J. W., Ade, P. A. R., Aird, K. A., Austermann, J. E., Beall, J. A., Bender, A. N., Benson, B. A., Bleem, L. E., Carlstrom, J. E., Chang, C. L., Chiang, H. C., Cho, H.-M., Citron, R., Crawford, T. M., de Haan, T., Dobbs, M. A., Everett, W., Gallicchio, J., Gao, J., George, E. M., Gilbert, A., Halverson, N. W., Hanson, D., Harrington, N., Hilton, G. C., Holder, G. P., Holzapfel, W. L., Hoover, S., Hou, Z., Hrubes, J. D., Huang, N., Hubmayr, J., Irwin, K. D., Keisler, R., Knox, L., Lee, A. T., Leitch, E. M., Li, D., Liang, C., Luong-Van, D., McMahon, J. J., Mehl, J., Meyer, S. S., Mocanu, L., Montroy, T. E., Natoli, T., Nibarger, J. P., Novosad, V., Padin, S., Pryke, C., Reichardt, C. L., Ruhl, J. E., Saliwanchik, B. R., Sayre, J. T., Schaffer, K. K., Smecher, G., Stark, A. A., Story, K. T., Tucker, C., Vanderlinde, K., Vieira, J. D., Wang, G., Whitehorn, N., Yefremenko, V., and Zahn, O., "Measurements of E-Mode Polarization and Temperature-E-Mode Correlation in the Cosmic Microwave Background from 100 Square Degrees of SPTpol Data," *ApJ* **805**, 36 (May 2015).

[23] Louis, T., Grace, E., Hasselfield, M., Lungu, M., Maurin, L., Addison, G. E., Ade, P. A. R., Aiola, S., Allison, R., Amiri, M., Angile, E., Battaglia, N., Beall, J. A., de Bernardis, F., Bond, J. R., Britton, J., Calabrese, E., Cho, H.-m., Choi, S. K., Coughlin, K., Crichton, D., Crowley, K., Datta, R., Devlin, M. J., Dicker, S. R., Dunkley, J., Dünner, R., Ferraro, S., Fox, A. E., Gallardo, P., Gralla, M., Halpern, M., Henderson, S., Hill, J. C., Hilton, G. C., Hilton, M., Hincks, A. D., Hlozek, R., Ho, S. P. P., Huang, Z., Hubmayr, J., Huffenberger, K. M., Hughes, J. P., Infante, L., Irwin, K., Muya Kasanda, S., Klein, J., Koopman, B., Kosowsky, A., Li, D., Madhavacheril, M., Marriage, T. A.,

McMahon, J., Menanteau, F., Moodley, K., Munson, C., Naess, S., Nati, F., Newburgh, L., Nibarger, J., Niemack, M. D., Nolta, M. R., Nuñez, C., Page, L. A., Pappas, C., Partridge, B., Rojas, F., Schaan, E., Schmitt, B. L., Sehgal, N., Sherwin, B. D., Sievers, J., Simon, S., Spergel, D. N., Staggs, S. T., Switzer, E. R., Thornton, R., Trac, H., Treu, J., Tucker, C., Van Engelen, A., Ward, J. T., and Wollack, E. J., "The Atacama Cosmology Telescope: Two-Season ACTPol Spectra and Parameters," *ArXiv e-prints* (Oct. 2016).

[24] Keisler, R., Hoover, S., Harrington, N., Henning, J. W., Ade, P. A. R., Aird, K. A., Austermann, J. E., Beall, J. A., Bender, A. N., Benson, B. A., Bleem, L. E., Carlstrom, J. E., Chang, C. L., Chiang, H. C., Cho, H.-M., Citron, R., Crawford, T. M., Crites, A. T., de Haan, T., Dobbs, M. A., Everett, W., Gallicchio, J., Gao, J., George, E. M., Gilbert, A., Halverson, N. W., Hanson, D., Hilton, G. C., Holder, G. P., Holzapfel, W. L., Hou, Z., Hrubes, J. D., Huang, N., Hubmayr, J., Irwin, K. D., Knox, L., Lee, A. T., Leitch, E. M., Li, D., Luong-Van, D., Marrone, D. P., McMahon, J. J., Mehl, J., Meyer, S. S., Mocanu, L., Natoli, T., Nibarger, J. P., Novosad, V., Padin, S., Pryke, C., Reichardt, C. L., Ruhl, J. E., Saliwanchik, B. R., Sayre, J. T., Schaffer, K. K., Shirokoff, E., Smecher, G., Stark, A. A., Story, K. T., Tucker, C., Vanderlinde, K., Vieira, J. D., Wang, G., Whitehorn, N., Yefremenko, V., and Zahn, O., "Measurements of Sub-degree B-mode Polarization in the Cosmic Microwave Background from 100 Square Degrees of SPTpol Data," *ApJ* **807**, 151 (July 2015).

[25] Paine, S., "The am atmospheric model (v. 9.2)," (Mar. 2017).

[26] Fosalba, P., Lazarian, A., Prunet, S., and Tauber, J. A., "Statistical Properties of Galactic Starlight Polarization," *ApJ* **564**, 762–772 (Jan. 2002).

[27] Draine, B. T. and Lazarian, A., "Magnetic dipole microwave emission from dust grains," *The Astrophysical Journal* **512**(2), 740 (1999).

[28] Ade, P. A. R., Aghanim, N., Ahmed, Z., Aikin, R. W., Alexander, K. D., Arnaud, M., Aumont, J., Baccigalupi, C., Banday, A. J., Barkats, D., Barreiro, R. B., Bartlett, J. G., Bartolo, N., Battaner, E., Benabed, K., Benoît, A., Benoit-Lévy, A., Benton, S. J., Bernard, J.-P., Bersanelli, M., Bielewicz, P., Bischoff, C. A., Bock, J. J., Bonaldi, A., Bonavera, L., Bond, J. R., Borrill, J., Bouchet, F. R., Boulanger, F., Brevik, J. A., Bucher, M., Buder, I., Bullock, E., Burigana, C., Butler, R. C., Buza, V., Calabrese, E., Cardoso, J.-F., Catalano, A., Challinor, A., Chary, R.-R., Chiang, H. C., Christensen, P. R., Colombo, L. P. L., Combet, C., Connors, J., Couchot, F., Coulais, A., Crill, B. P., Curto, A., Cuttaia, F., Danese, L., Davies, R. D., Davis, R. J., de Bernardis, P., de Rosa, A., de Zotti, G., Delabrouille, J., Delouis, J.-M., Désert, F.-X., Dickinson, C., Diego, J. M., Dole, H., Donzelli, S., Doré, O.,

Douspis, M., Dowell, C. D., Duband, L., Ducout, A., Dunkley, J., Dupac, X., Dvorkin, C., Efstathiou, G., Elsner, F., Enßlin, T. A., Eriksen, H. K., Falgarone, E., Filippini, J. P., Finelli, F., Fliescher, S., Forni, O., Frailis, M., Fraisse, A. A., Franceschi, E., Frejsel, A., Galeotta, S., Galli, S., Ganga, K., Ghosh, T., Giard, M., Gjerløw, E., Golwala, S. R., González-Nuevo, J., Górski, K. M., Gratton, S., Gregorio, A., Gruppuso, A., Gudmundsson, J. E., Halpern, M., Hansen, F. K., Hanson, D., Harrison, D. L., Hasselfield, M., Helou, G., Henrot-Versillé, S., Herranz, D., Hildebrandt, S. R., Hilton, G. C., Hivon, E., Hobson, M., Holmes, W. A., Hovest, W., Hristov, V. V., Huffenberger, K. M., Hui, H., Hurier, G., Irwin, K. D., Jaffe, A. H., Jaffe, T. R., Jewell, J., Jones, W. C., Juvela, M., Karakci, A., Karkare, K. S., Kaufman, J. P., Keating, B. G., Kefeli, S., Keihänen, E., Kernasovskiy, S. A., Keskitalo, R., Kisner, T. S., Kneissl, R., Knoche, J., Knox, L., Kovac, J. M., Krachmalnicoff, N., Kunz, M., Kuo, C. L., Kurki-Suonio, H., Lagache, G., Lähteenmäki, A., Lamarre, J.-M., Lasenby, A., Lattanzi, M., Lawrence, C. R., Leitch, E. M., Leonardi, R., Levrier, F., Lewis, A., Liguori, M., Lilje, P. B., Linden-Vørnle, M., López-Caniego, M., Lubin, P. M., Lueker, M., Macías-Pérez, J. F., Maffei, B., Maino, D., Mandolesi, N., Mangilli, A., Maris, M., Martin, P. G., Martínez-González, E., Masi, S., Mason, P., Matarrese, S., Megerian, K. G., Meinhold, P. R., Melchiorri, A., Mendes, L., Mennella, A., Migliaccio, M., Mitra, S., Miville-Deschênes, M.-A., Moneti, A., Montier, L., Morgante, G., Mortlock, D., Moss, A., Munshi, D., Murphy, J. A., Naselsky, P., Nati, F., Natoli, P., Netterfield, C. B., Nguyen, H. T., Nørgaard-Nielsen, H. U., Noviello, F., Novikov, D., Novikov, I., O'Brient, R., Ogburn, R. W., Orlando, A., Pagano, L., Pajot, F., Paladini, R., Paoletti, D., Partridge, B., Pasian, F., Patanchon, G., Pearson, T. J., Perdereau, O., Perotto, L., Pettorino, V., Piacentini, F., Piat, M., Pietrobon, D., Plaszczynski, S., Pointecouteau, E., Polenta, G., Ponthieu, N., Pratt, G. W., Prunet, S., Pryke, C., Puget, J.-L., Rachen, J. P., Reach, W. T., Rebolo, R., Reinecke, M., Remazeilles, M., Renault, C., Renzi, A., Richter, S., Ristorcelli, I., Rocha, G., Rossetti, M., Roudier, G., Rowan-Robinson, M., Rubiño Martín, J. A., Rusholme, B., Sandri, M., Santos, D., Savelainen, M., Savini, G., Schwarz, R., Scott, D., Seiffert, M. D., Sheehy, C. D., Spencer, L. D., Staniszewski, Z. K., Stolyarov, V., Sudiwala, R., Sunyaev, R., Sutton, D., Suur-Uski, A.-S., Sygnet, J.-F., Tauber, J. A., Teply, G. P., Terenzi, L., Thompson, K. L., Toffolatti, L., Tolan, J. E., Tomasi, M., Tristram, M., Tucci, M., Turner, A. D., Valenziano, L., Valiviita, J., Van Tent, B., Vibert, L., Vielva, P., Vieregg, A. G., Villa, F., Wade, L. A., Wandelt, B. D., Watson, R., Weber, A. C., Wehus, I. K., White, M., White, S. D. M., Willmert, J., Wong, C. L., Yoon, K. W., Yvon, D., Zacchei, A., and Zonca, A., "Joint analysis of bicep2/keck array and planck data," *Phys. Rev. Lett.* **114**, 101301 (Mar 2015).

[29] Cortiglioni, S. and Spoelstra, T. A. T., "The limitations of cosmic-microwave-

background measurements due to linear polarization of galactic radio emission.," *A&A* **302**, 1 (Oct. 1995).

[30] Corporation, Z. D., "Zemax: geometric ray tracing and optical analysis software." https://www.zemax.com.

[31] Hecht, E., [*Optics*], Pearson education, Addison-Wesley (2002).

[32] Rayleigh, L., "Wave theory of light," *Enc. Brit* **24**, 91 (1888).

[33] Barakat, R., "Rayleigh wavefront criterion," *JOSA* **55**(5), 572–573 (1965).

[34] Staniszewski, Z., Aikin, R. W., Amiri, M., Benton, S. J., Bischoff, C., Bock, J. J., Bonetti, J. A., Brevik, J. A., Burger, B., Dowell, C. D., Duband, L., Filippini, J. P., Golwala, S. R., Halpern, M., Hasselfield, M., Hilton, G., Hristov, V. V., Irwin, K., Kovac, J. M., Kuo, C. L., Lueker, M., Montroy, T., Nguyen, H. T., Ogburn, R. W., O'Brient, R., Orlando, A., Pryke, C., Reintsema, C., Ruhl, J. E., Schwarz, R., Sheehy, C., Stokes, S., Thompson, K. L., Teply, G., Tolan, J. E., Turner, A. D., Vieregg, A. G., Wilson, P., Wiebe, D., and Wong, C. L., "The Keck Array: A Multi Camera CMB Polarimeter at the South Pole," *Journal of Low Temperature Physics* **167**, 827–833 (June 2012).

[35] Page, L., Jackson, C., Barnes, C., Bennett, C., Halpern, M., Hinshaw, G., Jarosik, N., Kogut, A., Limon, M., Meyer, S. S., Spergel, D. N., Tucker, G. S., Wilkinson, D. T., Wollack, E., and Wright, E. L., "The Optical Design and Characterization of the Microwave Anisotropy Probe," *ApJ* **585**, 566–586 (Mar. 2003).

[36] Tran, H. T., "Polarization comparison between on-axis and off-axis dual reflector telescopes: Zemax and Grasp8 simulations," *New Astronomy Reviews* **47**, 1091–1096 (Dec. 2003).

[37] Garcia, R. D. M., "Fresnel boundary and interface conditions for polarized radiative transfer in a multilayer medium," *J. Quant. Spec. Radiat. Transf.* **113**, 306–317 (Mar. 2012).

[38] Ade, T. P. C. P. A. R., Akiba, Y., Anthony, A. E., Arnold, K., Atlas, M., Barron, D., Boettger, D., Borrill, J., Chapman, S., Chinone, Y., Dobbs, M., Elleflot, T., Errard, J., Fabbian, G., Feng, C., Flanigan, D., Gilbert, A., Grainger, W., Halverson, N. W., Hasegawa, M., Hattori, K., Hazumi, M., Holzapfel, W. L., Hori, Y., Howard, J., Hyland, P., Inoue, Y., Jaehnig, G. C., Jaffe, A. H., Keating, B., Kermish, Z., Keskitalo, R., Kisner, T., Jeune, M. L., Lee, A. T., Leitch, E. M., Linder, E., Lungu, M., Matsuda, F., Matsumura, T., Meng, X., Miller, N. J., Morii, H., Moyerman, S., Myers, M. J., Navaroli, M., Nishino, H., Orlando, A., Paar, H., Peloton, J., Poletti, D., Quealy, E., Rebeiz, G., Reichardt, C. L., Richards, P. L., Ross, C., Schanning, I., Schenck,

D. E., Sherwin, B. D., Shimizu, A., Shimmin, C., Shimon, M., Siritanasak, P., Smecher, G., Spieler, H., Stebor, N., Steinbach, B., Stompor, R., Suzuki, A., Takakura, S., Tomaru, T., Wilson, B., Yadav, A., and Zahn, O., "A measurement of the cosmic microwave background b-mode polarization power spectrum at sub-degree scales with polarbear," *The Astrophysical Journal* **794**(2), 171 (2014).

[39] Dragone, C., "Offset multireflector antennas with perfect pattern symmetry and polarization discrimination," *Bell System Technical Journal* **57**(7), 2663–2684 (1978).

[40] Mizugutch, Y., Akagawa, M., and Yokoi, H., "Offset dual reflector antenna," in [*ISA Proceedings*], **1**, 2–5 (1976).

[41] Barron, D., Ade, P., Anthony, A., Arnold, K., Boettger, D., Borrill, J., Chapman, S., Chinone, Y., Dobbs, M., Edwards, J., Errard, J., Fabbian, G., Flanigan, D., Fuller, G., Ghribi, A., Grainger, W., Halverson, N., Hasegawa, M., Hattori, K., Hazumi, M., Holzapfel, W., Howard, J., Hyland, P., Jaehnig, G., Jaffe, A., Keating, B., Kermish, Z., Keskitalo, R., Kisner, T., Lee, A. T., Le Jeune, M., Linder, E., Lungu, M., Matsuda, F., Matsumura, T., Meng, X., Miller, N. J., Morii, H., Moyerman, S., Myers, M., Nishino, H., Paar, H., Peloton, J., Quealy, E., Rebeiz, G., Reichardt, C. L., Richards, P. L., Ross, C., Shimizu, A., Shimmin, C., Shimon, M., Sholl, M., Siritanasak, P., Spieler, H., Stebor, N., Steinbach, B., Stompor, R., Suzuki, A., Tomaru, T., Tucker, C., Yadav, A., and Zahn, O., "The polarbear cosmic microwave background polarization experiment," *Journal of Low Temperature Physics* **176**(5), 726–732 (2014).

[42] Ruze, J., "Antenna Tolerance Theory – A Review," *IEEE Proceedings* **54** (Apr. 1966).

[43] Arnold, K., Ade, P. A. R., Anthony, A. E., Barron, D., Boettger, D., Borrill, J., Chapman, S., Chinone, Y., Dobbs, M. A., Errard, J., Fabbian, G., Flanigan, D., Fuller, G., Ghribi, A., Grainger, W., Halverson, N., Hasegawa, M., Hattori, K., Hazumi, M., Holzapfel, W. L., Howard, J., Hyland, P., Jaffe, A., Keating, B., Kermish, Z., Kisner, T., Le Jeune, M., Lee, A. T., Linder, E., Lungu, M., Matsuda, F., Matsumura, T., Miller, N. J., Meng, X., Morii, H., Moyerman, S., Myers, M. J., Nishino, H., Paar, H., Quealy, E., Reichardt, C., Richards, P. L., Ross, C., Shimizu, A., Shimmin, C., Shimon, M., Sholl, M., Siritanasak, P., Speiler, H., Stebor, N., Steinbach, B., Stompor, R., Suzuki, A., Tomaru, T., Tucker, C., and Zahn, O., "The bolometric focal plane array of the polarbear cmb experiment," *Proc. SPIE* **8452**, 84521D–84521D–12 (2012).

[44] Kermish, Z. D., Ade, P., Anthony, A., Arnold, K., Barron, D., Boettger, D.,

Borrill, J., Chapman, S., Chinone, Y., Dobbs, M. A., Errard, J., Fabbian, G., Flanigan, D., Fuller, G., Ghribi, A., Grainger, W., Halverson, N., Hasegawa, M., Hattori, K., Hazumi, M., Holzapfel, W. L., Howard, J., Hyland, P., Jaffe, A., Keating, B., Kisner, T., Lee, A. T., Le Jeune, M., Linder, E., Lungu, M., Matsuda, F., Matsumura, T., Meng, X., Miller, N. J., Morii, H., Moyerman, S., Myers, M. J., Nishino, H., Paar, H., Quealy, E., Reichardt, C. L., Richards, P. L., Ross, C., Shimizu, A., Shimon, M., Shimmin, C., Sholl, M., Siritanasak, P., Spieler, H., Stebor, N., Steinbach, B., Stompor, R., Suzuki, A., Tomaru, T., Tucker, C., and Zahn, O., "The polarbear experiment," *Proc. SPIE* **8452**, 84521C–84521C–15 (2012).

[45] Murphy, T., Sadler, E. M., Ekers, R. D., Massardi, M., Hancock, P. J., Mahony, E., Ricci, R., Burke-Spolaor, S., Calabretta, M., Chhetri, R., de Zotti, G., Edwards, P. G., Ekers, J. A., Jackson, C. A., Kesteven, M. J., Lindley, E., Newton-McGee, K., Phillips, C., Roberts, P., Sault, R. J., Staveley-Smith, L., Subrahmanyan, R., Walker, M. A., and Wilson, W. E., "The Australia Telescope 20 GHz Survey: the source catalogue," *MNRAS* **402**, 2403–2423 (Mar. 2010).

[46] Mangum, J., "'a telescope pointing algorithm for alma'," tech. rep., ALMA memo 366 (2001).

[47] Greve, A., Panis, J.-F., and Thum, C., "The pointing of the IRAM 30-m telescope.," *A&AS* **115**, 379 (Feb. 1996).

[48] Ade, P. A. R., Akiba, Y., Anthony, A. E., Arnold, K., Atlas, M., Barron, D., Boettger, D., Borrill, J., Chapman, S., Chinone, Y., Dobbs, M., Elleflot, T., Errard, J., Fabbian, G., Feng, C., Flanigan, D., Gilbert, A., Grainger, W., Halverson, N. W., Hasegawa, M., Hattori, K., Hazumi, M., Holzapfel, W. L., Hori, Y., Howard, J., Hyland, P., Inoue, Y., Jaehnig, G. C., Jaffe, A., Keating, B., Kermish, Z., Keskitalo, R., Kisner, T., Le Jeune, M., Lee, A. T., Linder, E., Leitch, E. M., Lungu, M., Matsuda, F., Matsumura, T., Meng, X., Miller, N. J., Morii, H., Moyerman, S., Myers, M. J., Navaroli, M., Nishino, H., Paar, H., Peloton, J., Quealy, E., Rebeiz, G., Reichardt, C. L., Richards, P. L., Ross, C., Schanning, I., Schenck, D. E., Sherwin, B., Shimizu, A., Shimmin, C., Shimon, M., Siritanasak, P., Smecher, G., Spieler, H., Stebor, N., Steinbach, B., Stompor, R., Suzuki, A., Takakura, S., Tomaru, T., Wilson, B., Yadav, A., and Zahn, O., "Measurement of the cosmic microwave background polarization lensing power spectrum with the polarbear experiment," *Phys. Rev. Lett.* **113**, 021301 (Jul 2014).

[49] Ade, P. A. R., Akiba, Y., Anthony, A. E., Arnold, K., Atlas, M., Barron, D., Boettger, D., Borrill, J., Borys, C., Chapman, S., Chinone, Y., Dobbs, M., Elleflot, T., Errard, J., Fabbian, G., Feng, C., Flanigan, D., Gilbert, A.,

Grainger, W., Halverson, N. W., Hasegawa, M., Hattori, K., Hazumi, M., Holzapfel, W. L., Hori, Y., Howard, J., Hyland, P., Inoue, Y., Jaehnig, G. C., Jaffe, A., Keating, B., Kermish, Z., Keskitalo, R., Kisner, T., Le Jeune, M., Lee, A. T., Leitch, E. M., Linder, E., Lungu, M., Matsuda, F., Matsumura, T., Meng, X., Miller, N. J., Morii, H., Moyerman, S., Myers, M. J., Navaroli, M., Nishino, H., Paar, H., Peloton, J., Poletti, D., Quealy, E., Rebeiz, G., Reichardt, C. L., Richards, P. L., Ross, C., Rotermund, K., Schanning, I., Schenck, D. E., Sherwin, B. D., Shimizu, A., Shimmin, C., Shimon, M., Siritanasak, P., Smecher, G., Spieler, H., Stebor, N., Steinbach, B., Stompor, R., Suzuki, A., Takakura, S., Tikhomirov, A., Tomaru, T., Wilson, B., Yadav, A., and Zahn, O., "Evidence for gravitational lensing of the cosmic microwave background polarization from cross-correlation with the cosmic infrared background," *Phys. Rev. Lett.* **112**, 131302 (Apr 2014).

[50] Martin, D., "Polarizing (martin-puplett) interferometric spectrometers for the near-and submillimeter spectra," *Infrared and millimeter waves* **6**, 65–148 (1982).

[51] Martin, D. and Puplett, E., "Polarised interferometric spectrometry for the millimetre and submillimetre spectrum," *Infrared Physics* **10**(2), 105 – 109 (1970).

[52] Lambert, D. K. and Richards, P. L., "Martin-puplett interferometer: an analysis," *Appl. Opt.* **17**, 1595–1602 (May 1978).

[53] Larsen, T., "A survey of the theory of wire grids," *IRE Transactions on Microwave Theory and Techniques* **10**(3), 191–201 (1962).

[54] Saini, K. and Bradley, R., "The sinuous antenna-a dual polarized element for wideband phased array feed application," *NRAO Electronics Division Internal Report* **301**, 13 (1996).

[55] Stebor, N., Ade, P., Akiba, Y., Aleman, C., Arnold, K., Baccigalupi, C., Barch, B., Barron, D., Beckman, S., Bender, A., Boettger, D., Borrill, J., Chapman, S., Chinone, Y., Cukierman, A., de Haan, T., Dobbs, M., Ducout, A., Dunner, R., Elleflot, T., Errard, J., Fabbian, G., Feeney, S., Feng, C., Fujino, T., Fuller, G., Gilbert, A. J., Goeckner-Wald, N., Groh, J., Hall, G., Halverson, N., Hamada, T., Hasegawa, M., Hattori, K., Hazumi, M., Hill, C., Holzapfel, W. L., Hori, Y., Howe, L., Inoue, Y., Irie, F., Jaehnig, G., Jaffe, A., Jeong, O., Katayama, N., Kaufman, J. P., Kazemzadeh, K., Keating, B. G., Kermish, Z., Keskitalo, R., Kisner, T., Kusaka, A., Le Jeune, M., Lee, A. T., Leon, D., Linder, E. V., Lowry, L., Matsuda, F., Matsumura, T., Miller, N., Montgomery, J., Navaroli, M., Nishino, H., Paar, H., Peloton, J., Poletti, D., Puglisi, G., Raum, C. R., Rebeiz, G. M., Reichardt, C. L., Richards, P. L., Ross, C., Rotermund, K. M., Segawa, Y., Sherwin, B. D., Shirley, I.,

Siritanasak, P., Steinmetz, L., Stompor, R., Suzuki, A., Tajima, O., Takada, S., Takatori, S., Teply, G. P., Tikhomirov, A., Tomaru, T., Westbrook, B., Whitehorn, N., Zahn, A., and Zahn, O., "The simons array cmb polarization experiment," *Proc. SPIE* **9914**, 99141H–99141H–9 (2016).

[56] Palanque-Delabrouille, N., Yèche, C., Baur, J., Magneville, C., Rossi, G., Lesgourgues, J., Borde, A., Burtin, E., LeGoff, J.-M., Rich, J., Viel, M., and Weinberg, D., "Neutrino masses and cosmology with lyman-alpha forest power spectrum," *Journal of Cosmology and Astroparticle Physics* **2015**(11), 011 (2015).

[57] Cuesta, A. J., Niro, V., and Verde, L., "Neutrino mass limits: robust information from the power spectrum of galaxy surveys," *Physics of the Dark Universe* **13**, 77–86 (2016).

[58] Shimon, M., Keating, B., Ponthieu, N., and Hivon, E., "Cmb polarization systematics due to beam asymmetry: Impact on inflationary science," *Phys. Rev. D* **77**, 083003 (Apr 2008).

[59] Miller, N. J., Shimon, M., and Keating, B. G., "Cmb beam systematics: Impact on lensing parameter estimation," *Phys. Rev. D* **79**, 063008 (Mar 2009).

[60] Miller, N. J., Shimon, M., and Keating, B. G., "Cmb polarization systematics due to beam asymmetry: Impact on cosmological birefringence," *Phys. Rev. D* **79**, 103002 (May 2009).

[61] Dragone, C., "A first-order treatment of aberrations in cassegrainian and gregorian antennas," *IEEE Transactions on Antennas and Propagation* **30**, 331–339 (May 1982).

[62] Dragone, C., "First-order correction of aberrations in cassegrainian and gregorian antennas," *IEEE Transactions on Antennas and Propagation* **31**, 764–775 (September 1983).

[63] Ludwig, A., "The definition of cross polarization," *IEEE Transactions on Antennas and Propagation* **21**, 116–119 (Jan 1973).

[64] Chu, T.-S. and Turrin, R., "Depolarization properties of offset reflector antennas," *IEEE Transactions on Antennas and Propagation* **21**, 339–345 (May 1973).

[65] Tran, H., Lee, A., Hanany, S., Milligan, M., and Renbarger, T., "Comparison of the crossed and the gregorian mizuguchi-dragone for wide-field millimeter-wave astronomy," *Appl. Opt.* **47**, 103–109 (Jan 2008).

[66] Bischoff, C., Brizius, A., Buder, I., Chinone, Y., Cleary, K., Dumoulin, R. N.,

Kusaka, A., Monsalve, R., Næss, S. K., Newburgh, L. B., Nixon, G., Reeves, R., Smith, K. M., Vanderlinde, K., Wehus, I. K., Bogdan, M., Bustos, R., Church, S. E., Davis, R., Dickinson, C., Eriksen, H. K., Gaier, T., Gundersen, J. O., Hasegawa, M., Hazumi, M., Holler, C., Huffenberger, K. M., Imbriale, W. A., Ishidoshiro, K., Jones, M. E., Kangaslahti, P., Kapner, D. J., Lawrence, C. R., Leitch, E. M., Limon, M., McMahon, J. J., Miller, A. D., Nagai, M., Nguyen, H., Pearson, T. J., Piccirillo, L., Radford, S. J. E., Readhead, A. C. S., Richards, J. L., Samtleben, D., Seiffert, M., Shepherd, M. C., Staggs, S. T., Tajima, O., Thompson, K. L., Williamson, R., Winstein, B., Wollack, E. J., and Zwart, J. T. L., "The q/u imaging experiment instrument," *The Astrophysical Journal* **768**(1), 9 (2013).

[67] TICRA, "Grasp10 and quast add-on: electromagnetic analysis of reflector antennas and scatters." http://www.ticra.com/grasp.

[68] Satoru, T., *Characterization of a continuous polarization modulator using a half-wave plate for measurements of degree-scale cosmic microwave background with the POLARBEAR experiment*, PhD thesis, Osaka University, Toyonaka (in preparation).

[69] Hivon, E., Górski, K. M., Netterfield, C. B., Crill, B. P., Prunet, S., and Hansen, F., "MASTER of the Cosmic Microwave Background Anisotropy Power Spectrum: A Fast Method for Statistical Analysis of Large and Complex Cosmic Microwave Background Data Sets," *ApJ* **567**, 2–17 (Mar. 2002).

[70] Ishino, H., Akiba, Y., Arnold, K., Barron, D., Borrill, J., Chendra, R., Chinone, Y., Cho, S., Cukierman, A., de Haan, T., Dobbs, M., Dominjon, A., Dotani, T., Elleflot, T., Errard, J., Fujino, T., Fuke, H., Funaki, T., Goeckner-Wald, N., Halverson, N., Harvey, P., Hasebe, T., Hasegawa, M., Hattori, K., Hattori, M., Hazumi, M., Hidehira, N., Hill, C., Hilton, G., Holzapfel, W., Hori, Y., Hubmayr, J., Ichiki, K., Imada, H., Inatani, J., Inoue, M., Inoue, Y., Irie, F., Irwin, K., Ishitsuka, H., Jeong, O., Kanai, H., Karatsu, K., Kashima, S., Katayama, N., Kawano, I., Kawasaki, T., Keating, B., Kernasovskiy, S., Keskitalo, R., Kibayashi, A., Kida, Y., Kimura, N., Kimura, K., Kisner, T., Kohri, K., Komatsu, E., Komatsu, K., Kuo, C.-L., Kuromiya, S., Kusaka, A., Lee, A., Li, D., Linder, E., Maki, M., Matsuhara, H., Matsumura, T., Matsuoka, S., Matsuura, S., Mima, S., Minami, Y., Mitsuda, K., Nagai, M., Nagasaki, T., Nagata, R., Nakajima, M., Nakamura, S., Namikawa, T., Naruse, M., Nishibori, T., Nishijo, K., Nishino, H., Noda, A., Noguchi, T., Ogawa, H., Ogburn, W., Oguri, S., Ohta, I., Okada, N., Okamoto, A., Okamura, T., Otani, C., Pisano, G., Rebeiz, G., Richards, P., Sakai, S., Sakurai, Y., Sato, Y., Sato, N., Segawa, Y., Sekiguchi, S., Sekimoto, Y., Sekine, M., Seljak, U., Sherwin, B., Shimizu, T., Shinozaki, K., Shu, S., Stompor, R., Sugai, H., Sugita, H., Suzuki, J., Suzuki, T., Suzuki, A., Tajima, O., Takada,

S., Takakura, S., Takano, K., Takatori, S., Takei, Y., Tanabe, D., Tomaru, T., Tomita, N., Turin, P., Uozumi, S., Utsunomiya, S., Uzawa, Y., Wada, T., Watanabe, H., Westbrook, B., Whitehorn, N., Yamada, Y., Yamamoto, R., Yamasaki, N., Yamashita, T., Yoshida, T., Yoshida, M., and Yotsumoto, K., "Litebird: lite satellite for the study of b-mode polarization and inflation from cosmic microwave background radiation detection," *Proc. SPIE* **9904**, 99040X–99040X–8 (2016).

[71] Benson, B. A., Ade, P. A. R., Ahmed, Z., Allen, S. W., Arnold, K., Austermann, J. E., Bender, A. N., Bleem, L. E., Carlstrom, J. E., Chang, C. L., Cho, H. M., Cliche, J. F., Crawford, T. M., Cukierman, A., de Haan, T., Dobbs, M. A., Dutcher, D., Everett, W., Gilbert, A., Halverson, N. W., Hanson, D., Harrington, N. L., Hattori, K., Henning, J. W., Hilton, G. C., Holder, G. P., Holzapfel, W. L., Irwin, K. D., Keisler, R., Knox, L., Kubik, D., Kuo, C. L., Lee, A. T., Leitch, E. M., Li, D., McDonald, M., Meyer, S. S., Montgomery, J., Myers, M., Natoli, T., Nguyen, H., Novosad, V., Padin, S., Pan, Z., Pearson, J., Reichardt, C., Ruhl, J. E., Saliwanchik, B. R., Simard, G., Smecher, G., Sayre, J. T., Shirokoff, E., Stark, A. A., Story, K., Suzuki, A., Thompson, K. L., Tucker, C., Vanderlinde, K., Vieira, J. D., Vikhlinin, A., Wang, G., Yefremenko, V., and Yoon, K. W., "Spt-3g: a next-generation cosmic microwave background polarization experiment on the south pole telescope," *Proc. SPIE* **9153**, 91531P–91531P–21 (2014).

[72] Ward, J. T., Austermann, J., Beall, J. A., Choi, S. K., Crowley, K. T., Devlin, M. J., Duff, S. M., Gallardo, P. A., Henderson, S. W., Ho, S.-P. P., Hilton, G., Hubmayr, J., Khavari, N., Klein, J., Koopman, B. J., Li, D., McMahon, J., Mumby, G., Nati, F., Niemack, M. D., Page, L. A., Salatino, M., Schillaci, A., Schmitt, B. L., Simon, S. M., Staggs, S. T., Thornton, R., Ullom, J. N., Vavagiakis, E. M., and Wollack, E. J., "Mechanical designs and development of tes bolometer detector arrays for the advanced actpol experiment," *Proc. SPIE* **9914**, 991437–991437–9 (2016).

[73] Essinger-Hileman, T., Ali, A., Amiri, M., Appel, J. W., Araujo, D., Bennett, C. L., Boone, F., Chan, M., Cho, H.-M., Chuss, D. T., Colazo, F., Crowe, E., Denis, K., Dünner, R., Eimer, J., Gothe, D., Halpern, M., Harrington, K., Hilton, G. C., Hinshaw, G. F., Huang, C., Irwin, K., Jones, G., Karakla, J., Kogut, A. J., Larson, D., Limon, M., Lowry, L., Marriage, T., Mehrle, N., Miller, A. D., Miller, N., Moseley, S. H., Novak, G., Reintsema, C., Rostem, K., Stevenson, T., Towner, D., U-Yen, K., Wagner, E., Watts, D., Wollack, E. J., Xu, Z., and Zeng, L., "CLASS: the cosmology large angular scale surveyor," *Proc. SPIE* **9153**, 91531I (July 2014).

[74] Hui, H., Ade, P. A. R., Ahmed, Z., Alexander, K. D., Amiri, M., Barkats, D., Benton, S. J., Bischoff, C. A., Bock, J. J., Boenish, H., Bowens-Rubin, R.,

Bowens-Rubin, R., Buder, I., Bullock, E., Buza, V., Connors, J., Filippini, J. P., Fliescher, S., Grayson, J. A., Halpern, M., Harrison, S., Hilton, G. C., Hristov, V. V., Irwin, K. D., Kang, J., Karkare, K. S., Karpel, E., Kefeli, S., Kernasovskiy, S. A., Kovac, J. M., Kuo, C. L., Leitch, E. M., Lueker, M., Megerian, K. G., Monticue, V., Namikawa, T., Netterfield, C. B., Nguyen, H. T., O'Brient, R., Ogburn, R. W., Pryke, C., Reintsema, C. D., Richter, S., Schwarz, R., Sorensen, C., Sheehy, C. D., Staniszewski, Z. K., Steinbach, B., Teply, G. P., Thompson, K. L., Tolan, J. E., Tucker, C., Turner, A. D., Vieregg, A. G., Wandui, A., Weber, A. C., Wiebe, D. V., Willmert, J., Wu, W. L. K., and Yoon, K. W., "BICEP3 focal plane design and detector performance," *Proc. SPIE* **9914**, 99140T (July 2016).

[75] Abazajian, K. N., Adshead, P., Ahmed, Z., Allen, S. W., Alonso, D., Arnold, K. S., Baccigalupi, C., Bartlett, J. G., Battaglia, N., Benson, B. A., Bischoff, C. A., Borrill, J., Buza, V., Calabrese, E., Caldwell, R., Carlstrom, J. E., Chang, C. L., Crawford, T. M., Cyr-Racine, F.-Y., De Bernardis, F., de Haan, T., di Serego Alighieri, S., Dunkley, J., Dvorkin, C., Errard, J., Fabbian, G., Feeney, S., Ferraro, S., Filippini, J. P., Flauger, R., Fuller, G. M., Gluscevic, V., Green, D., Grin, D., Grohs, E., Henning, J. W., Hill, J. C., Hlozek, R., Holder, G., Holzapfel, W., Hu, W., Huffenberger, K. M., Keskitalo, R., Knox, L., Kosowsky, A., Kovac, J., Kovetz, E. D., Kuo, C.-L., Kusaka, A., Le Jeune, M., Lee, A. T., Lilley, M., Loverde, M., Madhavacheril, M. S., Mantz, A., Marsh, D. J. E., McMahon, J., Meerburg, P. D., Meyers, J., Miller, A. D., Munoz, J. B., Nguyen, H. N., Niemack, M. D., Peloso, M., Peloton, J., Pogosian, L., Pryke, C., Raveri, M., Reichardt, C. L., Rocha, G., Rotti, A., Schaan, E., Schmittfull, M. M., Scott, D., Sehgal, N., Shandera, S., Sherwin, B. D., Smith, T. L., Sorbo, L., Starkman, G. D., Story, K. T., van Engelen, A., Vieira, J. D., Watson, S., Whitehorn, N., and Kimmy Wu, W. L., "CMB-S4 Science Book, First Edition," *ArXiv e-prints* (Oct. 2016).